



BRNO UNIVERSITY OF TECHNOLOGY

VYSOKÉ UČENÍ TECHNICKÉ V BRNĚ

CENTRAL EUROPEAN INSTITUTE OF TECHNOLOGY BUT

STŘEDOEVROPSKÝ TECHNOLOGICKÝ INSTITUT VUT

X-RAY MICRO AND NANO COMPUTED TOMOGRAPHY OF SOFT TISSUE

RENTGENOVÁ POČÍTAČOVÁ TOMOGRAFIE MĚKKÝCH TKÁNÍ

DOCTORAL THESIS

DIZERTAČNÍ PRÁCE

AUTHOR

AUTOR PRÁCE

Mgr. Michaela Kavková

SUPERVISOR

ŠKOLITEL

doc. Ing. Tomáš Zikmund, Ph.D.

BRNO 2023

Abstract

Industrial X-ray micro computed tomography (micro CT) is a non-destructive imaging technique used for visualization of internal structures of samples and creation of precise 3D models. The core of this thesis revolves around the practical implementation of industrial micro CT in biological research with focus on the imaging of soft tissues. The aim of this study was to explore the potential of industrial micro CT as a non-destructive imaging tool for soft tissue visualization and to propose complex methodology for preparation of the sample and the analysis of obtained data in the specialized software. In the thesis the case studies showcasing the diverse applications of micro CT in various developmental biology research domains are presented, providing the methodology for precise 3D analysis of the selected structures. The thesis concludes by summarizing the transformative potential of industrial micro CT in biological research, highlighting its ability to unveil intricate anatomical structures, track developmental processes, and enhance our understanding of complex biological systems.

Abstrakt

Průmyslová rentgenová počítačová mikro tomografie (mikro CT) je nedestruktivní zobrazovací technika používaná pro vizualizaci vnitřních struktur vzorků a tvorbu přesných 3D modelů. Jádro této práce se zaměřuje na praktickou implementaci průmyslového mikro CT v oblasti biologického výzkumu se zaměřením na zobrazování měkkých tkání. Cílem této práce bylo prozkoumat potenciál mikro CT zobrazování jako nedestruktivní metody pro vizualizaci měkkých tkání a navrhnout komplexní metodiku pro přípravu vzorků a analýzu získaných dat ve specializovaných programech. Na příkladu případových studií jsou prezentovány aplikace mikro CT zobrazování v různorodých oblastech výzkumu vývojové biologie, poskytující metodologii pro přesnou 3D analýzu vybraných struktur. V závěru práce je diskutován potenciál zobrazování průmyslovým mikro CT v biologickém výzkumu, zaměřeným na schopnosti identifikovat anatomické struktury, sledovat vývojové procesy a zlepšit naše chápání komplexních biologických systémů.

Keywords

X-ray micro computed tomography, soft tissues, advanced 3D imaging, micro CT contrasting protocols

Klíčová slova

Rentgenová počítačová tomografie, měkké tkáně, pokročilé 3D zobrazování, kontrastovací protokoly pro mikro CT

I declare that in this doctoral thesis, I am presenting the research I have conducted and was part of during my PhD study and that the literature review and other professional sources are properly cited in this work.

Mgr. Michaela Kavková

Acknowledgement

At first, I would like to thank my supervisor Tomáš Zikmund for giving me the opportunity to join his research group, I would also like to thank all of my colleagues from CT lab for the pleasant time we spent working on the research projects and the fun we had during the extra-lab activities. And last but not least I would like to thank Marcela Buchtová and her research group for letting me join on some of the most interesting research projects.

Poděkování

Na tomto místě bych ráda poděkovala svému vedoucímu Tomáši Zikmundovi za důvěru se kterou mě přijal do jeho výzkumné skupiny, všem bývalým i současným kolegům z CT laboratoře za příjemně strávený čas prací na projektech i aktivitami mimo laboratoř a závěrem bych ráda poděkovala Marcele Buchtové a její výzkumné skupině díky nimž jsem se mohla podílet na spoustě zajímavých projektů.

Table of Contents

1. Literature review	9
1.1. Model organisms in developmental biology.....	9
1.2. Imaging methods in biological research.....	9
1.3. Magnetic resonance imaging.....	10
1.3.1 Comparison of the MRI with the CT imaging.....	12
1.4. X-ray Computed Tomography.....	13
1.4.1. In vivo and ex vivo CT devices.....	14
1.4.2. Artifacts occurring during the CT measurement.....	16
1.4.3 Phantoms for calibrating CT measurements.....	18
1.5. Contrast agents used for visualization of soft tissues in micro CT imaging.....	19
1.5.1. In vivo micro CT contrast agents.....	19
1.5.2. Diffusion based staining agents (ex vivo).....	20
1.5.2.1. Staining with Iodine.....	20
1.5.2.2. Staining with Phosphotungstic acid.....	22
1.5.2.3. Staining with Osmium tetroxide.....	22
1.5.3. Corrosion casting contrasting agents.....	23
1.5.4. Tissue specific staining agents.....	24
1.6. Software for the analysis of micro CT data.....	25
2. Aims of the Doctoral Thesis	26
3. Methods	27
3.1. The pre-staining steps (tissue fixation, dehydration).....	27
3.2. Selection of the staining agents for visualization of soft tissues.....	27
3.3. Motion stabilization of the sample during scan.....	30
3.4. Micro CT devices.....	31
3.5. Analysis of the obtained micro CT data in specialized software.....	31
4. Results	33
4.1. Determining and optimizing the contrasting protocols.....	33
4.1.1. Novelty contrasting protocol for imaging of the mouse brain.....	33
4.1.2. Contrasting of the mouse embryo.....	37
4.1.3. Testing of the developed contrasting protocol on different types of samples.....	40
4.2. Applications of developed contrasting protocols and designing the data analysis.....	42

4.2.1. Visualizing the A β plaques in the rat brain in Alzheimer's disease research.....	42
4.2.2. Loss of function of CDK13 gene during development.....	48
4.2.3. The role of SATB2 gene in development of dentition.....	49
4.2.4. Role of the TMEM107 gene in eye development.....	52
4.2.5. Imaging of the emerging tooth ankylosis in chameleon embryo.....	54
5. Conclusions.....	59
6. References.....	61
7. Author publications and other outputs.....	71

Introduction

Embryos of several vertebrate species (*Mus musculus*, *Xenopus laevis* or *Danio rerio*) are popular model organisms for the research of the complex developmental processes. In order to fully understand the processes of morphogenesis the imaging methods are vital in revealing the underlying biological mechanisms. In the advanced research of complex biological samples, the precise three-dimensional visualizations of the morphology of embryos is important for understanding the mechanisms that drive embryogenesis.

Traditional methods of tissue analysis involve the sectioning of the sample for optical microscopy imaging, however the creation of the accurate 3D model from the sectioned sample risks distortion and degradation of spatial resolution. The recent advances in a field of X-ray micro Computed Tomography imaging - sensitive detectors, powerful X-ray sources and mainly the software enhancements of the data analysis - enabled the acquisition of the high resolution data of the very small samples. The opportunity to precisely visualize the small vertebrate embryos in 3D makes the micro CT imaging a great method in the primary biological research.

The increasing availability of micro CT devices has encouraged development of innovative staining procedures utilizing X-ray imaging to analyze soft-tissues which are typically poorly visible in the native micro CT scans. The contrasting protocols developed for visualization of soft tissues shows promising results in overcoming the limitations of soft tissues imaging such as naturally low radiodensity.

This thesis is focused on development of contrasting protocols and preparation of the biological samples for the purpose of micro CT imaging and design of the follow up advanced analyses of obtained tomographic data. The novelty 3D analyses, together with newly developed contrasting protocols can expand the applications of micro CT in soft tissues imaging, which is useful in the comparative and quantitative studies of animal morphology and development.

1. Literature review

1.1. Model organisms in developmental biology

Model organisms are specifically selected species of organisms which are used in biological research to investigate the function of genes and to describe complex biological processes.

By manipulating the expression of a particular gene, the function of the specific gene can be determined in the organism's biology. The model organisms are selected based on their short generation time and relatively simple genome, making it easier to observe the effects of genetic changes. Amongst the commonly used model in the research of developmental biology are the zebrafish (*Danio rerio*), xenopus frog (*Xenopus laevis*) and the mouse (*Mus musculus*).

The zebrafish is a popular model organism for studying vertebrate development and genetics. Its transparent embryos and rapid development make it easy to observe the effects of genetic changes on development, and its genome is well annotated (Roussel *et al.*, 2021).

In the area of embryonic development research, the *Xenopus* frog has a major advantage: it is its large, easily accessible eggs, which provide a unique platform for studying embryonic development, furthermore the embryos are transparent, which allows researchers to observe and manipulate development in real-time (Borodinsky *et al.*, 2017).

The mouse model is commonly used in developmental biology to study the embryonic development, organogenesis, morphogenesis, as well as the description of the causes of developmental defects. Mice are suitable model for this purpose because they are mammals, and their genome is similar to human genome (Wasserman *et al.*, 2000). The genetic manipulation of the mouse genome is easier in comparison to the other model organisms since it has been extensively sequenced and is well annotated (McGarvey *et al.*, 2015).

1.2. Imaging methods in biological research

From the times of invention of early microscopes to the most recent innovations in form of confocal/light sheet microscopes, magnetic resonance imaging and X-ray computed tomography, the introduction of advanced visualization techniques have greatly expanded our knowledge about the internal structures of biological systems. Each of these techniques has its strengths and limitations, and the choice of technique depends on the specific research question and the characteristics of the sample.

Visualization techniques in the biological research have traditionally included approaches such as serial histological sectioning and optical microscopy which uses visible light and lenses to magnify and focus an image. It can provide very high resolution images of small objects, such as cells, tissues, and microorganisms. However, the histological sectioning is not a perfect process, where some of the slices might be damaged causing the challenging aligning of the multiple slices of one sample into the final 3D model. The destructive process of slicing the sample and aligning them into a three dimensional dataset is intricate and thus this method is not suitable for imaging of large or dense objects in 3D space.

A major breakthrough in terms of feasibility of 3D imaging came with the introduction of computers into biomedical research. Digital images of histological sections could be directly captured with the aid of digital photographs (Rizzuto *et al.*, 1998) where the quality and resolution of digital images of histological sections captured using modern hi-tech microscopes (confocal, light sheet) are unparalleled compared to other imaging techniques. With help of specialized imaging software which allows processing of these digital images the generation and visualization of 3D models is possible.

Within a histological context, microscopic techniques like confocal and light sheet microscopy have a remarkable 2D resolution. They are both optical microscopy techniques which uses lasers to excite fluorescence in biological samples. Confocal microscopy uses a pinhole to selectively focus on a particular plane of the sample (Paddock 2000) while the light sheet microscopy uses a thin sheet of light to illuminate the sample (Wan *et al.*, 2019) The confocal microscopy is well suited for imaging of relatively thin samples such as sectioned tissues and cells. The light sheet microscopy best suited for the wholemount samples such as embryos, it can provide high-resolution, three-dimensional images of the internal structures of these samples. However, both of these imaging methods are limited by the penetration depth of the laser light, which can restrict imaging of the thicker samples (Elisa *et al.*, 2018).

More recently, non-destructive 3D imaging techniques such as micro computed tomography and the magnetic resonance imaging are becoming increasingly important in various scientific fields, especially since powerful computers and advanced software for 3D analysis allows anatomical visualization of a broad range of tissue types, specimens, and sizes.

1.3. Magnetic resonance imaging

Magnetic resonance imaging (MRI) is a non-invasive imaging technique which doesn't use ionizing radiation and provides detailed images of soft tissues and internal. MRI is an imaging technique which uses a strong magnetic field to create detailed images of the internal

structures of the examined object. The basic principle behind MRI is mapping the behavior of hydrogen atoms in the sample when exposed to a strong magnetic field (Van Geuns *et al.*, 1999).

The first clinical MRI scanner were introduced in the early 1980s, and it quickly became a valuable tool for diagnosing wide range of medical conditions. The modern MRI scanners are faster and produce even higher quality images than their predecessors, they are also capable of performing advanced imaging techniques, such as functional MRI (fMRI), which can be used to visualize brain activity in real time (Casey *et al.*, 2002). MRI is also capable of diagnosing a wide range of medical conditions, including brain and spinal cord injuries, tumors, and joint disorders.

The principle of the MRI imaging is based on the use of strong magnetic field inside the MRI scanner which causes the MR active atoms (such as hydrogen atoms) in the body to align with the field. A radio frequency pulse is then applied to the body, causing the hydrogen atoms to absorb energy and flip their orientation. As the atoms return to their original alignment, they release energy in the form of radio waves. The signal obtained from radio waves is processed by a computer, which produces a 3D image of the internal structures of examined sample (Van Geuns *et al.*, 1999). Different tissues in the body have different magnetic properties (tissues in the body contain different amounts of water), which allows the MRI machine to distinguish between the tissues and produce detailed images of soft tissues (Brown *et al.*, 2014). To improve the contrast between different tissues, additional radio waves can be applied at different frequencies, causing atoms in different tissues to release energy at different times. The resulting signals can then be analyzed to create detailed images of the body that differentiate between different types of tissue, such as muscle, fat, or bone (Casey *et al.*, 2002).

The strength of the magnetic field used in MRI is measured in tesla (T), with most clinical MRI machines operating at 1.5 T or 3 T. It can be commonly applied that the higher the field strength, the better image quality the particular scanner produces.

Nowadays MRI imaging is often used in preclinical and clinical imaging. MRI is capable of imaging of soft tissue in whole specimens in *ex vivo* as well as *in vivo*. The absence of ionizing radiation enables broad application of this technique in both human medicine and long-term studies involving small animals. Depending on the type of magnet used and the imaging equipment available, specimens of all sizes can be imaged. Typically, the coils used in preclinical (scientific) scanners provide enough room to fit entire mice or rats (Bock *et al.*, 2005), whereas those in clinical scanners can accommodate human-sized samples (Frisoni *et al.*, 2010)

In biology research, MRI is used to study a wide range of biological systems and processes. MRI can be used to visualize the anatomy of various organs and tissues, including the brain, heart, lungs, and muscles. This imaging technique can be also combined with contrast agents to visualize specific molecules or biomarkers *in vivo* which can help with functional studies of the distribution and kinetics of various molecules in biological systems (Wahsner *et al.*, 2018).

1.3.1 Comparison of the MRI with the CT imaging

The MRI imaging and the CT imaging are both commonly used 3D imaging techniques which provide detailed information about the internal structures of the body. Both techniques use different physical principles to create images, and each has its own advantages and disadvantages. When comparing the speed of the imaging the medical CT scans are typically faster than MRI scans and can produce high-quality images in just a few seconds (Flohr 2013). The industrial micro CT systems used for the ex-vivo have on the other hand comparable scan times as the MRI ranging in the hours scale (Bock *et al.*, 2005; Kavkova *et al.*, 2020). Voxel resolution is an important aspect of both MRI and CT imaging, as it determines the level of detail that can be visualized in the resulting images. Voxel is a 3D pixel that represents a smallest image element in the 3D data. Voxel resolution refers to the size of the voxel in each dimension, which is determined by the imaging parameters used during data acquisition. When comparing the voxel resolution of both methods, CT imaging has in general higher spatial resolution and smaller voxel size compared to MRI imaging (Bock *et al.*, 2005; Kavkova *et al.*, 2020). Also, from the principle of obtaining the data during the scan the CT produces the data with isotropic voxel size (the image elements are cubic) (Hsieh *et al.*, 2009) in contrast to the MRI in which in most cases the voxel size is not isotropic – the in plane resolution is equal in size but the thickness of a slice can differ (Rizzuto *et al.*, 1998). The isotropic voxel size ensures the higher fidelity of the obtained data.

Regarding the application potential of both techniques the CT imaging is particularly useful for imaging the bones, as it can provide detailed information about bone density and structure, it is often used to diagnose fractures, bone tumors, and osteoporosis (Sampson *et al.*, 2006). But the CT has limited ability to differentiate between soft tissues with similar densities, such as different types of organs and thus the CT scans often require the use of contrast material, to be able to visualize the soft tissues. In the clinical environment the contrast agents are commonly administered to the patient orally or intravascularly. In the case of ex-vivo imaging of the samples the contrast agent is the solution of the specific elements in which the sample is

submerged and the contrast agent diffuses into the sample (Zikmund *et al.*, 2018). MRI is on the other hand primarily designed for the imaging of soft tissues, such as the brain, muscles, and organs. MRI can provide detailed information about the structure and function of these tissues.

One of the disadvantages of the CT scans is that they involve exposure to ionizing radiation, which can increase the risk of cancer over time (Hui *et al.*, 2004). The amount of radiation exposure in a CT scan is typically higher than in other imaging modalities, such as x-rays. On the other hand, the MRI scans do not use ionizing radiation, making them a safer option for repeated and frequent *in vivo* imaging.

In summary, CT scans are generally faster and less expensive than MRI scans, and better at imaging bone, while MRI scans provide more detailed images of soft tissue structures and are safer for patients who need repeated imaging.

1.4. X-ray Computed Tomography

Computed tomography (CT) is a 3D imaging method using the X-rays to create detailed images of the inside structures of the examined sample.

The work of Johann Radon laid the theoretical foundation for CT imaging, in 1917 the mathematician published a mathematical formula for reconstructing a function from its projections later called the Radon transformation.

Only later with the development of the more precise machinery the first commercial CT scanner intended for the medical use was introduced in 1972. CT imaging was able to produce much more detailed and precise images compared to the previously used 2D X-ray images, enabling doctors to diagnose and treat a wide range of conditions with greater accuracy. Over the years, CT technology has continued to evolve and improve. The technology of CT imaging started to leak into the other sectors such as imaging of materials in Industry (Bartscher *et al.*, 2007). Modern CT scanners are faster, more powerful, and produce even higher quality images than their predecessors.

The principle of X-ray computed tomography imaging is based on the projecting of the X-ray beam produced by X-ray source through the examined specimen. The x-rays are attenuated by the sample in a specific pattern depending on the atomic composition of the sample. Attenuation refers to the reduction in the intensity of X-rays as it passes through scanned sample, the amount of attenuation depends on the atomic composition and thickness of the material, as well as the energy of the X-rays. The X-rays which pass through the examined sample are detected by the x-ray sensitive detectors and the series of radiograms are created.

During the acquisition of the data the radiograms from multiple angles around the specimen are obtained. The final step of CT scan is the tomographic reconstruction, the process in which the final 3D tomographic data is created from the obtained radiographs. The process of tomographic reconstruction is generally based on the filtered back projection algorithm, the obtained radiograms are processed into the 3D matrix of isotropic voxels (3D pixels) with values proportional to mean linear X-ray attenuation coefficient within each voxel (Hsieh *et al.*, 2009).

1.4.1. *In vivo* and *ex vivo* CT devices

In general, the computed tomography devices can be divided into two common groups based on the intended use of the scanner and the basic geometry of the system.

In vivo CT devices

In the first group are the medical CT systems where the setup consists of mobile X-ray source and detector which are rotating around patient in fixed position (Fig. 1). This setup is commonly referred as *in vivo* micro CT systems, where the main focus is on the speed of the scan since the least possible irradiation of the patient during the scan is highly desired. The other concern in this type of scanners is ensuring the stable position of the patient since the CT imaging is often used as a first method to assess the patients with traumatic injuries. Medical CT scanners typically obtain data with voxel size resolution in units of centimeters and the scan time mostly consists of only few seconds/minutes to reduce the irradiation of the living patient to minimum (Hsieh *et al.*, 2009; Du Plessis *et al.*, 2016).

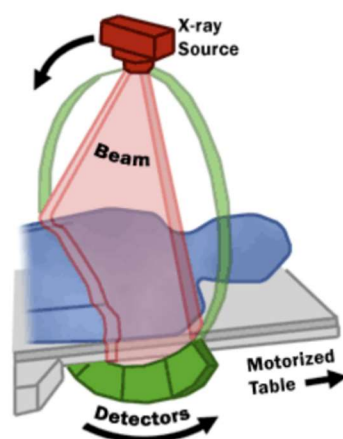


Figure 1: Clinical (*in vivo*) micro CT system (image source <https://www.sgihealth.com/ct/>).

Specialized scientific *in vivo* CT systems which work on the same basis as the medical ones offer the potential for longitudinal studies of living animals which can track changes in the structure of interest. The imaging is typically performed under anesthesia to minimize motion artifacts. The opportunity to perform multiple scans over time can reduce the number of animals needed and have a tremendous impact on studies of repair, adaptation, and growth. While the benefits of *in vivo* micro CT imaging are clear, there are additional issues which can have an impact on the obtained data. First are the potential effects of cumulative effect of ionizing radiation affecting the phenotype of the animal (development and growth) and genotype (creating mutations in DNA). A second potential complication of *in vivo* imaging is respiratory movement of the animal during the scan, which can decrease image quality creating motion artifacts, such as blurring or streaking. This problem can be solved by gating, a technique that is able to reduce motion-related artifacts by synchronizing the acquisition of data with the motion of the object being imaged. For example, in cardiac CT imaging, the acquisition of data can be gated to the cardiac cycle, by collecting the data only during a specific phase of the cardiac cycle when the heart is relatively still, and excluding the phases when the heart is moving (Hsieh *et al.*, 2009).

***Ex vivo* CT devices**

The second commonly used system geometry is the one where the X-ray source and the detector are in a fixed position while the specimen is rotating around its axis during the scanning process. This geometry is employed in most of the industrial micro CT systems where the focus is on the high precision of the measurement which is secured by the fixed position of x-ray source and detector (Fig. 2).

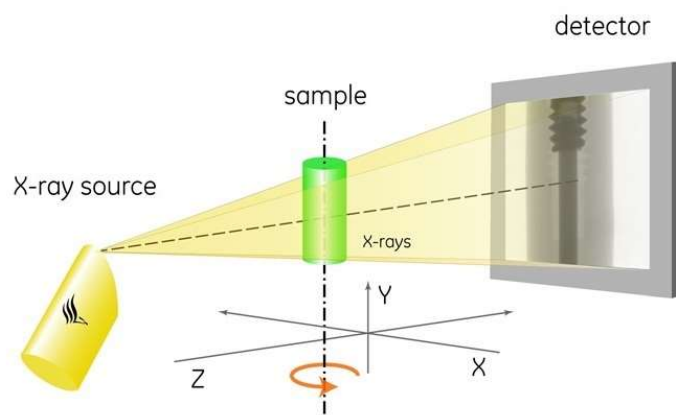


Figure 2: Industrial micro CT system (image source Welkenhuyzen *et al.*, 2009).

The industrial micro CT scanners, such as the ones we use in our laboratory, are designed for acquisition of high resolution tomographic data with voxel size resolution around 5-100 μm^3 . In the current literature the industrial micro CT systems are defined as systems able to obtain data with resolution in range of micrometers and nano CT devices are able to obtain data with submicron resolution (De Chiffre *et al.*, 2014).

In the industrial micro CT systems, most of the time the geometry of the x-ray beam is conical, this fact directly connects the achievable resolution of the scan with the dimensions of the sample. For the cone beam geometry, the magnification rule can apply as followed: the smaller the sample is and the closer it can be placed to the x-ray source in the area of cone beam the better magnification can be archived which results in higher resolution. In simpler words: the smaller sample is the higher resolution can be achieved (Du Plessis *et al.*, 2016). Because of this fact the industrial micro CT systems are suitable for the imaging of the very small mouse embryos, which are a commonly analyzed in the developmental biology research.

Based on the main function of the industrial micro CT systems which are focused on achieving scans with highest possible resolution, the samples are scanned for longer time and using higher energies than in the *in vivo* systems which results in the higher irradiation (Campbell and Sophocleous 2014). The high doses of irradiation over long period of time prohibits the scanning of the living animals on the industrial micro CT devices.

From the historical point of view, X-ray images and subsequently CT imaging has been widely used for imaging of dense structures such as bone and teeth because these tissues are fully mineralized and thus, they naturally attenuate the X-rays which is a basic principle required for proper imaging by X-ray based techniques (Bouxsein *et al.*, 2010; Swain and Xue 2009). Since the industrial system are strictly used to analyze *ex vivo* biological samples the samples can be prepared for the scan by applying various contrasting methods which can visualize the soft tissues (Metscher 2009a; Metscher 2009b). This was previously not possible due to the naturally very low X-ray attenuation of soft tissues. Contrast enhanced *ex vivo* micro CT imaging can be used to study the 3D structure of tissues, organs, and biomaterials, and can provide detailed information on the microarchitecture, morphology, and composition of the soft tissues.

1.4.2. Artifacts occurring during the CT measurement

Artifacts in the CT data are unwanted patterns or distortions in the image that can occur during the acquisition of the radiographs or during the tomographic reconstruction (Boas and Fleischmann 2012).

Motion artifacts occur when the scanned sample moves during the scan, causing blurring or distortion in the image. In the medical field this artifact is caused by the motion of the patient, in this case to reduce this artifact the patient can be sedated or if the cause of the movement is the breathing of the patient the respiratory gating can be applied (Walters *et al.*, 2004). In the case of the micro CT scans on the industrial CT devices the sample needs to be stabilized since it is placed on the rotating stage. The biological samples which need to stay hydrated during the scan can be placed in the agarose gel which fixes the sample in one position, preventing the movement (Kavková *et al.*, 2021). The samples which don't need to be hydrated can be simply fixed in the position by the polystyrene foam. In either the case the fixation agent needs to have very low X-ray attenuation in order to not to interfere with the tomographic measurement.

Beam hardening artifacts emerge in the data when the x-ray beams of lower energies are absorbed by the outer layers of the sample creating the apparent increase in density where the edge looks brighter than other parts of the image despite the material being homogenous. These artefacts can be prevented by filtering out the x-ray beams with lower energies by placing the metal filters in the trajectory of x-ray beam (Meganck *et al.*, 2009).

Ring artefacts are the concentric artificial rings occurring in tomographic images. These artefacts are caused by the small errors in detected intensity values which persists throughout CT acquisition, the detector gives a consistently erroneous reading during the measurement, resulting in a circular artefact. Ring artifacts can be removed either by the calibration of the detector pixels, or by the advanced reconstruction algorithms, such as iterative reconstruction algorithms which uses complex mathematical models to reconstruct the image from raw data (Kyriakou *et al.*, 2009).

Metal artifacts are caused by the high density objects (commonly metal objects) in the measured sample. In the medical field these often consists of dental fillings or hip prostheses. Metal artifacts in the data are showing like the light and dark streaks around the metal object. The artifacts originate from the dark shadows in the measured data due to the strong attenuation of the metal objects when x-rays pass through them (Boas and Fleischmann 2012). Metal artifacts can be reduced by iterative metal artifact reduction algorithms (Boas and Fleischmann 2011) or dual-energy CT can be used to reduce these artifacts by separating the high and low energy components of the CT scan (Bamberg *et al.*, 2011).

1.4.3 Phantoms for calibrating CT measurements

Phantoms are objects or materials designed to have well-defined and known characteristics that can be used for calibration purposes. In CT measurements the phantoms are either objects scanned together with the analyzed object to define the properties of the object or the phantoms are scanned prior to the scan of the sample to calibrate CT system (de Oliveira *et al.*, 2017).

In the medical field the phantoms for the Hounsfield unit (HU) are commonly used. The Hounsfield unit (HU) describes the amount of attenuation in medical CT devices, HU is a scale that relates the X-ray attenuation of the analyzed material to the attenuation of water and air. Water has a HU value of 0, while air has a negative value, and denser materials such as bone have positive HU values. These phantoms are used to calibrate the CT system for HU values. HU phantoms typically consist of a set of materials with known HU values, such as water, air, and bone, which can be imaged and used to calibrate the HU scale of the micro CT system (Mah *et al.*, 2010).

The hydroxyapatite (HA) phantoms are used for the determination of the bone density. These phantoms typically consist of a set of tubes with different concentrations of hydroxyapatite. The phantom is scanned together with the sample and in the postprocessing of the data the bone density of the sample is defined by comparing the sample with the scale of densities of HA in the phantom (Schweizer *et al.*, 2007).

Voxel size calibration phantoms are used in the industrial CT devices to calibrate the accuracy of the scan. These phantoms typically consist of a two ruby balls of defined diameter which are in a very precisely measured distance from each other. This phantom is measured before the actual scan of a sample. From the obtained scan the distance between the ruby balls is defined and compared with the actual distance between the ruby balls, the CT system is then calibrated with the obtained values (Blazek *et al.*, 2019).

The resolution phantoms are used for the determination of the spatial resolution of the CT device. Probably the best known spatial resolution phantom for the micro CT devices is the bar pattern QRM phantom, this phantom is a small object with a known pattern of high-contrast lines and dots of different sizes. The QRM phantom can be imaged at different magnifications and in the obtained data the system resolution at that magnification is determined by the smallest pattern in which the individual dots and lines can be distinguished (Mambrini *et al.*, 2022).

1.5. Contrast agents used for visualization of soft tissues in micro CT imaging

In most cases micro CT imaging of biological samples requires staining. Exceptions to this condition are fully mineralized bones and teeth (Kavková *et al.*, 2022), exoskeletons of several taxa of insects (Poinapen *et al.*, 2017) or mollusk shells (Monnet *et al.*, 2009) all of above mentioned structures are naturally radiopaque due to the high concentration of elements with high proton number. On the other hand, the soft tissues have naturally low attenuation of x-rays and thus their visualization in the micro CT data needs some additional steps. Some form of staining of soft tissues is a necessary strategy to increase their naturally low contrast in micro CT data. The main criteria for X-ray staining agent is that it has to be composed of molecules containing atoms with a high atomic number, which have high X-ray attenuation coefficient needed for proper visualization of soft tissue. Following list demonstrates the most common staining agents used for the visualization of soft tissues in the micro CT imaging.

1.5.1. *In vivo* micro CT contrast agents

In the *in vivo* micro CT scans of the living animals the imaging is focused either on the hard tissues such as bones or teeth which has high natural contrast due to the presence of hydroxyapatite, or the imaging of the blood vessels which requires injection of non-toxic contrast agent to allow imaging of the vasculature. In a number of diseases including cerebral ischemia or myocardial infarction, alterations in vessel anatomy, structure, and function are common findings (Dayan *et al.*, 1985) and all of these can be discovered in contrast enhanced *in vivo* micro CT imaging. The *in vivo* contrast agents are commonly applied intravascularly, they remain localized to the injected vasculature and are cleared from the organism by the kidney or liver (Badea *et al.*, 2008).

The older type of conventionally used *in vivo* contrast agents belongs Iopromide 300, Iomeprol 400 and barium sulfate (Kiessling *et al.*, 2004). Downside of using those agents is that all of them need to be injected continuously with a specific flow rate during the whole scan in order to sustain necessary concentration due to the fast elimination (from 1 to 3 min) of the staining agent from the blood pool (Kiessling *et al.*, 2004).

Amongst the newer contrast mediums belong long circulating blood-pool contrast agents based on iodine (Zheng *et al.*, 2007; Hallouard *et al.*, 2010; Nebuloni *et al.*, 2013), gold (Peng *et al.*, 2012; Cormode *et al.*, 2014) or bismuth (Rabin *et al.*, 2006). The advantage of using those agents is larger size of contrast agent molecules, often liposome bound which increases their ability to reside in the vascular circulation close to an hour (Badea *et al.*, 2005).

1.5.2. Diffusion based staining agents (*ex vivo*)

All of the below mentioned staining techniques are utilizing the staining solutions prepared with combination of different solvents and staining agents. The principle of this method is that the stained sample is submerged in the staining solution and the staining agent penetrates the sample by diffusion.

1.5.2.1. Staining with Iodine

Iodine is one of the most widely used contrast agents for the purpose of micro CT imaging due to its ease of handling, low price, and its ability to efficiently contrast the soft tissues. Iodine solutions permeates soft tissues rapidly as a general stain and allow for nearly histological quality imaging. The iodine binds generally to all structures in the tissue but exhibits stronger affinities to certain anatomical structures staining them more intensely which allows the distinction of the different tissues (Kiernan *et al.*, 2001). The iodine staining solutions are also not detrimental to the integrity of the DNA, which allows further tissue analysis after the micro CT imaging (Faulwetter *et al.*, 2013). The easy handling and good contrast imposed on samples by staining in iodine solutions resulted in a proliferation of various protocols for specimen preparations.

Several kinds of iodine staining solutions are currently used in *ex vivo* micro CT imaging. First type is I₂KI (Lugol's solution) which is made of iodine and potassium iodine dissolved in distilled water. Second type is I₂E or I₂M (alcohol based solution of iodine) which is made of iodine dissolved in ethanol or methanol. And lastly the commercially produced compounds of iodine which are mostly used in the clinical imaging.

Water based iodine staining solutions

Lugol's solution (I₂KI) is a water based solution of iodine. The elemental iodine on itself is not soluble in water, so in order to create the water based solution of iodine, the potassium iodide (KI) have to be added into the mixture. When the potassium iodide is combined with elemental iodine in water the triiodide ion is formed which enhances the aqueous solubility of iodine.

Lugol's solution is popularized as a diffusible contrast agent for contrasting of soft tissues in standard micro CT imaging. In the contrast solutions the iodine that contributes to staining comes from both I₂ and KI. The advantage of using the Lugol's iodine as a staining solution is that there is no need for dehydration of a sample and most I₂KI staining procedures consists only of soaking of fixed sample in Lugol's solution. On the other hand, the staining

with the water based iodine solution takes more time (when compared to the staining solutions of iodine dissolved in alcohol), since the water does not permeate the tissues as progressively as the ethanol or methanol.

This staining was successfully used in the anatomical research of zebrafish (Babaei *et al.*, 2016), for the visualization of key structures during cardiovascular development at various stages of mouse embryogenesis (Degenhardt *et al.*, 2010) or to create the mouse embryo atlas (Wong *et al.*, 2012). To be able to properly stain the larger samples the higher concentrations of iodine have to be administered to the sample as is demonstrated in the publications focused on cardiac imaging of dog heart (Aslanidi *et al.*, 2012) and on the imaging of the large specimen of adult White-fronted goose (Li *et al.*, 2015).

Ethanol or methanol based iodine staining solutions

Workflow of the contrasting protocols using the alcohol based iodine solutions starts with dehydration of the sample in the increasing alcohol series followed by immersion of the sample in the iodine staining solution. The dehydration of the sample can cause some shrinkage to the sample, but if the dehydration is managed slowly and gradually the shrinkage can be reduced to minimum. So far, the staining with alcohol based iodine staining solutions has been rather sporadic compared to the Lugol's solution which might be caused by the potential risk of shrinking of the sample.

The fast staining rate as well as the possibility to wash out the iodine from the sample in the clean solution of the alcohol (Kavková *et al.*, 2021) are lately favoring the utilization of this staining method in the biological research. It proved to be excellent staining solution for the staining of mouse brain (Zikmund *et al.*, 2018) as well as the rat brain (Kavková *et al.*, 2021), the fast staining rate proved to be the advantage in the staining of large samples of the ovaries from different species (Paulini *et al.*, 2017), the high contrast proved to be beneficial for the detection of tumor in lungs (Bidola *et al.*, 2019) or in the marine research of developing squid embryos (Kerbl *et al.*, 2013).

Commercially available iodine staining solutions

Several papers mention *ex vivo* staining with commercial iodine solutions primary used as *in vivo* angiography contrast agents. Iodinated contrast reagent called Hypaque, has been for example used for visualizing of mouse and rabbit brains (De Crespigny *et al.*, 2008).

1.5.2.2. Staining with Phosphotungstic acid

Phosphotungstic acid (PTA) is a larger molecule containing tungsten ions which are the primary source of the x-ray attenuation in this molecule. The PTA is commonly used as a general contrasting agent in micro CT imaging and is known to bind to certain proteins such as fibrin or collagen (Faulwetter *et al.*, 2013).

An *ex vivo* staining protocols based on PTA diffusion are more suitable for the staining of the smaller samples such as early stages of mouse embryos or the dissected mouse organs. The reason for this specific application is the larger dimensions of the PTA molecule. This causes the slow diffusion rate of the PTA through the tissue (approximately 1 mm per week) and in case of the large samples the staining would take several weeks to stain properly (Fernández *et al.*, 2014).

Following the previously stated properties of the PTA the staining solutions containing PTA has been used for the staining of small samples such as post-hatching paddlefish, axolotl larvae, pupa of the *Calliphora vicina* fly (Metscher 2009a) or even a small, marine invertebrates (Faulwetter *et al.*, 2013). PTA staining protocols are also appropriate for the staining of the dissected mouse organs, for example for the visualization of renal morphology in the explanted kidneys (Missbach-Guentner *et al.*, 2018). Although phosphotungstic acids successfully contrasts the soft tissue the usage of this staining agent requires caution because of possible decalcification of the hard tissues due to its acidic nature (Metscher 2009b).

Lastly, the staining protocols containing the PTA as a contrast agent are ideal for the use of the imaging of the museum samples as the PTA staining solution does not imply any visible color to the stained sample (in contrast to the iodine based staining solution which stain the sample in brown color). The completely stained and scanned samples can be returned to the museum without any visible changes back to the museum display (Lenihan *et al.*, 2014).

1.5.2.3. Staining with Osmium tetroxide

Osmium tetroxide is a commonly used fixative and stain in electron microscopy that can also be used to enhance the contrast of soft tissues in micro CT data. The osmium tetroxide binds with the unsaturated fatty acids in the lipids of the cell membrane and other cellular components (Kiernan *et al.*, 2001). One of the specific applications of OsO₄ in micro CT is imaging of coronary artery walls, since the OsO₄ have high affinity to lipids in tissue, it can clearly visualize the lipid deposition and therefore highlight arteriosclerotic plaques in arterial walls (Pai *et al.*, 2012). Overall, the staining procedures using osmium tetroxide have been applied to micro CT visualization of soft tissues rather sporadically. In the former research this

staining was utilized for example for phenotypic assessment of mouse embryos (Johnson *et al.*, 2006) to visualize the lung architecture of inflated porcine lungs (Litzlbauer *et al.*, 2006), for the imaging of the fragile respiratory organs of scorpions (Kamenz *et al.*, 2009) or for the marrow adipose tissue in the bone marrow of long bones (Scheller *et al.*, 2014).

The current trend in the utilization of the staining solutions is preferring other staining agents than the osmium tetroxide. One of the reasons why this staining agent is not commonly used anymore is its high toxicity and volatile character which makes it hazardous to work with, requiring particular safety measures and a well-equipped laboratory.

1.5.3. Corrosion casting contrasting agents

Corrosion casting is primarily *ex vivo* anatomical technique based on injection of casting compounds directly into lumina, such as those within blood vessels, bile ducts or lungs with intention of creating the model of the whole vascular system. For the purpose of micro CT imaging the casting material contains radiopaque substance which enables visualization of three-dimensional vascular architecture in a consistent manner. Subsequently dissolving away the surrounding tissue leaves a model of the intricate, three-dimensional architecture of vessels (Starosolski *et al.*, 2015).

Corrosion casting using lead chromate containing radiopaque liquid silicone Microfil® is frequently used in imaging of cerebral vasculature especially in research of cerebrovascular disorders, such as aneurysms, arteriovenous malformations, and ischemic and hemorrhagic stroke (Xie *et al.*, 2012; Langheinrich *et al.*, 2010; Ghanavati *et al.*, 2014; Stolz *et al.*, 2011; Holdsworth *et al.*, 2002, Perrien *et al.*, 2016) as this method can identify the pathological changes of the analyzed vessels as well as the measurement of the cerebral blood volume. The μ Angiofil polymer-based contrast agent has excellent filling capacity enabling visualization of the smallest brain capillaries which allows in situ analysis of the dura mater and leptomeningeal layers (Hlushchuk *et al.*, 2020).

Corrosion cast can also help with assessment of the liver lesions as they are the major cause of morbidity and mortality in polycystic kidney disease (Masyuk *et al.*, 2004). In combination with nano CT imaging the vascular corrosion cast of an entire mouse kidney can be scanned with resolution high enough that the glomerular capillaries are visualized in the quality comparable to similar models from confocal microscopy (Wagner *et al.*, 2011). Since the architecture of tumor vasculature is important both as a therapeutic target and prognostic biomarker the method of corrosion casting can be also used for investigation of the three-

dimensional properties of colonic tumor vasculature via tumor vascular casts (Folarin *et al.*, 2010).

The novelty, simultaneous imaging of two different vessel systems at the same time with the application of corrosion casting agent Microfill was recently published in cooperation with our research group (Hankeova *et al.*, 2021). Two kinds of Microfill resin were used to fill blood vessel and bile duct in case of liver and in case of lungs the blood vessels and the airway. In the resulting micro CT data, both systems can be distinguished based on their specific attenuation and the complex 3D model of both systems can be evaluated.

1.5.4. Tissue specific staining agents

Unlike the contrasting agents mentioned so far, which are staining the sample in a non-specific way, in some cases the staining of the specific structures by immunodetection with the use of antibody bound staining agents is possible. Immunodetection is significantly different approach when compared with classical micro CT staining protocols since most of the commonly used staining agents contrasts the sample in non-specific way where different types of tissue are distinguished only by their intake of staining agent.

On the other hand, the immunodetection methods are based on premise that antibodies bind their target with high specificity allowing the localization of their target to specific tissues. The basic scheme of immunodetection relies on primary and secondary antibodies. Primary antibody binds with high specificity the target molecule in a tissue that needs to be localized, secondary antibody binds the primary antibody and is tagged with either enzyme or fluorophore that creates signal for detection.

Novelty use of metal-based immunodetection for visualization of specific gene expression patterns by micro CT has been described by Metscher and Müller in 2011. The proposed method impairs the X-ray contrast to the sample by metal deposition scheme of an enzyme metallography, which means that the metal (silver) is reduced from the solution by the enzyme bound to the secondary antibody. The metallic deposits have sufficient X-ray density to generate attenuation values that are higher than unstained tissues in micro CT data, allowing antibodies to be localized in specific tissues. On the same principle works the detection of melanin in the developing zebrafish embryo (Katz *et al.*, 2021). In this case the procedure is based on the reduction of silver used for histological Fontana-Masson staining appears highly specific to melanin. This analysis enabled the visualization and computational analyses of regional melanin content and morphology in zebrafish embryo. In the cancer research the gold nanoparticles were coupled to Herceptin antibodies (specific marker of breast cancer) with the

aim to determine microlocalisation of the golden nanoparticles and quantify them in mouse tumor models by using micro CT imaging (Hainfeld *et al.*, 2011).

For the future of the micro CT imaging the method of specific detection of tissues bring a lot of potential, but so far this method can be applying only to the very small samples because penetration of the antibodies through the tissue is limited.

1.6. Software for the analysis of micro CT data

The visualizations and the quantitative analysis of the obtained micro CT data is a crucial step in the whole process of the micro CT analysis, for this step several open source and commercially available software can be utilized. The choice of software program depends on the specific needs of the project and the level of expertise required for the intended applications.

ImageJ/Fiji is a free, open-source software program widely used for the image analysis, including micro CT data. It provides basic image processing functions, such as brightness/contrast adjustments and noise reduction, however it is not primarily dedicated micro CT software (<https://imagej.net/ij/index.html>).

Avizo/Amira - both of this software are similar in terms of functionality and capabilities, Avizo is primarily marketed for material sciences and Amira for life sciences. They are commercial software programs developed by Thermo Fisher Scientific designed specifically for the visualization and analysis of 3D micro CT data. They provide wide range of advanced tools for segmentation, volume rendering, and quantitative analysis, making it a powerful tool for 3D data analysis.

VGStudio MAX is a commercial software program developed by Hexagon. VGStudio is designed specifically for the analysis and visualization of micro CT data. It provides advanced tools for segmentation, visualization, and quantitative analysis, as well as tools for creating animations. Together with the Avizo/Amira are most commonly used software for the precise analysis of micro CT data.

2. Aims of doctoral Thesis

The aims of this thesis focused on the industrial micro CT imaging of soft tissue were as following:

1. Evaluation and the determination of the most suitable contrasting protocols for the imaging of the samples for the specific scientific research projects. The performance of different contrast agents will be compared and their efficacy of enhancing the contrast of soft tissues in micro CT data will be evaluated. As a following step the protocols will be optimized for the imaging of various types of samples.
2. Working with the obtained micro CT data the analyses in the specialized software for the 3D analysis will be determined. The scope of various research project will be individually discussed and the optimal data analysis for the specific research question and goals will be designed.

3. Methods

3.1. The pre-staining steps (tissue fixation, dehydration)

The first of the pre-staining steps generally consists of the tissue fixation. Prevalently used fixation agent - paraformaldehyde reacts with the primary amine groups present on many biomolecules, including proteins, DNA, and RNA and covalently cross-links the molecules of a tissue which prevents the denaturation of a proteins and autolytic processes in a tissue.

In most of the samples the fixation consists of submersion of the freshly harvested sample in the solution of 4% or 10% water-based solutions of paraformaldehyde (PFA). The 4% percent solution is generally used on smaller samples e.g. early stages of embryos or dissected organs, the 10% solution is use on larger and older samples, e.g. postnatal mice. The concentration and overall fixation time depends on a dimension of a sample and on the type of tissue, generally applied rule is that the bigger and older the sample is the higher concentrations of a fixation agent is used and longer time of fixation needed (Kiernan *et al.*, 2001).

Since most of the staining solution tested and utilized in this work are alcohol based the second important pre-staining step is the dehydration of the sample, during the process of dehydration the water is gradually removed from the tissue and replaced by the alcohol solution. The sample needs to be gradually dehydrated to the same concentration of alcohol solution used in staining solution, to prevent damaging the sample. This process is ensued by subsequent immersion of a sample in 30%, 50%, 70%, 80% and 90% ethanol solution. The time in each concentration is adjusted according to the sample dimensions.

3.2. Selection of the staining agents for visualization of soft tissues

One of the main goals of my dissertation topic was establishing the staining protocols designed to increase the contrast of the soft tissues in the tomographic data and optimizing them for the imaging of specific samples analyzed in cooperation with several research groups mainly focused on biology research. The various factors can affect the result of the staining (type of staining agent, the concentration of a staining agent, concentration of a solvent in a staining solution and overall staining times). Based on the previous publications (Metscher 2009a; Metscher 2009b) the most commonly used staining agents - iodine and PTA (phosphotungstic acid) were selected as a reliable staining agents to pursue the development of the staining protocols suitable for the samples analyzed in the specific projects I was working on.

To visualize the staining progress of iodine and PTA, front legs of the E16.5 days old mouse embryo were stained in either iodine solution (1% I₂ in 90% MeOH) or PTA solution (1% PTA in 90% MeOH). To track the progress of staining of the soft tissues, several X-ray images of the samples were taken over 1 hour period in the 15 min intervals. The X-ray imaging was performed on the Rigaku nano3DX device with 2,014 μm pixel size, exposure time of 20 seconds and using the copper target.

The iodine dissolved in methanol proved to penetrate the sample much faster than the PTA dissolved in methanol. This occurrence is most likely due to the difference in the dimensions of small molecule of iodine (<https://pubchem.ncbi.nlm.nih.gov/compound/Iodine>) compared to large and complex molecule of PTA (<https://pubchem.ncbi.nlm.nih.gov/compound/Phosphotungstic-acid-hydrate>). The iodine proves to stain the sample fully in 30 minutes, on the contrary the PTA stains the sample much slower. The skin proves to be the barrier for the penetration of the larger molecule of the PTA - in the X-rays the PTA starts to stain the sample mainly in the place of the severed limb and in the smaller cuts in the palm of the leg (Fig. 3).

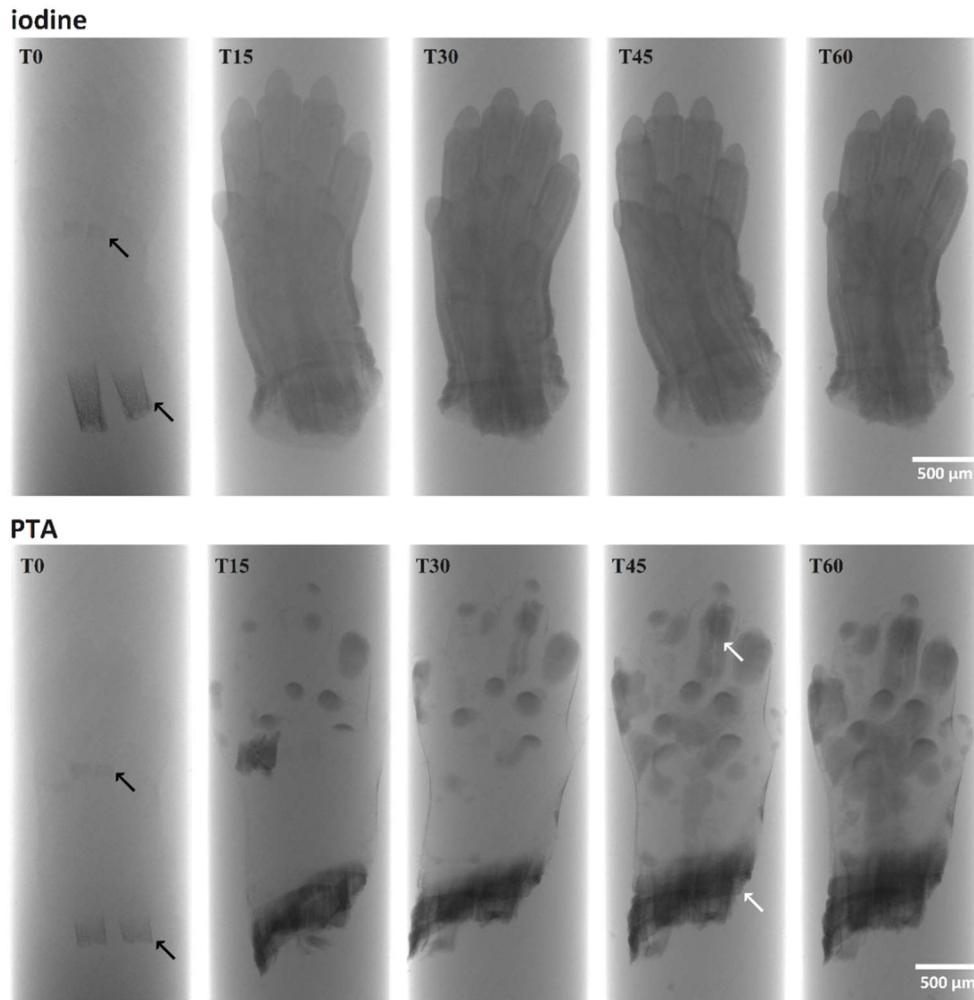


Figure 3: Comparison of iodine and PTA staining of the front leg of E16.5 mouse embryo documented over 1 hour time period. In both samples at T0 the only visible part of the leg is the mineralized bone (see the black arrow). The sample stained in iodine solution was contrasted fully in 30 minutes. In comparison, the sample contrasted in PTA solution is showing only the start of the staining process, the skin proves to be the main barrier for the PTA as it can be seen that it penetrates the sample in the in the place where the limb was severed and in the smaller cuts in the palm of the limb (see the white arrows).

To test the overall contrast, both staining agents were applied on the whole mouse embryo (for the practical demonstration the E15.5 stage was selected). In case of the staining solution containing the 1% iodine in 90% MeOH the total staining time in which the whole embryo was properly stained was 24 hours. In comparison the staining solution containing 1% PTA in 90% MeOH took 10 days and several changes of the staining solution to properly contrast the whole sample. At the end, even though the process of the staining differs in the

iodine and the PTA, the final overall contrast enhancement in the CT data is almost identical (Fig. 4).

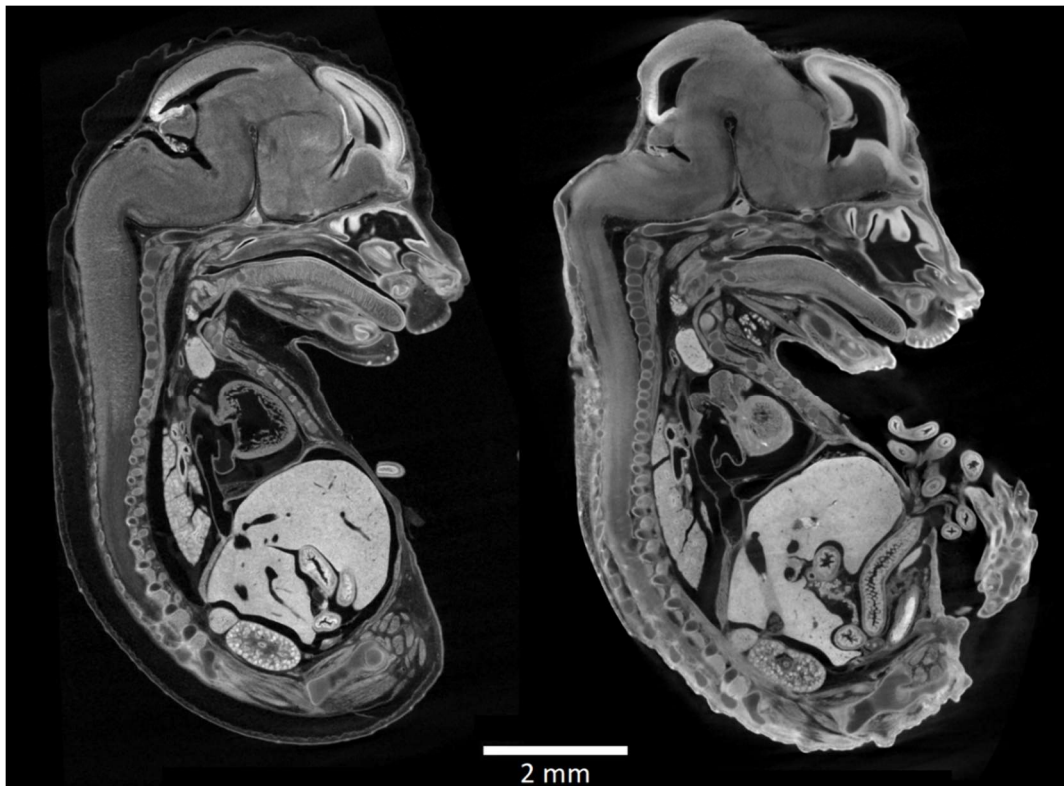


Figure 4: comparison of the E15.5 mouse embryo stained in iodine (left) and in PTA (right). The overall contrast in the sample stained in iodine and the PTA is comparable, in both cases the liver and the lungs are stained with highest intensity, also the cartilage is stained in negative way (due to the high density of this tissue and no native contrast) in both iodine and PTA.

3.3. Motion stabilization of the sample during scan

The stabilization of the sample during the scan is one of the most crucial steps. The need for fixation results from the basic fact that during the scan the sample is rotated over 360 degrees, if the sample was simply placed in some kind of liquid, it would be moving during the scan and the acquired data would be blurry.

Depending on the character of the sample several kinds of fixation are available. In the case of larger samples which does not need to be kept hydrated the "simple" position fixation with low attenuation materials such as styrofoam are applicable (Fig. 5). For the small samples that needs to stay hydrated, such as the mouse embryos, the best possible fixation is in either Eppendorf or Falcon tubes (depending on size) which are made of polypropylene plastic (it has low X-ray attenuation) and the sample is embedded in the 1% agarose gel (Fig. 5).



Figure 5: Motion stabilization of different kinds of samples, on the left is taxidermied sample of ameiva lizard fixated in position by styrofoam, on the right mouse embryo in the falcon tube and agarose gel.

3.4. Micro CT devices

For the purpose of scanning of the samples the micro CT devices GE phoenix v|tome|x L240 and RIGAKU nano3DX were utilized.

The RIGAKU nano3DX device was equipped with 16 bit, 3300×2500 pixels X-ray CCD camera detector and dual target X-ray tube emitting quasi-parallel X-ray beams. This device was used for specific applications, mainly very small samples (1-2 mm) in which the device was able to scan the sample in voxel resolution of 1-2 micrometers.

Most of the biological samples for the projects I was working on were scanned on the GE phoenix v|tome|x L240 device. This device utilizes the flat panel dynamic 41|100: 4000 x 4000 px detector and for the scanning of the biological samples the 180 kV / 15 W nanofocus tube was used.

3.5. Analysis of the obtained micro CT data in specialized software

For the processes of segmentation, visualization and quantification of the obtained micro CT data the Avizo and VGstudio MAX 3D software were used.

Since the contrasted biological samples cannot be simply thresholded to visualize the object of interest (due to the non-specific nature of the staining process, different tissues can have similar gray values) the need of manual or semi-manual segmentation still prevails. For the purpose of the manual segmentation the Avizo software have the best tools. This software

allows to go through the individual sections following the object of interest and mark only every 3rd to 8th section (depending on how much the segmented structure changes) to decrease the time spent on segmenting, the interpolation function of the software can be then applied to fill in the in-between sections. The resulting 3D model of the segmented structure can be exported as stl. file which is imported in VGstudio MAX in which all of the visualizations and analyses were conducted.

The VGstudio MAX is 3D analysis software, which includes modules for advanced image analysis. This software was used for all of the visualizations and advanced analyses of the obtained micro CT data presented in this work. The more basic analyses such as the measurements of volumes, length or angles are readily available and some of the values are automatically computed for all of the segmented structures. Since this software is primarily designated for the analysis of the industrial samples the use of the quantitative analyses for analysis of the biological samples brings unique data into the biological research. In the scope of this work and the related projects the modules of Wall thickness analysis, Pore analysis and the Unroll feature were amongst most commonly utilized. The Wall thickness analysis works based on the determining the thickness of the sample by fitting the 3D spheres inside the walls of the analyzed sample, the bigger the sphere can be fit in the particular part of the sample the higher is the value of the final wall thickness. The Pore analysis is used to characterize the set of pores/voids (in our case the analysis was used for the description of the amyloid plaques). Running this analysis provides the information about volume, surface, sphericity, and several other values. The Unroll feature provides unique way to display several objects of interest which are normally not visible in one section (e.g. teeth along the jaw). By placing the points of polyline alongside the structure to be visualized the software can unroll the structure and the sections perpendicular to the created unrolled section can be displayed.

4. Results

4.1. Determining and optimizing the contrasting protocols

The main thing to be considered in the design of the staining strategy is the dimension of the sample. In small specimens staining agents have to travel shorter distances to reach internal soft tissues. This implicates that for the staining of the smaller specimens the lower concentrations of staining solution as well as shorter staining times are sufficient. The larger specimens on the other hand often need to refresh the staining solution during the staining to stain the whole volume of the sample.

When selecting the appropriate staining agent, we need to consider the previously demonstrated properties of iodine and the PTA. The staining solution utilizing the alcohol based iodine solution penetrates the sample much faster than the PTA in the same solvent. The PTA is a large molecule and it penetrates into the tissue very slowly, the staining with the PTA solutions takes much more time than iodine and thus is not suitable for the staining of the larger samples because the staining could take up to several weeks (Koç *et al.*, 2019).

For the cases where micro CT analysis is followed by other analysis of the sample e.g. histological sectioning and the immunostaining the iodine can be easily removed from the tissue with the wash of the sample in the clean alcohol solution (Kavková *et al.*, 2021). On the other hand, the PTA staining is very stable in the tissue and when the stained sample is stored in the fridge the staining holds for several years.

4.1.1. Novelty contrasting protocol for imaging of the mouse brain

In neurobiological research, mice are commonly used as a model organism because of the similarity with human genome, which allows modelling the human-related pathologies in transgenic mice. In order to precisely describe the important structures in the brain in 3D, which is important to distinguish the pathologies in the brain, we have set a goal to define the staining protocol for the mouse brain which would allow to distinguish various structures of the brain.

Based on the previously published data (Metscher 2009a) we have created several combinations of staining agents (the iodine and the phosphotungstic acid were selected as they are commonly used and safe to work with) and different solvents. The samples were stained with following contrasting protocols (Fig. 6) - (A) 1% PTA in 90% MeOH for 21 days, (B) 1% PTA in 90% MeOH for 14 days, (C) 1% PTA in 100% MeOH for 16 days, (D) 1% PTA for 10 days + 1% iodine in 90% MeOH for additional 24h, (E) 1% iodine in 100% EtOH for 24h, (F)

1% iodine in 100% EtOH for 48h, (G) 1% iodine in 100% EtOH for 7 days, (H) 1% iodine in 90% MeOH for 24h, (I) 1% iodine in 100% EtOH for 24h. The obtained data were then analyzed to determine the best staining methodology for imaging of the mouse brain resulting in publication of the data in paper Zikmund *et al.*, 2018, the results from the paper are described in following text.

The best methodical way to compare the contrast of several samples in micro CT scan is to scan them all in one batch (or scan all of the samples separately with the calibration phantom). This prevents the fluctuations in the resulting histograms and reduces other influences which can impact the results of the scan. All of the samples were scanned together in separate tubes with the resolution of 18 μm which proved to be adequate to compare the contrast in the tested samples. The staining protocols were compared according to their ability to visualize brain structures in micro CT data. The best staining results were obtained with the staining solution containing 1% iodine in 90% methanol solution (Fig. 6, image H) as this staining solution proved to produce the highest contrast in the observed brain structures, successfully visualizing caudoputamen, anterior commissure, corpus callosum and lateral olfactory tract even in the lower resolution scan.



Figure 6: Comparison of the coronal sections of mouse brain samples selected from the original publication (Zikmund *et al.*, 2018). The compared images of differently contrasted brains are shown with the same histogram setting (possible due to the batch scan of all samples together). The contrasting protocol H (1% iodine in 90% MeOH for 24h) was determined as a best contrasting solution based on the analysis of obtained data, it had efficiently visualized the caudoputamen (CP), anterior commissure (ACO), corpus callosum (CC) and lateral olfactory tract (LOT).

During the follow up experiments using the staining protocol for the mouse brain we have discovered that in the case of staining of the brain, the intracardial perfusion with the PFA solution right after sacrificing the animal is crucial for the best possible staining results. In the figure 7, both of the brain samples were stained by the same protocol (1% iodine in 90% methanol 24 h). The sample A was cardially perfused which ensued better fixation of the brain tissue and thus better results of the staining compared to the sample B which was fixed only by the submersion in the PFA solution which did not ensured the proper fixation of the brain tissue and the staining was limited. For the process of image analysis, the histograms in both compared datasets (samples) were manually set in a way to display the best possible contrast without saturation of the structures with highest attenuation (white parts of the image).

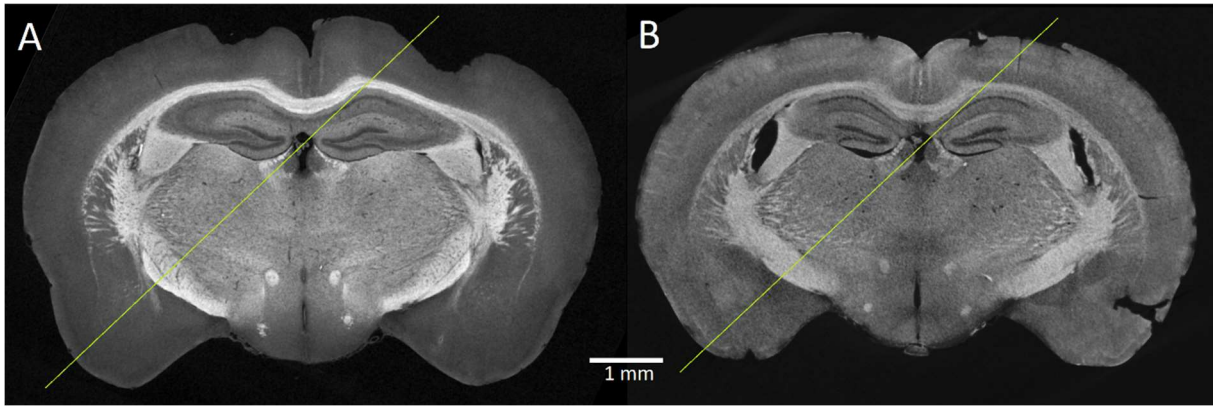


Figure 7: The brain fixated by the intracardial perfusion with the 4% PFA (A) displays the staining with more contrast in the corpus callosum, dentate gyrus, third ventricle, internal capsule, mamillothalamic tract, fornix, optic tract and caudoputamen than the brain which was fixated by submersion in the 4% PFA (B) even though both brains were stained by same method. Along the green lines were plotted the line profiles in the next figure.

To support the statement that the intracardial perfusion helps the contrasting process, the line profiles through the green lines in fig. 7 were plotted (Fig. 8) to show the differences in overall contrast. In the comparison of both line profiles, the line profile of the perfused mouse brain shows wider range of the detected gray values and thus confirming the higher efficiency of the staining solution in the perfused brain. The difference in overall contrast in the perfused and non-perfused brain can be clearly seen.

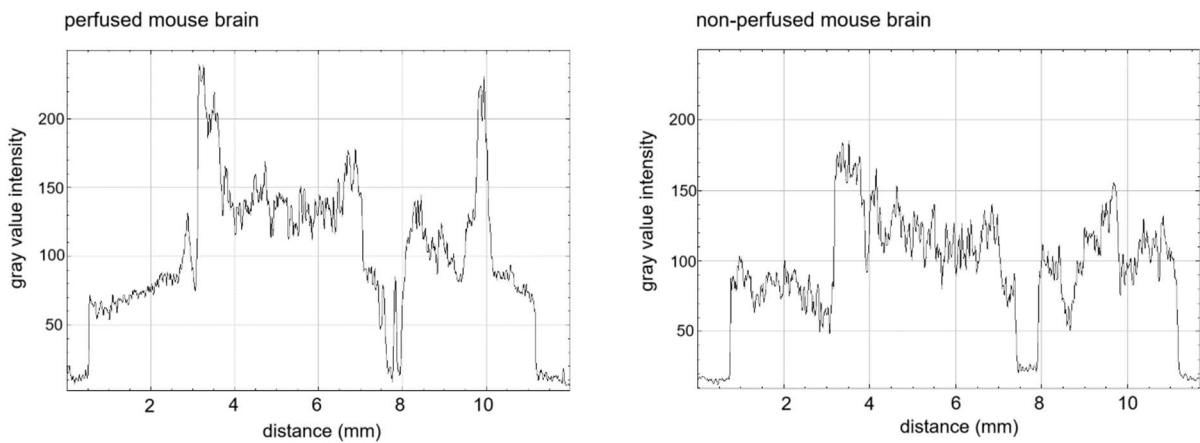


Figure 8: Comparison of the line profiles performed on perfused and non-perfused mouse brains in ImageJ.

4.1.2. Contrasting of the mouse embryo

As the mouse embryos are the most commonly used model organism in the developmental biology research, and most of the research groups I had cooperated with during the work on my dissertation topic, have worked with the mice, the need for the reliable staining protocol for the imaging of the mouse embryos of different developmental stages have emerged. The application of the micro CT imaging of the mouse embryo is the most beneficial in the stages where the embryos are too large for the whole mount imaging by the microscopes (e.g. light sheet, confocal) which is approximately E13.5 of embryonal development, simultaneously the developmental stage E18.5 is the oldest developmental stage used in the embryo research as the gestation period of mouse is 19 to 21 days. Based on these observations we have selected the developmental stages E13.5 - E18.5 (Fig. 9) of mouse embryo for the designing of the contrasting protocol.



Figure 9: developmental stages of mouse embryo from E13.5 (left) to E18.5 (right)

In the published literature the commonly used staining agents for the embryos are iodine and the PTA. Considering the previously stated properties of both PTA and the iodine, and the excellent results of the staining solution of 1% iodine in 90% MeOH in the case of staining the mice and rat brains, I have selected this solution for the further optimization for the purpose of staining the soft tissues of mice embryos.

In the process of determining the optimal time of staining for each developmental stage I took the inspecting "fast" scans of the stained sample to check the progress of penetration of the staining solution through the sample. In the figure 10 this process is documented on the E18.5 mouse embryo scanned at two time points during the staining. The image on the left is improperly stained embryo (after 2 days of staining) - in the 2 days the contrasted sample was submerged in the staining solution the staining agent (iodine) did not penetrate the whole

volume of the sample resulting in the lower overall contrast. The only properly stained part is the rostral part of the face - the oral mucosa presents lower barrier to the staining solution than the skin on the rest of the body. On the right side of the figure 10 is the same embryo which is fully stained after 4 days in the staining solution.

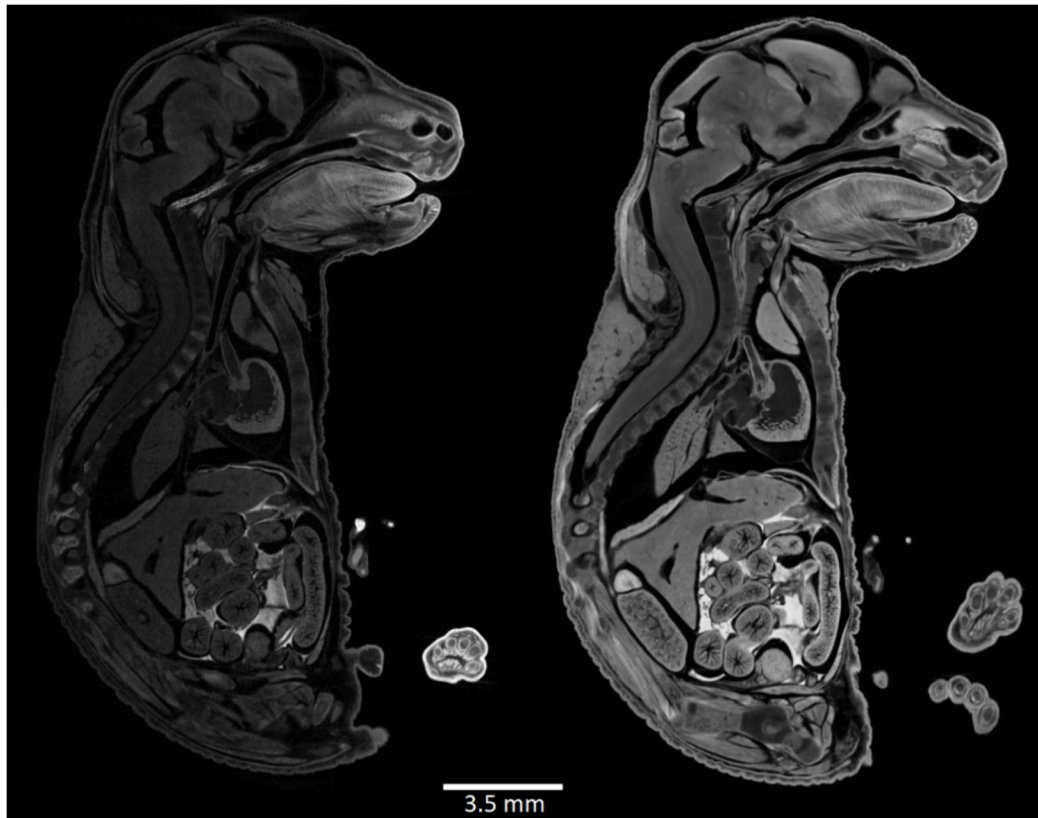


Figure 10: comparison of the improperly (left) and properly stained (right) E18.5 mouse embryo

For the optimization of the contrasting methodology, I have focused on the developmental stages E13.5 to E18.5. The following table 1 contains the overview of the contrasting protocols which I have determined for the staining of the selected developmental stages of mouse embryos.

Table 1: Staining protocols for the mouse embryo

sample	30% EtOH	50% EtOH	70% EtOH	80% EtOH	90% EtOH	1% iodine in 90% MeOH
E13.5	1 h	1 h	1 h	1 h	1 h	8 h
E14.5	2 h	2 h	2 h	2 h	2 h	12 h
E15.5	4 h	4 h	overnight	4 h	4 h	24 h
E16.5	8 h	overnight	8 h	overnight	8 h	1+1 days (refresh the staining solution after 24 h)
E17.5	12 h	12 h	12 h	12 h	12 h	2+1 days (refresh the staining solution after 24 h)
E18.5	12 h	12 h	12 h	12 h	12 h	2+2 days (refresh the staining solution after 48 h)

On the example of sagittal cross sections of all of the developmental stages of mouse embryo, for which the contrasting protocol was developed, the fully and properly stained samples are shown (Fig. 11). In the properly contrasted mouse embryo, the staining agent is uniformly distributed in the individual tissues without any dark, unstained spots.

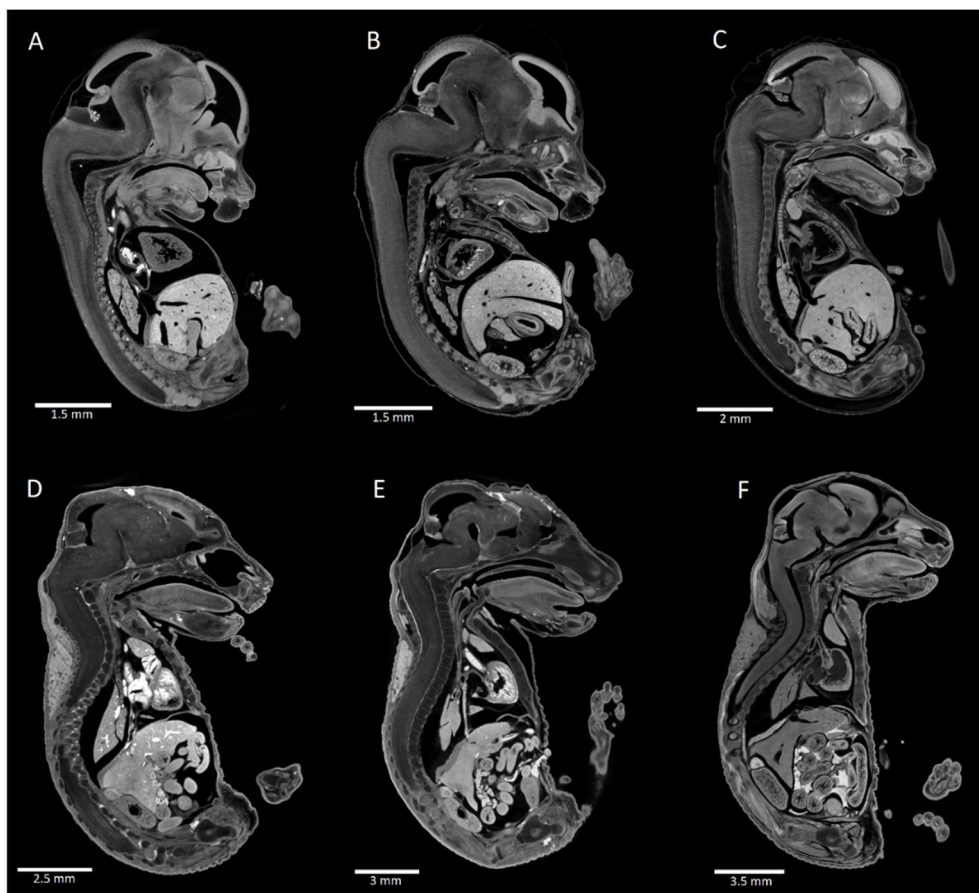


Figure 11: Middle sagittal sections of the mouse embryos properly stained in iodine solution. E13.5 (A), E14.5 (B), E15.5 (C), E16.5 (D), E17.5 (E), E18.5 (F).

4.1.3. Testing of the developed contrasting protocol on different types of samples

To test the versatility and efficiency of the proposed iodine contrasting solution I have selected and stained several different samples with low native X-ray attenuation.

The first showcased sample is the tadpole of the commonly used amphibian model organism *Xenopus laevis*. In order to fully stain the pre-metamorphosis developmental stage of the tadpole the sample was dehydrated for 8h in each concentration of EtOH (30%, 50%, 70%, 80% and 90 %) and then stained for 20h in 1% I₂ in 90% MeOH (Fig. 12).



Figure 12: The horizontal section and 3D render of the *Xenopus laevis* tadpole shows the fully contrasted soft tissues.

The seedpod of the *Capsella bursa-pastoris* was selected as the plant subject to test the staining properties of the iodine solution, the sample was dehydrated in the ethanol grades (30%, 50%, 70%, 80% and 90 % for 1 hour in each concentration) the sample was fully stained after 2 hours in the staining solution (Fig. 13).

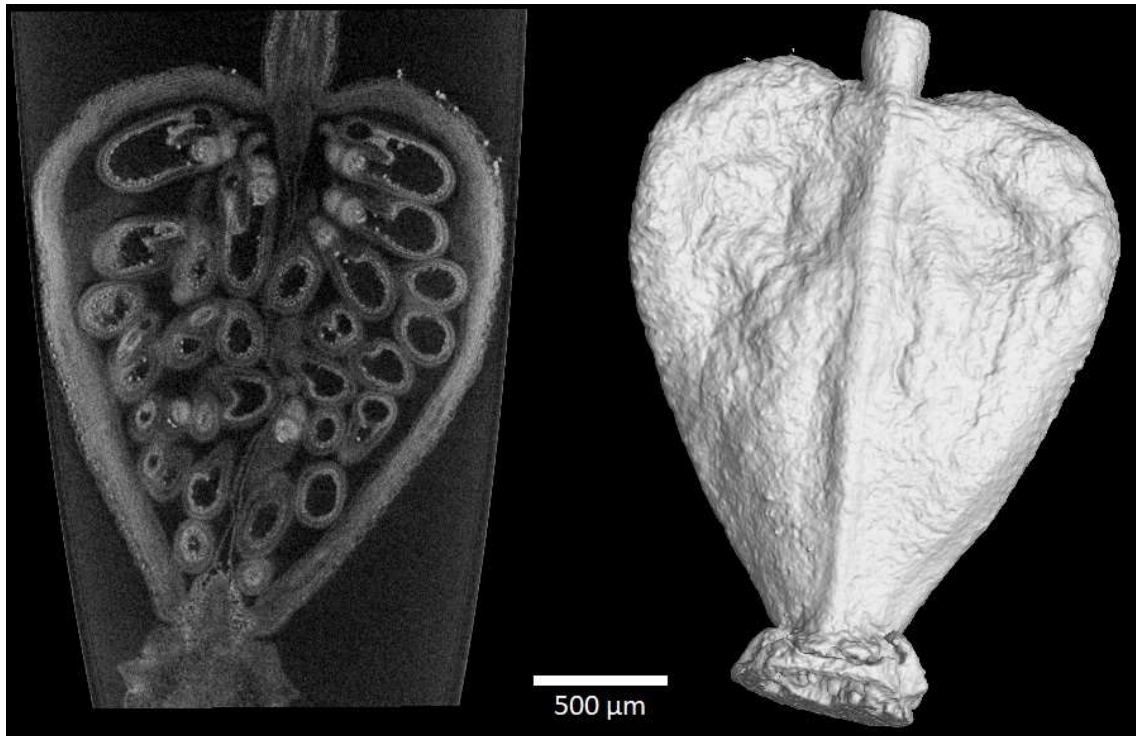


Figure 13: The staining in the proposed iodine solution was able to contrast the developing embryos of the future seeds in the seedpod of the *Capsella bursa-pastoris*.

The sample of the human heart from cadaver was obtained through the cooperation with Faculty hospital Motol in Prague. The section from the heart was dehydrated for 24 hours in each concentration of ethanol solution (30%, 50%, 70%, 80% and 90 %) and then placed in the iodine staining solution, after the 4 days in the staining solution the progress of the staining was evaluated by short CT scan. The 4 days determined to be not sufficient (Fig. 14) so the sample was submerged in the staining solution for the additional 7 days (refresh of the contrasting solution after 3 days), after which the sample was fully stained.

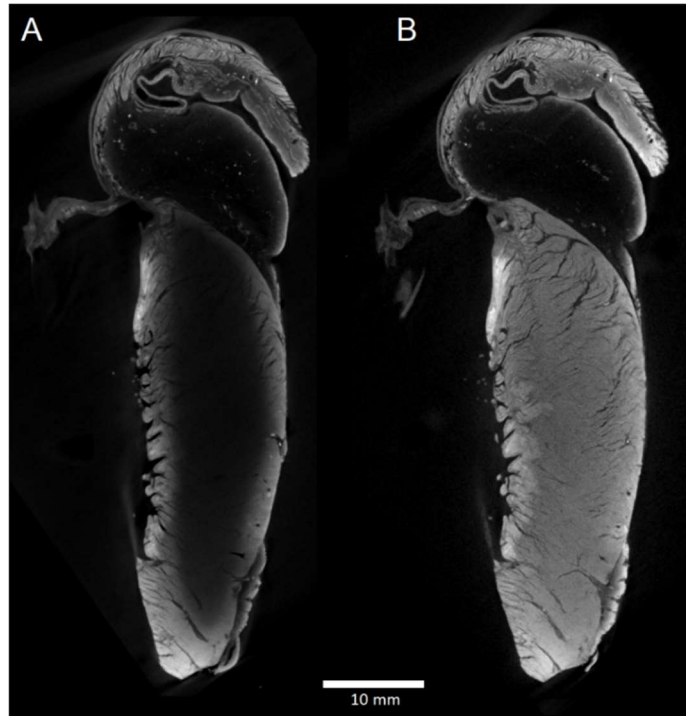


Figure 14: The section of the human heart was only partially stained after the 4 days in the iodine staining solution (A), to complete the staining the sample was submerged in the staining solution for additional 7 days (B).

4.2. Applications of developed contrasting protocols and designing the data analysis

The main objective of this work was to design the whole process of analyzing the sample from contrasting and scanning to determining the specific software analysis of the obtained data for each individual project I was working on, in the following part of this thesis I will present some of these projects.

4.2.1. Visualizing the A β plaques in the rat brain in Alzheimer's disease research

In the follow up research - my first author publication (Kavkova *et al.*, 2021) I have optimized the protocol for the staining of the mouse brain for the purpose of imaging of the rat brain. In cooperation with the research group focused on the research of Alzheimer's disease (AD) we have obtained several brains of transgenic rats. These brains contained the amyloid beta (A β) plaques which are the main cause of the Alzheimer's disease symptoms. It has been proposed that the reduction of A β deposits might help control the AD symptoms, which made the A β plaques the focus of targeted treatment of the AD. In order to test the effectiveness of an AD therapy focused on reduction of the A β plaques, there is a substantial need of a non-invasive, precise, and reproducible imaging method to analyze the location and size of the A β

plaques in the brain. In the majority of studies on rat models, the A β plaques were quantified histologically in sliced and immunostained brain tissue. While the histology and immunohistochemistry are important, standard routines for identifying and characterizing the plaque properties, it has not been previously determined whether the absorption based contrast enhanced X-ray micro CT imaging is capable of detecting and quantifying amyloid plaques in the brains of rodents.

In my paper I have proposed the protocol for 3D imaging of the A β plaques by micro CT which enables the analysis of plaque distribution in 3D without sectioning (which might induce artifacts related to section deformation or missing tissue due to the sectioning), where the proposed method can help the assessment of effectivity in newly tested drugs by quantifying the A β plaques in the brain.

The staining protocol which we previously developed for the mouse brain stains the different tissues of the brain based on their structure, this occurrence led to the theory that the dense structure of the amyloid protein clusters in the brain of transgenic rats should be stained in different fashion than the surrounding normal tissue. This premise was confirmed when the transgenic and the wildtype rat brains were stained in the optimized contrasting protocol and the whole rat brain was scanned with resolution of 9 μ m. The resulting scans (Fig. 15) clearly showed the amyloid plaques in the brain of the transgenic animal, which confirmed our hypothesis of possible visualization of the A β plaques with iodine solution.

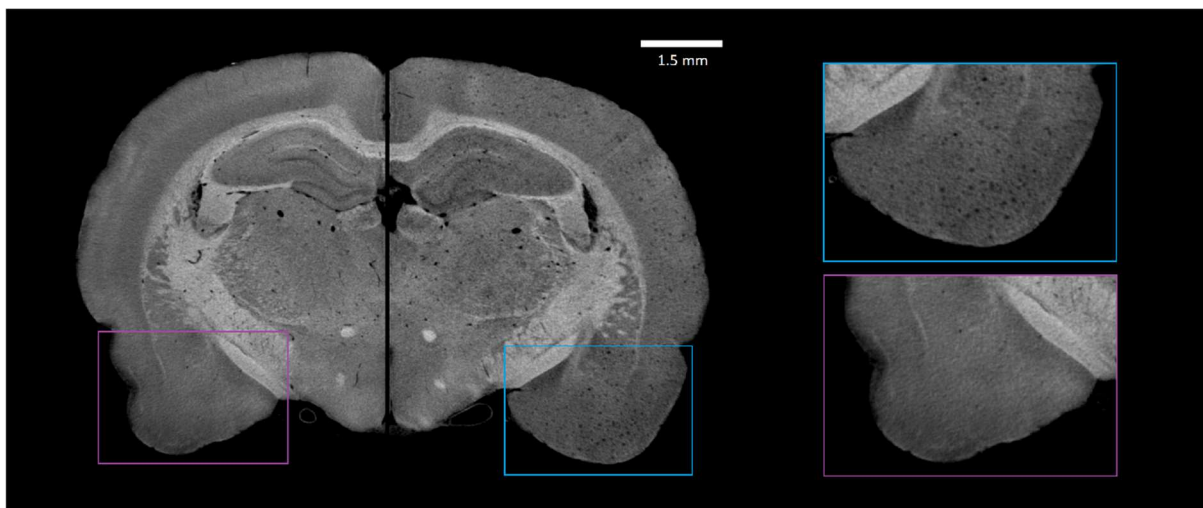


Figure 15: Comparison of the wt rat brain (left half of the brain) to the brain of the transgenic animal (right half of the brain) where the amyloid plaques are visible as the dark dots (Kavková *et al.*, 2021).

The nondestructive characteristic of the micro CT analysis also allowed the consecutive histological analysis of the rat brain. To assess the sensitivity of amyloid plaques detection using micro CT in contrast to the standard immunohistological staining of the brain, the brain after the micro CT analysis was washed in the clean ethanol solution for several days to clear out the iodine and subsequently sliced in the microtome to create histological sections. The dehydrated and previously iodine stained tissue was fragile while slicing, but several tissue sections were well preserved and immunostained for the presence of A β plaques (Fig. 16).

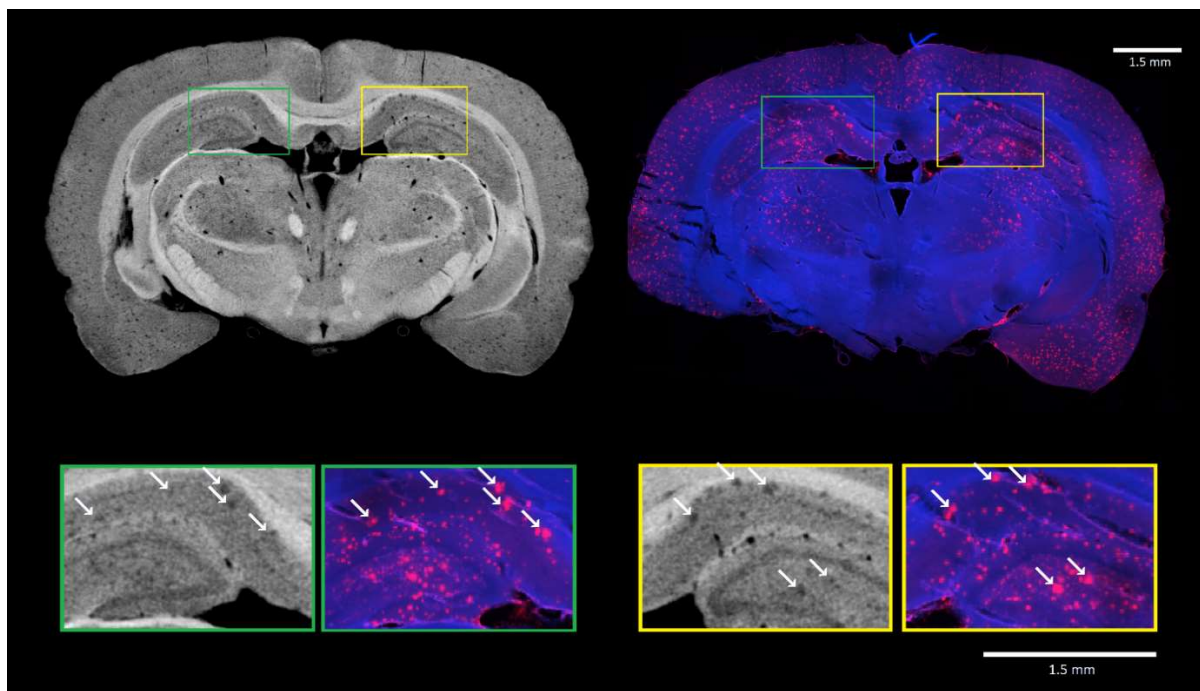


Figure 16: Confirmation of the identity of the detected A β plaques by follow up immunohistochemical staining (A β plaques in pink color) (Kavková *et al.*, 2021).

In the follow up step of the A β plaques analysis I have focused on the dorsal hippocampus which is a structure of brain severely impaired by the amyloid accumulation and cellular loss in AD. In the industrial micro CT setups (such as GE Phoenix L240 which is predominantly used in our lab for the analysis of the biological samples) which uses the cone beam geometry, the dimension of the sample directly determines the resulting voxel size of the obtained dataset. To acquire a 3D distribution of A β plaques with high resolution, we have decided to dissect the hippocampus and scan it again with a better resolution of 3 μ m. The smaller voxel size of the acquired hippocampus dataset allowed the identification of the smaller A β plaques and improved the readability of the large A β plaques' borders (Fig. 17).

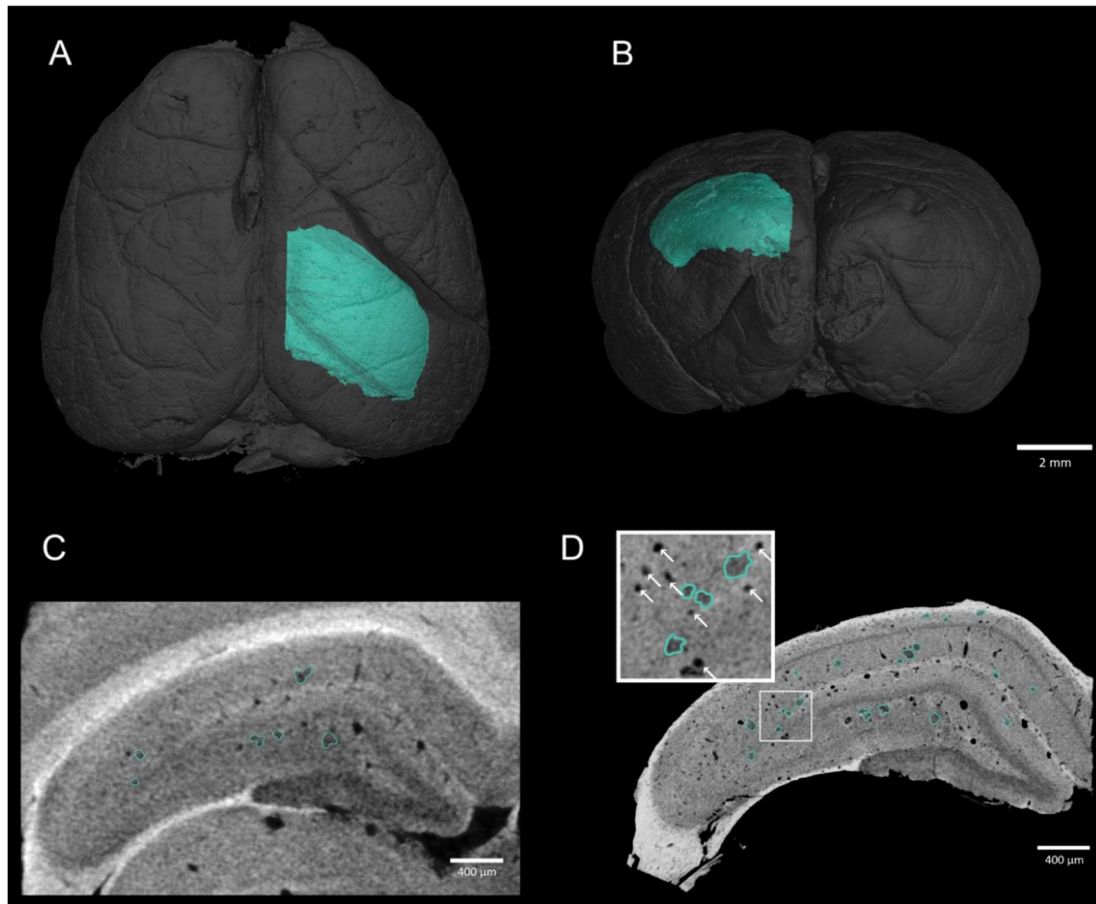


Figure 17: Horizontal (A) and coronal (B) 3D view of the rat brain with the visualized dissected hippocampus (green) used for the higher resolution scan. Comparison of the image quality in the same section of the hippocampus from the same animal - the scan of the whole brain (C) and the scan of the dissected hippocampus, the plaques are highlighted in green and the blood vessels are labeled by white arrows (D) (Kavková *et al.*, 2021).

The re-scanning of the hippocampus with better resolution allowed the use of various analysis in the software VG Studio MAX. Even though this software is primarily designed for the analysis of industrial samples it can precisely define the shape and the distribution of the amyloid plaques in the dissected hippocampus in a novel type of analysis. In the obtained data, the amyloid plaques had similar contrast as other tissues, this meant that they could not be detected with global thresholding methods and in order to analyze them they had to be segmented manually. After defining all of the segmented plaques in the dissected hippocampus by one region of interest, all plaques were counted and measured. In the dissected hippocampus total of 1666 individual plaques were identified. The volume of the smallest individual plaque was $895 \mu\text{m}^3$, indicating the lower limit for amyloid plaque detection in the presented micro CT

data with voxel size of 3 μm (in the immunohistological images even smaller plaques can be distinguished). The biggest identified plaque had a volume of 721,552 μm^3 .

As a next step in the analysis of the plaques I have assessed the variability of shape of plaques by measuring their compactness. The compactness score describes the shape of the analyzed object. In the range of compactness values 0-1 the score of one represented a perfect sphere (Fig. 18). The identified plaques had median of compactness at 0.396 which indicates that the analyzed plaques tend to have more irregular shape with protrusions.

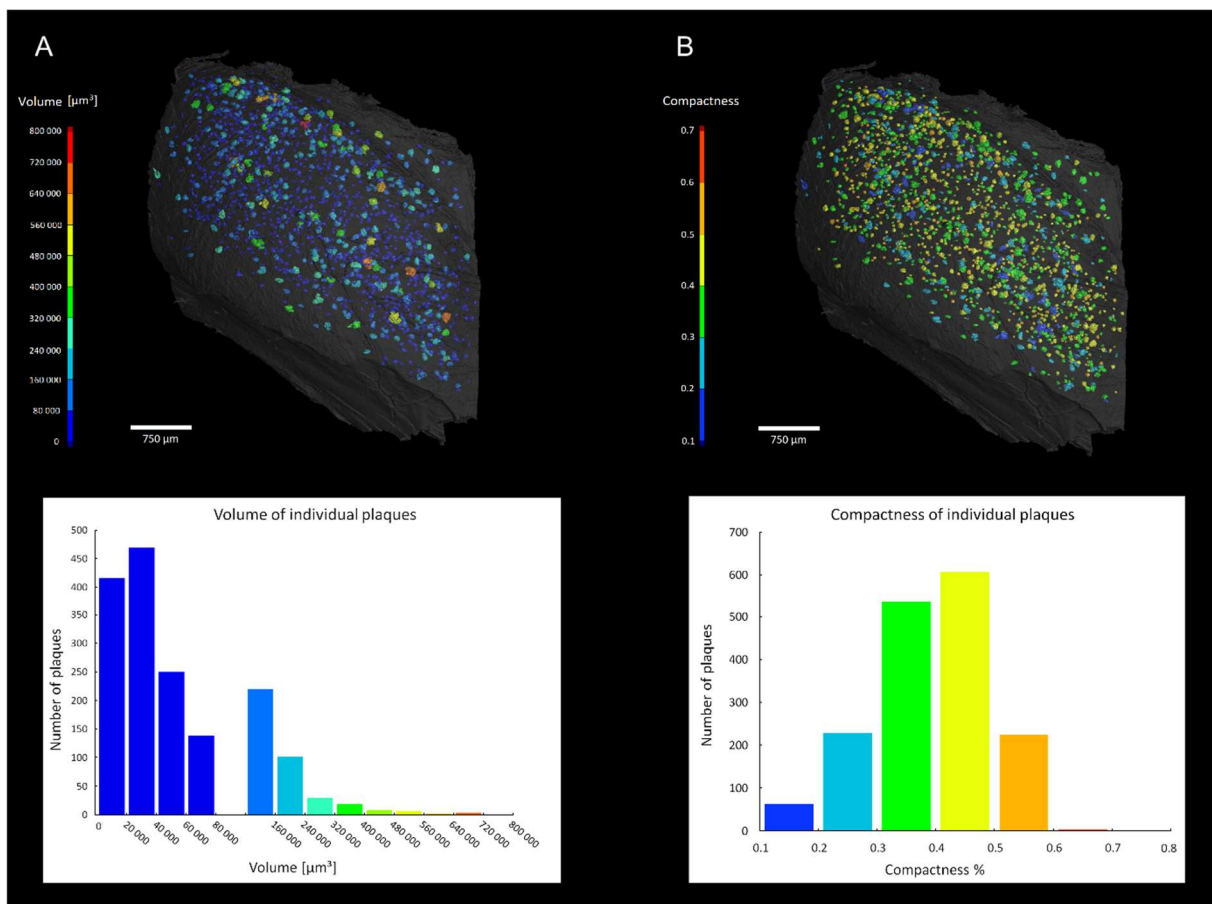


Figure 18: analysis of volume (A) and compactness (B) of the plaques in the transgenic rat hippocampus (Kavková *et al.*, 2021).

The accuracy of the generated 3D model of distribution of plaques in the hippocampal sample allowed me to define and quantify the inter-plaque distance and the distance of the plaques to the nearest blood vessel. Both of these values were quantified and compared to the datasets of randomly generated "plaques" to test if the plaques emerges randomly or in some specific pattern.

By measuring the inter-plaque distances, we have tested if the A β plaques are prone to form in clumps. To test this hypothesis we have compared the actual inter-plaque distances from the experimental dataset to the synthetically created dataset with the same shape, volume and same amount of plaques as the experimental dataset but in which the positions of the generated plaques were completely random. The median of distances from the experimental sample data was 101.1 μm , whereas the randomly generated dataset returned a distribution shift towards larger values - median distance 123.4 μm , confirming the hypothesis that the A β plaques tends to emerge in clumps. The Mann Whitney U test confirmed a statistically significant difference between the both measurements ($Z = 11.97$, $p < 0.001$).

Related to the inter-plaque distance analysis we have tested whether the relative distance between the plaques and the blood vessels follows a non-random pattern. Again, the dataset with random positions of the plaques was generated, this time leaving out the area of detected blood vessels. The distances of the plaques to the nearest blood vessel were then measured in both datasets. In the actual experimental dataset, the median distance between the plaque and the nearest vessel was 64.5 μm . The distances of generated "plaques" to a nearest vessel were measured with median of 89.1 μm . This suggests that the plaque-vessel distance is significantly shorter in experimental data than in the generated random sample, indicating that plaques tend to appear closer to the blood vessels where the oxygen level is higher. The statistical significance of this theory was confirmed by the Mann Whitney U test ($Z = 10.95$, $p < 0.001$).

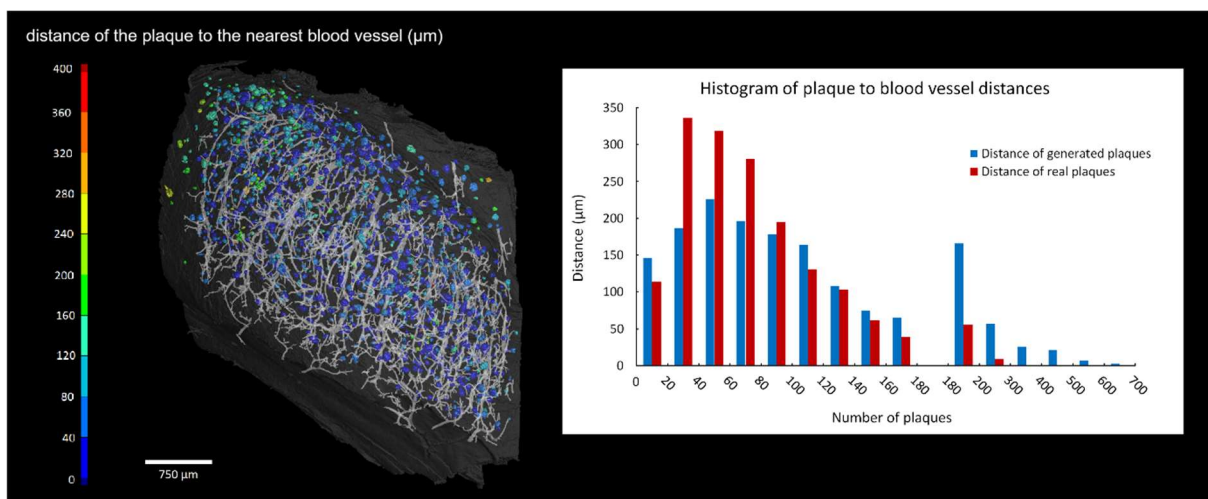


Figure 19: Visualization of the plaque distance to the nearest blood vessel and the comparison of the distances in the actual and generated data (Kavková *et al.*, 2021).

The absorption based contrast enhanced X-ray micro CT imaging is viable method for detection and 3D analysis of A β plaques in transgenic rodent models of Alzheimer's disease. Using iodine contrasted brain tissue isolated from the transgenic rat model we have proved that the micro CT imaging is capable of precise imaging of A β plaques without damaging the sample, making it possible to further analyze the sample. Micro CT analysis was able to visualize and quantify the various aspects of 3D spatial distribution of plaques which can help in the assessment of effectivity in newly tested drugs for treating AD patients.

4.2.2. Loss of function of CDK13 gene during development

Congenital heart defects, dysmorphic facial features and intellectual developmental disorders syndromes in humans was recently associated with mutation in CDK13 gene (Cyclin-dependent kinase 13). Within the project researching the impact of the complete loss of Cdk13 function during mammalian development, the Cdk13 knock-out (KO) mouse model was employed to explore a novel role of Cdk13 protein during mouse embryonic development (Nováková *et al.*, 2019).

As a part of the joined research, I have focused on the micro CT analysis of the E15.5 as this was oldest collected developmental stage - in the Cdk13-deficient animals the embryonal lethality was observed by the embryonic day E16.5. Based on the histological analyses conducted as part of the research, the heart, liver and kidneys were selected as targets for the detailed micro CT analysis. Since the E15.5 mouse embryos are too large for the 3D imaging by light sheet microscopy the micro CT analysis was selected for the task of imaging the morphological defects in detailed 3D models.

The samples of both KO and wt mouse embryos were contrasted with the staining protocol presented in my thesis. The selected organs were manually segmented and compared based on their volume and their appearance in tomographic slices and 3D models (Fig. 20).



Figure 20: Comparison of segmented internal organs of E15.5 mouse embryo. On the left wt mouse, right Cdk13 KO mouse. Liver (light pink), heart (red), kidneys (dark pink) (Nováková *et al.*, 2019).

The micro CT analysis of the contrasted E15.5 embryos revealed several developmental abnormalities. The heart wall of both ventricles in Cdk13 KO embryos appeared thinner in comparison to wt littermate controls. In addition, lung, liver and kidney in Cdk13 KO embryos were smaller and undeveloped. Based on further analyses, the lethality at the E16.5 stage was determined to be the result of heart failure most likely due to multiple heart defects followed by insufficient blood circulation caused by multiple organs dysfunctions.

4.2.3. The role of SATB2 gene in development of dentition

The SATB2 gene participates in the process of regulating various transcription factors both during early embryogenesis and later in the process of cell differentiation. Within the large scale gene expression profiling at early stages of odontogenesis in mouse embryo, the SATB2 gene have been identified to have specific role in regulatory processes involved in early odontogenesis and jaw patterning, exhibiting strong expression in the rostral jaw area in contrast to the caudal part of the jaw (Nevoránková *et al.*, 2023).

To uncover the effect of the SATB2 gene in jaw and teeth patterning, SATB2 knockout mouse strain was generated by the cooperating research group. The developmental stages of

E16.5 and E18.5 of mouse embryos were then selected for the micro CT analysis, where the main focus of the analysis would be the identification of the irregular teeth patterning and finding the morphological changes in the lower jaw causing the underbite observed in the SatB2 knockout mice.

Within the analysis of the developmental stage E18.5 we have decided to scan the embryos consecutively in native state and then contrasted with iodine (Fig. 21). Since in the E18.5 developmental stage the enchondral ossification already started (in contrast to the E16.5 where the ossifications are not yet visible in the CT data) and the ossifications of the bones are visible in X-ray due to the deposition of the hydroxyapatite, the imaging of the bones in E18.5 is possible. This approach allowed evaluation of the bone formation which would be impossible to do in the contrasted sample since the signal from the less ossified parts of the bone would be lost in the surrounding contrasted soft tissues.

As the following step the samples of both ages were stained according to the protocol presented in this thesis, based on their age.

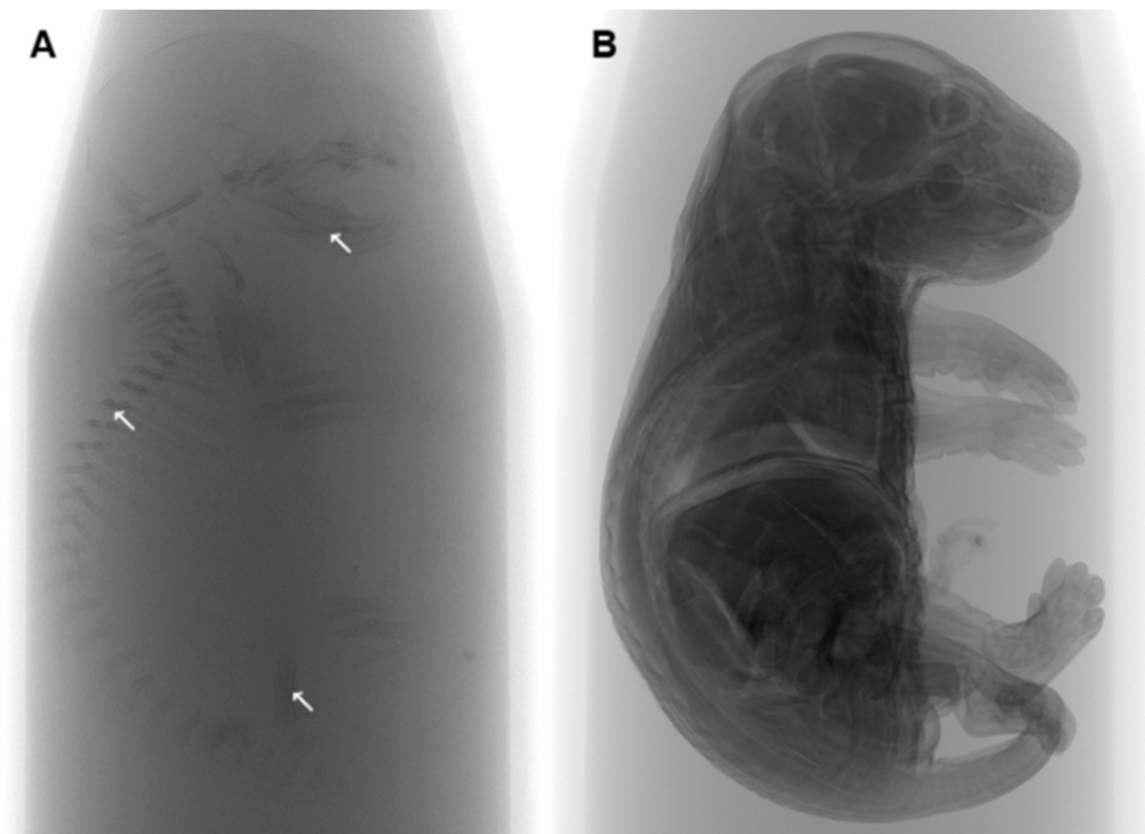


Figure 21: The X-ray image of the native sample (A) the bone ossifications are indicated by the white arrows. The same sample stained in the iodine solution (B) where all of the soft tissues are contrasted.

In the contrasted datasets the Meckel cartilage (intermediate structure involved in the lower jaw formation in mammals) and the tooth germs were manually segmented and subsequently analyzed. We have focused on the 3D morphometrics of the shape of developing tooth germs with focus on ectopic tooth and the morphological changes in Meckel cartilage caused by delay in its development.

The segmentation and creation of the 3D model of the tooth germs revealed the presence of the ectopic tooth (extra tooth not present in the normal teeth pattern) located in the rostral area of molars (Fig. 22). The further analysis of ectopic tooth position in relation to normal teeth was done through measurements of teeth volume and teeth lengths and distances between teeth in 3D space. The morphometrics revealed that the molar joined to the ectopic tooth is smaller than the corresponding molar in wt mouse and that the ectopic tooth does not cause shift of the original position of molar.

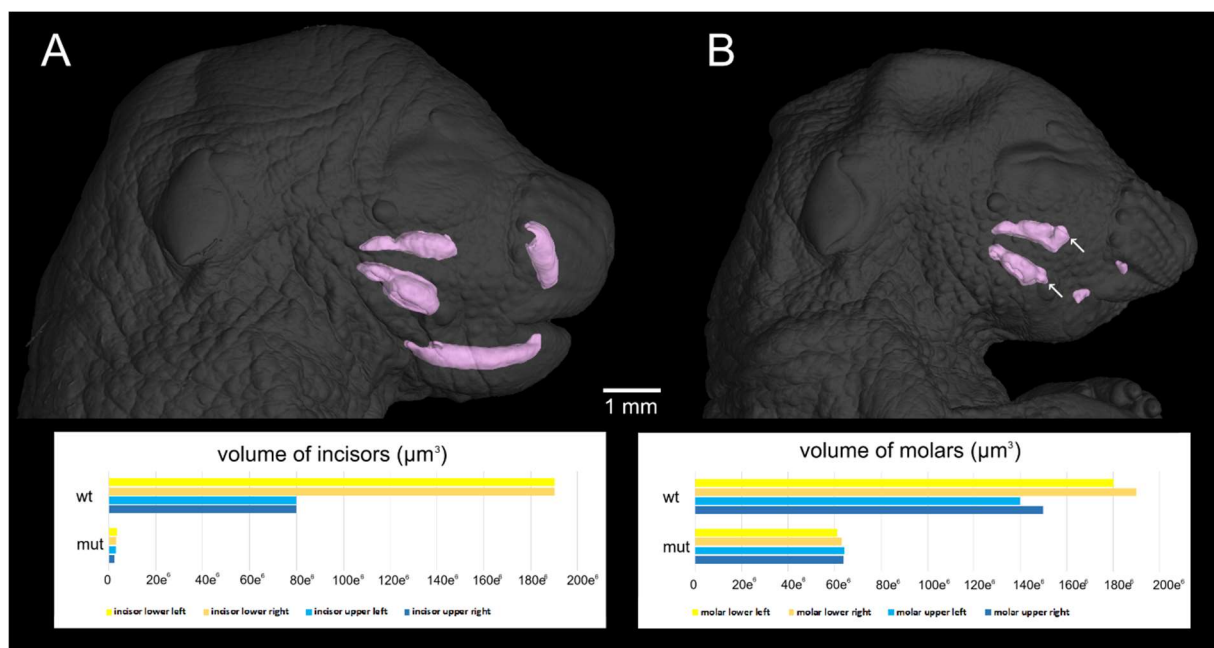


Figure 22: Segmented tooth germs in the E18.5 embryos. Wt mouse (A), in the mutant mouse (B) the ectopic molars are indicated in white arrows. In the mutant mouse the reduced abnormal growth of the incisors is clearly distinguished in the 3D reconstruction and even in the measured tooth germ volume indicated in the graph.

The SatB2 knockout mice embryos are distinct by the shortened lower jaw. The analysis of the obtained contrasted micro CT data revealed that the affected structure responsible for the truncation is the Meckel cartilage. The length of the Meckel cartilage was measured by placing the points of the polyline tool in the center of the transversal cross section of the cartilage. The

measured length of the cartilage was then defined by the length of the placed polyline. The follow up segmentation of this cartilage and creation of 3D model revealed the fusion of the rostral part of the cartilage in the chin to the lateral parts, revealing the morphological cause of the truncation of lower jaw (Fig. 23).

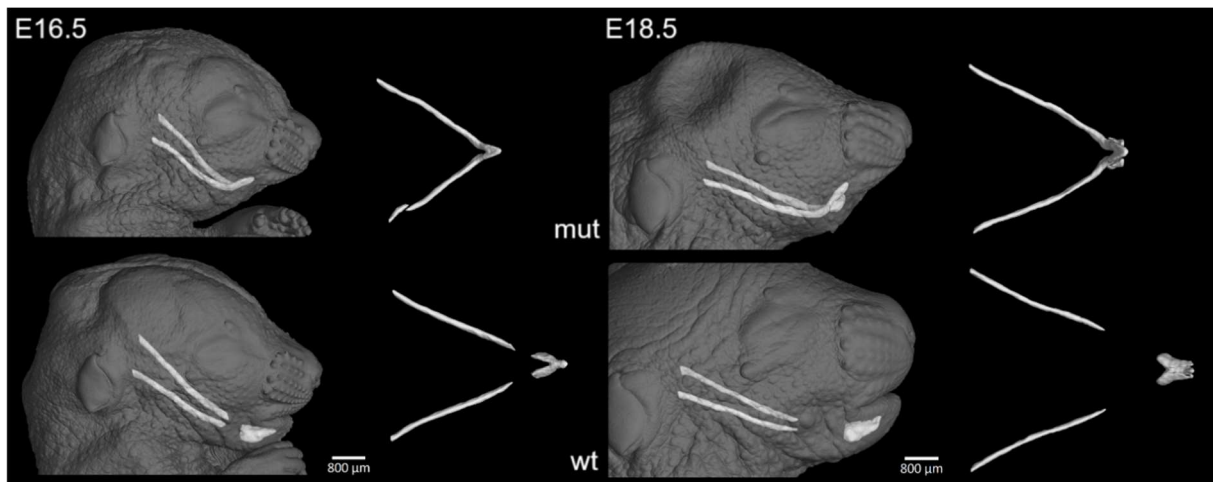


Figure 23: Visualization of the segmented Meckel cartilage, the knockout mice are showing distinct fusion of the rostral part of the cartilage in chin to the long lateral parts alongside the jaw.

The loss of SatB2 led to abnormal craniofacial patterning alongside the anterior-posterior axis. The obtained 3D micro CT data revealed shortening of the lower jaw with the middle element of Meckel's cartilage fused, abnormal smaller incisors detected in both upper and lower jaws and emergence of the ectopic molars. All of the above-mentioned morphological abnormalities were identified in the created 3D models, without the micro CT analysis the description of the aberrant gross morphology in the SatB2 deficient mouse embryos would be particularly difficult.

4.2.4. Role of the TMEM107 gene in eye development

The Tmem107 is a protein located the base of the cilium, the deficiency of this protein has been linked with the ciliopathy-associated syndromes. Mouse strains with knocked out Tmem107 display severe phenotypes such as microphthalmia, shorter snouts, expanded facial midlines, cleft palates, and extensive exencephaly (Cela *et al.*, 2018). The role of this gene in eye development is not yet fully understood which is why we have pursued the micro CT analysis of the Tmem107 deficient mouse embryos with focus on the distinctive ocular phenotypes including anophthalmia and microphthalmia (Dubaic *et al.*, 2023).

The mouse embryos at the E15.5 developmental stage were contrasted by the iodine staining protocol. As the focus of the publication was on close investigation of the eye development, the eyes in both mutant and the wt mice were manually segmented in order to obtain precise 3D model. To describe the defects in eye in detail, the wall thickness analysis of the segmented eyes was executed. The wall thickness analysis is one of the advanced analyses present in the VG Studio MAX software, the analysis is based on the fitting of the spheres with different diameter in the analyzed object (in this case the eye) in the 3D space. The resulting analysis revealed decreased retina volume in mutant *Tmem107* deficient embryos (Fig. 24).

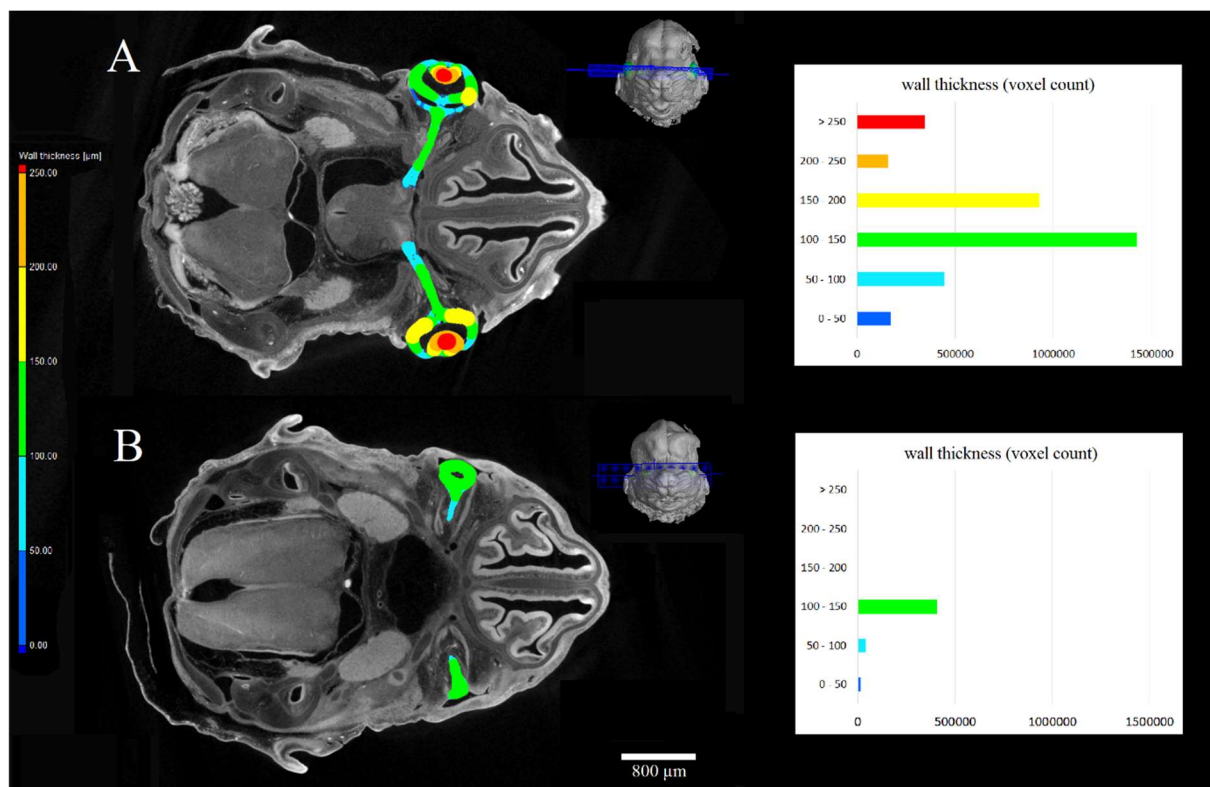


Figure 24: The wall thickness analysis of eyes in wildtype (A) and *Tmem107* deficient (B) E15.5 mouse embryos. The position of the section is indicated in the smaller 3D render for each sample.

In the created 3D model, the optic stalk length was measured with the polyline tool. This specific tool in the VGStudio MAX software enables measurement of length in the not-straight objects. This analysis revealed the distinct phenotype in form of shortened optic nerve in mutant embryos.

The micro CT analysis have helped analyze distinctive ocular phenotypes in *Tmem107* deficient mouse embryos by creating the precise 3D models which enabled the advanced analyses in the specialized software.

4.2.5. Imaging of the emerging tooth ankylosis in chameleon embryo

Unlike most of the reptiles, the chameleon teeth grow in a unique way where the adult teeth are firmly attached at the top of the jaw bone - this type of teeth attachment is called acrodont ankylosis.

In my first author paper we have focused on describing how symmetrically ankylosed teeth in veiled chameleon (*Chamaeleo calyptratus*) develops from asymmetrical tooth germs (Kavková *et al.*, 2020). Our main aim was to determine the developmental processes contributing to the morphogenesis of acrodont dentition and to analyze the asymmetrical structures occurring on the labial and lingual sides of the cervical loop (epithelial structure of the developing tooth, containing stem cell niche) using embryos of the veiled chameleon.

For the precise description of the asymmetries in the growth of bone and the surrounding soft tissue we have selected 5 distinct developmental stages of chameleon embryo. All of the analyzed samples were at first scanned in the native state to describe the anatomy of the jaw bone and teeth without losing the signal from less mineralized parts in the contrasted dataset. Consecutively, the samples were contrasted and scanned again.

Based on the preliminary histological analyses, the teeth appeared to develop asymmetrically along the labio-lingual axis. To assess this, we needed to measure the lengths of the labial and lingual side of the teeth and the distance of the tooth to the underlying jaw bone in the native scans. For this type of measurement, it was essential to create the section of each tooth perpendicular to the line of the jaw which proved to be problematic since the jaw is curved. As a first step of creating the perpendicular section of the tooth in curved jaw, the dataset needed to be oriented and registered. In the frontal and horizontal sections, the dataset was centered using the natural symmetry of the lower jaw, in the sagittal section the dataset was oriented to level the bone of the lower jaw. The following step in order to create the perpendicular section of the tooth was creating the polyline (curved line in 3D space) defined by the points placed in the highest points of individual teeth. Then through the unroll feature in the VGstudio MAX the "unrolled" section containing all of the teeth as well as the sections perpendicular to the unrolled plane were created (Fig. 25).

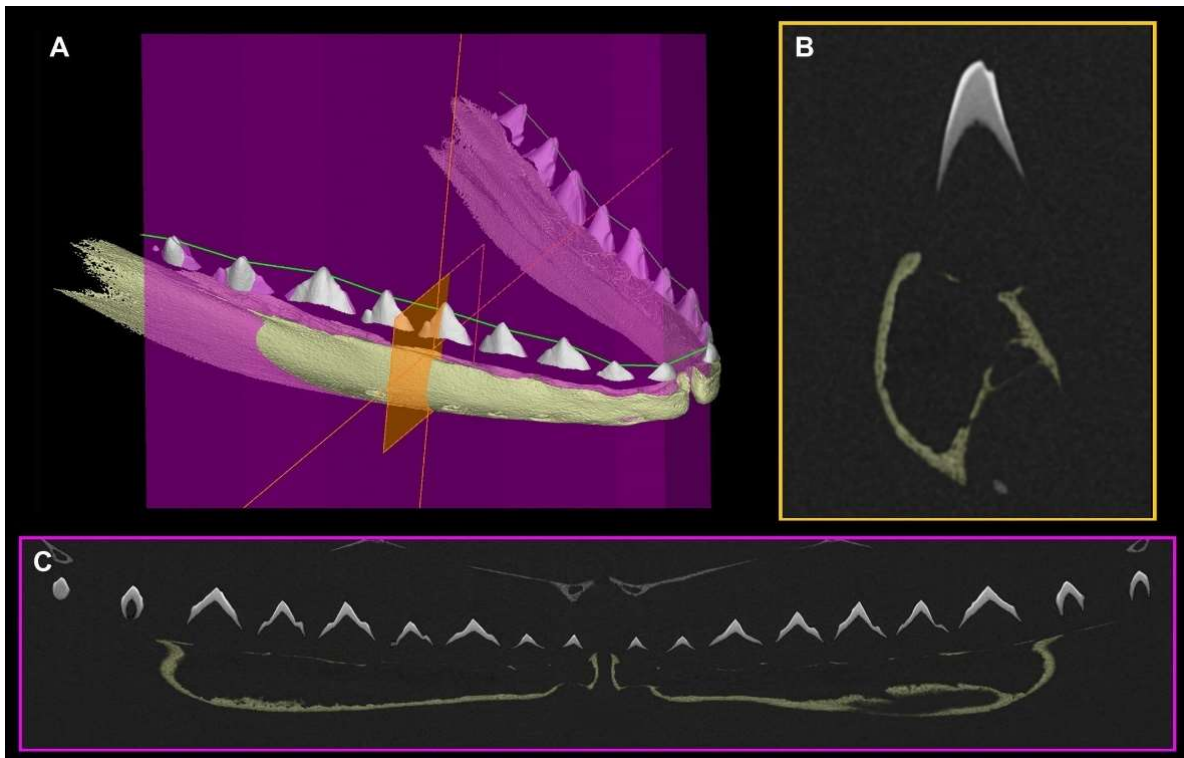


Figure 25: The green polyline is defined by points at the tip of all teeth in the lower jaw (A). The new plane of sections (magenta) was constructed using the polyline as guide (A, C). The plane of transversal section through the tooth (orange) is then perpendicular to the magenta plane (A, B) (Kavková *et al.*, 2020).

By moving the perpendicular section alongside the created polyline, the perpendicular section of each tooth was created and used for the follow up measurement. The lengths of the labial and lingual side of the teeth and the distance of the tooth to the underlying jaw bone were measured in these images (Fig. 26). These measurements revealed that in the earlier developmental stages the distance between the tooth and the jaw was larger on the lingual side than on the labial.

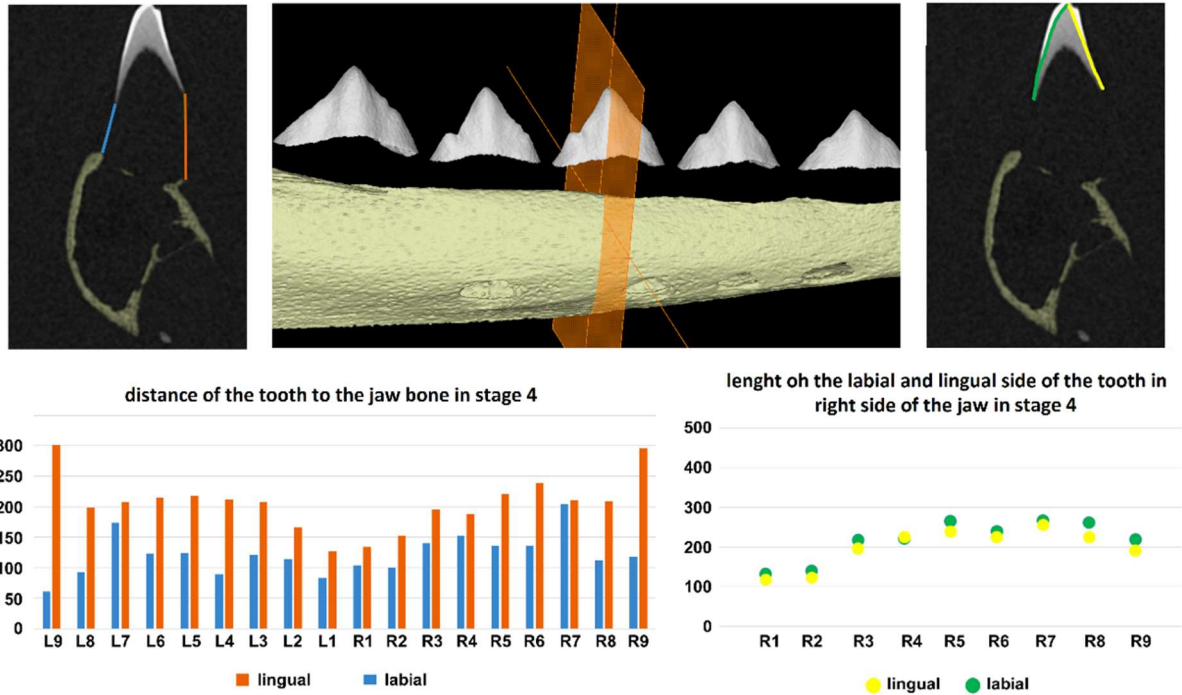


Figure 26: Morphometric measurements of the tooth to jaw bone distance and the measurement of the labial and lingual sides of the tooth are shown on the 4th developmental stage of chameleon embryo analyzed in the publication. In the graph, the teeth on the left side of the jaw are marked L1-L9, the teeth on the right side are marked as R1-R9 (Kavková *et al.*, 2020).

In the follow up analysis we have focused on the analyzing the angle of the growth of each tooth in relation to the underlying jaw bone. We decided to measure this angle since the spatial position of tooth and bone seemed to be not symmetrical in different developmental stages. The measured angle was defined by horizontal line placed in position of the dorsal bony lamellae and by the inclined line positioned through the center of each measured tooth (Fig. 27). Measurement of the angular inclination of the teeth axis to the dorsal bony lamellae revealed that the caudal teeth were positioned at a greater angle to the dorsal bony lamellae than the rostral teeth, more so in the younger developmental stages.

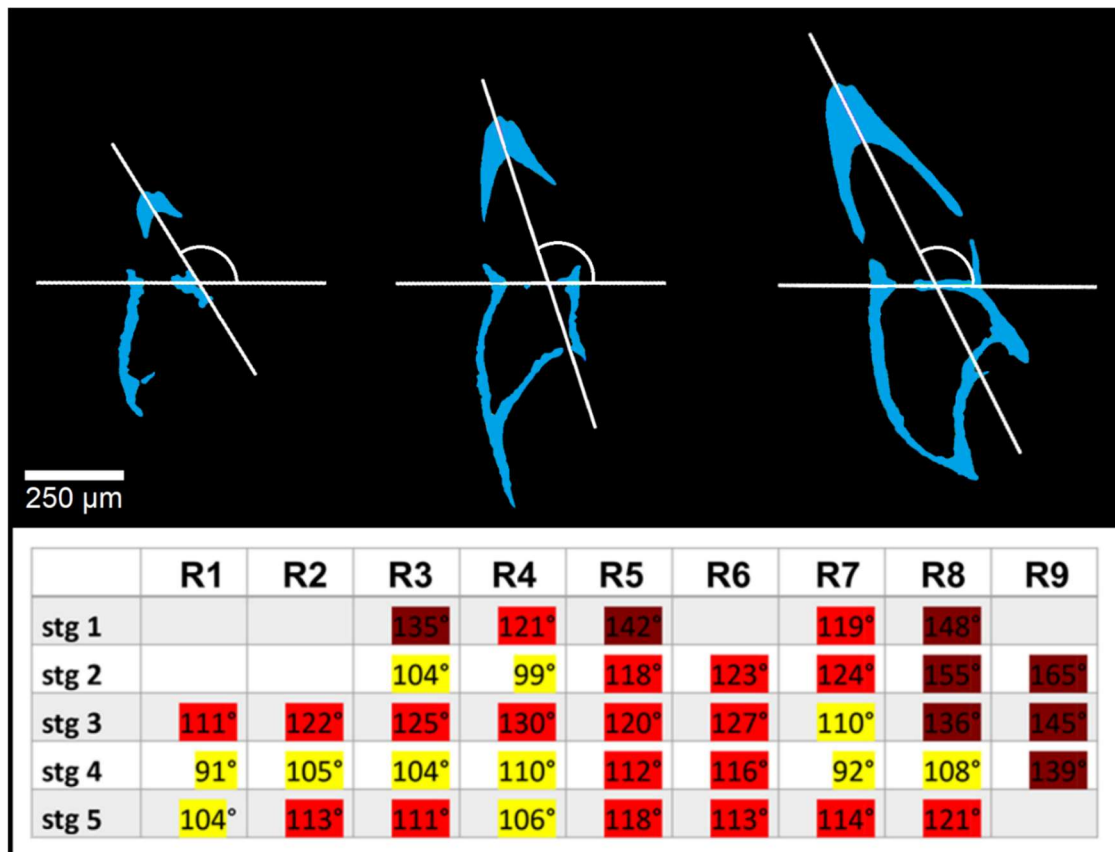


Figure 27: Measurement of the angle in which the teeth grown in relation to the bony lamellae of the jaw bone. The angles were measured in all 5 selected developmental stages (stg1-stg5). The displayed results are measured on the teeth in right side of the jaw (teeth are numbered R1-R9). The teeth in the caudal part of the jaw R8, R9 and the teeth in the younger stages 1 and 2 have higher angular inclination.

As a next step in the analysis of the asymmetrical growth of teeth in chameleon embryos, the samples were contrasted to obtain the information about the soft tissue of the cervical loop. The protocol for the mouse embryo staining was adjusted for the considerably smaller chameleon embryonal jaws as following: dehydration steps of 30%, 50%, 70%, 80% and 90% ethanol solution - 1.5 h in each concentration, after dehydration, samples were stained in the solution consisting of 1% iodine in 90% methanol for 16 h. After the scan, the segmentation of the cervical loop was carried out using Avizo 9.5 software (Fig. 28). As follows, the perpendicular section through the jaw was created using the polyline as was described in the analysis of the native scans. In the section through the center of each tooth (defined by the peak of each tooth) the length of the cervical loop was measured on the labial and lingual side (Fig. 28). The analysis highlighted significant differences between the size of the labial and lingual part of cervical loop even in the later stages where the symmetry of the hard tissues started to

develop. The differences in length of the lingual and labial part of the cervical loop were not consistent along the jaw, with the caudal teeth being more symmetrical in contrast to the teeth in the middle part of the jaw, where the most significant differences in length were observed.

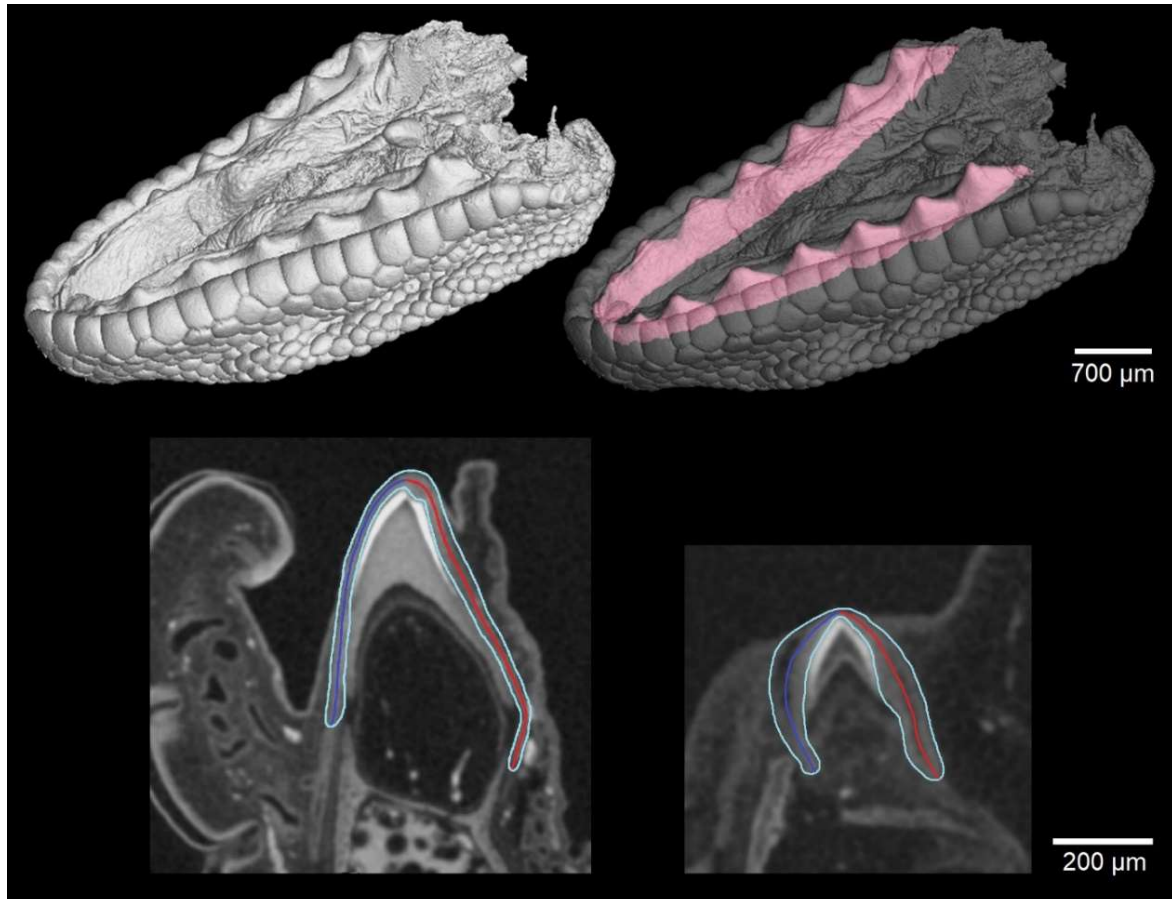


Figure 29: 3D render of lower jaw of the chameleon embryo with segmented cervical loop (pink). Visualization of the tracing in the measurement of the cervical loop length in labial (blue) and lingual (red) side of the tooth in the oldest analyzed stage 5 (left) and the youngest stage 1 on the right side (Kavková *et al.*, 2020).

The proposed micro CT analysis of both native and stained samples of chameleon embryos has revealed that the acrodont teeth of chameleons initially form asymmetrically, with differential extension of the cervical loop on the lingual and labial sides. This asymmetry was observed in the early stages of tooth development but later resolved to create the strict labio-lingual symmetry present in adult teeth in chameleon.

5. Conclusions

The topic of this thesis - X-ray micro and nano computed tomography of soft tissue - reflects a current trend of incorporating the advanced micro CT imaging into primary biological research as a valuable complementary method to generally used imaging methods. In the field of developmental biology research, industrial micro CT imaging has been increasingly utilized for the 3D imaging of the small samples, providing a non-invasive and high-resolution imaging tool for investigating the complex processes of tissue formation and morphogenesis.

One of the main objectives of this work was testing the ability of specific staining solutions to properly contrast the soft tissues and determining the optimal staining protocols. I have tested several staining methods on the model of the mouse brain and proposed the iodine-based protocol as the most suitable one.

The data obtained during the testing of the staining solutions on the mouse brain allowed the more focused testing of the contrasting of the mouse embryos. I have focused on the determining the optimal staining protocols for various developmental stages of mouse embryos. I was able to determine the protocols for the mouse embryo developmental stages E13.5 to E18.5. I have also tested the proposed iodine staining solution on various samples: the amphibian, plant and the human heart samples, successfully confirming the versatility of the presented contrasting protocol.

I have optimized the protocol for the staining of the mouse brain for the contrasting of the rat brain. For this project I have proposed that the staining protocol will be able to visualize the amyloid plaques in the brains of transgenic rats used as model for the Alzheimer disease. The theory was confirmed and I was able to fully describe the distribution of the amyloid plaques in the hippocampus as well as determine the software analysis of their attributes important to the development of the Alzheimer disease, publishing the results as my first author paper.

The establishment of the staining protocols for the mouse embryo originated in the need for the analysis of the samples in scope of the various projects focused on the role of specific genes during the development. In all of these projects I have applied the determined optimal protocol for each individual developmental stage. The obtained high resolution data then allowed me to propose specific analyses such as analysis of the affected organs of the Cdk13 deficient mice, the segmentations and quantitative analyses of the Meckel cartilage and tooth

germs in SatB2 mice and the quantitative analysis of the rudimentary eyes on the Tmem107 ^{-/-} mice.

Finally, I have focused on the analysis of asymmetrical tooth development in the chameleon embryos. In this project I have proposed the dual scanning of the embryos – native scan provided precise information about the tooth-bone interface and allowed the measurement of various dimensions of the teeth and the jaw bone, the follow up scans of the same samples stained in the optimized iodine protocol then allowed the description of the soft tissues surrounding the teeth.

In conclusion, in this work I have used the industrial micro CT imaging to gain new insights into the complex processes of developmental biology. I have designed contrasting protocols and software analyses for advanced industrial micro CT analysis of the biological samples. This work can contribute to the advancement of our understanding of developmental biology processes and the methods proposed in this work can be applied in other scientific research fields.

6. References

1. Aslanidi, O.V., *et al.* "Application of micro-computed tomography with iodine staining to cardiac imaging, segmentation, and computational model development." *IEEE transactions on medical imaging* 32.1 (2012): 8-17.
2. Babaei, F., *et al.* "Contrast-enhanced X-ray micro-computed tomography as a versatile method for anatomical studies of adult zebrafish." *Zebrafish* 13.4 (2016): 310-316.
3. Badea, C. T., *et al.* "4-D micro-CT of the mouse heart." *Molecular Imaging* 4.2 (2005): 15353500200504187.
4. Badea, C. T., *et al.* "In vivo small-animal imaging using micro-CT and digital subtraction angiography." *Physics in Medicine & Biology* 53.19 (2008): R319.
5. Bamberg, F., *et al.* "Metal artifact reduction by dual energy computed tomography using monoenergetic extrapolation." *European radiology* 21 (2011): 1424-1429.
6. Bartscher, M., *et al.* "Enhancement and proof of accuracy of industrial computed tomography (CT) measurements." *CIRP annals* 56.1 (2007): 495-498.
7. Bidola, P., *et al.* "A step towards valid detection and quantification of lung cancer volume in experimental mice with contrast agent-based X-ray microtomography." *Scientific reports* 9.1 (2019): 1-10.
8. Blazek, P., *et al.* "Voxel size and calibration for CT measurements with a small field of view." *Proceedings of the 9th Conference on Industrial Computed Tomography* (2019): Padova, Italy. 2019.
9. Boas, F. E. and Fleischmann D. "CT artifacts: causes and reduction techniques." *Imaging Med* 4.2 (2012): 229-240.

10. Boas, F. E. and Fleischmann D. "Evaluation of two iterative techniques for reducing metal artifacts in computed tomography." *Radiology* 259.3 (2011): 894-902.
11. Bock, N. A., *et al.* "In vivo multiple-mouse MRI at 7 Tesla." *Magnetic Resonance in Medicine: An Official Journal of the International Society for Magnetic Resonance in Medicine* 54.5 (2005): 1311-1316.
12. Borodinsky, L. N. "Xenopus laevis as a model organism for the study of spinal cord formation, development, function and regeneration." *Frontiers in neural circuits* 11 (2017): 90.
13. Brown, R. W., *et al.* "Magnetic resonance imaging: physical principles and sequence design." *John Wiley & Sons*, (2014).
14. Bouxsein, M. L., *et al.* "Guidelines for assessment of bone microstructure in rodents using micro-computed tomography." *Journal of bone and mineral research* 25.7 (2010): 1468-1486.
15. Campbell, G. M., and Sophocleous A. "Quantitative analysis of bone and soft tissue by micro-computed tomography: applications to ex vivo and in vivo studies." *BoneKEy reports* 3 (2014).
16. Casey, B. J., *et al.* "Functional magnetic resonance imaging: Basic principles of and application to developmental science." *Developmental Science* 5.3 (2002): 301-309.
17. Cela, P., *et al.* "Ciliopathy protein Tmem107 plays multiple roles in craniofacial development." *Journal of dental research* 97.1 (2018): 108-117.
18. Cormode, D. P., *et al.* "Nanoparticle contrast agents for computed tomography: a focus on micelles." *Contrast media & molecular imaging* 9.1 (2014): 37-52.
19. Dayan, A. D. "Man and Mouse: Animals in Medical Research." *Journal of the Royal Society of Medicine* 78.1 (1985): 88.

20. De Crespigny, A., *et al.* "3D micro-CT imaging of the postmortem brain." *Journal of neuroscience methods* 171.2 (2008): 207-213.
21. De Chiffre, L., *et al.* "Industrial applications of computed tomography." *CIRP Annals-Manufacturing Technology* 63.2 (2014): 655-677.
22. Degenhardt, K., *et al.* "Rapid 3D phenotyping of cardiovascular development in mouse embryos by micro-CT with iodine staining." *Circulation: Cardiovascular Imaging* 3.3 (2010): 314-322.
23. de Oliveira, M., *et al.* "Quality assurance phantoms for cone beam computed tomography: a systematic literature review." *Dentomaxillofacial Radiology* 46.3 (2017): 20160329.
24. Du Plessis, A., le Roux S. G., and Guelpa A. "Comparison of medical and industrial X-ray computed tomography for non-destructive testing." *Case Studies in Nondestructive Testing and Evaluation* 6 (2016): 17-25.
25. Dubaic, M., *et al.* "Role of ciliopathy protein TMEM107 in eye development: insights from a mouse model and retinal organoid." *Life Science Alliance* 6.12 (2023).
26. Elisa, Z. *et al.* "Technical implementations of light sheet microscopy." *Microscopy research and technique* 81.9 (2018): 941-958.
27. Faulwetter, S., *et al.* "Contrast enhancing techniques for the application of micro-CT in marine biodiversity studies." *Microscopy and analysis* 27.2 (2013): S4-S7.
28. Fernández, R., *et al.* "Sine systemate chaos? A versatile tool for earthworm taxonomy: non-destructive imaging of freshly fixed and museum specimens using micro-computed tomography." *PloS one* 9.5 (2014): e96617.
29. Flohr, T. "CT systems." *Current Radiology Reports* 1.1 (2013): 52-63.

30. Folarin, A. A., *et al.* "Three-dimensional analysis of tumour vascular corrosion casts using stereoinaging and micro-computed tomography." *Microvascular research* 80.1 (2010): 89-98.
31. Frisoni, G. B., *et al.* "The clinical use of structural MRI in Alzheimer disease." *Nature Reviews Neurology* 6.2 (2010): 67-77.
32. Ghanavati, S., *et al.* "A perfusion procedure for imaging of the mouse cerebral vasculature by X-ray micro-CT." *Journal of neuroscience methods* 221 (2014): 70-77.
33. Hainfeld, J. F., *et al.* "Micro-CT enables microlocalisation and quantification of Her2-targeted gold nanoparticles within tumour regions." *The British journal of radiology* 84.1002 (2011): 526-533.
34. Hallouard, F., *et al.* "Iodinated blood pool contrast media for preclinical X-ray imaging applications a review." *Biomaterials* 31.24 (2010): 6249-6268.
35. Hankeova, S., *et al.* "DUCT reveals architectural mechanisms contributing to bile duct recovery in a mouse model for Alagille syndrome." *Elife* 10 (2021): e60916.
36. Hlushchuk, R., *et al.* "Innovative high-resolution microCT imaging of animal brain vasculature." *Brain Structure and Function* 225.9 (2020): 2885-2895.
37. Holdsworth, D. W., and Thornton, M. M. "Micro-CT in small animal and specimen imaging." *Trends in Biotechnology* 20.8 (2002): S34-S39.
38. Hsieh, J. "Computed tomography: principles, design, artifacts, and recent advances." Bellingham, WA: *SPIE*, (2009).
39. Hui, S. K., *et al.* "CT-based analysis of dose homogeneity in total body irradiation using lateral beam." *Journal of applied clinical medical physics* 5.4 (2004): 71-79.
40. Johnson, J. T., *et al.* "Virtual histology of transgenic mouse embryos for high-throughput phenotyping." *PLoS Genetics* 2.4 (2006): e61.

41. Kamenz, C., and Weidemann G. "Heavy metal-A contrasting substance for micro-tomographical visualization of scorpion book lungs." *Micron* 40.8 (2009): 911-917.
42. Katz, S. R., *et al.* "Whole-organism 3D quantitative characterization of zebrafish melanin by silver deposition micro-CT." *Elife* 10 (2021): e68920.
43. Kavkova, M., *et al.* "Contrast enhanced X-ray computed tomography imaging of amyloid plaques in Alzheimer disease rat model on lab based micro CT system." *Scientific reports* 11.1 (2021): 1-10.
44. Kavkova, M., *et al.* "Coordinated labio-lingual asymmetries in dental and bone development create a symmetrical acrodont dentition." *Scientific reports* 10.1 (2020): 1-16.
45. Kerbl, A., *et al.* "Micro-CT in cephalopod research: investigating the internal anatomy of a sepiolid squid using a non-destructive technique with special focus on the ganglionic system." *Journal of Experimental Marine Biology and Ecology* 447 (2013): 140-148.
46. Kiernan, J. A. "Histological and histochemical methods." *Theory and practice. Arnold Editor* (2001).
47. Kiessling, F., *et al.* "Volumetric computed tomography (VCT): a new technology for noninvasive, high-resolution monitoring of tumor angiogenesis." *Nature medicine* 10.10 (2004): 1133.
48. Koç, M. M., *et al.* "Evaluation of X-ray tomography contrast agents: A review of production, protocols, and biological applications." *Microscopy research and technique* 82.6 (2019): 812-848.
49. Kyriakou, Y., *et al.* "Ring artifact correction for high-resolution micro CT." *Physics in medicine & biology* 54.17 (2009): N385.

50. Langheinrich, A. C., *et al.* "Evaluation of the middle cerebral artery occlusion techniques in the rat by in-vitro 3-dimensional micro-and nano computed tomography." *BMC neurology* 10.1 (2010): 1-10.
51. Lenihan, J., *et al.* "A dataset comprising four micro-computed tomography scans of freshly fixed and museum earthworm specimens." *GigaScience* 3.1 (2014): 2047-217X.
52. Li, Z., *et al.* "An investigation of the efficacy and mechanism of contrast-enhanced X-ray computed tomography utilizing iodine for large specimens through experimental and simulation approaches." *BMC physiology* 15.1 (2015): 1-16.
53. Litzlbauer, H. D., *et al.* "Three-dimensional imaging and morphometric analysis of alveolar tissue from microfocal X-ray-computed tomography." *American Journal of Physiology-Lung Cellular and Molecular Physiology* 291.3 (2006): L535-L545.
54. Mah, P., *et al.* "Deriving Hounsfield units using grey levels in cone beam computed tomography." *Dentomaxillofacial Radiology* 39.6 (2010): 323-335.
55. Mambrini, M., *et al.* "The importance of routine quality control for reproducible pulmonary measurements by in vivo micro-CT." *Scientific Reports* 12.1 (2022): 9695.
56. Masyuk, T. V., *et al.* "Biliary dysgenesis in the PCK rat, an orthologous model of autosomal recessive polycystic kidney disease." *The American journal of pathology* 165.5 (2004): 1719-1730.
57. McGarvey, K. M., *et al.* "Mouse genome annotation by the RefSeq project." *Mammalian Genome* 26 (2015): 379-390.
58. Meganck, J.A., *et al.* "Beam hardening artifacts in micro-computed tomography scanning can be reduced by X-ray beam filtration and the resulting images can be used to accurately measure BMD." *Bone* 45.6 (2009): 1104-1116.

59. Metscher, B. D. "Micro CT for comparative morphology: simple staining methods allow high-contrast 3D imaging of diverse non-mineralized animal tissues." *BMC physiology* 9.1 (2009a): 11.
60. Metscher, B. D. "MicroCT for developmental biology: A versatile tool for high-contrast 3D imaging at histological resolutions." *Developmental dynamics: an official publication of the American Association of Anatomists* 238.3 (2009b): 632-640.
61. Metscher, B. D., and Müller G. B. "MicroCT for molecular imaging: Quantitative visualization of complete three-dimensional distributions of gene products in embryonic limbs." *Developmental Dynamics* 240.10 (2011): 2301-2308.
62. Missbach-Guentner, J., *et al.* "3D virtual histology of murine kidneys—high resolution visualization of pathological alterations by micro computed tomography." *Scientific reports* 8.1 (2018): 1-14.
63. Monnet, C., *et al.* "Three-dimensional morphometric ontogeny of mollusc shells by micro-computed tomography and geometric analysis." *Palaeontologia electronica* 12.3/12A (2009): 1-13.
64. Nebuloni, L., *et al.* "A comparative analysis of water-soluble and blood-pool contrast agents for in vivo vascular imaging with micro-CT." *Academic radiology* 20.10 (2013): 1247-1255.
65. Nevoránková, P., *et al.* "Region-specific gene expression profiling of early mouse mandible uncovered SATB2 as a key molecule for teeth patterning. " *Journal of Anatomy* (2023)
66. Nováková, M., *et al.* "Mouse model of congenital heart defects, dysmorphic facial features and intellectual developmental disorders as a result of non-functional CDK13." *Frontiers in cell and developmental biology* 7 (2019): 155.
67. Paddock, S. W. "Principles and practices of laser scanning confocal microscopy." *Molecular biotechnology* 16 (2000): 127-149.

68. Pai, V. M., *et al.* "Coronary artery wall imaging in mice using osmium tetroxide and micro-computed tomography (micro-CT)." *Journal of Anatomy* 220.5 (2012): 514-524.
69. Paulini, F., *et al.* "Evaluation of ovarian structures using computerized microtomography." *Anais da Academia Brasileira de Ciências AHEAD* (2017): 0-0.
70. Peng, Ch., *et al.* "PEGylated dendrimer-entrapped gold nanoparticles for in vivo blood pool and tumor imaging by computed tomography." *Biomaterials* 33.4 (2012): 1107-1119.
71. Perrien, D. S., *et al.* "Novel methods for microCT-based analyses of vasculature in the renal cortex reveal a loss of perfusable arterioles and glomeruli in eNOS^{-/-}-mice." *BMC nephrology* 17.1 (2016): 1-10.
72. Poinapen, D., *et al.* "Micro-CT imaging of live insects using carbon dioxide gas-induced hypoxia as anesthetic with minimal impact on certain subsequent life history traits." *BMC Zoology* 2 (2017): 1-13.
73. Rabin, O., *et al.* "An X-ray computed tomography imaging agent based on long-circulating bismuth sulphide nanoparticles." *Nature materials* 5.2 (2006): 118-122.
74. Rizzuto, R., *et al.* "Digital imaging microscopy of living cells." *Trends in Cell Biology* 8.7 (1998): 288-292.
75. Roussel, Y., *et al.* "Modeling spinal locomotor circuits for movements in developing zebrafish." *Elife* 10 (2021): e67453.
76. Sampson, M. A., *et al.* "Computed tomography whole body imaging in multi-trauma: 7 years experience." *Clinical radiology* 61.4 (2006): 365-369.
77. Scheller, E. L., *et al.* "Use of osmium tetroxide staining with microcomputerized tomography to visualize and quantify bone marrow adipose tissue in vivo." *Methods in enzymology*. Vol. 537. (2014) : 123-139.

78. Schweizer, S., *et al.* "Preparation and characterization of calibration standards for bone density determination by micro-computed tomography." *Analyst* 132.10 (2007): 1040-1045.
79. Starosolski, Z., *et al.* "Ultra high-resolution in vivo computed tomography imaging of mouse cerebrovasculature using a long circulating blood pool contrast agent." *Scientific reports* 5 (2015): 10178.
80. Stolz, E., *et al.* "Angioarchitectural changes in subacute cerebral venous thrombosis. A synchrotron-based micro-and nano-CT study." *Neuroimage* 54.3 (2011): 1881-1886.
81. Swain, M. V. and Xue J. "State of the art of micro-CT applications in dental research." *International journal of oral science* 1.4 (2009): 177-188.
82. Van Geuns, R. M., *et al.* "Basic principles of magnetic resonance imaging." *Progress in cardiovascular diseases* 42.2 (1999): 149-156.
83. Wagner, R., *et al.* "High-resolution imaging of kidney vascular corrosion casts with Nano-CT." *Microscopy and Microanalysis* 17.2 (2011): 215-219.
84. Wahsner, J., *et al.* "Chemistry of MRI contrast agents: current challenges and new frontiers." *Chemical reviews* 119.2 (2018): 957-1057.
85. Walters, E. B., *et al.* "Improved method of in vivo respiratory-gated micro-CT imaging." *Physics in Medicine & Biology* 49.17 (2004): 4163.
86. Wan, Y., *et al.* "Light-sheet microscopy and its potential for understanding developmental processes." *Annual review of cell and developmental biology* 35 (2019): 655-681.
87. Wasserman, W. W., *et al.* "Human-mouse genome comparisons to locate regulatory sites." *Nature genetics* 26.2 (2000): 225-228.

88. Welkenhuyzen, F., *et al.* "Industrial computer tomography for dimensional metrology: Overview of influence factors and improvement strategies." *Optimes*, Shaker Publishing BV, (2009).
89. Wong, M. D., *et al.* "A novel 3D mouse embryo atlas based on micro-CT." *Development* 139.17 (2012): 3248-3256.
90. Xie, B., *et al.* "Micro-computed tomography for hemorrhage disruption of mouse brain vasculature." *Translational stroke research* 3.1 (2012): 174-179.
91. Zheng, J., *et al.* "In vivo performance of a liposomal vascular contrast agent for CT and MR-based image guidance applications." *Pharmaceutical research* 24.6 (2007): 1193-1201.
92. Zikmund, T., *et al.* "High-contrast differentiation resolution 3D imaging of rodent brain by X-ray computed microtomography." *Journal of Instrumentation* 13.02 (2018): C02039.

7. Author publications and other outputs

Publications - first author

Kavková M., Šulcová M., Dumková J., Zahradníček O., Kaiser J., Tucker A. S., Zikmund T., Buchtová M. (2020). **Coordinated labio-lingual asymmetries in dental and bone development create a symmetrical acrodont dentition.** *Scientific reports*, 10(1), 1-16.

Kavkova M., Zikmund T., Kala A., Salplachta J., Proskauer Pena S. L., Kaiser J., Jezek K. (2021). **Contrast enhanced X-ray computed tomography imaging of amyloid plaques in Alzheimer disease rat model on lab based micro CT system.** *Scientific reports*, 11(1), 1-10.

Kavková M., Šulcová M., Zikmund T., Pyszko M., Kaiser J., Buchtová M. (2022). **X-ray microtomography imaging of craniofacial hard tissues in selected reptile species with different types of dentition.** *GigaScience*, 11.

Publications - co-author

Cela P., Hampl M., Shylo N. A., Christopher K. J., Kavkova M., Landova M., Zikmund T., Weatherbee S.D., Kaiser J., Buchtova M., (2017). **Ciliopathy protein tmem107 plays multiple roles in craniofacial development.** *Journal of dental research*, 97(1), 108-117.

Zikmund T., Novotná M., Kavková M., Tesařová M., Kaucká M., Szarowská B., Adameyko I., Hrubá E., Buchtová M., Dražanová E., Starčuk Z., Kaiser J., (2018). **High-contrast differentiation resolution 3D imaging of rodent brain by X-ray computed microtomography.** *Journal of Instrumentation*, 13(02), C02039.

Nováková M., Hampl M., Vrábel D., Procházka J., Petrezselyová S., Procházková, M., Sedláček R., Kavková M., Zikmund T., Kaiser J., Juan H., Fann M., Buchtová M., Kohoutek J. (2019). **Mouse model of congenital heart defects, dysmorphic facial features and intellectual developmental disorders as a result of non-functional CDK13.** *Frontiers in cell and developmental biology*, 155.

Kastriti M. E., Stratigi A., Mariatos D., Theodosiou M., Savvaki M., Kavkova M., Theodorakis K., Vidaki M., Zikmund T., Kaiser J., Adameyko I., Karagogeos D. (2019). **Ablation of CNTN2+ pyramidal neurons during development results in defects in neocortical size and axonal tract formation.** *Frontiers in cellular neuroscience*, 454.

Landova Sulcova M., Zahradnicek O., Dumkova J., Dosedelova H., Krivanek J., Hampl M., Kavkova M., Zikmund T., Gregorovicova M., Sedmera D., Kaiser J., Tucker A. S., Buchtova M. (2020). **Developmental mechanisms driving complex tooth shape in reptiles.** *Developmental Dynamics*, 249(4), 441-464.

Hampl M., Dumkova J., Kavkova M., Dosedelova H., Bryjova A., Zahradnicek O., Pyszko M., Macholan M., Zikmund T., Kaiser J., Buchtova M. (2020). **Polarized sonic hedgehog protein localization and a shift in the expression of region-specific molecules is associated with the secondary palate development in the veiled chameleon.** *Frontiers in cell and developmental biology*, 572.

Krtička M., Nekuda V., Ira D., Sedláček R., Suchý T., Kavková M., Břínek A., Göpfrt E., Bilik A., Kaiser J., Křen L., Plánka L. (2021). **Microcomputed tomographic, biomechanical and histological analyses of lumbar interbody fusion with iliac crest bone graft in a pig model.** *Acta Veterinaria Brno*, 90(1), 69-75.

Hankeova S., Salplachta J., Zikmund T., Kavkova M., Van Hul N., Brinek A., Smekalova S., Laznovsky J., Dawit F., Jaros J., Bryja V., Lendahl U., Ellis E., Nemeth A., Fischler B., Hannezo E., Kaiser J., Andersson E. R. (2021). **DUCT reveals architectural mechanisms contributing to bile duct recovery in a mouse model for Alagille syndrome.** *Elife*, 10, e60916.

Kimura T., Bosakova M., Nonaka Y., Hrubá E., Yasuda K., Futakawa S., Kubota T., Fafílek B., Gregor T., Abraham S., Gomolkova R., Belaskova S., Pesl M., Csukasi F., Duran I., Fujiwara M., Kavkova M., Zikmund T., Kaiser J., Buchtova M., Krakow D., Nakamura Y., Ozono K., Krejci P. (2021). **An RNA aptamer restores defective bone growth in FGFR3-related skeletal dysplasia in mice.** *Science Translational Medicine*, 13(592), eaba4226.

Krticka M., Planka L., Vojtova L., Nekuda V., Stastny P., Sedlacek R., Brinek A., Kavkova M., Gopfert E., Hedvicakova V., Rampichova M., Kren L., Liskova K., Ira D., Dorazilová J., Suchy T., Zikmund T., Kaiser J., Stary D., Faldyna M., Trunec M. (2021). **Lumbar Interbody Fusion Conducted on a Porcine Model with a Bioresorbable Ceramic/Biopolymer Hybrid Implant Enriched with Hyperstable Fibroblast Growth Factor 2.** *Biomedicines*, 9(7), 733.

Kaucka M., Szarowska B., Kavkova M., Kastriti M. E., Kameneva P., Schmidt I., Peskova L., Arous A., Simon A., Kaiser J., Adameyko I. (2021). **Nerve-associated Schwann cell precursors contribute extracutaneous melanocytes to the heart, inner ear, supraorbital locations and brain meninges.** *Cellular and Molecular Life Sciences*, 78(16), 6033-6049.

Hruba E., Kavkova M., Dalecka L., Macholan M., Zikmund T., Varecha M., Bosakova M., Kaiser J., Krejci P., Hovorakova M., Buchtova M. (2021). **Loss of Sprouty produces a ciliopathic skeletal phenotype in mice through upregulation of Hedgehog signaling.** *Journal of Bone and Mineral Research*, 36(11), 2258-2274.

Hankeova S., Salplachta J., Van Hul N., Kavkova M., Iqbal A., Zikmund T., Kaiser J., Andersson E. R. (2021). **DUCT: Double Resin Casting followed by Micro-Computed Tomography for 3D Liver Analysis.** *JOVE- Journal of Visualized Experiments*, (175).

Hankeova S., Van Hul N., Laznovsky J., Verboven E., Mangold K., Hensens N., Adori C., Verhoef E., Zikmund T., Dawit F., Kavkova M., Salplachta J., Sjöqvist M., Johansson B., Hassan M., Fredriksson L., Baumgärtel K., Bryja V., Lendahl U., Jheon A., Alten F., Fahnehjelm K., Fischler B., Kaiser J., Andersson, E. R. (2022). **Sex differences and risk factors for bleeding in Alagille syndrome.** *EMBO Molecular Medicine*, e15809.

Kaucka M., Arous A., Tesarova M., Currie J., Boström J., Kavkova M., Petersen J., Yao Z., Bouchnita A., Hellander A., Zikmund T., Elewa A., Newton P., Fei J., Chagin A., Fried K., Tanaka E., Kaiser J., Simon A., Adameyko I. (2022). **Altered developmental programs and oriented cell divisions lead to bulky bones during salamander limb regeneration.** *Nature Communications*, 6949 (13)

Petersen J., Englmaier L., Artemov A., Poverennaya I., Mahmoud R., Boudierlique T., Tesarova M., Deviatiiarov R., Szilvásy-Szabó A., Akkuratov E., Reguera D., Zeberg H., Kaucka M.,

Kastriti M., Krivanek J., Radaszkiewicz T., Gömöröyová K., Knauth S., Potesil D., Zdrahal Z., Ganji R., Grabowski A., Buhl M., Zikmund T., Kavkova M., Axelson H., Lindgren D., Kramann R., Kuppe Ch., Erdélyi F., Máté Z., Szabó G., Koehne T., Harkany T., Fried K., Kaiser J., Boor P., Fekete C., Rozman J., Kasperek P., Prochazka J., Sedlacek R., Bryja V., Gusev O., Adameyko I. (2023) **A previously uncharacterized Factor Associated with Metabolism and Energy (FAME/C14orf105/CCDC198/1700011H14Rik) is related to evolutionary adaptation, energy balance, and kidney physiology.** *Nature Communications*, 3092 (14)

Gonzalez Lopez M., Huteckova B., Lavicky J., Zezula N., Rakultsev V., Fridrichova V., Tuaima H., Nottmeier C., Petersen J., Kavkova M., Zikmund T., Kaiser J., Lav R., Star H., Bryja V., Henyš P., Vořechovský M., Tucker A., Harnos J., Buchtova M., Krivanek J. (2023) **Spatiotemporal monitoring of hard tissue development reveals unknown features of tooth and bone development.** *Science Advances*, 9(31), eadi0482

Thomasen P. B., Salasova A., Kjaer-Sorensen K., Woloszczuková L., Lavický J., Login H., Tranberg-Jensen J., Almeida S., Beel S., Kavková M., Qvist P., Kjolby., Ovesen P. L., Nolte S., Vestergaard B., Udrea A. C., Nejsum L. N., Chao M., Van Damme P., Krivanek J., Dasen J., Oxvig C., Nykjær A. (2023) **SorCS2 binds progranulin to regulate motor neuron development** *Cell Reports*, 42(11)

Dubaic M., Peskova L., Hampl M., Weissova K., Celiker C., Shylo N., Hruha E., Kavkova M., Zikmund T., Weatherbee S., Kaiser J., Barta T., Buchtova M. (2023) **Role of ciliopathy protein TMEM107 in eye development: insights from a mouse model and retinal organoid.** *Life Science Alliance*, 6(12)

Nevoránková P., Šulcová M., Kavková M., Zimčík D., Moravcová Balková S., Peléšková K., Kristeková D., Jakešová V., Zikmund T., Kaiser J., Izakovičová Holá L., Kolář M., Buchtová M. (2023) **Region-specific gene expression profiling of early mouse mandible uncovered SATB2 as a key molecule for teeth patterning.** *Journal of Anatomy* - in revision

Grants

TACR - Zéta Grant 2018-2019

Advanced techniques for biological samples imaging using X-ray computed nanotomography

- *co-researcher*, TJ01000382, Brno University of Technology, Rigaku Innovative Technologies Europe s.r.o.

BUT Internal projects - Specific research 2018

-Preparation and imaging of mice brains on nanotomographig device Rigaku Nano3DX

(Příprava a zobrazování myších mozků na nanotomografickém zařízení Rigaku Nano3DX)

- *main researcher*, STI-J-18-5557, Brno University of Technology - whole funder

BUT Internal projects - Specific research 2019

X-ray micro computed tomography of transgenic rat brains as research model of Alzheimers disease (Rentgenová počítačová mikro tomografie transgenních potkaních mozků sloužících jako výzkumný model pro Alzheimerovu chorobu)

- *main researcher*, CEITEC VUT-J-19-6046, Brno University of Technology - whole funder

Research Internships

Freemovers - Programme of Student Mobility Support

20.11.2017 - 3.12.2017

Medical University of Vienna, Department of Neuroimmunology (Center for Brain Research)

Research group leader: Professor Igor Adameyko

Supervisor: Marketa Kaucka Petersen Ph.D.

Erasmus

1.10.2018 - 31.3.2019

Medical University of Vienna, Department of Neuroimmunology (Center for Brain Research)

Research group leader: Professor Igor Adameyko

Supervisor: Marketa Kaucka Petersen Ph.D.

Conference posters and presentations

Kavková M., Tesařová M., Zikmund T., Dražanová E., Kaucká M., Buchtová M., Kaiser J., **A comparison of X- ray computed tomography and magnetic resonance imaging of mouse brain.** *13th International Interdisciplinary Meeting on Bioanalysis*, (2016) Brno, Czech Republic - poster

Kavková M., Tesařová M., Zikmund T., Kaucká M., Adameyko I., Kaiser J., **Micro Computed Tomography Imaging of Mouse Embryo.** *Bioimplantology IX. International conference*, (2017) Brno, Czech Republic - poster

Kavková M., Zikmund T., Tesařová M., Novotná M., Kaucká M., Szarowská B., Adameyko I., Buchtová M., Kaiser J., **High-resolution 3D imaging of mouse brain by X-ray computed microtomography.** *XXVI International Symposium on Morphological Sciences*, (2018) Prague, Czech Republic - oral presentation

Kavková M., Hrubá E., Zikmund T., Buchtová M., Novotná M., Kaiser J., **Digital dissection of 3D model of adult mouse skeleton: x-ray micro computed tomography analysis.** *Visegrad Group Society for Developmental Biology Inaugural Meeting* (2018) Brno, Czech Republic - poster

Kavková M., Kastriti M.E., Savvaki M., Mariatos D., Theodorakis K., Vidaki M., Karagogeos D., Zikmund T., Adameyko I., Kaiser J. **3D X-ray computed microtomography analysis of callosal and commissural defects in mouse model of defective axonal tracts.** *European Developmental Biology Congress* (2019) Alicante, Spain - poster

Kavková M., Landová M., Dumková J., Hampl A., Zikmund T., Kaiser J., Buchtová M. **Bone pedicle development and their association to tooth germ in acrodont chameleons.** *International Congress of Vertebrate Morphology* (2019) Prague, Czech Republic - poster

Kavková M., Šulcová M., Zikmund T., Pyszko M., Kaiser J., Buchtová M. **X-ray Micro computed tomography imaging based collection of reptile skull models for morphological analysis of tooth attachment.** *2nd Conference of the Visegrad Group Society for Developmental Biology* (2021) Szeged, Hungary - oral presentation

Kavková M., Peléšková K., Šulcová M., Zikmund T., Kaiser J., Buchtová M. **Odontogenesis in SatB2 deficient mice.** *14th Tooth Morphogenesis and Differentiation* (2022) Prague, Czech Republic - poster

Kavková M., Harnoš J., Šulcová M., Zikmund T., Buchtová M., Kaiser J. **Micro CT analysis of head development in Xenopus laevis.** *19th International Congress of Developmental Biology* (2022) Algarve, Portugal - poster

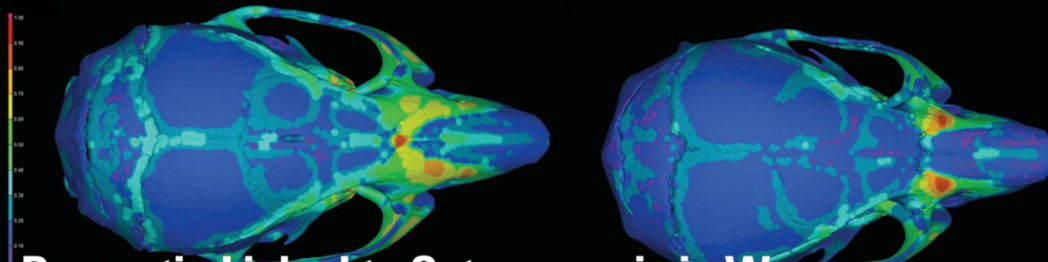
Cover page - Journal of Bone and Mineral Research volume 36, number 11

my image on the cover page JMBR created for publication Hrubá *et al.* **Loss of Sprouty produces a ciliopathic skeletal phenotype in mice through upregulation of Hedgehog signaling** (2021)

Volume 36
Number 11
November 2021
pp. 2103–2286

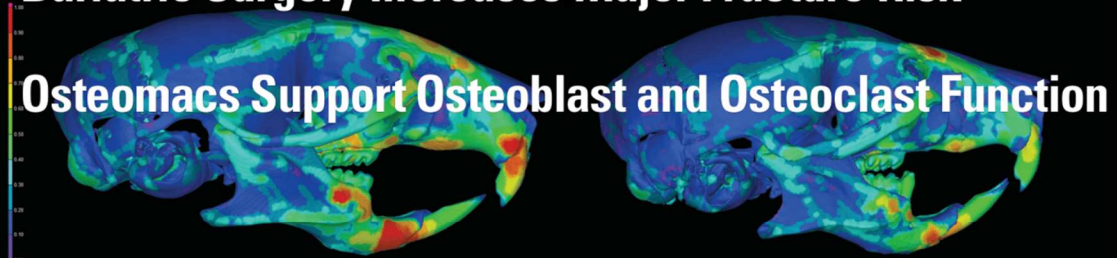
Journal of Bone and Mineral Research

JBMIR®



Dementia Linked to Osteoporosis in Women

Bariatric Surgery Increases Major Fracture Risk



Osteomacs Support Osteoblast and Osteoclast Function

WILEY

Published monthly by
The American Society for Bone and Mineral Research

ASBMR®



OPEN

Coordinated labio-lingual asymmetries in dental and bone development create a symmetrical acrodont dentition

M. Kavková^{1,7}, M. Šulcová^{2,6,7}, J. Dumková³, O. Zahradníček⁴, J. Kaiser¹, A. S. Tucker⁵, T. Zikmund¹ & M. Buchtová^{2,6}✉

Organs throughout the body develop both asymmetrically and symmetrically. Here, we assess how symmetrical teeth in reptiles can be created from asymmetrical tooth germs. Teeth of lepidosaurian reptiles are mostly anchored to the jaw bones by pleurodont ankylosis, where the tooth is held in place on the labial side only. Pleurodont teeth are characterized by significantly asymmetrical development of the labial and lingual sides of the cervical loop, which later leads to uneven deposition of hard tissue. On the other hand, acrodont teeth found in lizards of the Acrodonta clade (i.e. agamas, chameleons) are symmetrically ankylosed to the jaw bone. Here, we have focused on the formation of the symmetrical acrodont dentition of the veiled chameleon (*Chamaeleo calyptrotus*). Intriguingly, our results revealed distinct asymmetries in morphology of the labial and lingual sides of the cervical loop during early developmental stages, both at the gross and ultrastructural level, with specific patterns of cell proliferation and stem cell marker expression. Asymmetrical expression of ST14 was also observed, with a positive domain on the lingual side of the cervical loop overlapping with the SOX2 domain. In contrast, micro-CT analysis of hard tissues revealed that deposition of dentin and enamel was largely symmetrical at the mineralization stage, highlighting the difference between cervical loop morphology during early development and differentiation of odontoblasts throughout later odontogenesis. In conclusion, the early asymmetrical development of the enamel organ seems to be a plesiomorphic character for all squamate reptiles, while symmetrical and precisely orchestrated deposition of hard tissue during tooth formation in acrodont dentitions probably represents a novelty in the Acrodonta clade.

Teeth are firmly anchored to the jaw and palatal bones in lepidosaurian reptiles (Squamata and Rhynchocephalia). Several modes of tooth-bone attachment evolved in this reptilian lineage (Fig. 1)^{1–4}. In the majority of lizards and snakes, teeth are ankylosed to the inner side of the high labial wall of the tooth bearing element using a so called pleurodont implantation^{5–7}. This type of attachment creates a space for the successional dental lamina growth and continuous tooth replacement (polyphyodonty) on the unattached lingual side of the tooth⁸. Enamel organs of tooth germs in species with pleurodontly ankylosed teeth demonstrate labio-lingual asymmetrical growth of the cervical loop from early stages of tooth development. As was previously described in the ocelot gecko (*Paroedura picta*), the lingual side of the cervical loop protrudes deep into the underlying mesenchyme, whereas the labial side of the tooth base is shorter, meets the bony pedicles and undergoes ankylosis (Fig. 1)⁵. This pleurodont mode of attachment has been proposed to be the plesiomorphic condition in Lepidosauria^{3,9}.

In contrast, all teeth of extant chameleons and the majority of teeth in agamas are fused to the crest of the tooth-bearing skeletal element by acrodont ankylosis³. In this specific type of attachment, the tooth is located

¹Central European Institute of Technology, Brno University of Technology, Brno, Czech Republic. ²Department of Experimental Biology, Faculty of Science, Masaryk University, Brno, Czech Republic. ³Department of Histology and Embryology, Faculty of Medicine, Masaryk University, Brno, Czech Republic. ⁴Department of Radiation Dosimetry, Nuclear Physics Institute, Czech Academy of Sciences, Prague, Czech Republic. ⁵Centre for Craniofacial and Regenerative Biology, King's College London, Floor 27 Guy's Tower, Guy's Hospital, London Bridge, London, UK. ⁶Laboratory of Molecular Morphogenesis, Institute of Animal Physiology and Genetics, Czech Academy of Sciences, Veverí 97, 602 00 Brno, Czech Republic. ⁷These authors contributed equally: M. Kavková and M. Šulcová. ✉email: buchtova@iach.cz

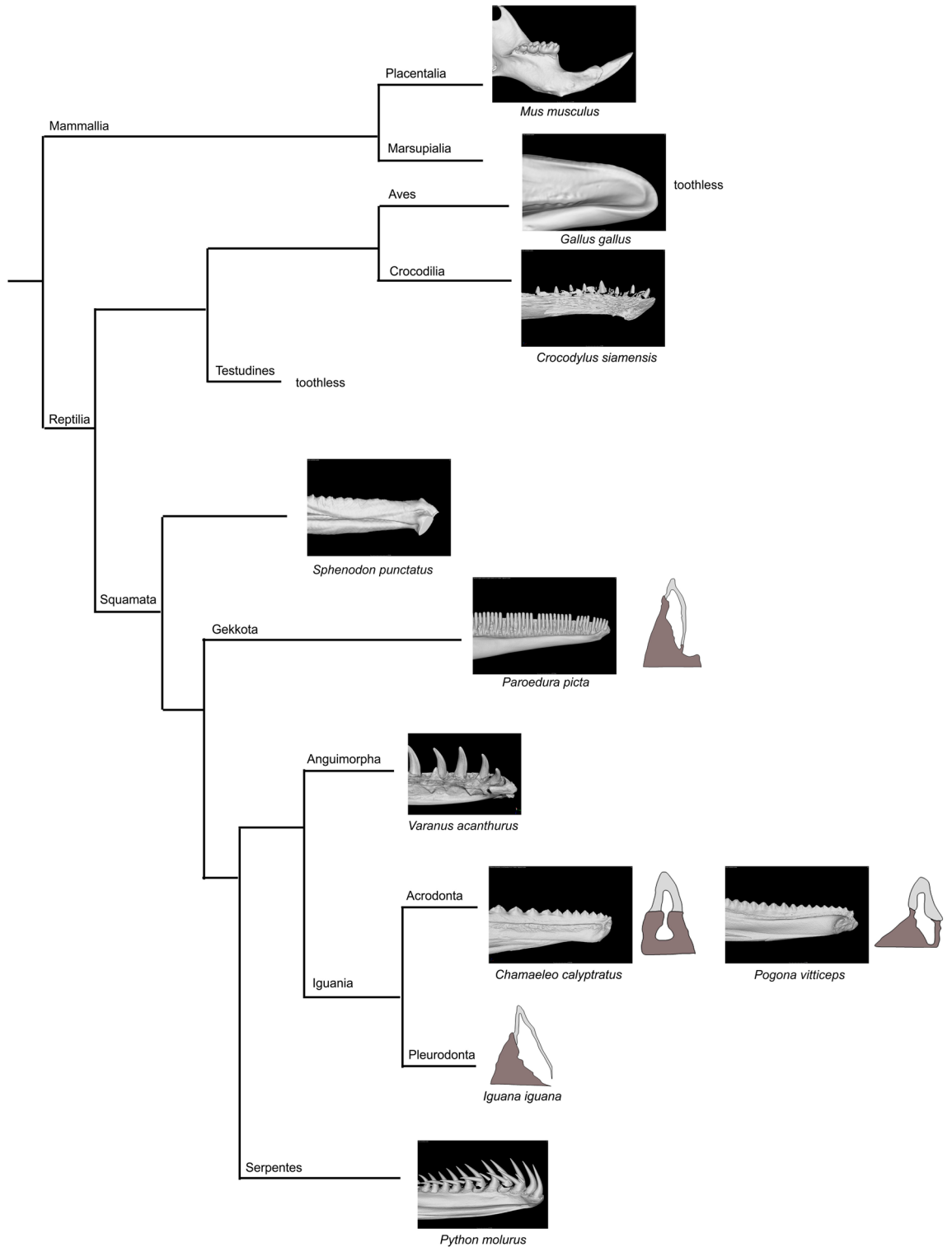


Figure 1. Simplified phylogenetic tree with displayed type of dentitions for selected species. Segment of the lower jaw in micro-CT view is displayed for selected vertebrate species to reveal possible tooth and bone relationship. Drawings of the transversal sections were modified based on³. Phylogenetic tree was adapted from¹⁵ and¹⁶.

at the top of a bony pedicle. Once the tooth is ankylosed to the underlying bone, it is stabilized and therefore most acrodont species only have one generation of teeth (monophyodont dentition)¹⁰. An exception might be the only extant Rhynchocephalia, tuatara (*Sphenodon punctatus*), which has some replacement ability and an

acrodont dentition (Fig. 1)^{9,11}, and some extinct reptiles such as *Opisthodontosaurus carrolli*¹². In some lizards, both acrodont and pleurodont teeth are found within the same jaw. In the bearded dragon (*Pogona vitticeps*, Fig. 1), the anterior teeth are pleurodont and can replace, while the posterior teeth are acrodont and limited to one set^{12,13}. From the fossil record, it appears that acrodont dentitions were derived from pleurodont. In extinct Chamaeleonidae and Agamidae (Fig. 1), a mix of pleurodont and acrodont attachment have been described¹⁴ similarly to extant agamas, again suggesting that pleurodonty is the basal state.

Given the distinct modes of attachment, it can be predicted that the development of the cervical loops might vary between the groups. We therefore aimed to determine the developmental processes contributing to the morphogenesis of acrodont dentition and to analyze possible symmetrical/asymmetrical features occurring on the labial and lingual sides of the cervical loop using embryos of the veiled chameleon (*Chamaeleo calytratus*). 3D reconstructions of contrasted soft tissue in micro-CT enabled us to provide comprehensive morphometric analysis highlighting asymmetries in both tooth germ and bone development. Together with analysis of cell proliferation and microscopic and submicroscopic changes, we were able to investigate the early asymmetries and how they resolved into the symmetrical acrodont pattern.

Material and methods

Animals. Specimens of veiled chameleon (*Chamaeleo calytratus*) and ocelot gecko (*Paroedura picta*) were obtained from a commercial breeder. Embryos and fetuses at different stages of development were collected to analyze the developmental progression. Eggs were incubated at the temperature of 27–29 °C. At selected time points, eggs were open, and embryos were euthanized by decapitation and fixed in 4% PFA at least overnight. To make our analysis easier for comparisons and interpretations, we focused only on the development of the lower jaw dentition and associated dentary bone morphogenesis.

All manipulations with chameleon and gecko embryos followed the specific rules for working with alive embryos as specified by the Central Commission for Animal Welfare of Ministry of Agriculture of the Czech Republic (§16a law No. 246/1992 Sb., for animal protection against cruelty). All analyses were performed in accordance with the guidelines, regulations and experimental protocols approved by the institutional and licensing committee including rules run by the Laboratory Animal Science Committee of the IAPG, v.v.i. (Liběchov, Czech Republic). Tissues were collected for analyses following embryo decapitation. No experiments were performed on embryos.

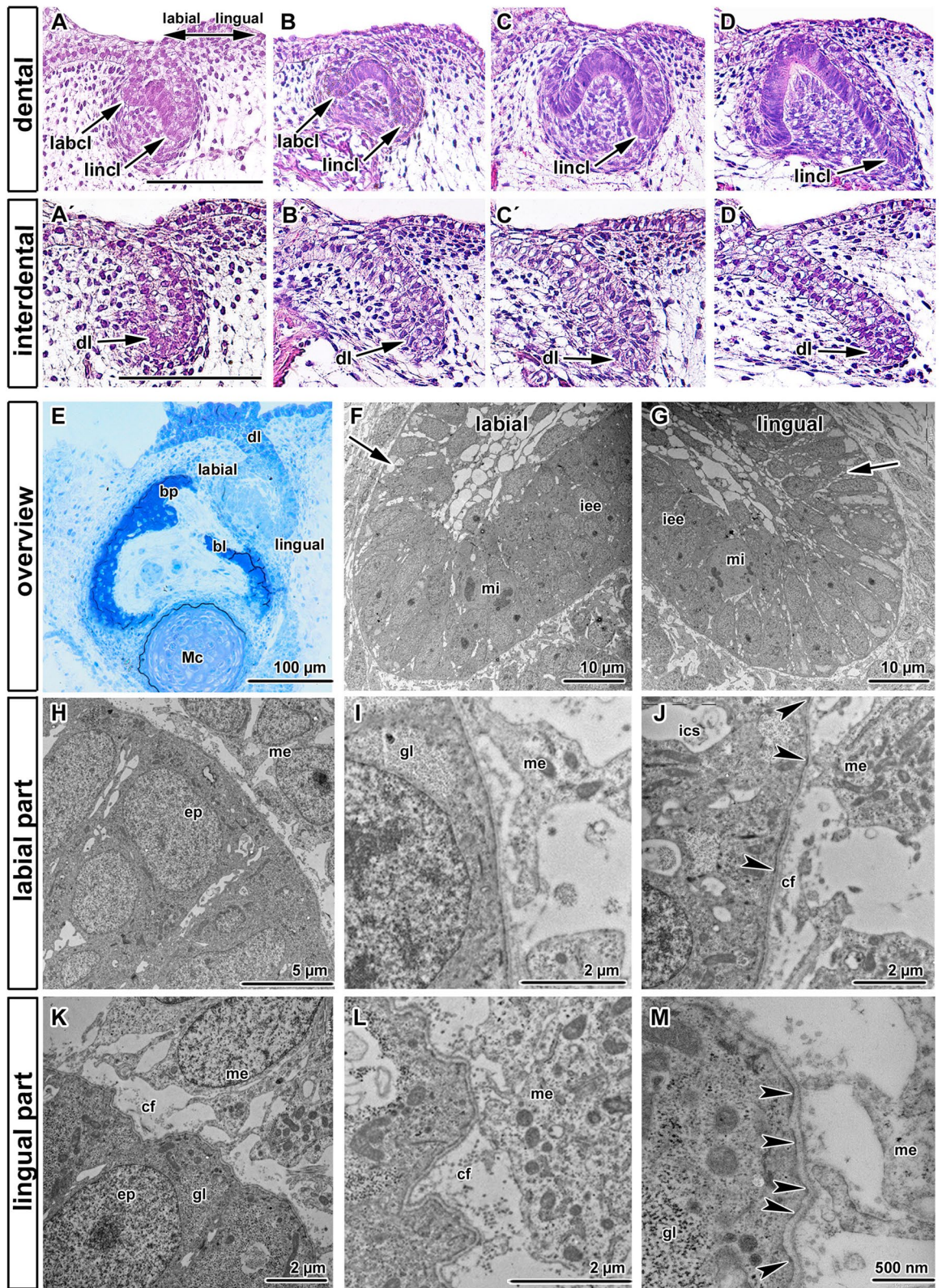
Embryo of tuatara (*Sphenodon punctatus*) was obtained from the Dendy collection at the King's College London Museum of Life Sciences (specimen R, London UK) and an adult animal from the collection at the Department of Anatomy of Charles University (Prague, Czech Republic). Embryo of bearded dragon (*Pogona vitticeps*) originated from Prof. Tucker's collection (London, UK). Material was used in accordance with museum guidelines and regulations. A phylogenetic tree was adapted from¹⁵ and¹⁶.

Histology and immunohistochemical labelling. To prepare histological sections for immunohistochemical and histological analysis, specimens were fixed in 4% PFA. Tissues from older specimens were decalcified in 12.5% EDTA in 4% PFA at RT followed by paraffin embedding. Paraffin embedded tissues were cut to obtain serial transverse histological sections, which were stained with Haematoxylin–Eosin. Alternative slides were deparaffinised and rehydrated through a series of ethanol followed by antigen retrieval in a water bath (97 °C) in citrate buffer (pH = 6) for 20 min. Blocking serum was applied to the samples for 20 min to prevent unspecific binding of antibodies. Next, slides were incubated with primary antibodies PCNA (Cat. No. M0879, Agilent Dako, Santa Clara, California, USA) for 1 h or ST14 (Cat. No. ABIN277391, Antibodies Online, Aachen, German) overnight, respectively. The secondary antibodies (goat anti-mouse Alexa Fluor488, cat. No. A-11001, Thermo Fisher, USA) were applied for 30 min. DRAQ5 Fluorescent Probe Solution (cat. No. 62251, Thermo Fisher, USA) was used for the counterstaining. Images were taken on confocal microscope Leica SP8 using 20× or 40× (water immersion) objectives (Leica Microsystems, Germany) with Leica Application Suite software. Final photo processing was performed by software Imaris (Bitplane, Zürich, Switzerland).

For SOX2 detection, slides were incubated overnight with the primary antibody SOX2 (Cat. No. 2748, Cell Signaling, Leiden, Netherland). The secondary biotinylated anti-rabbit antibody (1:200, part of the ABC kit, Vectastain, Vector Laboratories, Burlingame, USA) and avidin–biotin complex (ABC kit, Vectastain, Vector Laboratories, Burlingame, USA) were applied for 30 min each followed by visualization with diaminobenzidine (DAB, Cat. No. K3468, DAKO, USA). Slides were counterstained by Haematoxylin to visualize nuclei. Tissues were analyzed and photographed using a Leica DMLB2 microscope (Leica Microsystems, Wetzlar, Germany).

PCNA-positive cells were counted at cap and early bell stages of chameleon odontogenesis. Samples from two different animals were used for each developmental stage. Seven tooth sections were used for cell counting at the cap stage, and sixteen at the early bell stage. Every tooth germ was divided into four distinct areas: the outer enamel epithelium of the lingual side of the cervical loop, the inner enamel epithelium of the lingual side of the cervical loop, the outer enamel epithelium of the labial and lingual sides of the cervical loop. Statistical significance in difference of PCNA-positive cell number between labial and lingual sides of the cervical loop were evaluated by paired t-test (Excel, Microsoft Corporation, USA).

Transmission electron microscopy. Two samples from early developmental stages were fixed in 3% glutaraldehyde for 24 h. Mandibles were washed three times in 0.1 M cacodylate buffer and post-fixed in 1% OsO₄ solution for 1 h. Samples were embedded in epoxy resin Durcupan. Semithin sections were stained with Toluidine Blue to evaluate general morphology. Ultra-thin sections were placed on formvar-coated nickel grids and contrasted with lead citrate and uranyl acetate. More details were published previously elsewhere¹⁷.



◀**Figure 2.** Labio-lingual asymmetry of enamel organ in early chameleon embryos. (A–D) Microscopic structure of developing tooth germ visualized by HE staining. (A'–D') Interdental areas contain continuous dental lamina protruding in lingual direction. Late bud stage (A, A'), early cap stage (B, B'), late cap stage (C, C') and early bell stage (D, D'). Notice asymmetrical growth of labial and lingual part of cervical loop starting from very early stages of tooth germ development. Scale bar = 50 μ m. (E–M) Transmission electron microscopy of tooth germ at cap stage in chameleon revealed distinct differences between labial and lingual side of the cervical loop. (E) Overview of early cap stage on semithin section stained by Toluidine Blue. (F, G) Detailed overview of labial or lingual cervical loop with visible mitotic cells (mi). Intercellular spaces are larger in the outer enamel epithelium (arrows). (H, I) Details of the labial cervical loop with smooth basal membrane. Glycogen granules (gl) were situated in cells in upper part of the lingual and labial sides of the cervical loop (K). (J) Few hemidesmosomes were located in the labial part of the cervical loop (arrowheads). (K–M) In contrast, basal membrane of lingual cervical loop was distinctly folded with numerous collagen fibrils (cf) in its close proximity (K, L). Lamina lucida and lamina densa were strictly separated in this area and numerous hemidesmosomes were located in the lingual part of the cervical loop (L, M—arrowheads). *bl* bony lamella, *bp* bony pedicle, *cf* collagen fibrils, *dl* dental lamina, *ep* epithelial cell, *gl* glycogen, *ics* intercellular spaces, *iee* inner enamel epithelium, *labcl* labial part of the cervical loop, *lincl* lingual part of the cervical loop, *Mc* Meckel cartilage, *me* mesenchymal cell, *mi* mitosis.

Micro-CT measurement. Fourteen samples of embryonic chameleon jaws were selected for more detailed micro-CT analysis of hard tissue morphology (Fig. S1, Table S1). For the purpose of our study, we defined five developmental stages, with tooth development ranging from early mineralization to just prior to ankylosis, in order to highlight the dynamic relationship between the developing teeth and underlying bone.

In chameleons, differences in growth rate can occur, even between individuals from the same clutch of eggs. This is largely driven by differences in temperature, which can affect speed of development with lower temperature resulting in longer time to hatching^{18,19}. In addition, the duration of embryonic diapause can differ between clusters of eggs, so that time of oviposition does not necessarily correlate with actual developmental stage²⁰. Weight of embryos has been demonstrated to exhibit good correlation to developmental phase for staging of odontogenesis in mouse embryos²¹. We therefore used both number of embryonic days and embryonic weight to characterize our samples. Before scanning, all samples were embedded in 1% agarose gel in 1.5 ml Eppendorf tube in order to prevent the movement during the micro-CT scan. Samples were first scanned without staining in order to analyze the hard dental tissue and underlying jaw bone. For the evaluation of the soft tissue morphology and their relationship to hard tissues, five of the previously scanned samples were counterstained and underwent further analysis after re-scanning.

The staining protocol consisted of several dehydration steps including 30%, 50%, 70%, 80% and 90% ethanol solution—1.5 h in each concentration. After dehydration, samples were submerged in staining solution consisting of 1% iodine in 90% methanol for 16 h, after the staining step the samples were washed in 50% ethanol and embedded in 1% agarose.

The micro-CT scanning was performed using laboratory system GE phoenix v|tome|x L 240 (GE Sensing & Inspection Technologies GmbH, Germany), equipped with a 180 kV/15 W maximum power nanofocus X-ray tube and high contrast flat panel detector dynamic 41|100 (number of pixels: 4048 × 4048 px, pixel size 100 μ m). The measurements were carried out in an air-conditioned cabinet (21 °C). The X-ray tube current of 200 μ A, acceleration voltage of 60 kV and exposure time of 600 ms were common for all scanned samples. Number of images and voxel resolution were set individually for each sample depending on the size (Table S2). The tomographic reconstruction was done using the software GE phoenix datos|x 2.0 (GE Sensing & Inspection Technologies GmbH, Germany).

Micro-CT data processing. Data from micro-CT scans of fixed unstained samples were analysed and measured in VGStudio MAX 3.3 licensed software (Volume Graphics GmbH, Germany, <https://www.volumegraphics.com>). Schematics of the measurements and plane establishment in the jaw are shown in Fig. S2 with individual teeth labelled in a rostro-caudal direction (Fig. S3—teeth shown for right side).

The following measurements and analyses were performed using the unstained sample datasets:

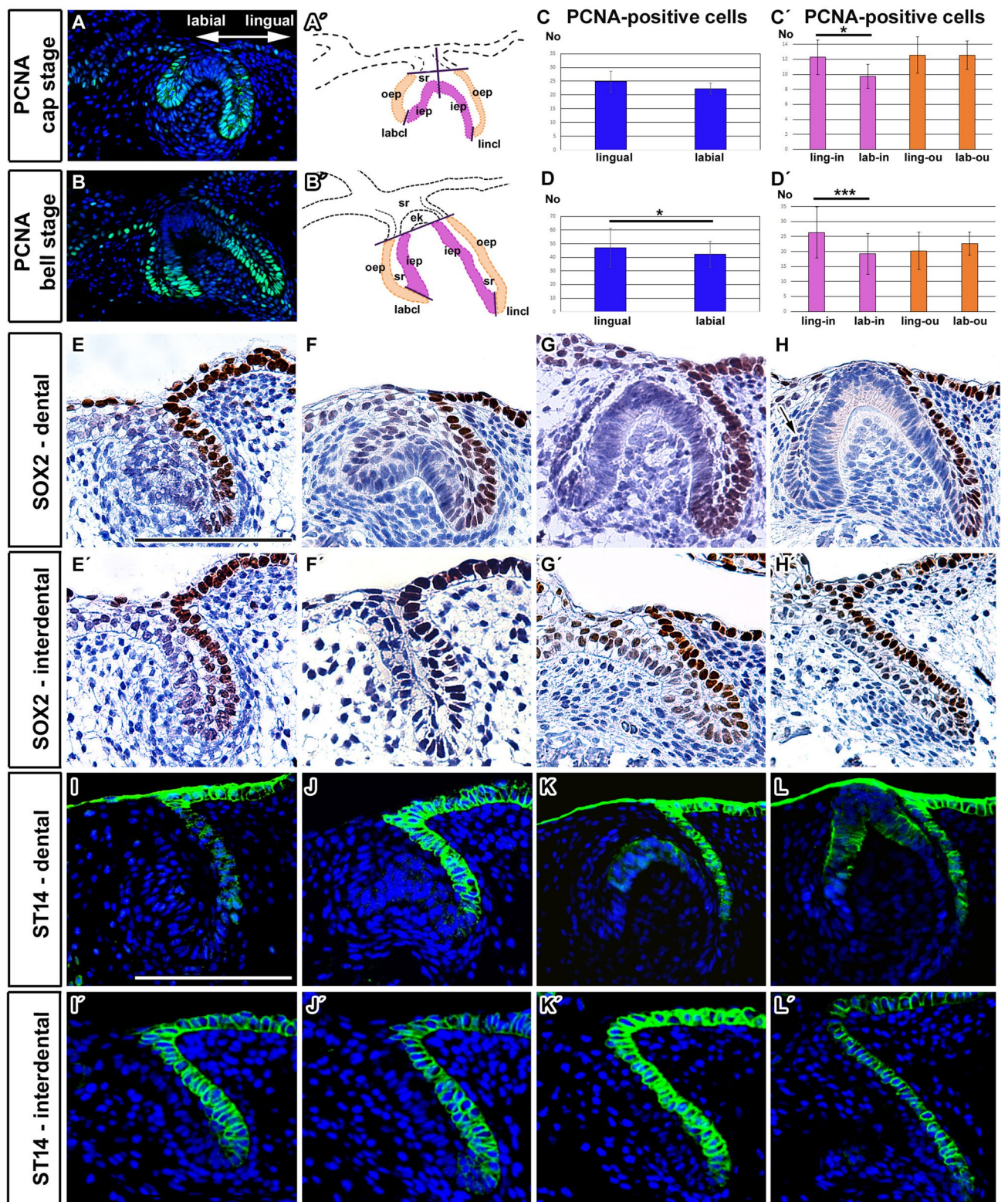
Tooth to jaw distance The distance between the teeth and the underlying bone was measured separately on the labial and lingual sides of the jaw in transversal sections through the jaw and tooth. These sections were defined by the polyline generated by placing points at the tips of teeth with the plane running perpendicular to the horizontal plane. For standardisation, the tooth to bone distance was measured at the highest point of each tooth.

Tooth to jaw angle The angle in which the tooth tilted towards the jaw (angle of inclination) was measured in the same plane as mentioned above.

Wall thickness Sphere based wall thickness analysis in VG studio software was used to assess the thickness of the examined samples by fitting spheres inside the sample in 3D space. The thickness was defined by the diameter of the fitted sphere.

Segmentation of the cervical loop in the iodine stained samples was carried out using Avizo 9.5 software. 3D models (in Stl format, <https://www.fei.com/software/avizo3d/>, Thermo Fisher Scientific, USA) of the cervical loop was then transferred in the VG studio software where the other analyses were performed.

The length of the cervical loop was measured on the labial and lingual side using transverse sections through the jaw (defined by the polyline) at the highest point of the tooth. The cervical loop extends around the forming dental papilla of the tooth germ as visualized in 3D by micro-CT (Fig. S4). However, in transversal sections through the head, we can only observe the lingual and labial sides of the loop and we use this nomenclature in the manuscript.



◀ **Figure 3.** Differences in proliferation, SOX2 and ST14 expression in the labial and lingual side of the enamel organ in chameleon. (A–D') Analysis of proliferation rate in chameleon tooth germs. (A, B) Localization of PCNA-positive cells in both labial and lingual sides of the cervical loop at the cap and bell stage. (A', B') Scheme with labeled areas where counting of PCNA-positive cells was performed. Outlined areas of proliferation analysis in the lingual and labial sides of the cervical loop. In order to detect differences in cell proliferation the number of PCNA-positive cells was counted separately for the inner (purple dotted line) and outer (orange dotted line) enamel epithelium of the labial and lingual cervical loop (separated by black line). (C, D) Graphs display numbers of PCNA-positive cells contributing to the lingual or labial part of the cervical loop. The lingual side of the cervical loop possesses more PCNA-positive cells in contrast to the labial side at the bell stage (D) but not at the cap stage (C). (C', D') Graphs display numbers of PCNA-positive cells contributing to the lingual (inner and outer enamel epithelium) and labial (inner and outer enamel epithelium) sides of the cervical loop. The lingual inner enamel epithelium contains more proliferating cells at the cap (C') and bell (D') stage. The graph values denote average \pm s.d., *** $p < 0.001$, * $p < 0.05$ using a paired t-test. *ek* enamel knot, *iep* inner enamel epithelium, *labcl* labial side of the cervical loop, *lincl* lingual side of the cervical loop, *oep* outer enamel epithelium, *sr* stellate reticulum. (E–H) SOX2-positive cells in chameleon enamel organ with detailed view (E'–H') on the lingual and labial part of the cervical loop and on the interdental area. (E, F) During early odontogenesis, strong SOX2 expression was detected predominantly in cells of the dental lamina situated on the lingual side of the developing tooth germ. (G, H) SOX2 expression persisted in the dental lamina cells even during early or late bell stages. SOX2 expression in the interdental area followed expression pattern in developing tooth germ with strong signal on its lingual side at early (E', F') or late developmental stages (G', H'). Scale bar = 50 μ m. (I–L') ST14 expression during chameleon odontogenesis. (I, J) Localized lingual ST14 expression was detected predominantly at the late bud stage and early cap stage. (K, L) Later in development, ST14 positive cells were situated both in the enamel knot area and the lingual cervical loop. (I'–L') ST14 expression was detected in the interdental area with same lingually located asymmetrical pattern at early (I', K') as well as late (K', L') developmental stages. Scale bar = 50 μ m.

Results

Early asymmetrical growth of the labial and lingual part of the cervical loop in an acrodont dentition as revealed by microscopic and ultrastructural analysis.

From the early cap stage, the enamel organ of the chameleon tooth germ grew asymmetrically into the underlying mesenchyme with a longer extension of the cervical loop observed on the lingual side (Fig. 2A–D). Later, at the bell stage, asymmetry between the lingual and labial sides of the cervical loop was even more pronounced, with prominent elongation of the lingual part of the tooth germ into the mesenchyme (Fig. 2D).

In the interdental spaces, an epithelial outgrowth was visible along the entire jaw (Fig. 2A'–D'). The dental lamina extended in a lingual direction from the outer enamel epithelium of the tooth germ. In 3D, it was evident that the lingual part of the cervical loop was continuous with the interdental dental lamina and dental lamina, which extended along the jaw (Fig. S4), similar to the situation previously described in snakes²². During the course of development, the cervical loop expanded into the interdental areas and later, the individual teeth fused with the neighboring teeth (Fig. S4).

As chameleon teeth exhibited distinct asymmetrical development of the cervical loop, which is typically observed in pleurodont dentitions, we next investigated the ultrastructure of the lingual and labial sides of the loop (Fig. 2E–M). The inner enamel epithelium of both parts of the cervical loop was formed by several layers of small round nuclei (Fig. 2E,G). Minimal intercellular spaces were observed between the cells in the loops, in contrast to the cells in the outer enamel epithelium (Fig. 2F). Mitotic events were observed in both the labial and lingual sides of the cervical loop (Fig. 2E,G). Close interactions between cells on the epithelio-mesenchymal interface were identified at the edge of the cervical loop, with long cytoplasmic processes of mesenchymal cells in direct contact with the basement membrane on both sides (Fig. 2H,K).

Despite these overall similarities, some distinct differences were observed, particularly at the epithelio-mesenchymal interface. The labial side of the cervical loop was surrounded by a smooth basal membrane without undulations (Fig. 2I,J). Separation of the basement membrane into the lamina lucida and lamina densa was distinct (Fig. 2I,J). In the area closely attached to the mitotically active cells, the basal membrane was fenestrated in several regions (data not shown). Large intercellular spaces with a size of up to 2 μ m were distinct between the cells of the outer enamel epithelium on the labial side (Fig. 2J).

In contrast, the basal membrane of the lingual cervical loop cells was irregularly folded with distinct basal cells, which contained numerous hemidesmosomes on their membranes (Fig. 2J,M). Many primary lysosomes were located in the basal area of these epithelial cells. Mitochondria were small and scattered throughout the cellular cytoplasm and they represented the dominant organelle in these cells. Large amounts of glycogen were present in the basal areas of these cells (Fig. 2K,M). In contrast to the labial side, the lingual basement membrane was clearly subdivided into a lamina lucida and lamina densa (Fig. 2L,M). Numerous collagen fibrils were located directly beneath the basement membrane in the lingual part of the cervical loop (Fig. 2L), in contrast to the minimal numbers of fibrils in the labial part of the cervical loop (Fig. 2J). Long cellular processes of the mesenchymal cells protruded towards the epithelial cells (Fig. 2M). Numerous folds were found in the lingual part of the cervical loop and we observed significantly higher number of hemidesmosomes (Fig. 2J,M). The cervical loop of a tooth is therefore not a uniform structure with distinct differences on its labial and lingual sides.

Asymmetrical extension is associated with differential proliferation between the labial and lingual sides of the cervical loop. Next, we analyzed the developmental processes that might be con-

tributing to the asymmetrical extension of the cervical loop. We focused on cell proliferation at early stages of cervical loop elongation, at the cap and bell stage, before the dental lamina has separated from the outer enamel epithelium.

PCNA-positive cells were found to be located within the cervical loop at both stages analyzed (Fig. 3A,A',B,B'). Significantly more PCNA-positive cells were observed on the lingual side of the loop at the bell stage, with no difference at the cap stage (Fig. 3C,D; Student pair t-test $p=0.172$ at the cap stage and $p=0.037$ at the bell stage). To evaluate the pattern of proliferation in more detail, the number of dividing cells in the inner and outer epithelial layers were counted for each side of the cervical loop (Fig. 3A',B'). At both analyzed stages, there were significantly more PCNA-positive cells within the lingual inner enamel epithelium compared to the labial inner enamel epithelium (Student pair t-test $p=0.0488$ at the cap stage and $p=0.0002$ at the bell stage). In contrast, no difference was observed between the lingual and labial outer enamel epithelium at either stage (Student pair t-test $p=1.000$ at the cap stage and $p=0.139$ at the bell stage) (Fig. 3C',D').

SOX2 is differentially expressed on the lingual and labial sides of the cervical loop similar to pleurodont dentitions. SOX2 expression is asymmetrically localized from early stages of mammalian and pleurodont reptile tooth development⁸, therefore we were interested if SOX2 expression would also be restricted to the lingual part of the cervical loop in the chameleon, where there is no tooth replacement and the successional dental lamina is only rudimentary.

In chameleon embryos, strong SOX2 expression was observed in the lingual part of the cervical loop through all analyzed stages (Fig. 3E–H; S5). The strongest signal was located in the lingual outer epithelium from very early stages of development (Fig. 3E–H). We detected SOX2 expression not only in the areas where a tooth would initiate but also in the interdental areas between teeth. Surprisingly, interdental dental lamina exhibited similar asymmetrical expression of SOX2, located on the lingual side of the epithelial protrusion (Fig. 3E'–H') even though this region does not form teeth.

A few SOX2-positive cells were also found in the distal areas of the lingual inner enamel epithelium and lingual stellate reticulum (Fig. 3F,G,H). Even during early mineralization stages, SOX2-positive cells were found at the tip of the lingual part of the cervical loop overlapping with the inner enamel epithelium (Fig. S5A, A'). A few SOX2-positive cells were detected also in the stellate reticulum (Fig. S5). Later in development, SOX2 positive signal was located only in the outer layer of the dental lamina (Fig. S5).

The labial stellate reticulum and the inner enamel epithelium were SOX2-negative throughout development (Figs. 3G,H; S5), along with the differentiating odontoblasts and ameloblasts (Figs. 3G,H; S5).

ST14 exhibits asymmetrical expression in the cervical loop with positive domain overlapping with SOX2-positive cells. To further determine labio-lingual differences, we analyzed the expression of ST14 (matriptase) during chameleon odontogenesis. Matriptase is a serine protease, which plays critical role in the maintenance of epithelial integrity in numerous tissues^{23–25}, and is also expressed in the enamel knot during murine tooth development¹⁷. At early stages of development (bud to cap), ST14 was expressed on the lingual side of the cervical loop (Fig. 3I,J). Within interdental region, expression of ST14 also defined the lingual side of the lamina (Fig. 3I'–L'). At the bell stage, expression was maintained on the lingual side of the loop with a new domain of expression in the differentiating ameloblasts (Fig. 3K,L). Thus, the lingual side of the cervical loop is distinct molecularly from the labial side and shares an expression pattern with the connected interdental lamina.

The cervical loop retains asymmetrical morphology during mineralization stages. The labial part of the cervical loop remained shorter and directed lingually during stages of mineralization (Fig. 4A–D). The anlagen of the dental lamina appeared at the tip of the lingual part of the cervical loop as a protrusion of the outer enamel epithelium (Fig. 4C,D). Epithelial outgrowth in the interdental area was also directed lingually, similar to that observed at younger stages (Fig. 4E–H). This lingual direction fits with the differential proliferation pattern observed in the inner and outer epithelium of the cervical loop (Fig. 3C',D').

In the iodine contrasted micro-CT data, we were able to measure the length of the cervical loop in cross section through the center of the tooth (Fig. 4I–L). The analysis highlighted significant differences between the size of the labial and lingual part of cervical loop even in these later stages (Fig. 4I–L). The differences in length of the lingual and labial part of the cervical loop were not consistent along the jaw, with the anterior teeth being more symmetrical in comparison to the teeth that developed in the middle of the lower jaw, where the most significant differences in length were observed (Fig. 4I–L).

Asymmetric association of the tooth and forming bone. While adult chameleon teeth are located above the bone, during late development the mineralized tooth germs were positioned at an angle to the forming jawbone (Fig. 5A–D). Moreover, the shape of the bone and the cervical loop did not correspond, indicating that the cervical loop did not grow directly towards the bone (Fig. 5A–C). As the teeth formed, the bony pedicles were initiated and extended upwards (Fig. 5D).

Based on histological analyses, development of the dentary bone, which holds the teeth, also appeared to develop asymmetrically along the labio-lingual axis. To assess this, we analyzed dentary bone morphology in more detail using 3D reconstruction. Micro-CT imaging revealed that mineralization of the dentary bone was enhanced on the labial side of the lower jaw (Fig. 5E–I, E'–I'). As the tooth-bone junction started to develop, bony lamellae mineralized just above Meckel's cartilage, and these lamellae, together with the bony spicules located more lingually, were then remodeled to correspond to the shape of the cervical loop (Fig. 5H',I'). Distinct differences in bone thickness were evident along the lower jaw (Fig. 5E'–I'). The bone appeared thicker on the labial side of the jaw at all developmental stages and also in the areas where the lamellae would later fuse (Fig. 5E'–I').

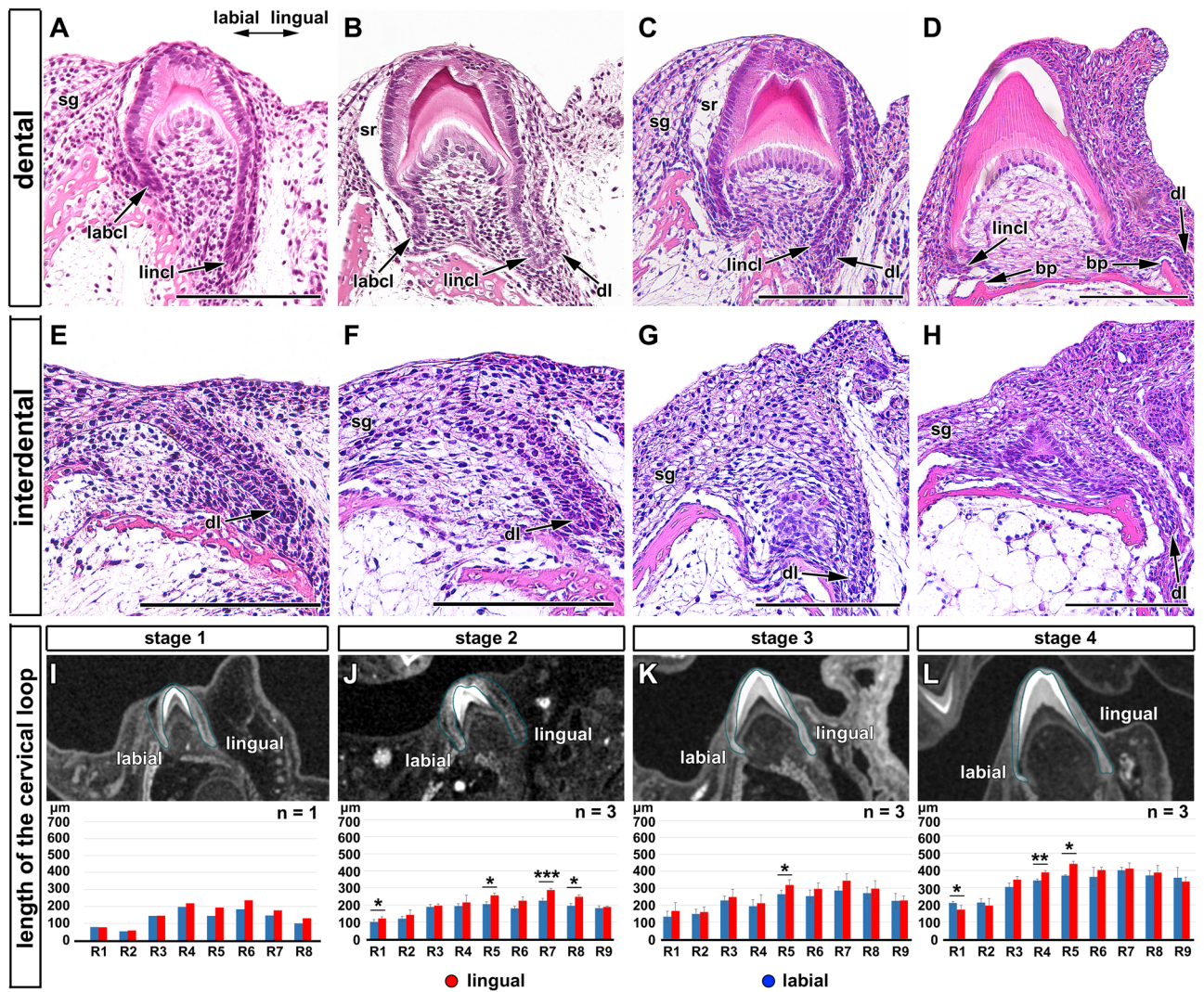


Figure 4. Labio-lingual asymmetry of enamel organ during mineralization stages in chameleon embryos. (A–D) Transversal histological sections through the central cusp of the tooth from early (A, B) to late (C, D) mineralization stage. Dental areas exhibiting distinct differences in the lingual and labial part of the cervical loop (arrows). (E–H) Detailed view on the interdentary areas with dental lamina protruding lingually at early (E, F) and late (G, H) mineralization stages. *bp* bone pedicle, *dl* dental lamina, *labcl* labial cervical loop, *lincl* lingual cervical loop, *sg* salivary glands, *sr* stellate reticulum. Scale bars (A–H) = 50 μ m. (I–L) Analysis of the length of the labial (blue) and lingual (red) parts of cervical loop revealed differences between the size of labial and lingual part of cervical loop at early (I, J) and late (K, L) mineralization stages. The lengths of labial and lingual part were not consistent along the jaw. The lingual part of the loop remained slightly longer throughout all analysed stages. R1 to R9 refer to the individual position of teeth on the right side of the jaw in order from the most rostral teeth (R1) to the tooth in the caudal area (R9). *n* = number of analysed mandibles for each stage. Pair t-test was used to analyze statistical significance of differences between labial and lingual part of the tooth. **p* < 0.05, ***p* < 0.01, ****p* < 0.001.

Micro-CT of hard tissues was used to determine the relative position of each tooth in relation to the underlying bones during development (Fig. S3; movable models of individual stage Fig. S6–S10). The spatial relationship of tooth and bone was not synchronized during these mineralization stages (Fig. 5E'–I'). Measurement of the angle between the dorsal bony lamellae and tooth axis (Fig. 5J) revealed that all teeth were inclined labially on the jaw. Caudal teeth were positioned at a greater angle to the dorsal bony lamellae and exhibited a larger displacement (Fig. 5K).

Tooth-bone distances were asymmetrical with larger distances on the lingual side. As the hard tissues of the tooth and bone need to come together to form an attachment, we investigated the distance between the dentin and the bone on both sides of the tooth at several developmental stages (Fig. 6A, B). Despite the fact that the lingual loop was considerably longer than the labial loop, the distance between the bone and dental hard tissue was larger on the lingual side in comparison to the labial side (Fig. 6C–G). For those stages

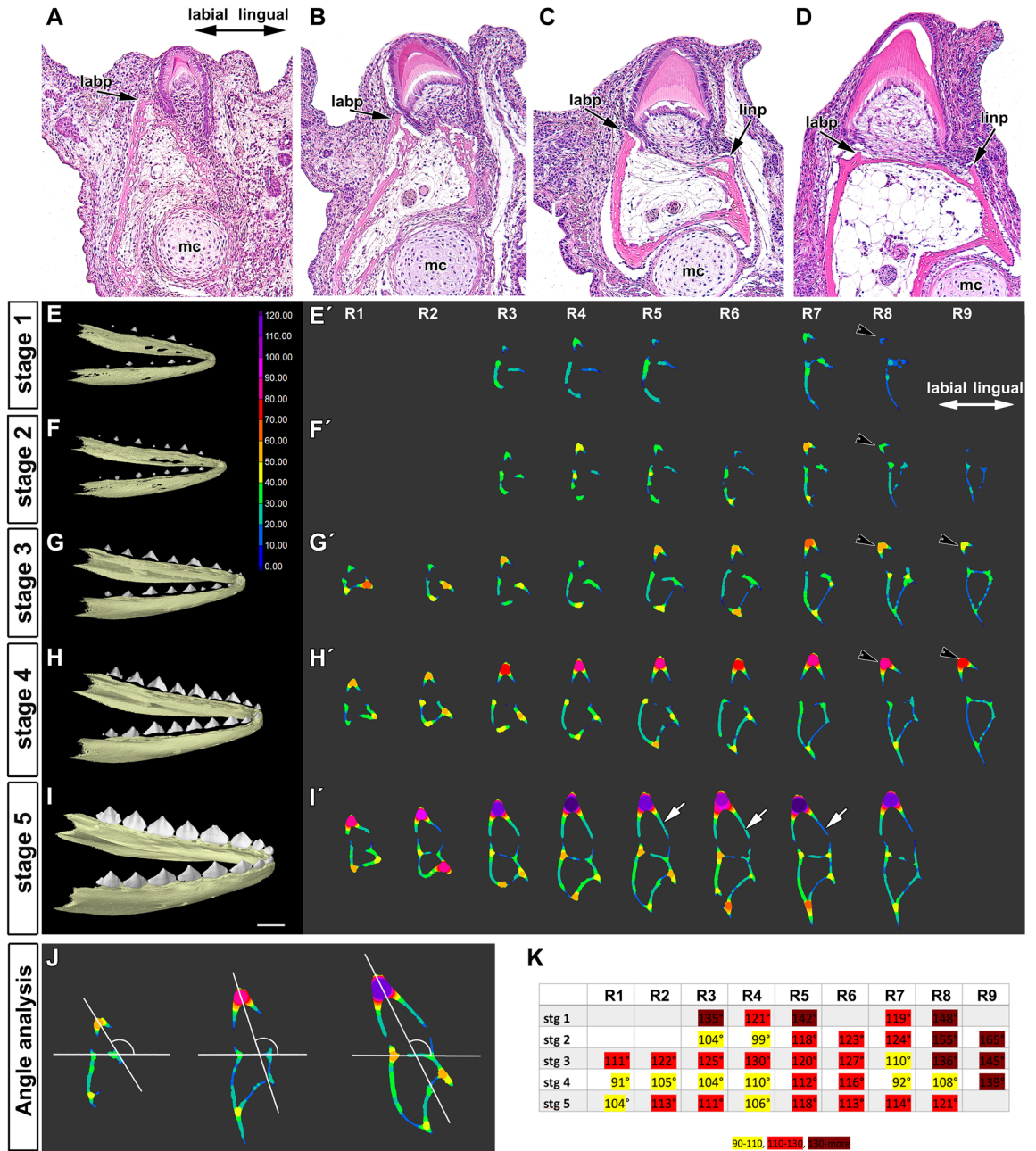


Figure 5. Tooth-bone relationship during prehatching development of chameleon. (A–D) Position of tooth and underlying bone during tooth germ development visualized by Haematoxylin–Eosin staining. (A) At early mineralization stage, labial bony pedicle (*labp*) was formed in close proximity to the labial part of the cervical loop. (B) Later in development, lingual bony pedicle (*linp*) approached extending lingual part of the cervical loop. (C) Once the bony pedicles were fully developed, bony lamellae were starting to form. (D) Spatial relationship between tooth and bone just before the attachment, when cells of the cervical loop were in direct contact with bone forming cells. *mc* Meckel cartilage. Scale bar = 50 μ m. (E–I) Lateral view on the 3D images of whole lower jaws and teeth in chameleon embryos (E’–I’). Transversal sections through the central area on each tooth with applied wall thickness analysis. Analysis was performed at five different stages: stage 1 (E, E’), stage 2 (F, F’), stage 3 (G, G’), stage 4 (H, H’) and stage 5 (I, I’). Micro-CT imaging revealed that the bone lamellae were thicker on the labial part of the jaw in all analysed developmental stages of chameleon embryo and in the areas of future lamellae branching/fusion. The initiation of bony pedicles mineralization was initiated on the labial side of the dentary bone and later during development progressed to the lingual side. R1 to R9 refer to the individual position of teeth on the right side of the jaw in order from the most rostral teeth (R1) to the tooth in the caudal area (R9). The unit in the colour scale is in μ m. White arrows indicate visibly longer hard tissue of the lingual cervical loop. (J, K) Analysis of the tooth tilt towards the jaw in the transversal section of the teeth. (J) Measurements performed for selected teeth: tooth R7 at stage 2, tooth R8 at stage 4, tooth R5 at stage 5. (K) Analysis of the angle between dorsal bony lamellae and tooth axis revealed that the early stages of teeth were located with larger angle to the dorsal bony lamellae (K), labelled by black arrows in E’–H’. Moreover, caudal teeth were inclined in the jaw under different angle in comparison to the rostral teeth. R right tooth on the lower jaw.

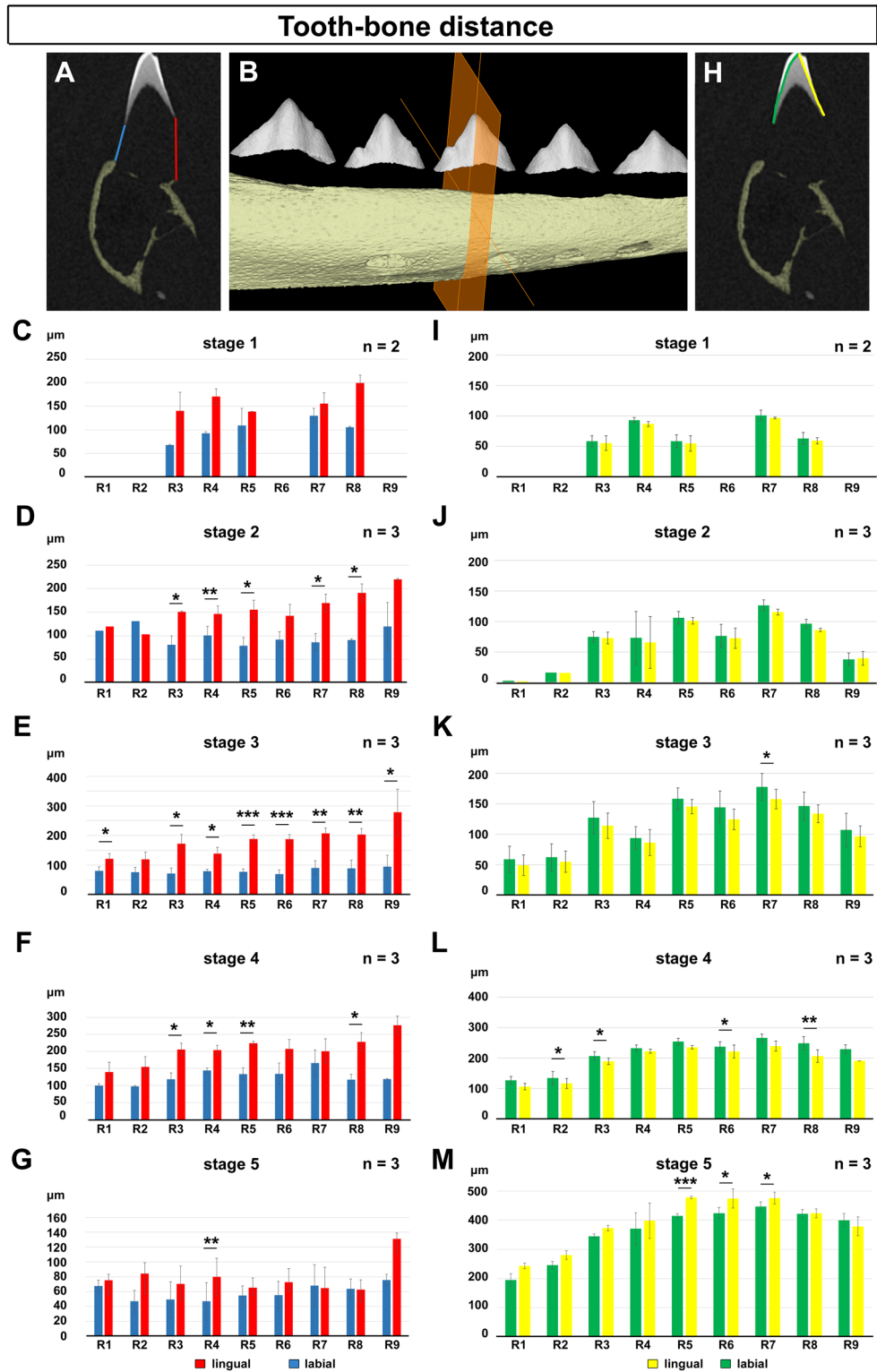


Figure 6. Tooth-bone distance and dentin deposition in chameleon. (A–G) Tooth to bone distance was measured on the transversal section through the central cusp (B). The distance was measured separately on the labial (blue) and lingual (red) side between the dentin and the nearest edge of the bony lamellae (A). Tooth-bone distance was found to be larger in the lingual side of the cervical loop at all analysed stages. (H–M) Analysis of dentin deposition on the labial (green) and lingual (yellow) side of the tooth germ. Analysis was performed at five different stages: stage1 (C, I), stage 2 (D, J), stage 3 (E, K), stage 4 (F, L) and stage 5 (G, M). n = number of analysed mandibles for each stage. Pair t-test was used to evaluate statistical significance of differences between labial and lingual part of the tooth. * $p < 0.05$, ** $p < 0.01$, *** $p < 0.001$.

where we had enough specimens, the differences were confirmed as statistically significant, although there was variation between tooth positions. By stage 5, the differences were generally not significant, suggesting the two sides of the bone and tooth had aligned, however, we identified much larger variation at this stage, which may have influenced the analysis (Fig. 6G). Overall, the largest gap on the lingual side was evident at stage 3 (up to 400 μm), reducing to about 80 μm by stage 5 (Fig. 6E–G).

Dental hard tissues were deposited symmetrically, independent of length of the cervical loop.

As we observed asymmetrical morphology of the soft dental tissues and bone deposition, including obvious differences in tooth–bone distances in the lingual and labial areas, we asked if deposition of hard dental tissue followed this pattern. Therefore, we analyzed the differences in the length of the hard tissue deposited on the lingual and labial sides of the cervical loop (Fig. 6H). We expected that odontoblast and ameloblast differentiation might follow the growth of the cervical loop. Bone deposition and soft dental tissues exhibited asymmetrical morphology from the beginning of development, the first deposition of dentin was symmetrical with no obvious differences between the labial and lingual sides (Fig. 6I,J). This symmetry was largely maintained at stage 3, with only one tooth in the jaw showing a statistical difference (Fig. 6K). At stage 4 and 5, this symmetry was briefly disrupted, with more dentin production initially on the labial side of the tooth (Fig. 6L) followed by higher production on the lingual side by stage 5 (Fig. 6M). Our findings therefore reveal the absence of an association between the length of the cervical loop and the progression of cell differentiation.

Cervical loop development varies across reptiles with acrodont dentitions. The described asymmetrical growth of the cervical loop in chameleon (Fig. 7A–D) appears to represent a common condition, which has been described in many other reptilian species with pleurodont attachment^{1,5,26}. In the pleurodont gecko (Fig. 7E,F), the embryonic lingual part of the cervical loop was longer and thinner during all prehatching stages and the dental lamina cleaved off from the lingual outer enamel epithelium at the bell stage (Fig. 7G,H), similar to that previously described^{5,13,27}.

The fact that both an acrodont (chameleon) and pleurodont (gecko, python) reptiles have asymmetrical cervical loops might suggest this state as a general feature of reptile dentitions. To investigate this further we assessed the development of the cervical loop in two other acrodont species, the bearded dragon (*Pogona vitticeps*) and tuatara (*Sphenodon punctatus*). In the caudal acrodont teeth of the bearded dragon (Fig. 7I,J), we observed a shorter cervical loop on the labial side during mineralization (Fig. 7K,L), which was evident in different regions of the jaw^{13,28}. Agreeing with previous reports, a small rudimentary dental lamina was observed budding off from the lingual side of the cervical loop in the acrodont teeth (Fig. 7K). The bearded dragon, like the chameleon, therefore, has retained asymmetrical cervical loops, despite having an acrodont dentition in the majority of the jaw. In contrast, in the tuatara (Fig. 7M,N), which unlike the other reptiles described is a Rhyncocephalia, the two sides of the cervical loop in section appeared very symmetrical, evident in both anterior as well as in posterior teeth (Fig. 7O,P). Interestingly, the relationship of the dental lamina and primary tooth appeared different in tuatara, with the successional lamina extending from an area close to the oral surface rather than being closely associated with the lingual side of the cervical loop (Fig. 7O).

Discussion

Labio-lingual asymmetries in cervical loop morphology. Shaping of the tooth–bone interface, and the spatial relationship between these two tissues, has not previously been well described in non-mammalian species. Here we have focused on the processes contributing to the formation of the symmetrical morphology of dental tissues in the chameleon. Our analysis has revealed that the acrodont teeth of chameleons initially form asymmetrically, with differential extension of the cervical loop on the lingual and labial sides. This asymmetry was evident from early stages of tooth development but later resolved to create the strict labio-lingual symmetry observed in adult teeth.

The asymmetry observed in the developing chameleon and bearded dragon, mirrors that observed in the gecko and snake, which have a pleurodont attachment. Our findings, therefore, support the view that pleurodonty is a plesiomorphic character and has been adapted to create an acrodont attachment. The differences between labial and lingual sides of the cervical loop seems to be both morphologically and functionally tightly associated with development of the dental lamina, even in chameleon where a replacement dentition is not formed and only a rudimentary successional dental lamina is visible. In contrast, in the tuatara, where the dental lamina was less tightly associated with the lingual side of the cervical loop, the loop was symmetrical. The asymmetrical nature of developing teeth in squamates is, therefore, likely to be a consequence of the close relationship of the epithelium on the lingual side of the cervical loop and the dental lamina. In contrast, we observed no clear link between symmetrical/asymmetrical growth of the cervical loop and the type of attachment or whether a replacement tooth formed or not.

Variations in size of the labial and lingual parts of the cervical loop have also been observed in mammalian species. Very small asymmetries are visible at early stage of mice molar development, where the lingual side of the cervical loop is slightly longer and thinner than the labial side²⁹. More obvious disparities have been widely studied in rodent incisors, where the lingual side of the cervical loop is less robust in comparison to the labial cervical loop, which houses a stem cell population for regeneration³⁰. This asymmetry is already visible from the bud stage of tooth development and has a clear functional consequence, creating the asymmetry in enamel formation in the tooth. In contrast, it appears to be no functional difference in the two sides of the cervical loop in the chameleon.

The asymmetrical morphology was confirmed at the ultrastructural level, with differences in cell junctions and basal membrane morphology. The basal membrane of the lingual cervical loop cells contained numerous

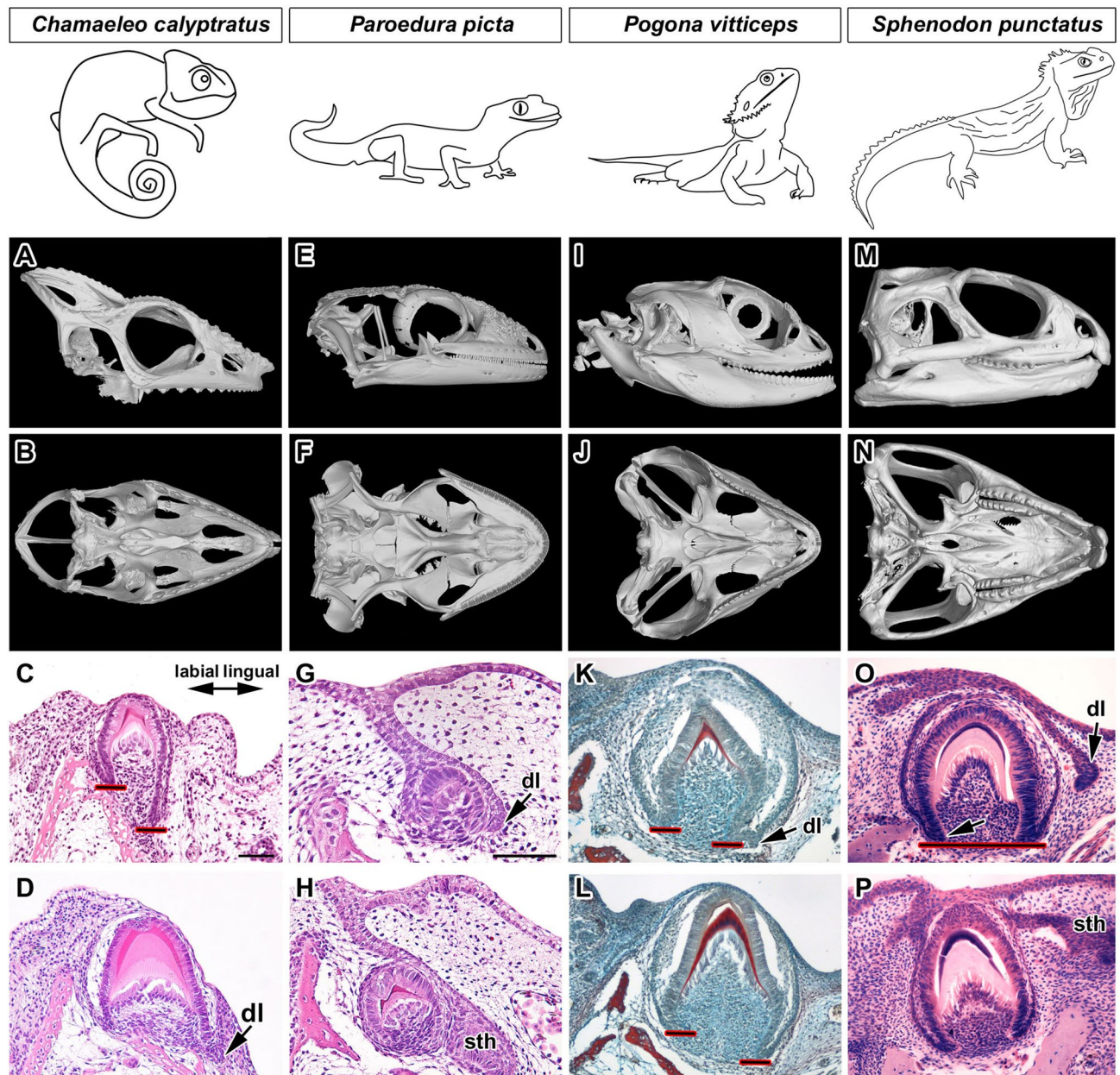


Figure 7. Comparison of tooth symmetry/asymmetry of selected reptilian species. (A–D) *Chamaeleo calytratus*. (A, B) Lateral and palatal view of the skull of *Chamaeleo calytratus* displaying complex teeth located in one row on the upper jaw. (C, D) Asymmetrical tooth germs at two different developmental stages. (E–H) *Paroedura picta*. (E–F) Lateral and palatal view of the skull of *Paroedura picta* displaying complex teeth located in one row on the upper jaw. (G, H) Asymmetrical tooth germs at two different developmental stages. (I–L) *Pogona vitticeps*. (I, J) Lateral and palatal view of the skull of *Pogona vitticeps* displaying complex teeth located in one row on the upper jaw. (K, L) Asymmetry in the development of the cervical loop was evident in acrodont tooth germs developing in the posterior area (L) of the jaw during mineralization stages at day 55 post-oviposition. (M–P) *Sphenodon punctatus*. (M, N) Lateral and palatal view of the skull of *Sphenodon punctatus* displaying complex teeth located in two rows posteriorly on the upper jaw. The teeth of the lower jaw fit into the groove between the two rows of teeth on the upper jaw. (O, P) Symmetrical tooth germs were observed in both the posterior (O) and more anterior (P) regions of the jaw. Specimen R, 5 months old. *dl* dental lamina, *sth* successional tooth, *black line with red outlines* ending of the cervical loop. Scale bar = 50 μ m.

hemidesmosomes. Moreover, numerous folds were located in the lingual side of the cervical loop while the labial side was smooth. Comparable folding of basal membrane was also observed in mouse molars during the bending of the inner enamel epithelium at the bell stage²⁹. Desmosomes and hemidesmosomes can provide mechanical integrity to the dental epithelial tissues³¹ and differences in their distribution might be involved in remodeling of

the cervical loop. Abundant cells packed with glycogen were observed in the outer enamel epithelium with higher amounts of glycogen granules on the lingual side of the cervical loop. It was previously suggested that highly glycogen packed cells undergo cell degeneration²⁹. However, in the case of the chameleon, these cells seemed to be very metabolically active and did not exhibit other features of cellular regression. Increased glycogen storage has also been observed during transition from preameloblasts to ameloblasts^{32,33}. Moreover, some glucose transporters (GLUT1) with a high affinity for glucose exhibit strong expression in active and proliferating cells in mice³³. Therefore, in chameleon, the distribution of large glycogen deposits in cells of the early tooth germ may be associated with the high proliferation status of the epithelial cells in the cervical loop area.

Labio-lingual difference in gene expression. Previously, it was reported that even small alteration in cellular dynamics can finely tune tooth size³⁴, therefore we decided to analyze possible differences in the number of proliferating cells in the labial and lingual sides of the cervical loop. A significant difference was observed between the lingual and labial sides of the loop at the bell stage, with more proliferating cells on the lingual side. In contrast, no difference was observed in the number of proliferating cells within the loop at the cap stage. However, when the epithelium was divided into inner and outer enamel epithelium, significantly more proliferating cells were observed within the lingual inner enamel epithelium compared to the labial inner enamel epithelium at both the cap and bell stages. The asymmetry in the loops is therefore likely to be driven, in part, by the difference in proliferation of the inner enamel epithelium on either side of the loop. This arrangement would also be predicted to result in an overall extension of the cervical loop in a lingual direction, agreeing with the histology and soft tissue micro-CT data. Although significant differences in proliferation were highlighted, particularly at the bell stage, other mechanisms are likely to also drive the differential extension of the cervical loop. At both the cap and bell stages obvious shape differences were identified between the two sides of the cervical loop, where the labial side was short and thick while the lingual side was thinner and elongated. Processes such as cell rearrangement and intercalation may therefore help to drive the changes in cervical loop shape.

Localized SOX2 expression as a stem cell marker has been previously described in the lingual side of the tooth germ, in the dental lamina of reptiles as well as in the dental lamina during serial addition of mammalian molars⁸. SRY-related HMG box-containing transcription factor-2 (SOX2) is a key factor that plays an important role in maintaining pluripotency of stem cells³⁵. Expression of SOX2 has been previously found to be restricted in the stem cell niche and SOX2 is involved in successional dental lamina development in a number of different vertebrate species⁸. Similarly, we observed SOX2 expression largely restricted to the lingual side of the tooth germ, despite the fact that there is no replacement and the dental lamina is only rudimentary³⁶. The early presence of SOX2, therefore, does not indicate whether a replacement tooth will form or not. SOX2 has previously been found to control and promote proliferation, with the inhibition of SOX2 leading to suppression of cell proliferation and invasion³⁷. However, we identified no difference in proliferation between the SOX2-positive outer lingual loop and the SOX2-negative outer labial loop, suggesting SOX2 does not boost proliferation at the cap and bell stages.

Expression of SOX2 was continuous along the jaw in the chameleon, similar to that recently described in the minipig³⁸. In animals with a dental lamina running along the jaw the expression of SOX2 may therefore act to promote formation of an interdental lamina. Previously, it has been proposed that *Sox2* expression relates to the competence of the interdental epithelium for tooth initiation³⁹.

Previously, we revealed that matriptase (also known as ST14, TADG15, or epithin) is expressed in the enamel knot at the cap stage but also exhibits distinct expression in the tooth germ of chameleons¹⁷. Here, we asked if the expression in the tooth germ is restricted to specific part of the dental loop and how the expression pattern appears in the interdental areas. We found ST14 signal located only on the lingual side of the cervical loop. In the interdental areas, ST14 expression was also restricted to the lingual side. The role of ST14 in odontogenesis has not been studied yet but its expression makes it an interesting gene for further study. As matriptase displays trypsin-like serine protease activity and it is able to cleave and activate numerous substrates, it is possible that matriptase may regulate local signaling that contributes to the formation and function of the dental epithelium.

Dental hard tissue deposition does not follow the pattern of the cervical loop. Adult chameleon teeth are typically located just above the dentary bone and ankylosed to the tip of bony pedicles^{26,40}. We expected that odontoblast and ameloblast differentiation might follow the growth of the cervical loop, however, despite the asymmetrical extension of the loop, the deposition of dental hard tissue was symmetrical. This was in contrast to the maintained asymmetry typical for pleurodont dentition in the gecko, which is achieved by extended dentin deposition on the lingual side during odontogenesis⁵. Loop extension and the extent of hard tissue deposition is therefore independently regulated in the chameleon. How cells recognize the necessity to continue to differentiate or prevent their progression along the cervical loop would be an interesting area to analyse in future studies. The generation of a symmetrical structure from an asymmetrical template, as observed in the chameleon tooth, may additionally shed light on the creation of other symmetrical structures in the body⁴¹.

Conclusion

Overall, our studies highlight the close relationship between the lingual side of the cervical loop and the dental lamina in squamates, both morphologically and molecularly. We show that it is not necessary to have a symmetrical cervical loop to form a symmetrical tooth, but that this can be generated by asymmetrical development in the tooth and bone, and finally we suggest that symmetrical teeth in squamates evolved from asymmetrical pleurodont teeth.

Received: 28 January 2020; Accepted: 26 November 2020

Published online: 16 December 2020

References

- LeBlanc, A. R. H., Brink, K. S., Cullen, T. M. & Reisz, R. R. Evolutionary implications of tooth attachment versus tooth implantation: a case study using dinosaur, crocodylian, and mammalian teeth. *J. Vertebr. Paleontol.* **37**, 19. <https://doi.org/10.1080/02724634.2017.1354006> (2017).
- Luan, X. H., Ito, Y. & Diekwisch, T. G. H. Evolution and development of Hertwig's epithelial root sheath. *Dev. Dyn.* **235**, 1167–1180. <https://doi.org/10.1002/dvdy.20674> (2006).
- Bertin, T. J. C., Thivichon-Prince, B., LeBlanc, A. R. H., Caldwell, M. W. & Viriot, L. Current perspectives on tooth implantation, attachment, and replacement in amniota. *Front. Physiol.* **9**, 20. <https://doi.org/10.3389/fphys.2018.01630> (2018).
- Gaenger, P. Evolution of tooth attachment in lower vertebrates to tetrapods. In *Development, Function, and Evolution of Teeth* (Teaford, M.F., Smith, M.M. & Ferguson, M.W.J.) 173–185 (Cambridge University Press, Cambridge, 2000).
- Zahradnick, O., Horacek, I. & Tucker, A. S. Tooth development in a model reptile: functional and null generation teeth in the gecko *Paroedura picta*. *J. Anat.* **221**, 195–208. <https://doi.org/10.1111/j.1469-7580.2012.01531.x> (2012).
- Delgado, S., Davit-Beal, T., Allizard, F. & Sire, J. Y. Tooth development in a scincid lizard, *Chalcides viridanus* (Squamata), with particular attention to enamel formation. *Cell Tissue Res.* **319**, 71–89. <https://doi.org/10.1007/s00441-004-0950-2> (2005).
- Osborn, J. W. The ontogeny of tooth succession in *Lacerta vivipara* Jacquin (1787). *Proc. R. Soc. Lond. B. Biol. Sci.* **179**, 261–289. <https://doi.org/10.1098/rspb.1971.0097> (1971).
- Juuri, E. *et al.* Sox2 marks epithelial competence to generate teeth in mammals and reptiles. *Development* **140**, 1424–1432. <https://doi.org/10.1242/dev.089599> (2013).
- Jenkins, K. M., Jones, M. E. H., Zirkmund, T., Boyde, A. & Daza, J. D. A Review of tooth implantation among rhynchocephalians (Lepidosauria). *J. Herpetol.* **51**, 300–306. <https://doi.org/10.1670/16-146> (2017).
- Buchtova, M., Zahradnick, O., Balkova, S. & Tucker, A. S. Odontogenesis in the Veiled Chameleon (*Chamaeleo calytratus*). *Arch. Oral Biol.* **58**, 118–133. <https://doi.org/10.1016/j.archoralbio.2012.10.019> (2013).
- Harrison, H. S. The development and succession of teeth in *Hatteria punctata*. *Q. J. Microsc. Sci.* **44**, 161–U113 (1901).
- Haridy, Y., LeBlanc, A. R. H. & Reisz, R. R. The Permian reptile *Opisthodontosaurus carrolli*: a model for acrodont tooth replacement and dental ontogeny. *J. Anat.* **232**, 371–382. <https://doi.org/10.1111/joa.12754> (2018).
- Salomies, L., Eymann, J., Khan, I. & Di-Poi, N. The alternative regenerative strategy of bearded dragon unveils the key processes underlying vertebrate tooth renewal. *Elife* <https://doi.org/10.7554/eLife.47702> (2019).
- Simoes, T. R., Wilner, E., Caldwell, M. W., Weinschutz, L. C. & Kellner, A. W. A. A stem acrodontan lizard in the Cretaceous of Brazil revises early lizard evolution in Gondwana. *Nat. Commun.* **6**, 8. <https://doi.org/10.1038/ncomms9149> (2015).
- Hedges, S. B. Amniote phylogeny and the position of turtles. *BMC Biol.* **10**, 64. <https://doi.org/10.1186/1741-7007-10-64> (2012).
- Zheng, Y. & Wiens, J. J. Combining phylogenomic and supermatrix approaches, and a time-calibrated phylogeny for squamate reptiles (lizards and snakes) based on 52 genes and 4162 species. *Mol. Phylogenet. Evol.* **94**, 537–547. <https://doi.org/10.1016/j.ympev.2015.10.009> (2016).
- Sulcova, M. L. *et al.* Developmental mechanisms driving complex tooth shape in reptiles. *Dev. Dynam.* <https://doi.org/10.1002/dvdy.138> (2020).
- Diaz-Paniagua, C. & Cuadrado, M. Influence of incubation conditions on hatching success, embryo development and hatchling phenotype of common chameleon (*Chamaeleo chamaeleon*) eggs. *Amphibia-Reptilia* **24**, 429–440. <https://doi.org/10.1163/156853803322763891> (2003).
- Diaz-Paniagua, C. Effect of cold temperature on the length of incubation of *Chamaeleo chamaeleon*. *Amphibia-Reptilia* **28**, 387–392. <https://doi.org/10.1163/156853807781374782> (2007).
- Andrews, R. M. Effects of temperature on embryonic development of the veiled chameleon, *Chamaeleo calytratus*. *Comp. Biochem. Physiol. A* **148**, 698–706. <https://doi.org/10.1016/j.cbpa.2007.08.026> (2007).
- Peterka, M., Lesot, H. & Peterkova, R. Body weight in mouse embryos specifies staging of tooth development. *Connect. Tissue Res.* **43**, 186–190. <https://doi.org/10.1080/03008200290000673> (2002).
- Buchtova, M., Handrigan, G. R., Tucker, A. S., Lozanoff, S., Town, L., Fu, K., Diewert, V. M., Wicking, C. & Richman, J. M. Initiation and patterning of the snake dentition are dependent on Sonic hedgehog signaling. *Dev. Biol.* **319**(1), 132–145 (2008).
- List, K. *et al.* Epithelial integrity is maintained by a matriptase-dependent proteolytic pathway. *Am. J. Pathol.* **175**, 1453–1463. <https://doi.org/10.2353/ajpath.2009.090240> (2009).
- List, K. *et al.* Matriptase/MT-SP1 is required for postnatal survival, epidermal barrier function, hair follicle development, and thymic homeostasis. *Oncogene* **21**, 3765–3779. <https://doi.org/10.1038/sj/onc/1205502> (2002).
- Oberst, M. D. *et al.* Characterization of matriptase expression in normal human tissues. *J. Histochem. Cytochem.* **51**, 1017–1025. <https://doi.org/10.1177/002215540305100805> (2003).
- Zahradnick, O., Buchtova, M., Dosedelova, H. & Tucker, A. S. The development of complex tooth shape in reptiles. *Front. Physiol.* **5**, 7. <https://doi.org/10.3389/fphys.2014.00074> (2014).
- Handrigan, G. R. & Richman, J. M. Autocrine and paracrine Shh signaling are necessary for tooth morphogenesis, but not tooth replacement in snakes and lizards (Squamata). *Dev. Biol.* **337**, 171–186. <https://doi.org/10.1016/j.ydbio.2009.10.020> (2010).
- Handrigan, G. R. & Richman, J. M. Unicuspid and bicuspid tooth crown formation in squamates. *J. Exp. Zool. B* **316B**, 598–608. <https://doi.org/10.1002/jezmd.21438> (2011).
- Lesot, H. *et al.* Initial features of the inner dental epithelium histo-morphogenesis in the first lower molar in mouse. *Int. J. Dev. Biol.* **43**, 245–254 (1999).
- Hu, J. K. H., Mushegyan, V. & Klein, O. D. On the cutting edge of organ renewal: identification, regulation, and evolution of incisor stem cells. *Genesis* **52**, 79–92. <https://doi.org/10.1002/dvg.22732> (2014).
- Green, K. J. & Jones, J. C. R. Desmosomes and hemidesmosomes: Structure and function of molecular components. *Faseb J.* **10**, 871–881 (1996).
- Ohshima, H., Wartiovaara, J. & Thesleff, I. Developmental regulation and ultrastructure of glycogen deposits during murine tooth morphogenesis. *Cell Tissue Res.* **297**, 271–281. <https://doi.org/10.1007/s004410051355> (1999).
- Ida-Yonemochi, H. *et al.* Glucose uptake mediated by glucose transporter 1 is essential for early tooth morphogenesis and size determination of murine molars. *Dev. Biol.* **363**, 52–61. <https://doi.org/10.1016/j.ydbio.2011.12.020> (2012).
- Morita, R. *et al.* Coordination of cellular dynamics contributes to tooth epithelium deformations. *PLoS ONE* **11**, 20. <https://doi.org/10.1371/journal.pone.0161336> (2016).
- Arnold, K. *et al.* Sox2(+) adult stem and progenitor cells are important for tissue regeneration and survival of mice. *Cell Stem Cell* **9**, 317–329. <https://doi.org/10.1016/j.stem.2011.09.001> (2011).
- Buchtova, M., Stembirek, J., Glocova, K., Matalova, E. & Tucker, A. S. Early regression of the dental lamina underlies the development of diphyodont dentitions. *J. Dent. Res.* **91**, 491–498. <https://doi.org/10.1177/0022034512442896> (2012).
- Luo, J. F., Yan, R. C., He, X. B. & He, J. SOX2 inhibits cell proliferation and metastasis, promotes apoptotic by downregulating CCND1 and PARP in gastric cancer. *Am. J. Transl. Res.* **10**, 639–647 (2018).

38. Popa, E. M., Buchtova, M. & Tucker, A. S. Revitalising the rudimentary replacement dentition in the mouse. *Development* **146**, 11. <https://doi.org/10.1242/dev.171363> (2019).
39. Jussila, M., Yanezl, X. C. & Thesleff, I. Initiation of teeth from the dental lamina in the ferret. *Differentiation* **87**, 32–43. <https://doi.org/10.1016/j.diff.2013.11.004> (2014).
40. Dosedelova, H. *et al.* Age-related changes in the tooth-bone interface area of acrodont dentition in the chameleon. *J. Anat.* **229**, 356–368. <https://doi.org/10.1111/joa.12490> (2016).
41. Grimes, D. T. Making and breaking symmetry in development, growth and disease. *Development* **146**, 12. <https://doi.org/10.1242/dev.170985> (2019).

Acknowledgements

The project was supported by the Czech Science Foundation (Project No. 17-14886S) and by CEITEC 2020 (LQ1601) with financial support from the National Sustainability Programme II and CEITEC NRI (MEYS CR, 2016–2019 to TZ lab). Revisions of manuscript were supported by the Ministry of Health (NU20-06-00189). We acknowledge the core facility CELLIM supported by the Czech-BioImaging large RI project (LM2018129 funded by MEYS CR) for their support with obtaining scientific data presented in this paper. We are thankful to the curators of the UK and Czech museums (especially prof. David Sedmera) for providing samples of tuatara for our analyses and the University of Veterinary and Pharmaceutical Sciences for agama samples for microCT analyses (especially dr. Martin Pyszko).

Author contributions

M.B., T.Z., O.Z. and A.S.T. conceived and designed the experiments. M.K., M.S. and J.D. performed experiments. M.K., M.S., J.D., M.B., J.K., and T.Z. analyzed the data. M.B., A.S.T., O.Z. and J.K. contributed reagents and materials. M.K., M.S., J.D., A.S.T. and M.B. wrote the paper. All authors read and approved the final manuscript.

Competing interests

The authors declare no competing interests.

Additional information

Supplementary Information The online version contains supplementary material available at <https://doi.org/10.1038/s41598-020-78939-2>.

Correspondence and requests for materials should be addressed to M.B.

Reprints and permissions information is available at www.nature.com/reprints.

Publisher's note Springer Nature remains neutral with regard to jurisdictional claims in published maps and institutional affiliations.



Open Access This article is licensed under a Creative Commons Attribution 4.0 International License, which permits use, sharing, adaptation, distribution and reproduction in any medium or format, as long as you give appropriate credit to the original author(s) and the source, provide a link to the Creative Commons licence, and indicate if changes were made. The images or other third party material in this article are included in the article's Creative Commons licence, unless indicated otherwise in a credit line to the material. If material is not included in the article's Creative Commons licence and your intended use is not permitted by statutory regulation or exceeds the permitted use, you will need to obtain permission directly from the copyright holder. To view a copy of this licence, visit <http://creativecommons.org/licenses/by/4.0/>.

© The Author(s) 2020



OPEN

Contrast enhanced X-ray computed tomography imaging of amyloid plaques in Alzheimer disease rat model on lab based micro CT system

Michaela Kavkova¹✉, Tomas Zikmund¹, Annu Kala², Jakub Salplachta¹,
Stephanie L. Proskauer Pena², Josef Kaiser¹ & Karel Jezek²✉

Amyloid plaques are small (~ 50 μm), highly-dense aggregates of amyloid beta ($\text{A}\beta$) protein in brain tissue, supposed to play a key role in pathogenesis of Alzheimer's disease (AD). Plaques' in vivo detection, spatial distribution and quantitative characterization could be an essential marker in diagnostics and evaluation of AD progress. However, current imaging methods in clinics possess substantial limits in sensitivity towards $\text{A}\beta$ plaques to play a considerable role in AD screening. Contrast enhanced X-ray micro computed tomography (micro CT) is an emerging highly sensitive imaging technique capable of high resolution visualization of rodent brain. In this study we show the absorption based contrast enhanced X-ray micro CT imaging is viable method for detection and 3D analysis of $\text{A}\beta$ plaques in transgenic rodent models of Alzheimer's disease. Using iodine contrasted brain tissue isolated from the Tg-F344-AD rat model we show the micro CT imaging is capable of precise imaging of $\text{A}\beta$ plaques, making possible to further analyze various aspects of their 3D spatial distribution and other properties.

Alzheimer's disease (AD) is the most common cause of dementia worldwide, extensively interfering with personal, social, and health care levels of human society. AD progression is characterized by a gradual deterioration of cognitive abilities, starting with often unnoticed declarative memory impairment, followed by problems with spatial orientation, and ending with an inability to cope with daily life routine. The rare early onset form can affect individuals in their 40 s or 50 s, but the AD risk rapidly increases after the age of 65. While the etiology of AD remains still unclear, there are several hypothesized mechanisms reflecting molecular changes observed in brain tissue of AD patients, mainly the deposits of amyloid beta and hyperphosphorylated tau protein¹⁻³. The classical "amyloid cascade hypothesis"⁴ states that the amyloid beta ($\text{A}\beta$) plaques are the causative agent of Alzheimer's pathology. The $\text{A}\beta$ plaques are small (~ 50 μm), dense objects composed of clumped fibrils of amyloid β ($\text{A}\beta$), a peptidic product of the amyloid precursor protein. Their formation induces a local inflammation resulting in progressive cellular loss and related cognitive inability. It has been therefore assumed that the reduction of $\text{A}\beta$ deposits might help to control the AD course. Numerous approaches have been designed to reduce the $\text{A}\beta$ content in the brain tissue⁵. In order to test the effectiveness of such an AD therapy, there is a substantial need of a non-invasive, precise, and reproducible imaging method to analyze the location and size of the $\text{A}\beta$ plaques in the brain.

In the large majority of studies on mouse and rat models, the amyloid plaques were quantified histologically in sliced and stained brain tissue. While the histology and immunohistochemistry still remain important routines for characterizing the plaque properties, imaging techniques represent a powerful tool for a precise 3D analysis of plaque distribution.

So far all the attempts to image the amyloid plaques in rodent brain by Computed Tomography (CT) have been performed on mouse brain (*mus musculus*). The experiments were performed with synchrotron X-ray sources using variations of phase contrast imaging to visualize the $\text{A}\beta$ plaques⁶⁻¹¹. Overall, in all published

¹Central European Institute of Technology, Brno University of Technology, Brno, Czech Republic. ²Faculty of Medicine in Pilsen, Charles University, Pilsen, Czech Republic. ✉email: michaela.kavkova@ceitec.vutbr.cz; karel.jezek@lfp.cuni.cz

papers on the topic of A β plaques detection, the authors were able to identify the A β plaques in the mouse brain using phase contrast imaging, some even performing quantitative analyses¹¹. However, imaging at synchrotron facilities is often limited by the narrow field of view resulting in a need of several scans for the imaging of one brain. Also, the access to synchrotron facilities is very limited and burdened by the high price of the CT scans.

Absorption based contrast enhanced X-ray micro CT imaging utilizing a lab based industrial micro CT devices is an emerging imaging technique which uses the staining solutions with high proton number elements to employ the contrast in soft tissues of biological samples which are in their native state invisible to X-rays^{12,13}. Contrast enhanced micro CT imaging has been previously proved to be a promising method for a precise 3D analysis of wide variety of samples such as the developing cartilage of nasal capsule of mice^{14–17}, development of palate^{18,19}, complex tooth shape in reptiles²⁰, research of congenital heart and kidneys defects²¹, formation of mammalian neck muscles²² and even a noninvasive observation of a human embryo²³. One of the advantages of micro CT imaging is the possibility to translate a micro CT generated 3D model into a 3D pdf format, which enables an easier communication of obtained data²⁴.

The main advantage of absorption based contrast enhanced X-ray micro CT imaging is the possibility to obtain precise 3D information about inner structures of the entire brain without sectioning (which might induce artifacts related to brain deformation or missing tissue due to the sectioning). The micro CT imaging of rodent brain has been previously used for the visualization of vascular system of mouse brain filled with radio-opaque silicone rubber Microfil^{25–31}, as a tool for localization of cerebral ischemia^{32,33} to test the efficiency of different micro CT contrasting agents^{24–38}, and even for the analysis of specific structures of the brain³⁹.

However, it has not been previously determined whether the absorption based contrast enhanced X-ray micro CT imaging is capable of detecting and quantifying amyloid plaques in the brains of rodents. In this study, we optimized the mouse brain staining protocol⁴⁰ for the staining of a much larger rat brain. The lab based industrial micro CT device GE Phoenix v|tome|x L 240 was utilized to scan the contrast enhanced brains of a recent rat AD model to determine whether amyloid plaques could be detected by contrast enhanced micro CT imaging. Further, the exploration of the possibilities of A β plaque analyses provided by obtained high resolution micro CT data was pursued. This experimental setup promises a faster, more precise and accessible alternative to the synchrotron based micro CT imaging of the A β plaque deposits.

Results

We used brains from three 18 months old female rats (two transgenic TgF-344 AD animals and one wild type control). The micro CT scan slices of iodine stained brains from transgenic and wild type samples are shown in the Fig. 1a (for an animated movie see the [Supplementary material](#)). Besides the basic anatomical structures visualized equally across both brains, the transgenic brain expressed a large amount of dark grey spots—most likely suspect A β plaques that were condensed widely in cortical (neocortex, hippocampus) and some subcortical areas.

Beta amyloid is the main component of amyloid plaques. Because of their dense protein content, we expected the applied iodine based contrasting protocol would preferably stain the tissue around the amyloid plaques, resulting in their “negative” highlight in the micro CT data. The golden standard for beta amyloid detection is its immunostaining by binding to a specific antibody tagged by fluorescent probe. Here, we used this approach to validate the identity of lower density loci detected by micro CT in the transgenic samples. To confirm the identity of the suspect plaques, the iodine stained brain samples were washed in ethanol solution after the micro CT scanning, cut into histological sections and finally specifically stained for the amyloid protein. For selected histological slices we identified their respective sections in the micro CT data. The resulting comparison is displayed in Fig. 1b which shows the corresponding slice as a micro CT image (1b) and as a histological section (Fig. 1c, detailed view in Fig. 1d). The placements of the suspect A β plaques overlapped with the immunodetected A β plaques positions (arrows in Fig. 1d). This match strongly supports the fact that the introduced micro CT protocol sufficiently detects individual amyloid plaques in ex vivo whole brain.

In the industrial micro CT setups that use the cone beam geometry, the dimension of the sample is one of the main factors that determine the resulting voxel size of the obtained dataset. To acquire a 3D distribution of A β plaques in the best possible details, we decided to image an isolated part of the brain and to scan it again with a smaller voxel size. We focused on the dorsal hippocampus as this structure is severely impaired by the amyloid accumulation and cellular loss in AD. The dissected dorsal part of the hippocampus is showed in Fig. 2a,b. While the whole brain scan delivered a voxel size of 9 μm (Fig. 2c), in the case of isolated hippocampus we achieved a voxel dimension of 3 μm (Fig. 2d). The comparison of both scans convincingly shows that the readability of the large amyloid plaques’ borders and especially the visibility of small plaques was compromised, even though they were distinguishable in the whole brain scan. On the contrary, the dissected sample yielded a considerably higher level of detail, enabling to detect a large amount of plaques of various sizes.

The next step was designed to assess the sensitivity of amyloid plaques detection using micro CT in contrast to the standard immunohistological staining. After the CT measurement, we sliced the isolated hippocampal tissue sample. Despite the dehydrated and iodine stained tissue turned out to be highly fragile while slicing, we were able to select four well preserved tissue sections and immunostained them for the A β presence. Then the corresponding micro CT sections were identified and their match was evaluated (Fig. 3a,b). The areas of A β deposit cross sections were marked by different observers. Each of the micro CT/histology image pairs was treated as independent. We obtained the plaque area median value of 597.9 μm^2 (IQR 862.3 μm^2) from CT data, whereas only 28.9 μm^2 (IQR 105.4 μm^2) from the histological sections, respectively. The plaque size histograms are depicted in Fig. 3c. This showed a considerable sensitivity difference between both methods, as the immunodetection returned more than one order higher amount of A β plaque sections in the lowest size category (0–500 μm^2), accounting for its low median values. Besides the invisibility of smallest deposits on the scans, the comparison of the detailed images in Fig. 3a,b showed that the plaque border was harder to read in the micro CT

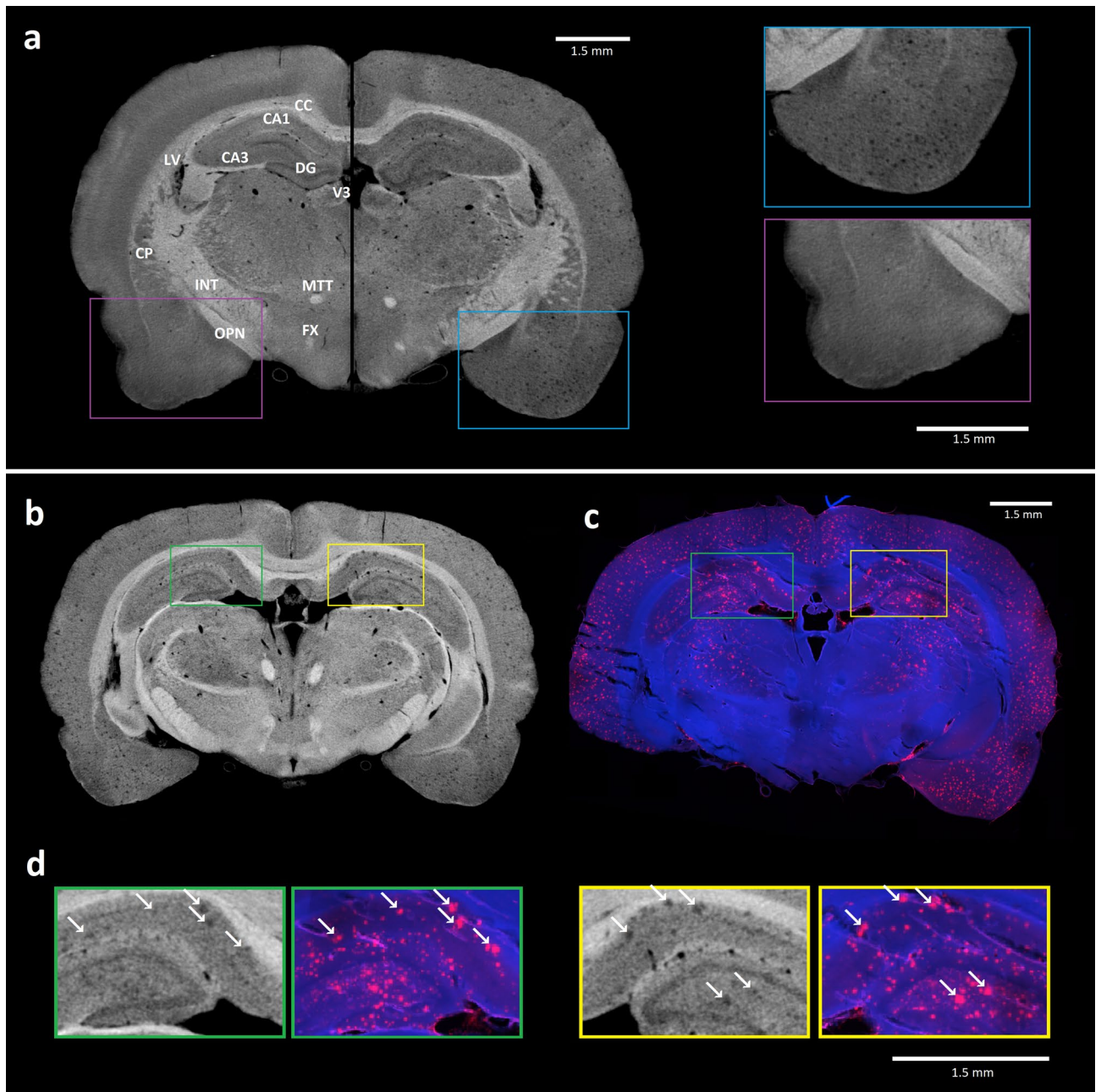


Figure 1. Confirmation of plaques identity in micro CT data: (a) Composed picture of the micro CT scan sections from control (left side) and transgenic (right side) rat brain. The transgenic tissue exhibits a large amount of suspect amyloid plaques (right part of the brain). Selected detail image of corresponding areas that are shown in pink and blue frames. Basic anatomical structures visualized in micro CT scan: CA1 and CA3 cornu Ammonis 1 and 3 of hippocampus, CC corpus callosum, CP caudoputamen, DG dentate gyrus, FX fornix, INT internal capsule, LV lateral ventricle, MTT mammillothalamic tract, OPN olivary pretectal nucleus, V3 third ventricle. Micro CT image (b) and immunohistology section with detected plaques (c) of corresponding coronal brain sections from the transgenic rat no. 60 confirms the presence of plaques in micro CT scan. Selected plaques are indicated by white arrows in enlarged slice windows (d)⁴¹.

data. This also might have caused an overestimation of the sizes of some of the smallest deposits. Consequently, they might have been marked as larger and so they were scored within the category of 501–1000 μm^2 .

The data obtained from the micro CT scan of the dissected hippocampus was chosen for a subsequent 3D analysis. Since the A β plaques had similar contrast values as other tissue structures, they could not be detected with global thresholding methods. Hence, a manual segmentation of the plaques was performed. After defining the region of interest, all segmented plaques were counted and measured. In the dissected hippocampus (total volume = 13.88 mm^3) we identified in total 1666 individual plaques. The volume of the smallest individual deposit was 895 μm^3 , indicating the lower limit for amyloid plaque identification in the present micro CT data. The biggest identified A β plaque had a volume of 721,552 μm^3 , the dataset of measured volumes was characterized

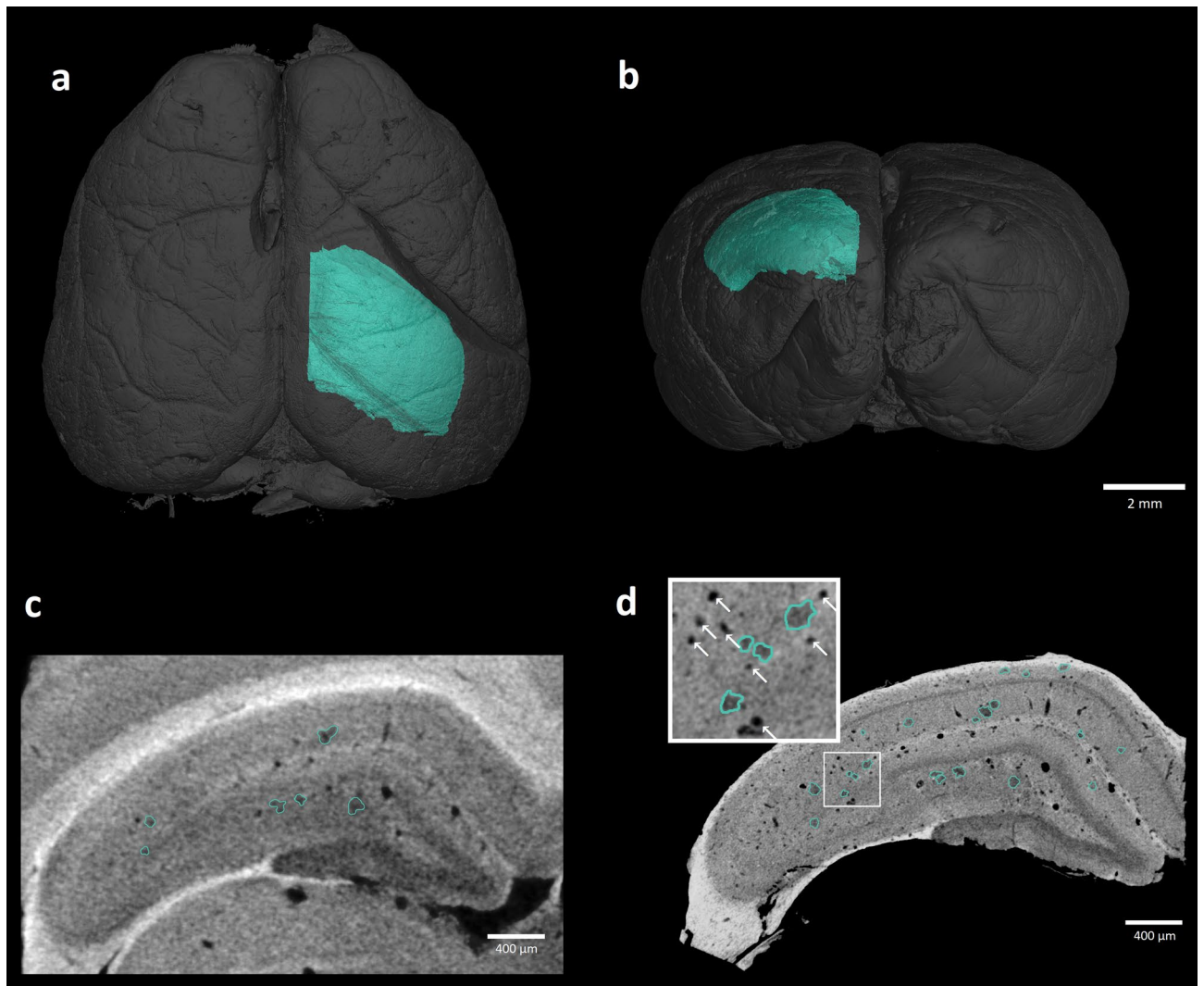


Figure 2. Detailed scan of the dissected dorsal hippocampus: Horizontal (a) and coronal (b) reconstructed view of the brain with dissected right dorsal hippocampus (green) used for the isolated scan. The same hippocampal tissue sample imaged by two different micro CT approaches (c,d) where the suspect plaques are highlighted in green. Panel (c) shows the section taken from the whole brain scan. Panel (d) depicts the same area after the isolated scanning that achieved smaller voxel size, in the magnified image the blood vessels are labeled by white arrows^{41,42}.

by median value $38,423 \mu\text{m}^3$ and IQR of $57,512 \mu\text{m}^3$. The distribution of the $\text{A}\beta$ plaques in 3D space with their color coded volumes is shown in Fig. 4a. Next, we assessed the shapes' variability of $\text{A}\beta$ plaques by measuring their compactness. The volume of the plaque was divided by the volume of the sphere circumscribed to the plaque. The values ranged between 0–1 where score of one represented a perfect sphere (Fig. 4b). The identified plaques had median of compactness at 0.396 with interquartile range 0.135. To alleviate supposed bias that could be caused by an eventual imperfection in defining boundaries in the smaller plaques, we additionally restricted the measurement to subset of plaques with volume larger than its median value (50% of the population). The corresponding compactness had a comparable median of 0.383 and IQR of 0.149.

A precise 3D model of the plaque occurrence in the hippocampal sample allowed to quantify their spatial distribution including the relation to other labeled structures. We evaluated the distances of plaques to the nearest blood vessel and the inter-plaque distance (Fig. 5). The reconstructed 3D model returned the median distance between the plaques and the nearest vessel of $64.5 \mu\text{m}$ with IQR $62.3 \mu\text{m}$ (Fig. 5a). We then investigated whether their relation followed a non-random pattern. For each of the 1666 plaques we generated a random coordinate within the dissected part of hippocampus, leaving out the detected blood vessels. We measured the respective distances of generated “plaques” to a nearest vessel with median of $89.1 \mu\text{m}$ and IQR $103 \mu\text{m}$. The comparison between the sets of experimental and randomly generated data returned the plaque-vessel distance significantly shorter in experimental data than in the random sample ($Z = 10.95$, $p < 0.001$, Mann Whitney U test), indicating the plaques tended to appear closer to the blood vessels than if their distribution was random. Finally we tested whether the plaques aggregated together irrespectively of the vessels. The same method of generating dataset with random positions was applied, and the distances between the two closest plaques were measured within the

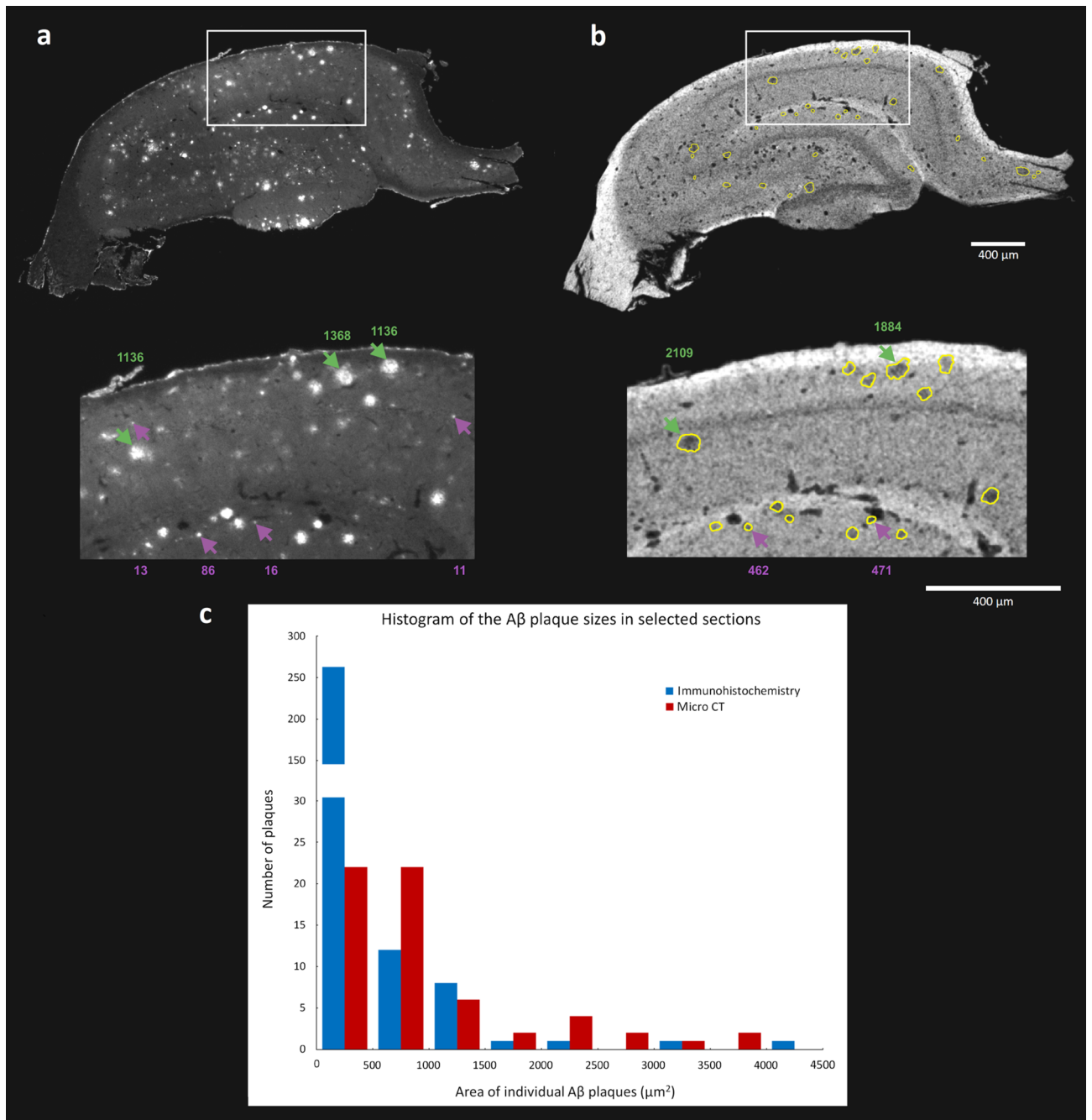


Figure 3. Comparison of the precision in identification of plaques in micro CT data versus the immunohistological detection: Comparison of corresponding sections from the same rat brain showing immunodetected A β plaques (a) and the micro CT data where the yellow line represents the manually selected plaque boundaries (b). The purple arrows indicate examples of the plaque cross sections corresponding to the smallest fraction (0–500 μm^2) while the green arrows mark the larger size cases. The corresponding area values in μm^2 are reported in proper colors above and under both pictures. The histogram (c) depicts the size interval distribution of detected A β plaque sections in the selected slices using immunohistochemistry and micro CT imaging, respectively^{41–43}.

experimental and the random positions datasets, respectively (Fig. 5b). The median of distances from the tissue sample data was 101.1 μm with IQR = 46.5 μm , whereas the randomly generated dataset returned a distribution shift towards larger values (median distance 123.4 μm and IQR 62.7 μm). The Mann Whitney U test confirmed a statistically significant difference between the both measurements ($Z = 11.97$, $p < 0.001$).

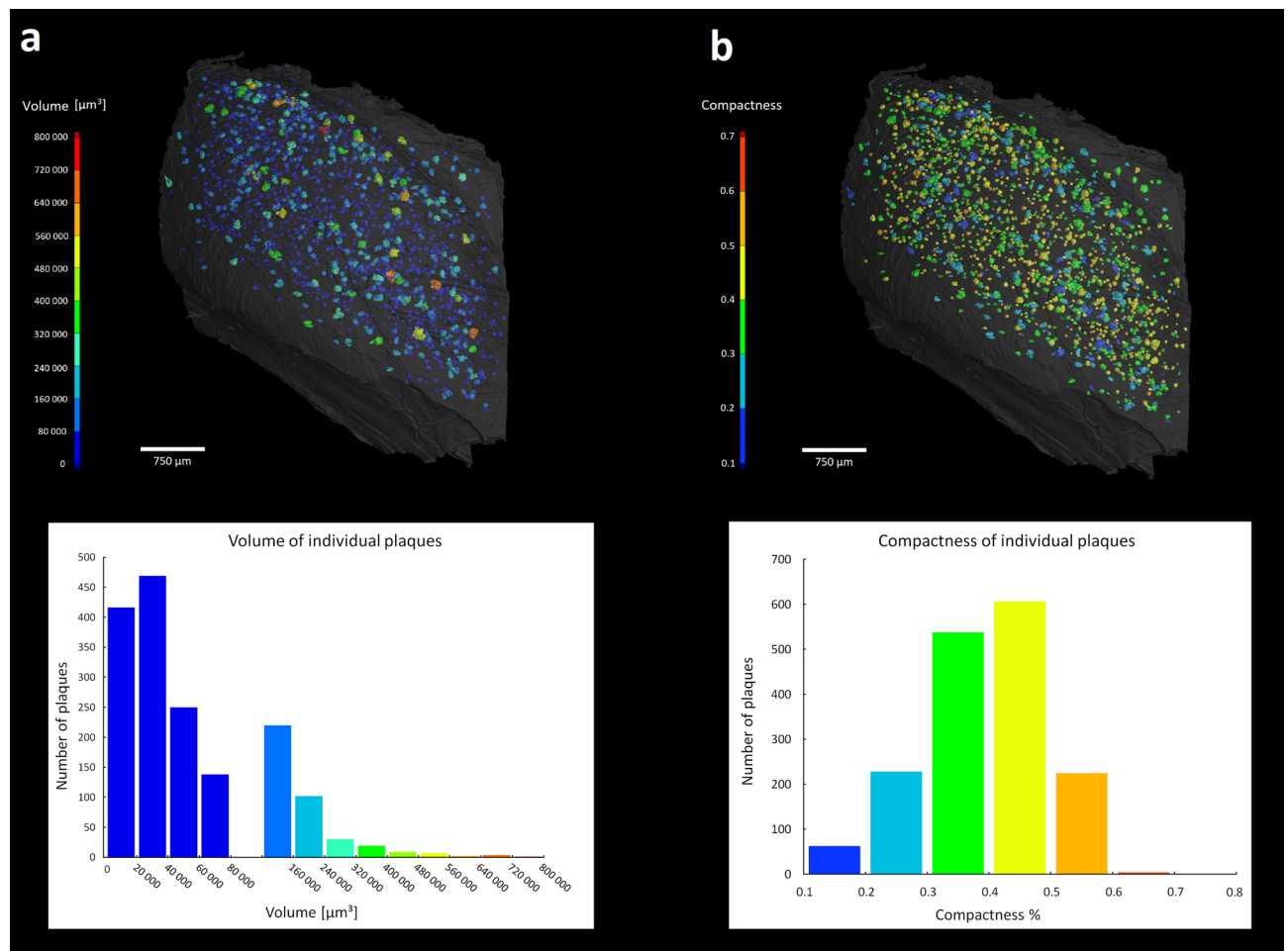


Figure 4. 3D quantitative analysis of the A β plaques size and shape in hippocampus: Panel (a) shows the plaques 3D distribution color coded respective to their size, with the corresponding histogram in the same color scale on the right. Panel (b) illustrates the same plaques color scaled according their compactness (red codes for higher similarity to a sphere) with the respective histogram (right)^{41,42}.

Discussion

In this paper, we present the absorption based contrast enhanced X-ray micro CT imaging performed on the industrial lab based CT system as an imaging tool for a 3D analysis of A β plaques of transgenic rat brains used as a model in Alzheimer disease research.

The detection of amyloid plaques in rodent brain by Computed Tomography (CT) has been attempted so far by using the mouse brain (*mus musculus*) and the experiments have been performed with synchrotron X-ray sources using variations of phase contrast imaging to visualize the A β plaques in a brain. TOMCAT beamline of the Swiss Light Source, Astolfo et al.⁶ demonstrated that synchrotron-based X-ray phase contrast imaging can be used for the 3D visualization and basic quantification of A β plaques in the mouse brain. At the same synchrotron facility the Pinzer et al.⁷ analyzed the neocortex of mouse brain via differential phase contrast imaging and accompanied their findings with complementary thioflavin S staining of the brain to confirm the presence of the A β plaques in brain in CT data. The diffraction enhanced imaging phase contrast X-ray imaging technique was applied by the Connor et al.⁸ at National Synchrotron Light Source, Brookhaven National Laboratory, USA. In that study, several scans of the one brain were needed in order to obtain a full scan of the brain. A comparison of the affected and wild type mouse brain was shown and the identity of A β plaques was confirmed by applying specific immunostaining on the A β plaques. The X-ray phase contrast tomography was applied for the purpose of the amyloid plaque imaging specifically to describe the microenvironment of the A β plaque at European Synchrotron Radiation Facility, Grenoble, France⁹. Finally, the research group of Noda-Saita et al.¹⁰ at High Energy Accelerator Research Organization, Ibaraki, Japan used phase-contrast X-ray CT imaging to describe the density of A β plaques supporting their findings with a complementary immunodetection of A β plaques in the mouse brain and with scans of control brains.

Unfortunately, the synchrotron facilities are not readily available for general use since the complicated imaging setups imply higher costs of equipment, its service and its maintenance. Moreover, the multiple scans have to be acquired to retrieve the information from the whole brain sample because of the sample's size limitations. This restricts a wide use of synchrotron based CT imaging in the Alzheimer's disease research, despite the obvious advantages for the quantification of amyloid plaques.

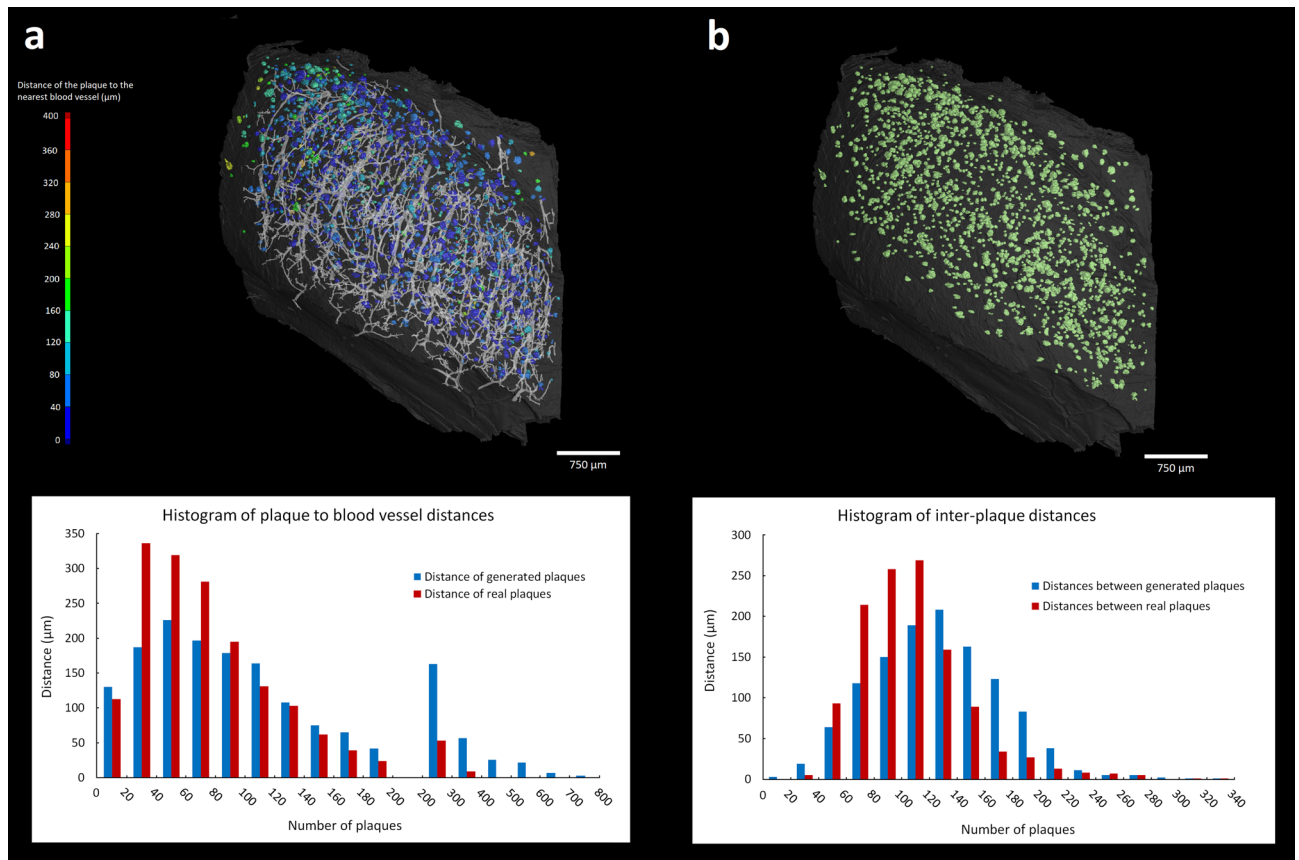


Figure 5. 3D quantitative analysis of the plaques distribution in hippocampus: Horizontal view of the hippocampus with color coded distances of individual plaques to the nearest blood vessel (**a**) and the corresponding histogram showing the distances to the nearest blood vessel of randomly generated (in blue) and the real (in red) plaques, respectively. Horizontal view of the hippocampus depicting the distribution of the plaques inside the hippocampus (**b**) and the corresponding histogram showing the distribution of randomly generated plaques (in blue), and the distribution of real plaques (in red)^{41,42}.

This fact led us to the idea of developing an imaging method for detection of amyloid plaques in the rat brain applicable to easily accessible industrial X-ray lab-based devices. Absorption based contrast enhanced X-ray micro CT imaging as an alternative to the synchrotron based phase contrast imaging techniques retrieves not only a 3D distribution of amyloid plaques with decent voxel resolution, but also provides valuable data for quantitative analysis of the amyloid plaques (total number, volume, shape).

The immunodetection of amyloid plaques performed on histological slices is the golden standard of identification of plaques in the brain tissue. In this paper, we used this method to validate our findings. In order to precisely correlate the micro CT data with the immunodetection of the plaques, we used the brain which had been previously scanned on micro CT. Then, we performed a classical histological sectioning and carried out the immunodetection of the plaques. The comparison of data from the same brain analyzed by both techniques showed a good agreement between immunodetection and micro CT imaging. Even though the immunodetection is indisputably more sensitive in detection of smaller plaques, it lacks a convenient approach to the 3D analysis across large brain volumes. This comparison thus highlights the advantages of contrast enhanced micro CT imaging. The immunostaining based affirmation of plaque identity detected by micro CT shows that the absorption-based contrast enhanced micro CT imaging is robust in detection of amyloid plaques. While its applicability as described in this report is not suitable for *in vivo* experiments for the staining protocol toxicity or because of the high irradiation dose, we believe the CT brain imaging approach in the context of Alzheimer's disease research has a considerable potential for further development.

Materials and methods

Animals. Brains from three 18 months old female rats (two transgenic TgF-344 AD animals and one wild type control) obtained from the local breeding colony at Faculty of Medicine in Pilsen, Charles University, were used to collect the data. All protocols followed in this study were approved by the Ethical Committee of the Ministry of Education, Youth and Sports of the Czech Republic (approval no. MSMT-12048/2019-14) according to the Guide for the Care and Use of Laboratory Animals (Protection of Animals from Cruelty Law Act No. 246/92, Czech Republic).

Sample	Rat brain F60 +	Rat brain F61-	Rat brain F87 +	Hippocampus F87 +
Voltage [kV]	60	60	60	60
Current [μ A]	200	200	200	200
Timing [ms]	600	600	600	700
Source spot size [μ m]	5	5	5	5
Sample/source distance [mm]	40.8	40.8	40.8	11.9
Sample/detector distance [mm]	864.9	864.9	864.9	785.4
Images	2200	2200	2200	2400
Time [min.]	80	80	80	100
Voxel size [μ m ³]	9	9	9	3

Table 1. Micro CT scan settings.

Micro CT staining. At the beginning of the experiments the rats were overdosed with pentobarbital and intracardially perfused with saline, followed by 4% PFA. Then the brains were manually extracted and post-fixed in 4% PFA for another 3 h. Afterwards, the samples were dehydrated in ethanol solutions of different concentrations which increased: 30%, 50%, 70%, 80% and 90%. The process lasted 12 h for each concentration. After the dehydration, samples were submerged in a staining solution consisting of 1% iodine in 90% methanol for 72 h, where the staining solution was refreshed after the first 24 h. Then the samples were washed in 50% ethanol and embedded in 1% agarose gel. In one of the transgenic animals, after the whole brain scan, the dorsal hippocampus was dissected and embedded in 1% agarose gel for another scan.

Micro CT measurement. Before scanning, all samples were embedded in 1% agarose gel in 15 ml Falcon tubes in order to prevent movement during the imaging procedure. The micro CT scanning was performed using a laboratory system GE Phoenix v|tome|x L 240 (GE Sensing & Inspection Technologies GmbH, Germany), equipped with a 180 kV/15 W maximum power nanofocus X-ray tube and a high contrast flat panel detector dynamic 41|100 (number of pixels: 4048 \times 4048 px, pixel size 100 μ m). The measurements were carried out in an air-conditioned cabinet (21 °C). The parameters for each scan are indicated in the Table 1. The tomographic reconstruction was realized by software GE phoenix datos|x 2.0 (GE Sensing & Inspection Technologies GmbH).

Micro CT data processing. All 3D visualizations and measurements were performed in VG Studio MAX 3.4 software (Volume Graphics GmbH)⁴¹. The segmentation of plaques in the hippocampus sample was carried out using Avizo 9.5 software (Thermo Fisher Scientific)⁴². In the first step we isolated the hippocampus from the background by creating the corresponding region of interest (ROI). Blood vessels were segmented by global thresholding based on the grey level (vessels appeared as the darkest part since they did not contain any iodine), continuity, and their resulting prolonged and branched 3D shape. The amyloid plaques were segmented manually in Avizo 9.5 software by selecting the plaque areas across the sections under the following criteria: the area of the plaque should be distinguishably darker than the surrounding tissue and its volume should extend across at least 3 following sections. The boundaries of smaller plaques were selected section by section, in bigger plaques (some were spread over more than 30 sections) we interpolated between every other slice while any inconsistencies were additionally manually corrected.

For the analysis of A β distribution we generated datasets of plaques coordinates (Matlab R2020a). First, the coordinates of plaques centroids were extracted from the segmented 3D binary data to represent the experimental dataset. Then the random dataset of “plaque’s” centroids was created within the volume of the sample leaving out its vascular system. The resulting coordinates then represented centroids of randomly distributed A β plaques with total amount corresponding to the experimental dataset. The analysis of A β plaque position in relation to the blood vessels was carried out in VG studio. Both real plaques centroid positions and simulated plaques centroid positions were imported in form of binary image data. The distance of the centroid to the nearest blood vessel was measured via pore analysis module. Subsequently, the intra-plaques distances were analyzed separately in simulated plaque centroids and real plaque centroids. The nearest neighboring centroid of each centroid was found using 3D Euclidean distances analysis in Matlab R2020a. Repeating combinations of the nearest neighbors were excluded from the subsequent analysis.

Statistical analysis. The non-parametric Mann–Whitney test was applied to compare the detected and random datasets (https://www.statskingdom.com/170median_mann_whitney.html).

Histology and immunohistochemical labeling. After the CT measurements, the sample tissue was embedded in a paraffin block and cut into 10 μ thick sections using an Automated Microtome (Leica RM2255). The slices were then deparaffinized and rehydrated. Phosphate buffer saline (PBS, 0.1 M) was applied for washing. To block the non-specific binding, normal goat serum (ab138478, Abcam) was used. The sections were then incubated overnight at 4 °C with the primary antibody (ab2539, Abcam, 1:200, 1 mg/ml) against amyloid beta. Next day, the sections were washed with 1X PBS (0.01 M) thrice (5', 10' and 15') to remove the unbound anti-

body remnants. Staining was visualized with an Alexa Fluor 647-conjugated goat anti-rabbit antibody (Jackson ImmunoResearch Laboratories) applied in 1:500 dilution at 37 °C for 4 h. All the sections were then counterstained with DAPI to label the nuclei and glass mounted using fluoroshield mounting medium (Merck). The Amyloid beta plaques were visualized using fluorescent microscopy (Olympus), and quantified in open source Fiji image analysis software⁴³.

Data availability

Datasets used in this publication are available on request at corresponding authors.

Received: 3 December 2020; Accepted: 18 February 2021

Published online: 16 March 2021

References

- Hardy, J. & Selkoe, D. J. The amyloid hypothesis of Alzheimer's disease: Progress and problems on the road to therapeutics. *Science* **297**(5580), 353–356 (2002).
- Kametani, F. & Hasegawa, M. Reconsideration of amyloid hypothesis and tau hypothesis in Alzheimer's disease. *Front. Neurosci.* **12**, 25 (2018).
- Zempel, H. & Mandelkow, E. Lost after translation: Missorting of Tau protein and consequences for Alzheimer disease. *Trends Neurosci.* **37**(12), 721–732 (2014).
- Hardy, J. A. & Higgins, G. A. Alzheimer's disease: The amyloid cascade hypothesis. *Science* **256**(5054), 184–186 (1992).
- Cao, J., Hou, J., Ping, J. & Cai, D. Advances in developing novel therapeutic strategies for Alzheimer's disease. *Mol. Neurodegen.* **13**(1), 64 (2018).
- Astolfo, A., Lathuiliere, A., Laversenne, V., Schneider, B. & Stampanoni, M. Amyloid- β plaque deposition measured using propagation-based X-ray phase contrast CT imaging. *J. Synchr. Radiat.* **23**(3), 813–819 (2016).
- Pinzer, B. R. *et al.* Imaging brain amyloid deposition using grating-based differential phase contrast tomography. *Neuroimage.* **61**(4), 1336–1346 (2012).
- Connor, D. M. *et al.* Computed tomography of amyloid plaques in a mouse model of Alzheimer's disease using diffraction enhanced imaging. *Neuroimage.* **46**(4), 908–914 (2009).
- Massimi, L. *et al.* Exploring Alzheimer's disease mouse brain through X-ray phase contrast tomography: From the cell to the organ. *NeuroImage.* **184**, 490–495 (2019).
- Noda-Saita, K. *et al.* Quantitative analysis of amyloid plaques in a mouse model of Alzheimer's disease by phase-contrast X-ray computed tomography. *Neuroscience* **138**(4), 1205–1213 (2006).
- Massimi, L. *et al.* Assessment of plaque morphology in Alzheimer's mouse cerebellum using three-dimensional X-ray phase-based virtual histology. *Sci. Rep.* **10**(1), 1–10 (2020).
- Metscher, B. D. MicroCT for developmental biology: A versatile tool for high-contrast 3D imaging at histological resolutions. *Dev. Dyn.* **238**(3), 632–640 (2009).
- Metscher, B. D. MicroCT for comparative morphology: Simple staining methods allow high-contrast 3D imaging of diverse non-mineralized animal tissues. *BMC Physiol.* **9**(1), 11 (2009).
- Li, L. *et al.* Superficial cells are self-renewing chondrocyte progenitors, which form the articular cartilage in juvenile mice. *FASEB J.* **31**(3), 1067–1084 (2017).
- Kaucka, M. *et al.* Oriented clonal cell dynamics enables accurate growth and shaping of vertebrate cartilage. *Elife.* **6**, e25902 (2017).
- Kaucka, M. *et al.* Analysis of neural crest-derived clones reveals novel aspects of facial development. *Sci. Adv.* **2**(8), e1600060 (2016).
- Kaucka, M. *et al.* Signals from the brain and olfactory epithelium control shaping of the mammalian nasal capsule cartilage. *Elife.* **7**, e34465 (2018).
- Celá, P. *et al.* Ciliopathy protein Tmem107 plays multiple roles in craniofacial development. *J. Dent. Res.* **97**(1), 108–117 (2018).
- HAMPL, M. *et al.* Polarized sonic hedgehog protein localization and a shift in the expression of region-specific molecules is associated with the secondary palate development in the veiled chameleon. *Front. Cell Dev. Biol.* **8**, 572 (2020).
- Landova Sulcova, M. *et al.* Developmental mechanisms driving complex tooth shape in reptiles. *Dev. Dyn.* **249**(4), 441–464 (2020).
- Kohoutek, J. *et al.* Mouse model of congenital heart defects, dysmorphic facial features and intellectual developmental disorders as a result of nonfunctional CDK13. *Front. Cell Dev. Biol.* **7**, 155 (2019).
- Heude, E. *et al.* Unique morphogenetic signatures define mammalian neck muscles and associated connective tissues. *Elife.* **7**, e40179 (2018).
- Vymazalová, K., Vargová, L., Zikmund, T. & Kaiser, J. The possibilities of studying human embryos and fetuses using micro-CT: A technical note. *Anat. Sci. Int.* **92**(2), 299–303 (2017).
- Tesařová, M. *et al.* An interactive and intuitive visualisation method for X-ray computed tomography data of biological samples in 3D Portable Document Format. *Sci. Rep.* **9**(1), 1–8 (2019).
- Stolz, E. *et al.* Angioarchitectural changes in subacute cerebral venous thrombosis A synchrotron-based micro- and nano-CT study. *Neuroimage* **54**(3), 1881–1886 (2011).
- Heinzer, S. *et al.* Hierarchical microimaging for multiscale analysis of large vascular networks. *Neuroimage.* **32**(2), 626–636 (2006).
- Ghanavati, S., Lisa, X. Y., Lerch, J. P. & Sled, J. G. A perfusion procedure for imaging of the mouse cerebral vasculature by X-ray micro-CT. *J. Neurosci. Methods* **221**, 70–77 (2014).
- Langheinrich, A. C. *et al.* Evaluation of the middle cerebral artery occlusion techniques in the rat by in-vitro 3-dimensional micro- and nano computed tomography. *BMC Neurol.* **10**(1), 36 (2010).
- Chugh, B. P. *et al.* Measurement of cerebral blood volume in mouse brain regions using micro-computed tomography. *Neuroimage.* **47**(4), 1312–1318 (2009).
- Xie, B., Miao, P., Sun, Y., Wang, Y. & Yang, G. Y. Micro-computed tomography for hemorrhage disruption of mouse brain vasculature. *Transl. Stroke Res.* **3**(1), 174–179 (2012).
- Dorr, A., Sled, J. G. & Kabani, N. Three-dimensional cerebral vasculature of the CBA mouse brain: A magnetic resonance imaging and micro computed tomography study. *Neuroimage.* **35**(4), 1409–1423 (2007).
- Hayasaka, N. *et al.* In vivo diagnostic imaging using micro-CT: sequential and comparative evaluation of rodent models for hepatic/brain ischemia and stroke. *PLoS ONE* **7**(2), e32342 (2012).
- Dobrivojević, M., Boháček, I., Erjavec, I., Gorup, D. & Gajović, S. Computed microtomography visualization and quantification of mouse ischemic brain lesion by nonionic radio contrast agents. *Croatian Med. J.* **54**(1), 3–11 (2013).
- Anderson, R. & Maga, A. M. A novel procedure for rapid imaging of adult mouse brains with microCT using iodine-based contrast. *PLoS ONE* **10**(11), e0142974 (2015).
- de Crespigny, A. *et al.* 3D micro-CT imaging of the postmortem brain. *J. Neurosci. Methods* **171**(2), 207–213 (2008).

36. Saito, S. & Murase, K. Ex vivo imaging of mouse brain using micro-CT with non-ionic iodinated contrast agent: A comparison with myelin staining. *Br. J. Radiol.* **85**(1019), e973–e978 (2012).
37. Bautista, N. S. *et al.* Ex vivo micro-CT imaging of murine brain models using non-ionic iodinated contrast. *Am. Inst. Phys. Conf. Proc.* **1**(1626), 197–200 (2014).
38. Hainfeld, J. F. *et al.* Gold nanoparticle imaging and radiotherapy of brain tumors in mice. *Nanomedicine.* **8**(10), 1601–1609 (2013).
39. Kastriti, M. E. *et al.* Ablation of CNTN2+ pyramidal neurons during development results in defects in neocortical size and axonal tract formation. *Front. Cell. Neurosci.* **13**, 454 (2019).
40. Zikmund, T. *et al.* High-contrast differentiation resolution 3D imaging of rodent brain by X-ray computed microtomography. *J. Instrum.* **13**(02), C02039 (2018).
41. Volume Graphics. <https://www.volumegraphics.com> 2020 (accessed 30 October 2020).
42. Thermo Fisher Scientific. <https://www.fei.com/software/avizo3d/>.
43. Fiji. <https://imagej.net/Fiji>.

Acknowledgements

This research was carried out under the project CEITEC 2020 (LQ1601) with financial support from the Ministry of Education, Youth and Sports of the Czech Republic under the National Sustainability Programme II and CzechNanoLab Research Infrastructure supported by MEYS CR (LM2018110), projects PRIMUS 27051, Progres Q39, FIND No. CZ.02.1.01/0.0/0.0/16_019/0000787 provided by the Ministry of Education, Youth and Sports of the Czech Republic, and GAUK 12539. We are grateful to Marketa Slajerova for help with processing the samples.

Author contributions

M.K., T.Z., J.K. and K.J. designed the study, M.K. performed the CT scanning and staining, M.K. and J.S. analyzed the CT data, A.K. and S.L.P.P. processed and analyzed the histology, M.K. and K.J. wrote the manuscript.

Competing interests

The authors declare no competing interests.

Additional information

Supplementary Information The online version contains supplementary material available at <https://doi.org/10.1038/s41598-021-84579-x>.

Correspondence and requests for materials should be addressed to M.K. or K.J.

Reprints and permissions information is available at www.nature.com/reprints.

Publisher's note Springer Nature remains neutral with regard to jurisdictional claims in published maps and institutional affiliations.



Open Access This article is licensed under a Creative Commons Attribution 4.0 International License, which permits use, sharing, adaptation, distribution and reproduction in any medium or format, as long as you give appropriate credit to the original author(s) and the source, provide a link to the Creative Commons licence, and indicate if changes were made. The images or other third party material in this article are included in the article's Creative Commons licence, unless indicated otherwise in a credit line to the material. If material is not included in the article's Creative Commons licence and your intended use is not permitted by statutory regulation or exceeds the permitted use, you will need to obtain permission directly from the copyright holder. To view a copy of this licence, visit <http://creativecommons.org/licenses/by/4.0/>.

© The Author(s) 2021

X-ray microtomography imaging of craniofacial hard tissues in selected reptile species with different types of dentition

Michaela Kavková ¹, Marie Šulcová ^{2,3}, Tomáš Zikmund ¹, Martin Pyszko ⁴, Jozef Kaiser ¹ and Marcela Buchtová ^{1,2,3,*}

¹Central European Institute of Technology, Brno University of Technology, 616 69 Brno, Czech Republic

²Department of Experimental Biology, Faculty of Science, Masaryk University, 612 42 Brno, Czech Republic

³Laboratory of Molecular Morphogenesis, Institute of Animal Physiology and Genetics, v.v.i., Czech Academy of Sciences, 602 00 Brno, Czech Republic

⁴Department of Anatomy, Histology and Embryology, Faculty of Veterinary Medicine, University of Veterinary Sciences Brno, 625 00 Brno, Czech Republic

*Correspondence address. Marcela Buchtova, Laboratory of Molecular Morphogenesis, Institute of Animal Physiology and Genetics, v.v.i., Czech Academy of Sciences, Veveří 97, 60200 Brno, Czech Republic. E-mail: buchtova@iach.cz

Abstract

Background: Reptiles exhibit a large heterogeneity in teeth morphology. The main variability comprises the different tooth shape, the type of tooth attachment to the underlying bone, or the ability to replace the teeth.

Findings: Here, we provide full datasets of microtomography scans and 3D models of reptilian dentitions and skulls. We selected representative species for each of 9 reptilian families on the basis of their characteristic dental features. Because there are ≥ 4 different types of tooth-bone attachments, ranging from the mammalian-like thecodont attachment found in crocodylians to the simple acrodont implantation observed in some lizards, we aimed to evaluate species with different types of tooth-bone attachments. Moreover, another interesting feature varying in reptilian species is the complexity of tooth shape or the number of tooth generations, which can be associated with the type of tooth attachment to the jawbone. Therefore, selected model species also include animals with distinct tooth morphology along the jaw or different number of tooth generations. The development of tooth attachment and relationship of the tooth to the jaw can be further analysed in detail on a large collection of pre-hatching stages of chameleon. Next, we introduce different possibilities for how these datasets can be further used to study tooth-bone relationships or tooth morphology in 3D space. Moreover, these datasets can be valuable for additional morphological and morphometric analyses of reptilian skulls or their individually segmented skeletal elements.

Conclusions: Our collection of microcomputed tomography scans can bring new insight into dental or skeletal research. The broad selection of reptilian species, together with their unique dental features and high quality of these scans including complete series of developmental stages of our model species and provide large opportunities for their reuse. Scans can be further used for virtual reality, 3D printing, or in education.

Keywords: micro-CT, 3D imaging, reptiles, tooth-bone attachment, skull, craniofacial bones, tooth replacement

Background

Teeth are composed from the hardest tissues in the body of all living and extinct animals. This tissue is resistant against external intervention; therefore, its structure is sometimes the only entity that persists long enough to become useful for paleontologists to describe each fossil and place samples in the context of other extinct animals. This organ exhibits an extensive heterogeneity reflecting animal lifestyle. In herbivores, the structure of the skull including teeth is adapted to improve the grinding of plant food. In contrast, the shape of teeth in carnivorous predators is designed for the capture and processing of the prey's flesh [1].

Large heterogeneity in tooth shapes and, more importantly, the way the dentition is placed in the jaw was found especially in reptiles [2, 3]. There are ≥ 4 distinct types of tooth-bone attachments, ranging from mammalian-like thecodont implantation, observed in crocodiles, to the simpler acrodont type found in some lizards [4]. Tooth-bone implantation can also exhibit region-specific character across the jaw. In bearded dragons (*Pogona vitticeps*), 2 types (acrodont and pleurodont) of tooth-bone attachments are present within the jaw, with the pleurodont type located in the rostral area

and the acrodont in the caudal part of the jaw [5]. Specialized complex tissue serving as an adhesive component connecting the jawbone and teeth in monitor lizards is called “plicidentin” [6].

The way the tooth is placed in the jawbone also reflects the number of tooth generations that can be initiated in certain species. Tooth replacement represents another interesting feature varying in reptiles. In chameleons, which are strictly monophodont with only 1 tooth generation, teeth are firmly attached to the jawbone, and if the tooth is lost owing to injury or during a fight, the jawbone is extensively damaged [7]. Also, the whole process of odontogenesis across individual developmental stages is peculiar, especially because of asymmetrically developing tooth germ giving rise to symmetrically ankylosed teeth [8]. However, most reptiles (e.g., geckos, *Anolis*, skinks, *Ameiva*, iguanas, and snakes) possess an unlimited and lifelong supply of new tooth generations. The type of tooth attachment is less robust in these species to ensure the constant loss of functional teeth and growth of the replacement teeth [2, 9–12].

Here, we provide full datasets of our microcomputed tomography (micro-CT) scans from various reptilian species, which can be

Received: November 1, 2021. Revised: December 19, 2021. Accepted: January 28, 2022

© The Author(s) 2022. Published by Oxford University Press GigaScience. This is an Open Access article distributed under the terms of the Creative Commons Attribution License (<https://creativecommons.org/licenses/by/4.0/>), which permits unrestricted reuse, distribution, and reproduction in any medium, provided the original work is properly cited.

further used for comparative morphology of the different types of tooth-bone attachments in selected representatives encompassing key species with distinct dental features. The provided datasets are also suitable for the evaluation of tooth shape differences between species or across the jaws, dental replacement patterns, to determine the facial and cranial bone structure in these species, or to analyse a large spectrum of morphometric parameters in 2 or 3 dimensions across reptiles. Moreover, this dataset is enlarged on a wide range of chameleon embryos of different ages to expand the amount of data available for further analysis such as the progression of reptilian odontogenesis with emphasis on changes in morphology of the teeth and skeletal elements with the possibility of evaluating how their relationship changes in time.

Sampling Strategy

For this study, we enlarged the list of scanned model species, which have been used for the purpose of our previously published studies focused on tooth development [7, 8, 13, 14], by species possessing further unique features among reptiles. As a source of information for the selection of key reptilian specimens, we used a detailed review discussing the different aspects of the tooth to bone relationship across amniotes [2]. Therefore, different animal species were selected according to their unique type of tooth shape and tooth-bone relationship on which we are preferentially focused in our studies; however, these datasets can be used for numerous additional analyses that we also briefly introduce here.

Anolis equestris is a representative of Iguanidae, which possess so-called iguana-type implantation. In this type of attachment, the labial side of the tooth is attached to the high labial wall of the jaw; therefore it remains shorter. However, the lingual side of the tooth extends deeper into the jaw to contact the jawbone, which makes this type of attachment strongly asymmetrical. In terms of the replacement potential, this species is pleurodont with an unlimited number of tooth generations [11]. The shape of their teeth varies along the jaw. Rostral teeth are simple and conical and do not exhibit any morphological uniqueness. However, in the caudal area of the jaw, the tip of the teeth is larger and split into 3 cusps: 1 central and 2 lateral cusps.

Another selected species, commonly demonstrated as a typical pleurodont and polyphyodont, is *Paroedura picta*, belonging to the family of Gekkonidae. Geckos possess uniformly shaped teeth along the whole jaw. On the top of each tooth, there is deep groove, which divides the tooth tip into 2 ridges along the whole tooth.

Pleurodont dentition with homogenous tooth shape is typical for *Scincus scincus* from the Scincidae family. Similar to the gecko, there is an apparent uniformity in their tooth shape along the jaw. Teeth are sharp with a visible deep dent at their tip. There are several small teeth located on the palate. The whole skull is covered by scales, forming an armour-like structure, which had to be segmented to visualize the bones of the skull and teeth before 3D processing of micro-CT images.

Timon lepidus (previously called *Lacerta lepida*, Lacertidae), a lizard species commonly found in southwestern Europe, is another representative of pleurodont species. In the rostral part of the jaw, teeth exhibit simple monocuspid morphology, while in the caudal jaw area, teeth display 3 cusps on their tip, similarly to *A. equestris*. There are also distinct palatal teeth attached to the pterygoid bone.

As a transitional species bearing both pleurodont and acrodont type of the dentition, we selected *Pogona vitticeps* (Agamidae).

Bearded dragons possess pleurodont teeth in the most rostral part of the jaw, which exhibit the ability of lifelong replacement. However, most of the teeth are acrodonly ankylosed to the underlying jawbone [5]. These two types of dentition are easily recognizable because the pleurodont teeth are monocuspid and sharply point to each other. In contrast, the acrodon dentition forms together with the jawbone compact structure, where caudal teeth are closely attached to each other on their lateral sides with complex shape consisting of 1 central and two lateral cusps.

Completely ankylosed teeth are found in *Chamaeleo calypttratus* (Chamaeleonidae). There is visible heterogeneity in tooth shape along the jaw, ranging from smaller teeth in the very rostral part of the jaw to tricuspid teeth in the caudal area, where teeth are also noticeably larger. A number of publications have described chameleon dentition in detail, with micro-CT used as one of the key methods [7, 8, 14]. In these studies, mostly the embryos were used to describe the process of odontogenesis. Therefore, so far, we know that chameleon teeth germs develop asymmetrically, closely recalling pleurodont implantation [8]. Also, the patterning of the tooth germ initiation is precisely coordinated, with the first calcified tooth appearing caudally followed by next teeth placed rostrally [15].

A unique type of tooth-jaw attachment was found in monitor lizards, where infoldings of plicidentin contribute to the junction between the tooth and the jaw [6]. To examine this so-called Varanus-type of implantation, we performed micro-CT scans of *Varanus beccarii* (Varanidae). The overall morphology of individual teeth in *Varanus* is rather simple and successional tooth generations grow in posterior-lingual direction to the functional teeth [11].

In *Salvator rufescens* (Teiidae), the heterogeneity of dentition includes both tooth shape and the type of tooth to bone attachment. In the rostral area, simple and sharp monocuspid teeth are located. More caudally, the simplicity of the tooth is replaced by teeth with bulbous shape, which helps with crunching the prey such as shellfish, small birds, or rodents. This type of implantation, often termed Dracaena-type, is unique because the teeth are seated in shallow sockets, which are deeper in the rostral area [11].

Bitis gabonica is a representative of poisonous snakes (Viperidae), with venomous teeth located in the rostral area of the upper jaw (**Model 1**). Their venomous teeth represent the longest fangs of venomous snakes, with a length of ~5 cm. Gaboon vipers also possess simple conical teeth arranged into two rows in the upper jaw (inner—palatal and outer—maxillary row) and one row (mandibular) in the lower jaw. Teeth, including fangs, are replaced several times through life (polyphyodont dentition), and they exhibit a typical pleurodont type of attachment [16, 17].

As an example of nonvenomous snakes, we selected *Python regius* (Pythonidae), which is a constrictor lacking typical venomous teeth. Simple shaped teeth with sharp monocuspid morphology are curved caudally deeper to the python jaw; similar to vipers, they are arranged into two rows in the upper jaw and one row in the lower jaw. Their polyphyodont dentition is associated with pleurodont type of tooth attachment along the entire jaw [10, 16, 17].

Besides the squamate species, we also examined a specimen of *Caiman crocodilus* (Alligatoridae). All Crocodylians are known to possess tooth implantation resembling those in mammals, called thecodont gomphosis. In this type of dentition, teeth are situated in deep bony alveolus with the presence of bundles of both mineralized and non-mineralized periodontal ligaments mediating the junction force between the tooth and jawbone [18].

Source of Samples

All analysed specimens originated from private breeders. Deceased animals were part of the collection of the Department of Anatomy, Histology and Embryology at the Faculty of Veterinary Medicine, University of Veterinary Sciences Brno (Brno, Czech Republic).

All embryonic stages of chameleon were obtained from a commercial breeder. Embryos were collected at 6 different developmental stages and fixed in 4% paraformaldehyde at least overnight. All manipulations followed the rules for working with live embryos as specified by the Central Commission for Animal Welfare of the Ministry of Agriculture of the Czech Republic). All analyses were performed in accordance with the guidelines, regulations, and experimental protocols approved by the institutional and licensing committee including rules overseen by the Laboratory Animal Science Committee of the Institute of Animal Physiology and Genetics, v.v.i. (Liběchov, Czech Republic). No experiments were performed on live embryos.

Micro-CT Scanning

Frozen reptile skulls were thawed in pure ethanol. To stabilize against motion during micro-CT scanning, all of the samples were placed in a plastic container selected to fit the sample and embedded in 1% agarose gel.

Eleven samples of various reptilian adult heads and 6 samples of chameleon embryo stages were selected for the aforementioned detailed micro-CT analysis of hard tissue morphology (Fig. 1, Table 1).

Several samples of chameleon embryos were also selected to showcase the development of the ankylotic teeth in pre-hatching stages (see list in Table 3). The micro-CT scanning was performed using laboratory system GE phoenix v|tome|x L 240 (GE Sensing & Inspection Technologies GmbH, Hürth, Germany), equipped with a 180 kV/15W maximum power nanofocus X-ray tube and high-contrast flat panel detector dynamic 41|100 (4,048 × 4,048 pixels, pixel size 100 μm). The measurements were carried out in an air-conditioned cabinet (21°C). Instrumental settings for each sample are displayed in Tables 1 and 4. The tomographic reconstruction was performed using the software GE phoenix datos|x 2.0 (GE Sensing & Inspection Technologies GmbH, Germany).

Data Quality Control and Limitations

Because all analysed samples of adult reptile skulls were preserved prior to scanning and then handled in the same way, the main variable in data quality was the different voxel size of each dataset, owing to differing sample size. The smallest sample was the skull of *S. scincus* at 21 mm with voxel size of 13 μm, and the largest skull was *S. rufescens* at 98 mm with voxel size of 48 μm.

The difference in voxel size was directly linked to the dimensions of the sample. Considering the field of view given by the detector used and the cone beam geometry of the X-ray source of GE L240, this fact engenders a rule of thumb: the smaller the sample is, the closer to the x-ray source in the cone beam it can be placed, which finally results in smaller voxel size (higher resolution). Even though the samples display variable voxel size, this does not necessarily have to limit the analysis of the data. Larger specimens demonstrate voxel size with lower resolution than the smaller samples; however the structures being analysed are larger in these animals and are therefore easily recognizable.

In the case of the chameleon embryo samples, the embryo dimensions were mostly the same and the difference in voxel size from the smallest embryo to the largest was only 1 μm.

Samples of all reptile skulls and chameleon embryos were scanned in intact form (90% ethanol was used to fix the tissues in the adult reptile skulls, and 4% paraformaldehyde was used to fix the embryonic samples). Based on the principle of micro-CT imaging of the samples in native form without any type of staining, only the dense mineralized structures such as teeth and bones (and in the case of *S. scincus* the scales) can be visualized. Therefore, a limitation of the present dataset is a lack of information about the soft-tissue appearance and morphology in adult tissues. Because our main aim was to examine reptile skulls and tooth to bone attachment, the staining agent would affect visualization of smaller bone borders, which would become poorly distinguishable from background after counterstaining.

Tooth Spacing Analyses by Polyline Tool

The polyline tool was used to create open “unrolled” images of the lower jaw (Fig. 2A). Each dataset was oriented on the basis of the main anatomical directions. In the coronal and horizontal direction, the sections were oriented to be symmetrically aligned. In the sagittal plane, where symmetry is not present, the sections were rotated to visualize as many teeth as was possible for the lower jaw. In the oriented dataset, points defining the polyline were placed on the selected tips of the teeth in the lower jaw (Fig. 2B). Finally, the unrolled images of the lower jaw were generated in a new plane defined by the polyline. The unrolled images can be used to evaluate replacement patterns (Fig. 2) or to display and determine changes in teeth spacing throughout the lower jaw as visualized in embryonic chameleon stages (Fig. 3).

The analysis of the tooth spacing in the unrolled data was slightly complicated by the fact that during the initial freezing of samples, some of them were not frozen in an optimal horizontal position, and after thawing, some structures such as the loose joint in the rostral part of the jaw in snakes were slightly bent, resulting in imperfectly oriented and unsymmetrical images. Even if in certain samples the symmetry of the unrolled images was not ideal, the required information about tooth spacing can be extracted from two separate images for each half of the jaw.

Micro-CT Data Analysis of Tooth-Bone Attachment

The morphology of the tooth-bone interface and their regional differences were evaluated from micro-CT scans in VGStudio MAX 3.3 software (Volume Graphics GmbH, Germany). To achieve the optimal transverse sections through the jaw, previously generated polyline was used. The transverse sections were produced in a plane perpendicular to that of the original horizontal section. The coronal sections were oriented on the basis of the curve of the polyline (Fig. 4).

Such projections could be further used for the description of different tooth-bone relationships with regard to the individual bone appearance and the nature of tissue mediating the interface. Moreover, because the section could be placed anywhere throughout the skull, such structures as palatal teeth appearance and their distribution, temporomandibular joint morphology, or the spatial relationship among individual craniofacial bones can be studied.

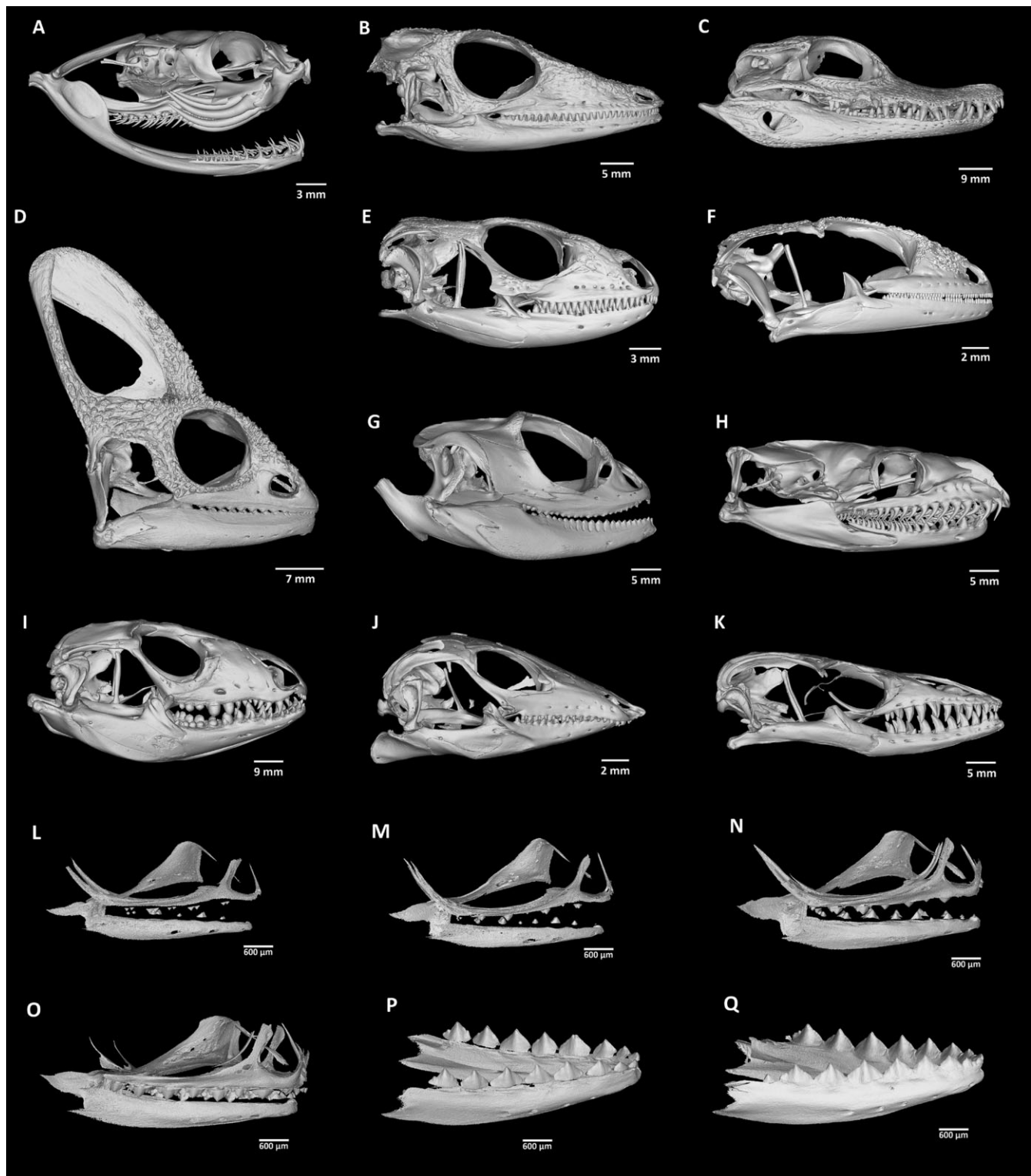


Figure 1: Skull morphology of analysed reptiles (lateral view of micro-CT images). (A) *Bitis gabonica*, (B) *Anolis equestris*, (C) *Caiman crocodilus*, (D) *Chamaeleo calytratus*, (E) *Timon lepidus*, (F) *Paroedura picta*, (G) *Pogona vitticeps*, (H) *Python regius*, (I) *Salvator rufescens*, (J) *Scincus scincus*, (K) *Varanus beccarii*, (L–Q) 6 pre-hatching stages of *Chamaeleo calytratus*.

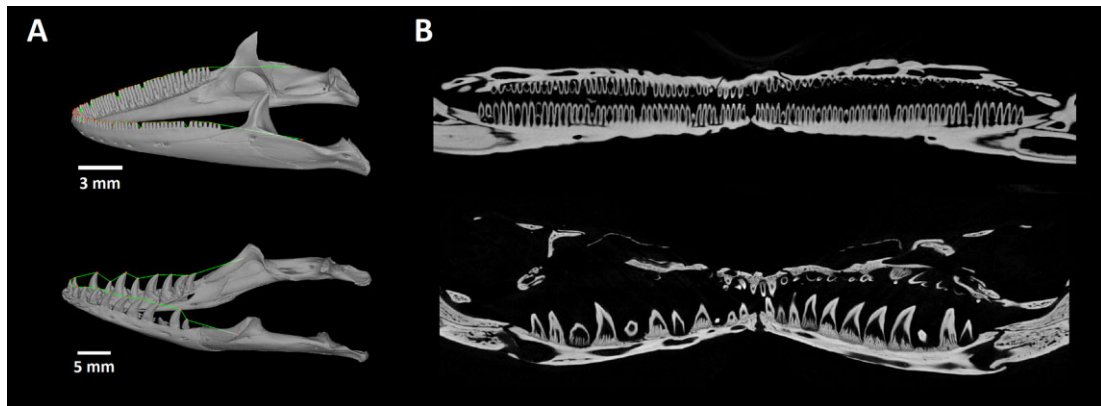
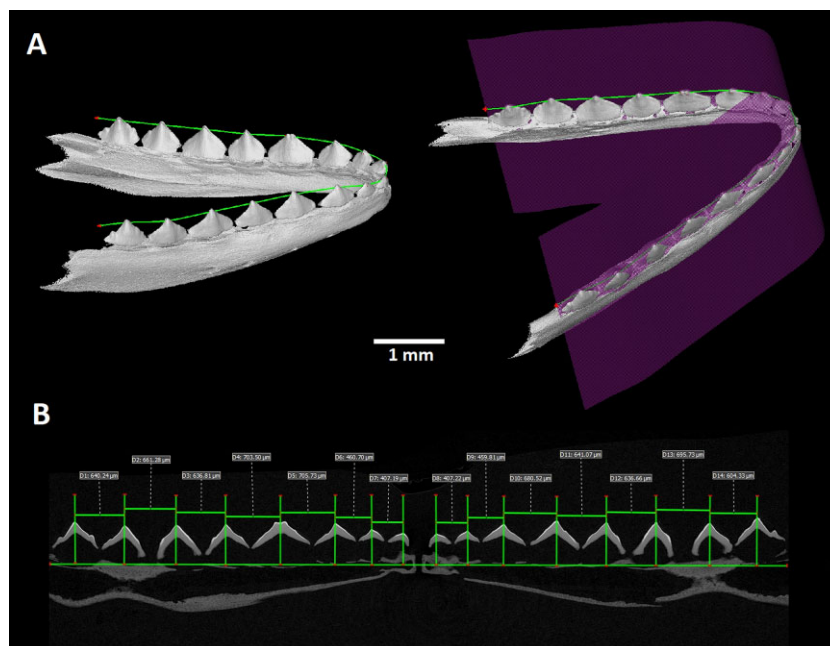
Skull Wall Thickness Analysis

Micro-CT scans can be used to evaluate hard-tissue density and thickness, which could serve as a source of valuable information for deciphering different aspects of skull anatomy, as well as their interspecies differences.

VG Studio software enables two methods of wall thickness analysis: a ray-based method and a sphere-based method. The ray-based method defines the wall thickness by searching the opposite surface by sending a measurement ray perpendicularly to the first surface. Calculated wall thickness is then defined by

Table 1: Scanning parameters for individual analysed animal samples

Sample	Voltage (kV)	Current (μ A)	Timing (ms)	Images	Filter (mm)	Time (min)	Resolution (μ m)
<i>Anolis equestris</i>	60	230	500	2,400	0.2 Al	100	24
<i>Bitis gabonica</i>	60	230	500	2,600	0.2 Al	105	19
<i>Caiman crocodilus</i>	60	230	500	2,000	0.2 Al	75	45
<i>Chamaeleo calypttratus</i>	60	230	500	2,600	0.2 Al	90	26
<i>Timon lepidus</i>	60	230	500	2,600	0.2 Al	105	18
<i>Paroedura picta</i>	60	200	750	2,500	0.2 Al	100	12.5
<i>Pogona vitticeps</i>	60	230	500	2,600	0.2 Al	110	25
<i>Python regius</i>	60	230	500	2,500	0.2 Al	105	24.5
<i>Salvator rufescens</i>	60	230	500	2,600	0.2 Al	105	48
<i>Scincus scincus</i>	60	230	500	2,100	0.2 Al	80	13
<i>Varanus beccarii</i>	60	230	500	2,600	0.2 Al	110	28

**Figure 2:** Visualization of unrolled lower jaw using polyline tool. Examples of *Paroedura picta* and *Varanus beccarii* skulls, the design of polyline, and unrolling of the lower jaw are displayed. In the 3D render image, the points defining the polyline are presented as red dots and the produced polyline is labelled in green.**Figure 3:** Visualization of tooth spacing while using unrolled data of chameleon embryonic jaw. The exact placement of the unrolled section through the lower jaw is marked by the purple plane shown in the 3D render. In the unrolled image the distances between individual teeth are measured.

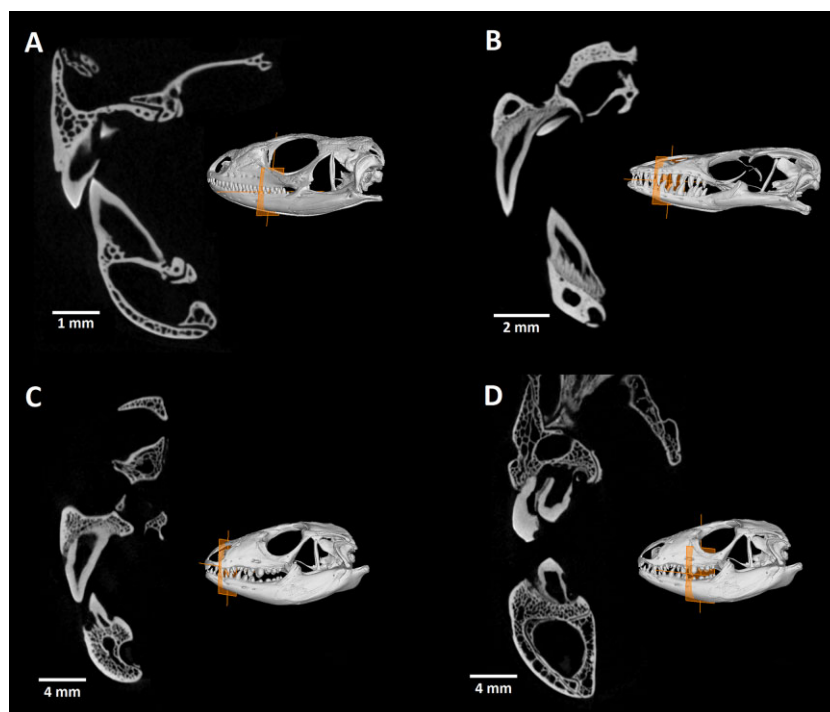


Figure 4: Tooth-bone attachment in different reptiles displayed on transverse sections through the jaw. Orange plane in the 3D render of each skull demonstrates the positioning of section through the jaw. (A) In *Timon lepidus*, the most common appearance of reptilian tooth-bone interface is presented with typical asymmetrical pleurodont teeth. (B) Transverse section of *Varanus beccarii* jaw clearly displays the tissue called plicidentin, which connects the dentin of tooth to bone pedicles. (C and D) *Salvator rufescens* possesses different types and depth of tooth implantation across the jawbone.

Table 2: Volumes of analysed skulls

Species	Volume (mm ³)		
	Skull	Maxilla	Mandible
<i>Anolis equestris</i>	870	584	286
<i>Bitis gabonica</i>	232	181	51
<i>Caiman crocodilus</i>	6,409	4,108	2,301
<i>Chamaeleo calypratus</i>	1,441	1,062	379
<i>Timon lepidus</i>	197	133	64
<i>Paroedura picta</i>	113	81	32
<i>Pogona vitticeps</i>	2,236	1,384	852
<i>Python regius</i>	1,817	1,308	509
<i>Salvator rufescens</i>	10,869	6,232	4,637
<i>Scincus scincus</i>	108	71	37
<i>Varanus beccarii</i>	1,130	757	373

the shortest distance between 2 crossed rays from opposite surfaces. The sphere-based method evaluates the wall thickness by fitting spheres inside the sample in 3D space. The thickness of the analysed structure is then defined by the diameter of the fitted sphere.

In the case of complex bone structure, the sphere-based measurement of wall thickness analysis is more accurate; therefore here we introduce data from this type of analysis on our selected species (Fig. 5, Supplementary Video S1). The colour scale of the wall thickness analysis displays the hard-tissue elements, which exhibit more gracile morphology, and we were able to distinguish them from reinforced elements. This information can facilitate the estimation of strains influencing specific parts of the skull leading to food-processing adaptations.

Analysis of Single Tooth Morphology

The high resolution of the obtained micro-CT data enables precise segmentation of specific structures of the analysed sample. As an example, the teeth of several species were segmented. The process of segmentation includes the global thresholding step to define the hard tissues from background. In the following step, the object of interest (in our case the venomous tooth of *B. gabonica* and replacement tooth of *C. crocodilus*) is roughly marked by 3D brush, and by intersecting the rough model of the tooth with the defined bones, the precise model of the tooth is created.

Samples of *B. gabonica* and *C. crocodilus* were selected to display some possibilities for more detailed tooth analysis (Model 1, Fig. 6 and 7). These species represent different types of tooth morphology (venomous teeth in *B. gabonica* and simple conical teeth in *C. crocodilus*), as well as tooth implantation (pleurodont implantation in *B. gabonica* and thecodont implantation in *C. crocodilus*).

In the case of *B. gabonica*, venom teeth from the left side of the skull were segmented and visualized (Fig. 6, Supplementary Video S2). The volume of teeth can be easily measured (the volume of the largest visualized tooth was 3.88 mm³ in this sample) (Fig. 6). Transparent visualization enables us to determine dental pulp morphology and analyse its shape in individual teeth or its communication to bone marrow as we discussed previously in chameleon [7].

Micro-CT analysis of *C. crocodilus* teeth enabled us to visualize the next generation of teeth hidden in the currently employed tooth (Fig. 7, Supplementary Video S3). The shape and volume of individual teeth can be evaluated along the jaw and compared across regions. Here, the smaller tooth volume was 1.22 mm³ and the volume of the largest tooth was 11.44 mm³.

Table 3: List of analysed chameleon embryo samples

Sample	Date		Embryo age (days)	Weight (g)	
	Clutch laying	Embryo collection		Egg	Embryo
Stage 1 (CHM379)	12.01.2019	20.05.2019	128	1.23	0.25
Stage 2 (CHM313)	08.05.2018	31.08.2018	115	1.31	0.37
Stage 3 (CHM389)	12.01.2019	27.05.2019	135	1.77	0.4
Stage 4 (CHM397)	12.01.2019	06.06.2019	145	1.47	0.44
Stage 5 (CHM327)	21.06.2018	14.11.2018	146	1.81	0.65
Stage 6 (CHM351)	21.06.2018	10.12.2018	173	1.38	0.82

Table 4: Scanning parameters for individual analysed pre-hatching embryos

Sample	Voltage (kV)	Current (μ A)	Timing (ms)	Images	Filter (mm)	Time (min)	Resolution (μ m)
Stage 1 (CHM379)	60	200	600	2,500	0.2 Al	105	2.5
Stage 2 (CHM313)	60	200	600	2,400	0.2 Al	105	3.5
Stage 3 (CHM389)	60	200	600	2,400	0.2 Al	105	3
Stage 4 (CHM397)	60	200	600	2,400	0.2 Al	105	3
Stage 5 (CHM327)	60	200	600	2,200	0.2 Al	85	3
Stage 6 (CHM351)	60	200	600	2,300	0.2 Al	85	3.5

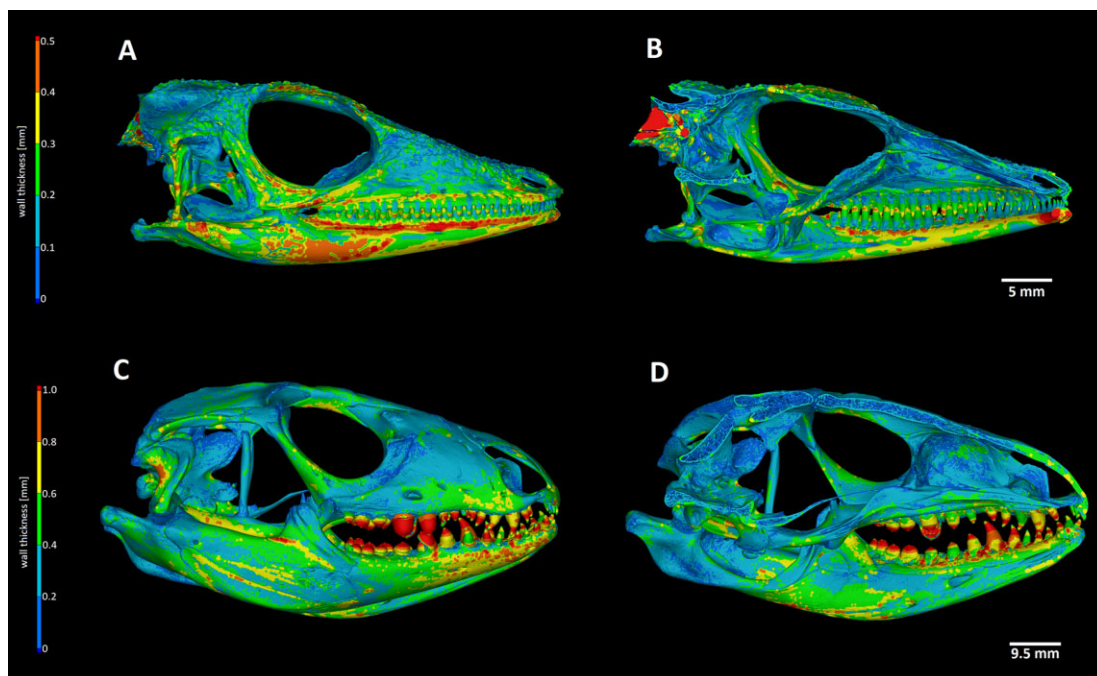


Figure 5: Wall thickness analysis of reptilian teeth and adjacent jaws. (A) *Anolis equestris*: The thickest area on the anolis skull is localized along the upper part of the lower jaw, suggesting its importance as a support during food processing. (B) Sagittal section through the midline of the skull in *A. equestris*. (C) *Salvator rufescens*: In contrast to anolis, wall thickness analysis displayed the greatest tissue density in bulbous caudal teeth, which need to be strong enough to process hard materials such as shells. (D) Sagittal section through the midline of the skull of *S. rufescens*.

This type of analysis offers great potential for investigating a number of aspects such as precise tooth shape and morphology description, dental pulp filling and/or venomous canal formation, replacement pattern in polyphyodont species, and visualization of individual tooth generation. All of the aforementioned analyses can be applied to any craniofacial structure of interest. The only condition is previous careful segmentation of the analysed structure before undertaking further analyses.

Palatal Tooth Analyses

The presence of palatal teeth in reptiles is diverse (Fig. 8). Some species do not bare teeth in the palatal area (chameleons), while in other species, they play an important role in food transport through the oral cavity (venomous snakes) [19]. Palatal teeth can also serve as a tool for processing of plant food or cracking hard-shell prey [20]. The overall morphology of palatal teeth is rather simple in comparison with that of marginal teeth [19]. The pres-

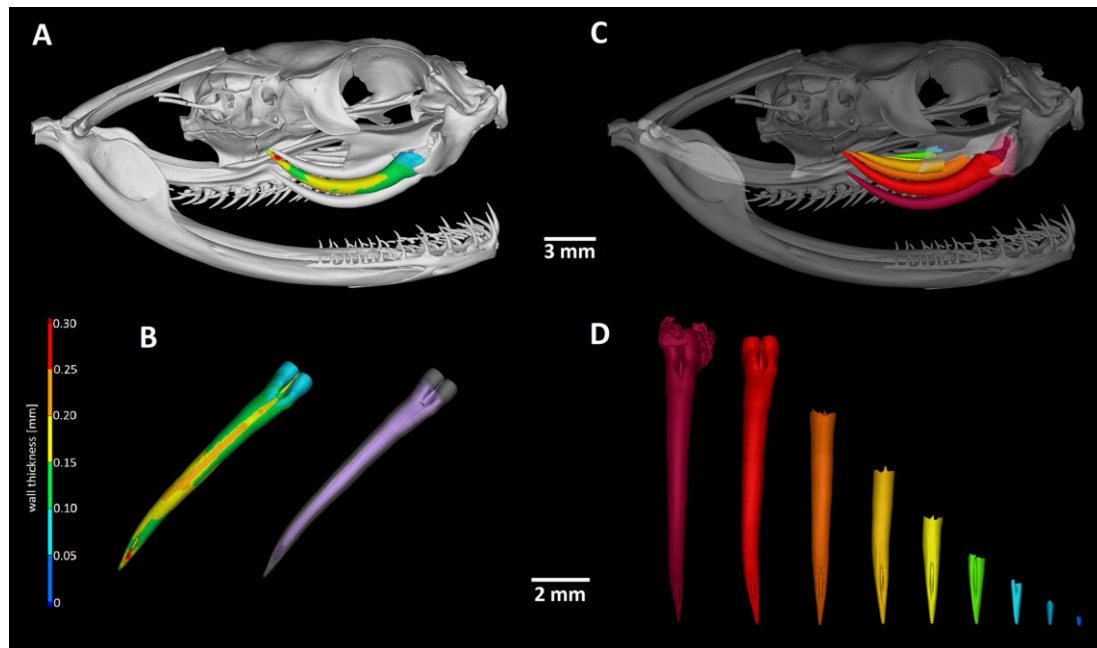


Figure 6: Segmentation and analyses of individual teeth in *Bitis gabonica*. (A) The second generation of the venomous tooth on the left side of the upper jaw was selected for wall thickness analysis. (B) Detail view on the second largest segmented tooth with applied wall thickness analysis, where red colour labels the thickest area of the fang and blue the thinnest areas. The same tooth was made partially transparent to display the inner structure of the tooth. (C) All of the venomous teeth on the left side of the upper jaw were segmented to uncover replacement tooth generations. (D) Detail view on all generations of fangs visualized in different colour. Note differences in the size and position of distal openings among individual generations.

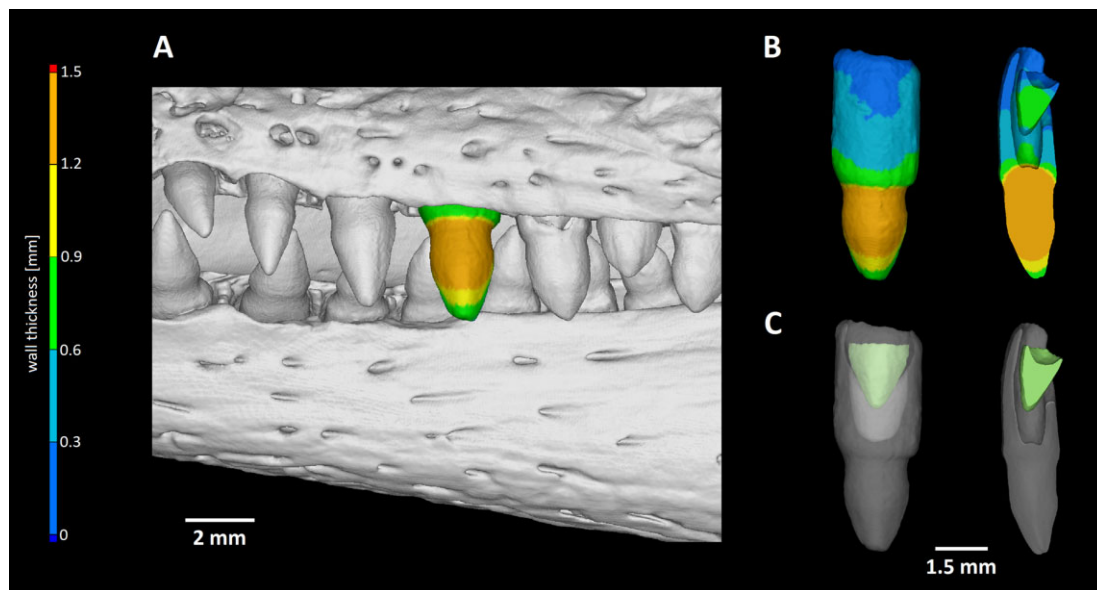


Figure 7: Visualization of replacement teeth in *Caiman crocodilus*. (A) Localization of individual teeth in the jaw with one segmented tooth. For precise morphology description, wall thickness analysis was applied. Orange colour labels the thickest areas of the tooth. (B) Segmented tooth is visualized without surrounding jawbone by wall thickness analyses. Horizontal section through the analysed tooth revealed new generation of teeth located inside of functional tooth. (C) Replacement tooth is labelled in green and functional tooth is translucent to visualize the position of next generation formation.

ence or absence of structures such as palatal teeth could also predicate evolutionary similarity across reptiles. Therefore, the present dataset could broaden this under-evaluated topic and offer valuable information for further study.

Segmentation of Selected Craniofacial Bones

Our dataset also provides great potential in the possibility to evaluate not only dentition morphology or individual teeth but also

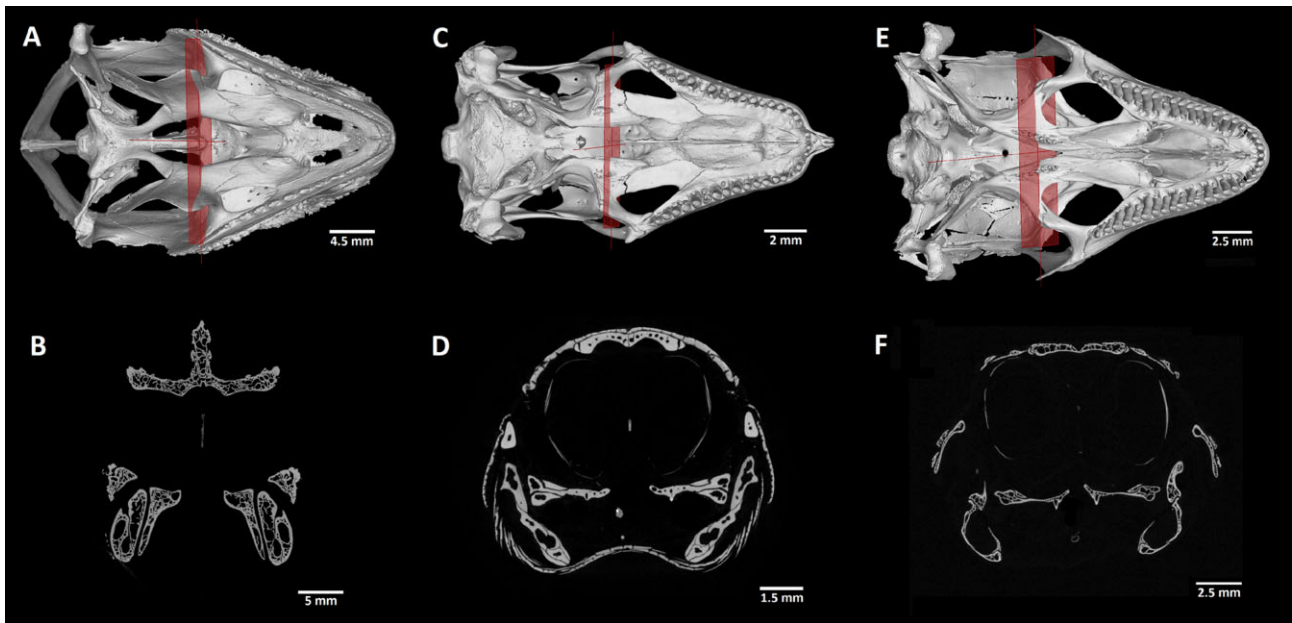


Figure 8: Palatal view on the upper jaw and transverse sections through the palatal teeth. (A) *Chamaeleo calyptrotus*: palatal view of 3D render image. (B) *Chamaeleo calyptrotus*: transversae section through the skull defined by the red plane indicated in 3D render displays the absence of palatal teeth. (C) *Scincus scincus*: palatal view of 3D render image uncovers two pairs of palatal teeth located on the pterygoid bone. (D) *S. scincus*: transverse section through the skull defined by the red plane indicated in 3D render visualizes the palatal teeth; yellow arrow indicates the location of teeth. (E) *Timon lepidus*: palatal view of 3D render image displays long row of palatal teeth. (F) *Timon lepidus*: transverse section through the skull defined by the red plane indicated in 3D render demonstrates the palatal teeth.

other hard craniofacial tissues. Thus, the dataset represents a robust system that could be applied for examination of any scanned skeletal structure. Precise segmentation is crucial because once the structure in question is visibly discriminated, further evaluation of its morphology and/or the interspecies differences is much easier and more accurate. However, this tool also provides the flexibility of describing each skeletal structure in detail separately or in context with individual surrounding elements. Besides the study of interspecies differences, segmented structures could be used for study of intersex variability in skull morphology or dynamics of bone development/progress.

Here, VG Studio Max software was used to segment the craniofacial bones (Figs. 9 and 10, Supplementary Video S4). The first module used was “surface determination,” which was applied to distinguish the bones from the background. The region of interest (ROI) of all bones was determined. In the following step, the tool “3D brush” was used to mark the approximate ROI of selected bones contributing to the palate. The final step was then generation of the ROI containing only the selected bone by intersecting the ROI of all bones with the marked ROI of the bone.

Volume Analyses of Skulls and Skeletal Elements

To make our analysis of segmented skull bones more detailed and therefore highly applicable, a volume analysis was subsequently applied. Volumes of whole skull or bones of interest can be analysed from 3D data (see examples in Table 2). Acquired data could be used for assessing interspecies differences in bone volumes, which could be then used for deciphering of evolutionary questions and other related topics.

Further Biological Potential

Indisputable biological potential of the present dataset lies in the number of different species that were scanned and the quality of the scans, as well as large possibilities for subsequent analysis on the acquired data. Therefore, this dataset can be used for further studies concerning comparative ecology and evolutionary biology or morphological/anatomical topics. Here, we introduce different possibilities of data reuse potential with the main focus on craniofacial structures.

The acquired data could be helpful in the study of different types of tooth-bone attachment and implantations, which is, according to recent publications, a broadly studied topic [8, 10, 11, 21–24] that varies across species. Another interesting feature concerning teeth is the analysis of tooth spacing, which we addressed using a specific tool in VG studio Max that allows the jaw to be “unrolled” to display all the teeth at once. Micro-CT analysis also enables the process of tooth replacement to be precisely described with closer focus on the position of the next tooth generations in comparison to the first generation or deciphering of the general replacement pattern, which can be also evaluated in our dataset. Thanks to the segmentation tool, study of the poison flow throughout the venomous canal in fangs is possible, as is determination of dental pulp changes across the jaw.

Moreover, the obtained data could be used for further studies by those who are particularly interested in reptilian skull anatomy (e.g., temporomandibular joint, columella, palatal bones, or other structures) and its evolutionary differences across diverse species. These skeletal elements can be evaluated by the tool, which enables the precise segmentation of individual structure. These segmented bones could be further processed to get precise information about their shape, volume, and relationship to other surrounding structures in 3 dimensions. Furthermore, wall thickness

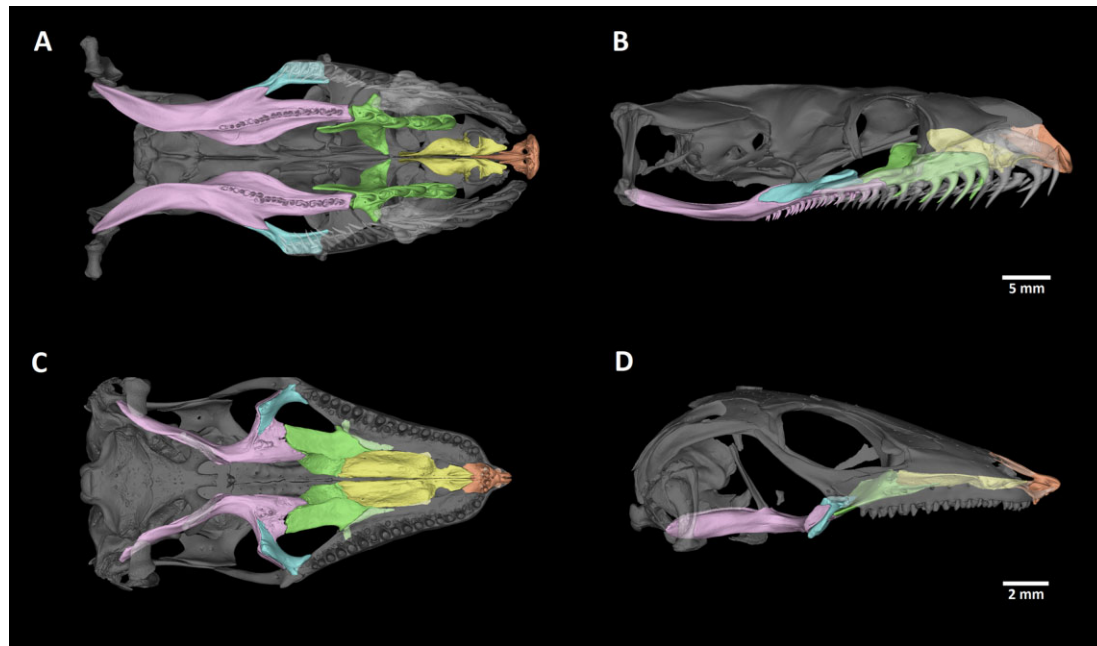


Figure 9: Arrangement of bones contributing to the palate in *Python regius* and *Scincus scincus*. (A) Palatal view of the upper jaw of *Python regius*. (B) Sagittal view of the bones supporting the palate in *P. regius*. (C) Palatal view of the upper jaw of *S. scincus*. (D) Sagittal view of the bones supporting the palate in *S. scincus*. Individual skeletal elements were segmented and labelled as follows: orange: premaxillary bone; yellow: vomer; green: palatal bone; pink: pterygoid; blue: ectopterygoid. The bones of the skull surrounding the segmented palatal bones were made semi-transparent to improve the display of the analysed areas.

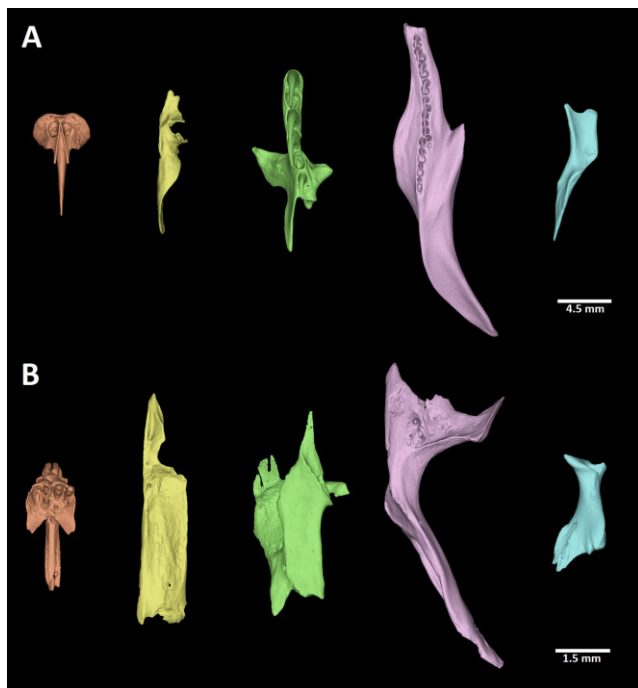


Figure 10: Segmented bones contributing to the palate in selected reptiles. (A) *Python regius*, (B) *Scincus scincus*. Palatal view of individual segmented skeletal elements in both species: orange: premaxillary bone; yellow: vomer; green: palatal bone; pink: pterygoid; blue: ectopterygoid.

analysis can be useful to study structural aspects of skeletal elements.

To broaden our knowledge about reptilian skull anatomy, morphology, and development, the scans of multiple chameleon embryos are provided. The entire present analysis, in combination,

will provide comprehensive and detailed information about both dental and bone tissue morphology in selected model species across reptilians.

Popularization/Educational Potential of Present Dataset

The 3D-printed models of entire analysed reptilian skulls or individual segmented skeletal elements of interest can also be used as an innovative learning support for university or secondary school students. Both 3D-printed and virtual reality models could also be presented to the general public, e.g., at museums without any need to possess original skulls or taxidermy mounts (Fig. 11). Use of 3D scans for virtual reality enables not only detailed view of individual structures but also the option of walking through a skull or inside of individual skeletal elements.

Data Availability

Volumetric data of all scanned animals are available in 8-bit tiff stack files via the GigaScience database GigaDB [25]. These tiff stacks include the raw tomographic sections. The data were reduced from original 16 to 8 bit to make the data more compact to download and to make it more available for analysis, considering that the larger datasets need high computational power to even open them. The stl models of skulls were created for all analysed samples; these models are highly detailed, which makes them suitable for 3D printing at higher magnifications. Additional tiff stacks of demonstrated analyses (unrolled lower jaw) are included. Finally, videos displaying individual analyses in detail (such as wall thickness analyses, teeth or bone segmentation) or transverse sections through the head are also included. Models are also available via the Sketchfab repository <https://sketchfab.com/GigaDB/collections/reptile-skull>.

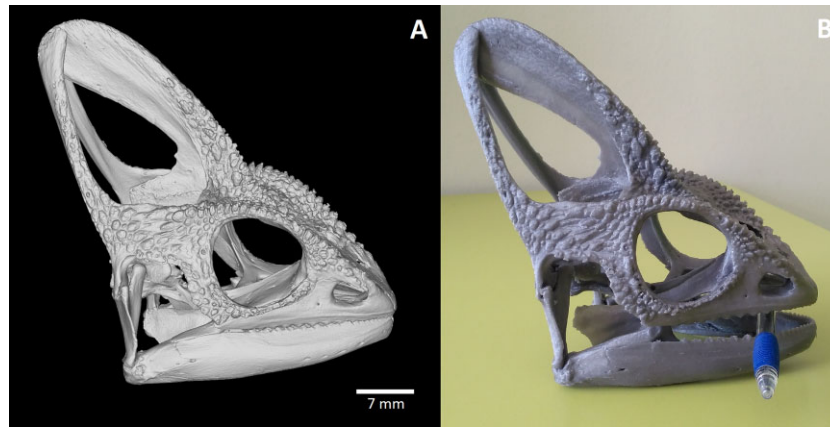


Figure 11: 3D-printed skull of *Chamaeleo calytratus* from generated stl model. (A) 3D stl model of the scanned *C. calytratus* skull generated in VG Studio MAX, (B) 3D printed model of the skull. For the purpose of 3D printing, the generated stl model was 3.5× magnified. The PRUSA MK3S printer with the PLA filament and 0.15-mm printing layer was used to create the model; total print time was 40 hours.



Model 1: *Bitis gabonica*. Because the 3D surface-rendered image is very large for convenient download and inspection, we provide a lower-resolution version for web-based 3D visualization in Sketchfab. This model was smoothed using Amira, with the modified version uploaded to Sketchfab. The complete Sketchfab collection is embedded in the GigaDB dataset [25] and is also available via <https://sketchfab.com/3d-models/skull-of-bitis-gabonica-gaboon-viper-dbc0dcdf11114bbea98bf235170456d8>.

Additional Files

Supplementary Video S1: *Salvator rufescens* in 3D view while using wall thickness analyses

Supplementary Video S2: 3D view of individual fang teeth in *Bitis gabonica*

Supplementary Video S3: 3D visualization of replacement teeth in *Caiman crocodilus*

Supplementary Video S4: *Scincus scincus* in 3D view with focus on segmented palatal elements

Abbreviations

micro-CT: microcomputed tomography; ROI: region of interest; stl: standard template library.

Competing Interests

The authors declare that they have no competing interests.

Funding

This study was supported by the Ministry of Health, Czech Republic (NU20-06-00189) and the CzechNanoLab Research Infrastructure supported by MEYS CR (LM2018110).

Authors' Contributions

Data analyses: M.K.

Visualization: M.K., M.S.

Validation: T.Z.

Conceived and designed experiments: T.Z., M.B.

Grant support: M.B.

Contributed reagents and materials: M.P., J.K.

Software: T.Z., J.K.

Writing of original manuscript: M.K., M.S., M.B.

Writing—review & editing: T.Z., M.P., M.B.

Acknowledgements

The authors thank Oldřich Zahradníček for samples of *Paroedura picta* and *Pogona vitticeps*.

References

- Watanabe, A, Fabre, AC, Felice, RN, et al.. Ecomorphological diversification in squamates from conserved pattern of cranial integration. *Proc Natl Acad Sci U S A* 2019;**116**(29):14688–97.
- Bertin, TJC, Thivichon-Prince, B, LeBlanc, ARH, et al.. Current perspectives on tooth implantation, attachment, and replacement in Amniota. *Front Physiol* 2018;**9**:20.
- Lafuma, F, Corfe, IJ, Clavel, J, et al.. Multiple evolutionary origins and losses of tooth complexity in squamates. *Nat Commun* 2021;**12**(1):6001.
- Gaengler, P. Evolution of tooth attachment in lower vertebrates to tetrapods. In: MF Teaford, MM Smith, MWJ Ferguson, eds. *Development, Function and Evolution of Teeth*. Cambridge: Cambridge University Press; 2000:173–85.
- Salomies, L, Eymann, J, Khan, I, et al.. The alternative regenerative strategy of bearded dragon unveils the key processes underlying vertebrate tooth renewal. *Elife* 2019;**8**:e47702.

- Maxwell, EE, Caldwell, MW, Lamoureux, DO, et al.. Histology of tooth attachment tissues and Plicidentine in Varanus (Reptilia: Squamata), and a discussion of the evolution of amniote tooth attachment. *J Morphol* 2011;**272**:1170–81.
- Dosedelova, H, Stepankova, K, Zikmund, T, et al.. Age-related changes in the tooth-bone interface area of acrodont dentition in the chameleon. *J Anat* 2016;**229**:356–68.
- Kavkova, M, Sulcova, M, Dumkova, J, et al.. Coordinated labio-lingual asymmetries in dental and bone development create a symmetrical acrodont dentition. *Sci Rep* 2020;**10**:16.
- Delgado, S, Davit-Beal, T, Allizard, F, et al.. Tooth development in a scincid lizard, *Chalcides viridanus* (Squamata), with particular attention to enamel formation. *Cell Tissue Res* 2005;**319**:71–89.
- du Plessis, A, Broeckhoven, C, le Roux, SG. Snake fangs: 3D morphological and mechanical analysis by microCT, simulation, and physical compression testing. *Gigascience* 2017;**7**(1):doi:10.1093/gigascience/gix126.
- LeBlanc, ARH, Paparella, I, Lamoureux, DO, et al.. Tooth attachment and pleurodont implantation in lizards: histology, development, and evolution. *J Anat* 2021;**238**:1156–78.
- Zahradnicek, O, Horacek, I, Tucker, AS. Tooth development in a model reptile: functional and null generation teeth in the gecko *Paroedura picta*. *J Anat* 2012;**221**:195–208.
- Hampl, M, Dumkova, J, Kavkova, M, et al.. Polarized sonic hedgehog protein localization and a shift in the expression of region-specific molecules is associated with the secondary palate development in the veiled chameleon. *Front Cell Dev Biol* 2020;**8**:572.
- Sulcova Landova, M, Zahradnicek, O, Dumkova, J, et al.. Developmental mechanisms driving complex tooth shape in reptiles. *Dev Dyn* 2020;**249**:441–64.
- Buchtova, M, Zahradnicek, O, Balkova, S, et al.. Odontogenesis in the veiled chameleon (*Chamaeleo calyptratus*). *Arch Oral Biol* 2013;**58**:118–33.
- LeBlanc, ARH, Lamoureux, DO, Caldwell, MW. Mosasaurs and snakes have a periodontal ligament: timing and extent of calcification, not tissue complexity, determines tooth attachment mode in reptiles. *J Anat* 2017;**231**:869–85.
- Zaher, H, Rieppel, O. Tooth implantation and replacement in squamates, with special reference to mosasaur lizards and snakes. *Am Mus Nov* 1999;**3271**:1–19.
- McIntosh, JE, Anderton, X, Flores-De-Jacoby, L, et al.. Caiman periodontium as an intermediate between basal vertebrate ankylosis-type attachment and mammalian “true” periodontium. *Microsc Res Tech* 2002;**59**:449–59.
- Mahler, L, Kearney, M. The palatal dentition in squamate reptiles: morphology, development attachment, and replacement. *Integr Comp Biol* 2005;**45**:1036.
- Matsumoto, R, Evans, SE. The palatal dentition of tetrapods and its functional significance. *J Anat* 2017;**230**:47–65.
- Haridy, Y, LeBlanc, ARH, Reisz, RR. The Permian reptile *Opisthodontosaurus carrolli*: a model for acrodont tooth replacement and dental ontogeny. *J Anat* 2018;**232**:371–82.
- LeBlanc, ARH, Brink, KS, Cullen, TM, et al.. Evolutionary implications of tooth attachment versus tooth implantation: a case study using dinosaur, crocodylian, and mammal teeth. *J Vertebr Paleontol* 2017;**37**:19.
- LeBlanc, ARH, Brink, KS, Whitney, MR, et al.. Dental ontogeny in extinct synapsids reveals a complex evolutionary history of the mammalian tooth attachment system. *Proc R Soc Lond B Biol Sci* 2018;**285**(1890):20181792.
- Palci, A, LeBlanc, ARH, Panagiotopoulou, O, et al.. Plicidentine and the repeated origins of snake venom fangs. *Proc R Soc Lond B Biol Sci* 2021;**288**(1956):20211391.
- Kavkova, M, Šulcová, M, Zikmund, T, et al.. Supporting data for “X-ray microtomography imaging of craniofacial hard tissues in selected reptile species with different types of dentition.” *GigaScience Database*. 2022; <http://dx.doi.org/10.5524/100987>.



Mouse Model of Congenital Heart Defects, Dymorphic Facial Features and Intellectual Developmental Disorders as a Result of Non-functional CDK13

Monika Nováková¹, Marek Hampel^{2,3}, Dávid Vrábel¹, Jan Procházka^{4,5},
Silvia Petrezselyová^{4,5}, Michaela Procházková^{4,5}, Radislav Sedláček^{4,5},
Michaela Kavková⁶, Tomáš Zikmund⁶, Jozef Kaiser⁶, Hsien-Chia Juan⁷, Ming-Ji Fann⁷,
Marcela Buchtová^{2,3*} and Jiří Kohoutek^{1*}

OPEN ACCESS

Edited by:

Eleonora Napoli,
University of California, Davis,
United States

Reviewed by:

Junichi Iwata,
University of Texas Health Science
Center at Houston, United States
Julie Siegenthaler,
University of Colorado Denver,
United States

*Correspondence:

Marcela Buchtová
buchtova@iach.cz
Jiří Kohoutek
kohoutek@vri.cz

Specialty section:

This article was submitted to
Cellular Biochemistry,
a section of the journal
Frontiers in Cell and Developmental
Biology

Received: 13 February 2019

Accepted: 23 July 2019

Published: 07 August 2019

Citation:

Nováková M, Hampel M, Vrábel D,
Procházka J, Petrezselyová S,
Procházková M, Sedláček R,
Kavková M, Zikmund T, Kaiser J,
Juan H-C, Fann M-J, Buchtová M
and Kohoutek J (2019) Mouse Model
of Congenital Heart Defects,
Dymorphic Facial Features
and Intellectual Developmental
Disorders as a Result
of Non-functional CDK13.
Front. Cell Dev. Biol. 7:155.
doi: 10.3389/fcell.2019.00155

¹ Department of Chemistry and Toxicology, Veterinary Research Institute, Brno, Czechia, ² Laboratory of Molecular Morphogenesis, Institute of Animal Physiology and Genetics, Czech Academy of Sciences, Brno, Czechia, ³ Department of Experimental Biology, Faculty of Science, Masaryk University, Brno, Czechia, ⁴ Laboratory of Transgenic Models of Diseases, Institute of Molecular Genetics, Czech Academy of Sciences, Prague, Czechia, ⁵ Czech Centre for Phenogenomics, Institute of Molecular Genetics, Czech Academy of Sciences, Prague, Czechia, ⁶ Central European Institute of Technology, Brno University of Technology, Brno, Czechia, ⁷ Department of Life Sciences, Institute of Genome Sciences, National Yang-Ming University, Taipei, Taiwan

Congenital heart defects, dymorphic facial features and intellectual developmental disorders (CHDFIDD) syndrome in humans was recently associated with mutation in *CDK13* gene. In order to assess the loss of function of *Cdk13* during mouse development, we employed gene trap knock-out (KO) allele in *Cdk13* gene. Embryonic lethality of *Cdk13*-deficient animals was observed by the embryonic day (E) 16.5, while live embryos were observed on E15.5. At this stage, improper development of multiple organs has been documented, partly resembling defects observed in patients with mutated *CDK13*. In particular, overall developmental delay, incomplete secondary palate formation with variability in severity among *Cdk13*-deficient animals or complete midline deficiency, kidney failure accompanied by congenital heart defects were detected. Based on further analyses, the lethality at this stage is a result of heart failure most likely due to multiple heart defects followed by insufficient blood circulation resulting in multiple organs dysfunctions. Thus, *Cdk13* KO mice might be a very useful model for further studies focused on delineating signaling circuits and molecular mechanisms underlying CHDFIDD caused by mutation in *CDK13* gene.

Keywords: cyclin-dependent kinase (CDK), cyclin, transcription regulation, development, mouse, cyclin-dependent kinase 13, cyclin K

INTRODUCTION

Recently, *de novo* missense variants in *Cyclin-dependent kinase 13 (CDK13)* gene have been identified as an emerging factor involved in the onset of congenital heart defects (CHD) in humans (Sifrim et al., 2016). Documented CHD cases were characterized by ventral and atrial septal defects accompanied by pulmonary valve abnormalities. CHD patients had syndromic facial gestalt, and two patients had agenesis of the corpus callosum. Additional mutations within the *CDK13* gene were recognized in humans resembling at clinical level many symptoms previously associated

with loss of function of *CDK13* or newly described symptoms, such as autism spectrum disorder, seizures, feeding difficulties and craniofacial dysmorphism including short upslanting palpebral fissures, hypertelorism or telecanthus, medial epicanthic folds, low-set, posteriorly rotated ears and small mouth with thin upper lip vermilion (Hamilton et al., 2018). In addition, genome wide search for *de novo* mutations responsible for developmental disorders in patients in Great Britain and Republic of Ireland led to identification of 14 genes that previously lacked compelling evidence of involvement in developmental disorders, among them the *CDK13* gene (Deciphering Developmental Disorders Study, 2017). However, heart defects do not seem to be the key feature of this disorder since patients with heterozygous constitutional mutation in *CDK13* lacking cardiac anomalies were reported by two groups (Carneiro et al., 2018; Uehara et al., 2018). Spectrum of clinical phenotypes of patients with *CDK13* mutations varies from mild to severe with the ubiquitous intellectual disability and developmental delay (ID/DD) (van den Akker et al., 2018). Based on these observations, congenital heart defects, dysmorphic facial features and intellectual development disorder (CHDFIDD) have been recognized as novel syndrome caused by *de novo* variants of *CDK13* gene (Sifrim et al., 2016; Bostwick et al., 2017; Carneiro et al., 2018; van den Akker et al., 2018).

Human CDK13 protein consists of 1512-amino acids with a conserved kinase domain surrounded by N- and C-terminal arms of undefined function (Kohoutek and Blazek, 2012). In order to be active, CDK13 binds cyclin K (CycK) and forms enzymatically active complex (Ko et al., 2001; Even et al., 2006; Bartkowiak et al., 2010; Blazek et al., 2011; Cheng et al., 2012; Dai et al., 2012; Kohoutek and Blazek, 2012; Liang et al., 2015). CDK13 belongs to the family of transcription-associated cyclin-dependent kinases phosphorylating the carboxyl-terminal domain (CTD) of RNA polymerase II (RNAPII). In particular, the CDK13 phosphorylates serine 2 (Ser2) and to a lesser extent also serine 5 (Ser5) within $Y^1S^2P^3T^4S^5P^6S^7$ heptapeptides within the CTD of RNAPII *in vitro* (Greifenberg et al., 2016). Nevertheless, downregulation of CDK13 in tumor derived cell lines had a very small, if any, effect on level of Ser2 within CTD of RNAPII (Blazek et al., 2011; Greifenberg et al., 2016). In parallel to CDK13, there is CDK12 in mammalian cells able to associate with CycK as well (Blazek et al., 2011; Dai et al., 2012; Liang et al., 2015). Even though CDK13 shares high amino acid similarity with CDK12, both kinases appear to function in mutually exclusive complexes in mammalian cells (Blazek et al., 2011; Kohoutek and Blazek, 2012; Greenleaf, 2018).

In comparison to CDK12, there is a limited number of papers envisioning the likely function of CDK13 in various biological processes. For instance, the CDK13 was proposed to be involved in oncogenesis; yet, its precise function is still under examination (Kim et al., 2012; Pan et al., 2012). Even though factors involved in RNA processing, RNA splicing, polyadenylation and RNA cleavage were demonstrated to bind CDK13 as a result of global protein-protein interactions, truly associating partners of this kinase are still unknown (Davidson et al., 2014; Bartkowiak and Greenleaf, 2015; Liang et al., 2015). In addition to involvement of CDK13 in diverse cellular processes, this protein participates

in regulation of alternative splicing of HIV-1 or influenza virus replication, thus suppressing viral production (Berro et al., 2008; Bakre et al., 2013). In developing mouse embryos and murine cells, CDK13 regulates hematopoiesis, stemness and axonal elongation, suggesting an important function in neuronal development (Pan et al., 2012; Chen et al., 2014).

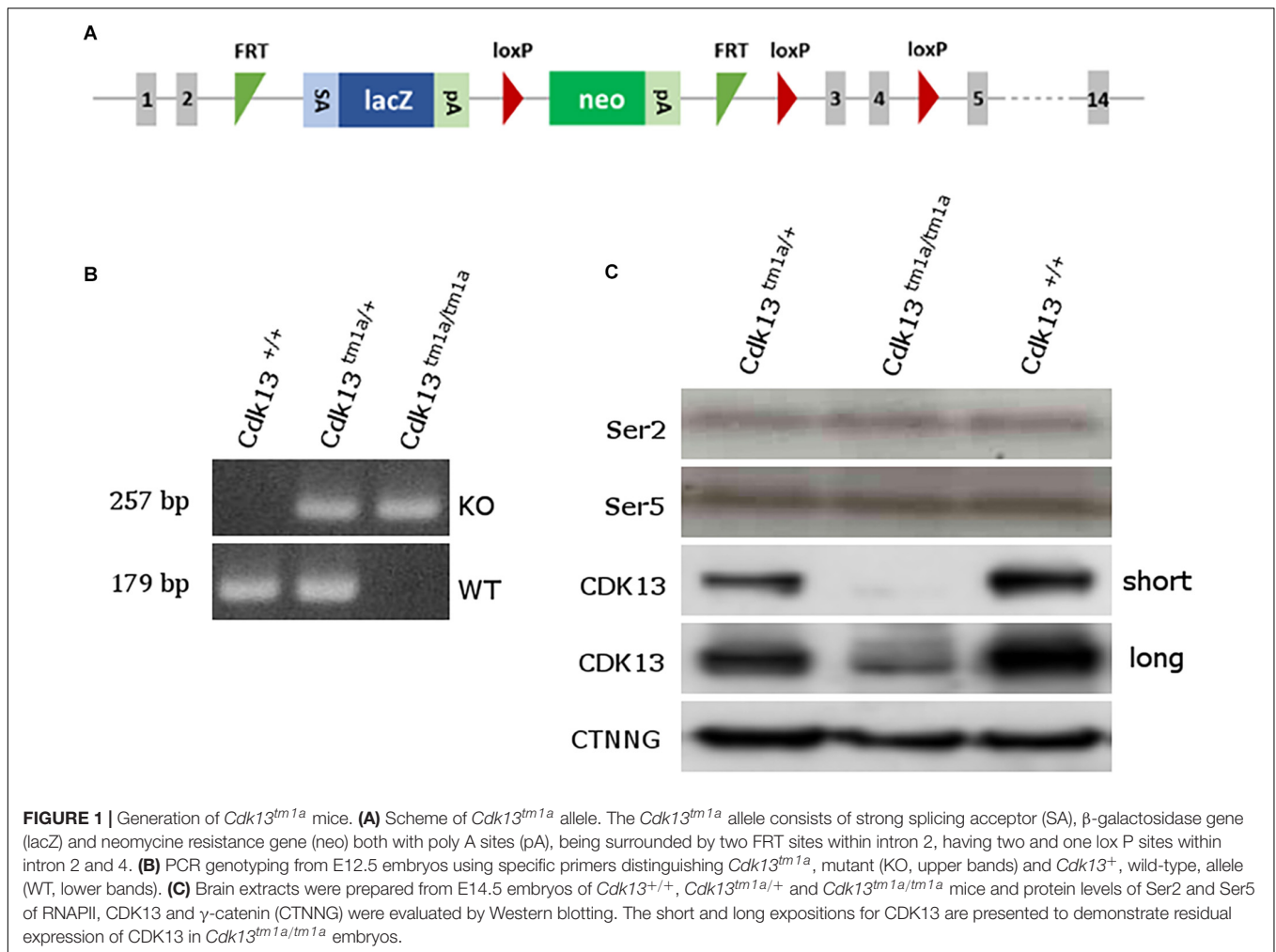
To this date, the impact of complete loss of *Cdk13* function during mammalian development has not been investigated. Therefore, we employed a *Cdk13* knock-out (KO) mouse model to explore a novel role of *Cdk13* during mouse embryonic development. We observed embryonic lethality of *Cdk13* KO animals at the embryonic day 16.5. At this stage, improper development of multiple organs has been observed (heart, brain, kidney, liver, and palate formation) resembling phenotype of human patients with *de novo* missense variants of *CDK13* gene. Therefore, our *Cdk13*-deficient mice may become an important model to study dysregulation of developmental processes occurring in human patients.

RESULTS

Disruption of Cdk13 Gene Leads to Embryonic Lethality in Mice

To examine the role of CDK13 during mouse development, the mice carrying *Cdk13^{tm1a}* allele were generated at the Transgenic and Archiving Module CCP (Institute of Molecular Genetics of the CAS, Prague). The *Cdk13^{tm1a}* allele of *Cdk13* gene enables cessation of transcription due to presence of two strong poly A sites leading to production of the aberrant transcript of *Cdk13* mRNA resulting in non-functional truncated form of CDK13 protein harboring only N-terminal part of this protein, without kinase domain and C-terminal part (**Figure 1A**). Heterozygous *Cdk13^{tm1a/+}* mice were intercrossed to obtain *Cdk13^{tm1a/tm1a}* offspring. Newborn mice were genotyped with specific sets of primers able to distinguish inserted cassette (257 bp PCR product, KO) and wild-type (179 bp PCR product, WT) alleles of *Cdk13* gene (**Figure 1B**). Although the offspring with *Cdk13* WT and heterozygous alleles was born at the expected Mendelian ratio, appeared normal and fertile, *Cdk13^{tm1a/tm1a}* mice were not born at all. This finding suggested that a homozygous deficiency in *Cdk13* gene leads to embryonic lethality in mice. To determine the precise stage, when the embryonic lethality occurs, mouse embryos were collected at various gestation time points (**Table 1**). There were no living *Cdk13^{tm1a/tm1a}* embryos after the embryonic stage 15.5 (E15.5) judging by the lack of their heart beating. Moreover, from E13.5 to E16.5, we observed increased number of absorbed embryos as a reflection of empty decidua (**Table 1**). Based on these finding, we concluded that the deficiency of *Cdk13* causes severe adverse developmental defects and consequent death from E14.5 resulting in total lethality before E16.5.

To confirm the loss of CDK13 protein in *Cdk13^{tm1a/tm1a}* mice, developing brain from WT and *Cdk13^{tm1a/tm1a}* homozygous embryos at E14.5 were collected and western blot analyses were carried out with specific antibodies recognizing CDK13 protein. As expected, the WT form of CDK13 was present in *Cdk13^{+/+}*



and *Cdk13^{tm1a/+}* mice, but surprisingly, corroborated residual expression of CDK13 protein was detected in the embryonic brain of *Cdk13^{tm1a/tm1a}* homozygous embryos (Figure 1C), suggesting that *Cdk13^{tm1a/tm1a}* mice represent a hypomorphic

mutant phenotype. Because the anti-Cdk13 antibody used in western blot recognizes its N-terminal part of CDK13, we were curious if the truncated form of CDK13, as a result of terminated transcription within intron 2, will be expressed in mice bearing the *Cdk13^{tm1a}* allele. Indeed, the truncated form of CDK13 was detected in *Cdk13^{tm1a/+}* and *Cdk13^{tm1a/tm1a}* animals (Supplementary Figure S1). Since CDK13 was demonstrated to phosphorylate CTD of RNAPII *in vitro*, we decided to evaluate phosphorylation status of CTD in hypomorphic mice. Thus, the effect of CDK13 downregulation on Ser2 was evaluated in the animal tissue. Even though expression of CDK13 was significantly lowered in *Cdk13^{tm1a/tm1a}* mice, no effect on either Ser2 or Ser5 phosphorylation within CTD of RNAPII was detected (Figure 1C). The Ser5 phosphorylation was checked in parallel since it is phosphorylated by other CDK kinase, CDK7 in particular (Kohoutek, 2009).

Cdk13 Loss Causes Growth Retardation, Developmental Delay and Its Failure

To examine deficiency of CDK13 protein in *Cdk13^{tm1a/tm1a}* mice, morphology at different embryonic stages compared to the WT animals was examined and various abnormalities were

TABLE 1 | Genotypes of offspring from *Cdk13^{tm1a/+}* intercross.

Stage	<i>Cdk13^{+/+}</i>	<i>Cdk13^{tm1a/+}</i>	<i>Cdk13^{tm1a/tm1a}</i>	Litters	Empty decidua
	(25%)	(50%)	(25%)		
E9.5	4 (21.1%)	12 (63.2%)	3 (15.8%)*	3	2
E10.5	4 (20%)	10 (50%)	6 (30%)*	2	0
E11.5	14 (31.8%)	23 (52.3%)	7 (15.9%)*	6	4
E12.5	31 (30.7%)	52 (51.5%)	18 (17.8%)*,#	15	13
E13.5	6 (16.2%)	18 (48.6%)	13 (35.1%)*	5	5
E14.5	48 (27.6%)	95 (54.6%)	31 (17.8%)*,#	26	9
E15.5	21 (27.5%)	34 (58%)	10 (14.5%)*	11	5
E16.5	8 (25%)	18 (56.3%)	6 (18.7%)*,#	4	0
P0	39 (33.1%)	79 (66.9%)	0	28	

*Growth retardation, #dead embryo.

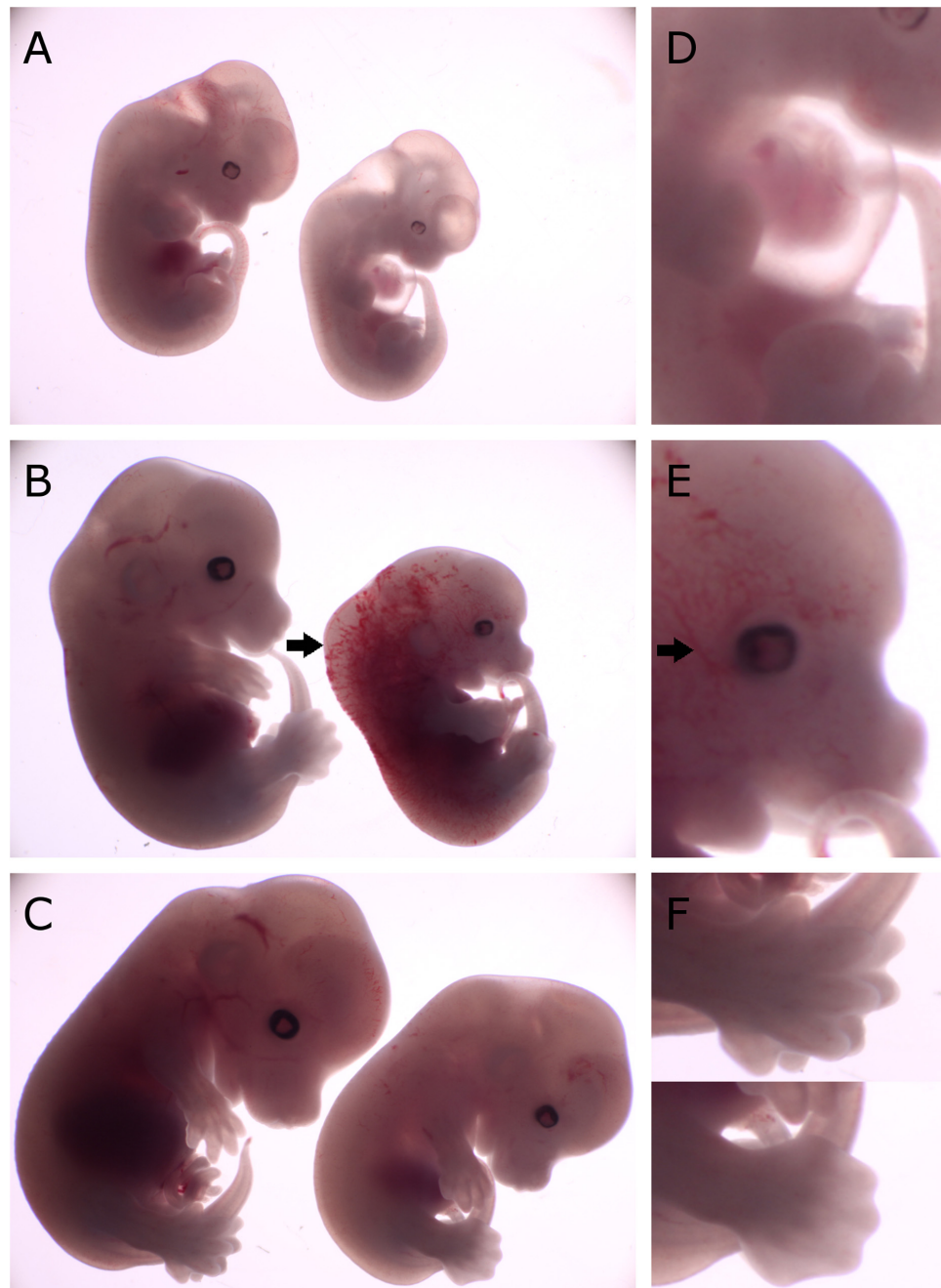


FIGURE 2 | Comparison of gross morphology of wild-type, *Cdk13^{tm1a/+}* and *Cdk13^{tm1a/tm1a}* embryos at various stages. *Cdk13^{tm1a/tm1a}* embryos display significant growth retardation compared to wild-type and heterozygous embryos. **(D–F)** Detailed images of *Cdk13^{tm1a/tm1a}* at relevant developmental stages. **(A)** Heterozygous and *Cdk13^{tm1a/tm1a}* embryos at E12.5. **(D)** Occasional chest wall deformities manifest as hypomorphs. **(B)** Wild-type and *Cdk13^{tm1a/tm1a}* embryos at E13.5. *Cdk13^{tm1a/tm1a}* embryo exhibits nuchal edema (black arrow). **(E)** Hypervascularization of the peripheral vessels capillaries (black arrow). **(C)** Wild-type and *Cdk13^{tm1a/tm1a}* embryos at E14.5. **(F, top)** Wild-type embryo demonstrates deep indentations between the developing fingers of embryos E14.5, although not yet separated. **(F, bottom)** In contrast, *Cdk13^{tm1a/tm1a}* embryo appears to be 1 day delayed in development as evidenced by the shallow indentation of the footpad, which is characteristic of embryos at E13.5.

observed in *Cdk13^{tm1a/tm1a}* embryos at each stage of gestation (**Supplementary Figure S2**). Observed growth retardation of *Cdk13*-deficient mice is presented in detail (**Figure 2**); however, the severity of the developmental delay was variable. On average,

the *Cdk13^{tm1a/tm1a}* embryos appeared to be one embryonic day behind in comparison to their littermate controls as evidenced by the shallow indentation of the footpad, which is characteristic of embryos at E13.5 (**Figure 2F, bottom**).

In contrast, *Cdk13*^{+/+} littermates exhibited deep indentations between the developing toes (not yet separated), what is characteristic of embryos at 14.5 (Figure 2F, top). In addition, the retarded embryo exhibited nuchal edema (black arrow, Figure 2B), which correlates with the presence of cardiovascular phenotypes. Occasionally, the pericardial effusion were detected in developing *Cdk13*^{tm1a/tm1a} embryos, most likely caused by dysfunction of the heart (Figure 2D). Summary of various developmental defects associated with hypomorphic *Cdk13*^{tm1a} allele is presented in Supplementary Table S1.

Cdk13 Is Indispensable for the Development of Several Organs

To narrow down possible cause of embryonic lethality, embryos at E14.5 were contrasted with Lugol's solution to visualize gross morphology of individual soft tissues by microCT (Figure 3). Indeed, several developmental abnormalities were detected within developing embryos. The heart wall of both ventricles in *Cdk13*^{tm1a/tm1a} embryos (Figures 3B,D) appeared thinner in comparison to *Cdk13*^{+/+} littermate controls (Figures 3A,C). In addition, lung, liver and kidney in *Cdk13*^{tm1a/tm1a} embryos were smaller and undeveloped (Figures 3D,F,H) in comparison to *Cdk13*^{+/+} littermates (Figures 3C,E,G). However, detailed 3D reconstruction of liver and kidney (Figures 3I–P) with movable display of E14.5 embryos of *Cdk13*^{tm1a/tm1a} and *Cdk13*^{+/+} genotypes (Supplementary Figures S3A,B) revealed no defect in general gross morphology of these organs.

To uncover possible discrepancies in developmental speed of individual organs, the volume analysis was performed with normalization to total body volume of given embryo. Liver size of *Cdk13*^{tm1a/tm1a} embryos represented only about 46% in comparison to *Cdk13*^{+/+} littermates (Figures 3, 11). Similarly, kidney size of *Cdk13*^{tm1a/tm1a} animals comprised only about 52% in comparison to *Cdk13*^{+/+}. In parallel, histological sections of selected organs were analyzed at stages between E14.5 and E16 (Figure 4). Decelerated development of kidneys was identified in *Cdk13*^{tm1a/tm1a} embryos at E14.5 and E16 (Figures 4D,F) including nephron differentiation as shown by altered proportional representation of individual nephron stages at E14.5 (Figure 4G). Moreover, statistically significant reduction in the number of S-shaped bodies and glomeruli was observed in *Cdk13*^{tm1a/tm1a} embryos (Figure 4H). At lethality stage E16.5, kidney tissue exhibited tissue abrogation with only few, much reduced tubules visible (data not shown), very likely caused by general pre-necrotic changes.

Brains of *Cdk13*^{tm1a/tm1a} embryos appeared developmentally delayed as demonstrated by reduced size as compared to littermate controls. Depicted in Figure 5 are E14.5 controls and *Cdk13*^{tm1a/tm1a} mutant samples from two separate litters. The two litters were developmentally at different stages, pre-palatal fusion in the control embryo depicted (Figures 5A,B) and post-palatal fusion in the control embryo depicted (Figures 5E,F). In order to assess the developmental delay in *Cdk13*^{tm1a/tm1a} embryos the cell proliferation was examined by Ki67 staining, a marker of proliferating cells (Figures 5A'–H', embryos A and C, as well as E and G are littermates, representative pictures of two

embryos are shown to display variability in mutant phenotype). As evident from performed quantification, there was decrease in number of proliferating cells in *Cdk13*^{tm1a/tm1a} embryos in comparison to *Cdk13*^{+/+} littermate controls, but this decrease was not statistically significant (Figure 5I).

The analysis of craniofacial area revealed also defective palatal shelves development in several *Cdk13*^{tm1a/tm1a} embryos resulting in their insufficient horizontal growth and the formation of the cleft palate at E15.5 (Figure 6) in *Cdk13*^{tm1a/tm1a} mouse. Incomplete secondary palate formation exhibited variability in severity among *Cdk13*-deficient animals. Observed penetrance of secondary cleft palate was 2/4 animals at E15.5. In addition, *Cdk13*^{tm1a/tm1a} mouse at E15.5 had smaller number of initiated nasal glands in comparison to the controls (Supplementary Figure S4, compare A–D and B–E).

Embryonic Lethality in *Cdk13*^{tm1a/tm1a} Mice Is Due to Heart Failure

The heart is the one of the first organs to form during mammalian development. During heart development, significant changes in organ morphology and cardiomyocyte differentiation and organization reflect the increasing needs of growing embryos for nutrition and oxygen supply. Any of these developmental steps are critical for further development of whole embryos. Therefore, we analyzed the microscopic structure of the heart and found that the heart wall of *Cdk13*^{tm1a/tm1a} mice embryos was less compact in comparison to the heart wall of *Cdk13*^{+/+} mice (Figures 7C,D). Further, apparent disruption of tissue architecture was detected in *Cdk13*^{tm1a/tm1a} embryos with the reduction of myocardium (Figure 7, compare C, E and G to D, F and H). The heart volume was slightly increased to 103% (organ ratio to total body volume) in *Cdk13*^{tm1a/tm1a} mice compared to *Cdk13*^{+/+} animals. However, the total volume of heart tissue to the organ volume was significantly lower in case of *Cdk13*^{tm1a/tm1a} embryos (62.5%) in comparison to WT littermates (80%) suggestive of the thinner heart wall at E15.5 in *Cdk13*^{tm1a/tm1a} embryos. Percent soft tissue volumes were measured by microCT using Bruker-microCT CT-analyzer, where the object volume representing soft tissues was divided by total VOI volume. The VOI area referring to the heart volume was selected from the dataset manually. Also, decreased expression of myosin was detected in ventricle myocardium of 14.5 hearts (Supplementary Figure S5, compare B and B' to E and E').

Since the heart mass of *Cdk13*^{tm1a/tm1a} E14.5 – E16 embryos is significantly reduced with hypomorphic muscular layers of myocardium compared with *Cdk13*^{+/+} mice (heart/body ratio), we presume that heart developmental defect is the cause of embryonic lethality. In order to evaluate cardiac circulatory physiology, we performed non-invasive ultrasound Doppler imaging to quantitatively assess the hemodynamic function in E14.5 and E15.5 embryos. Out of nine *Cdk13*^{tm1a/tm1a} embryos dissected at E14.5 stage, only one was found dead (Table 2). All the other *Cdk13*^{tm1a/tm1a} embryos at this stage exhibited comparable blood flow velocities and velocity-time integral (VTI) in dorsal aorta (Figures 8A,B). However, this situation changed

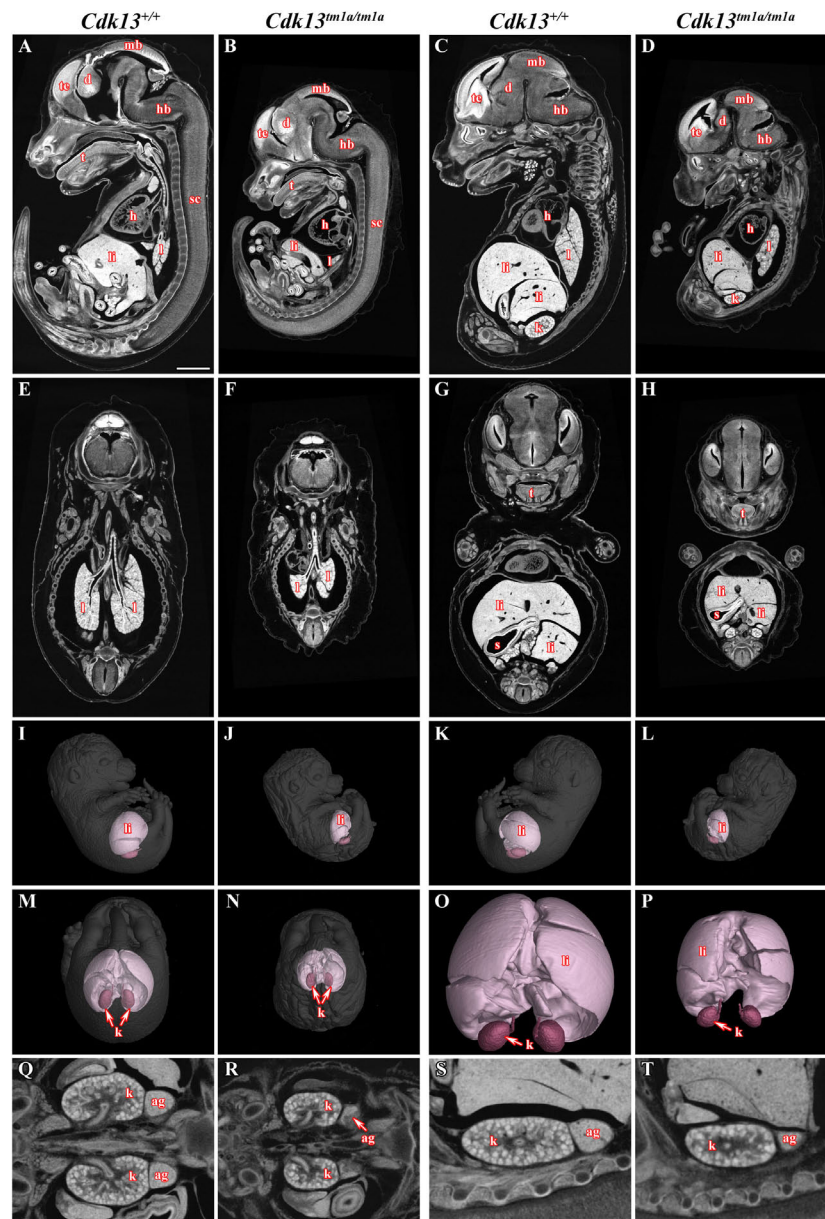


FIGURE 3 | MicroCT analysis of wild-type and *Cdk13^{tm1a/tm1a}* embryos. High-contrast differentiation resolution by X-ray computed microtomography, where Lugol's staining was used to visualize the soft tissues. Sagittal sections through body midline (**A,B**) and more lateral plane at E15.5 (**C,D**). Horizontal sections through lung (**E,F**) and liver (**G,H**). 3D reconstruction of kidney and liver in the right side view of embryo (**I,J**) and left side view (**K,L**) and caudal view (**M,N**) with embryo outlined in gray where segmentation of serial sections was used for the liver and kidney reconstruction. (**O,P**) High power of 3D imaging for liver and kidney. Horizontal view (**Q,R**) and sagittal detailed view (**S,T**) on kidney and suprarenal gland. Abbreviation used for individual organs: ag, adrenal gland; d, diencephalon; h, heart; hb, hindbrain; k, kidney; l, lung; li, liver; mb, midbrain; t, tongue; te, telencephalon; s, stomach; sc, spinal cord. Scale bar = 1 mm.

dramatically at embryonic stage E15.5 (**Figures 8C,D**), where only few *Cdk13^{tm1a/tm1a}* embryos retained normal blood flow parameters (5/16), while the rest of the embryos heart functions declined (standard measurements were not possible due to irregular or spare heart beating 11/16); moreover, an increased portion of embryos were already dead (**Table 2**).

The assessment of cardiac function in developmental interval E14.5 – E15.5 embryos showed dramatic failure

in heart function, probably corresponding to increasing needs of embryos at E15.5 for blood supply in growing organ systems, which is very challenging for the defective heart to achieve. The preserved blood flow in few *Cdk13^{tm1a/tm1a}* embryos was probably due to the observed variability of the embryo size. Our findings suggest that the heart failure appears in most cases during the transition from E14.5 to E15.5.

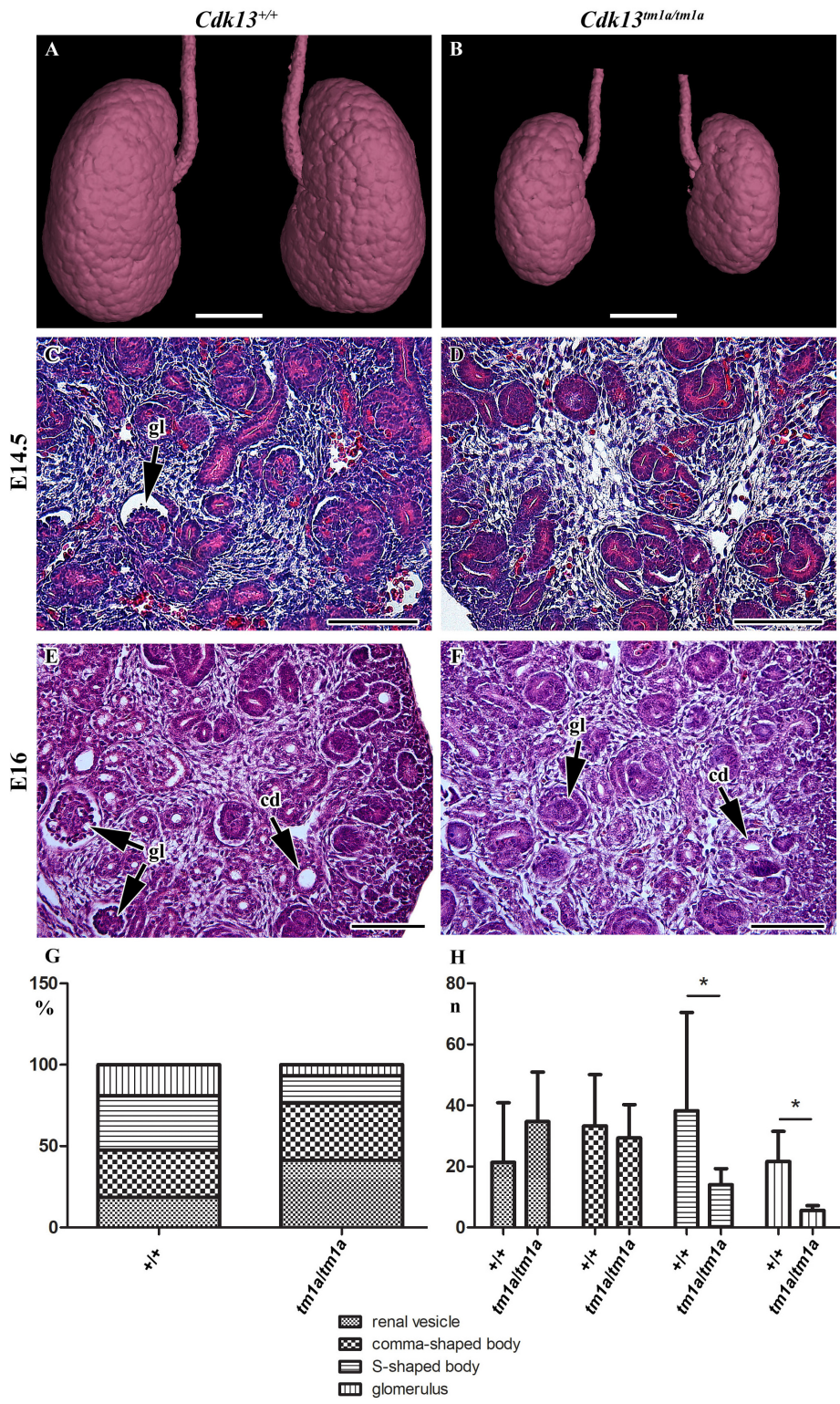


FIGURE 4 | Gross anatomy and microscopic structure of kidney in wild-type and *Cdk13^{tm1a/tm1a}* embryos. **(A,B)** High power view on segmented kidneys from Lugol's stained sections and visualized by X-ray computed microtomography. Growth retardation of kidney is visible in *Cdk13^{tm1a/tm1a}* embryos at E14.5 **(D)** and E16 **(F)** in contrast to littermate wild-type, *Cdk13^{+/+}*, controls **(C** for E14.5 and **E** for E16). **(E,F)** Only very few just forming glomeruli (gl) were found in *Cdk13^{tm1a/tm1a}* embryos. **(G)** Relative quantification of individual developmental stages of nephrogenesis in *Cdk13^{+/+}* and *Cdk13^{tm1a/tm1a}* embryos. **(H)** Increased amount of renal vesicles together with the reduction of S-shaped bodies and glomeruli (gl) was found in *Cdk13^{tm1a/tm1a}* embryos. The graph values denote median \pm s.d., **p* < 0.05, by unpaired *t*-test. Scale bar **(A,B)** = 0.3 mm, scale bar **(C–H)** = 100 μ m.

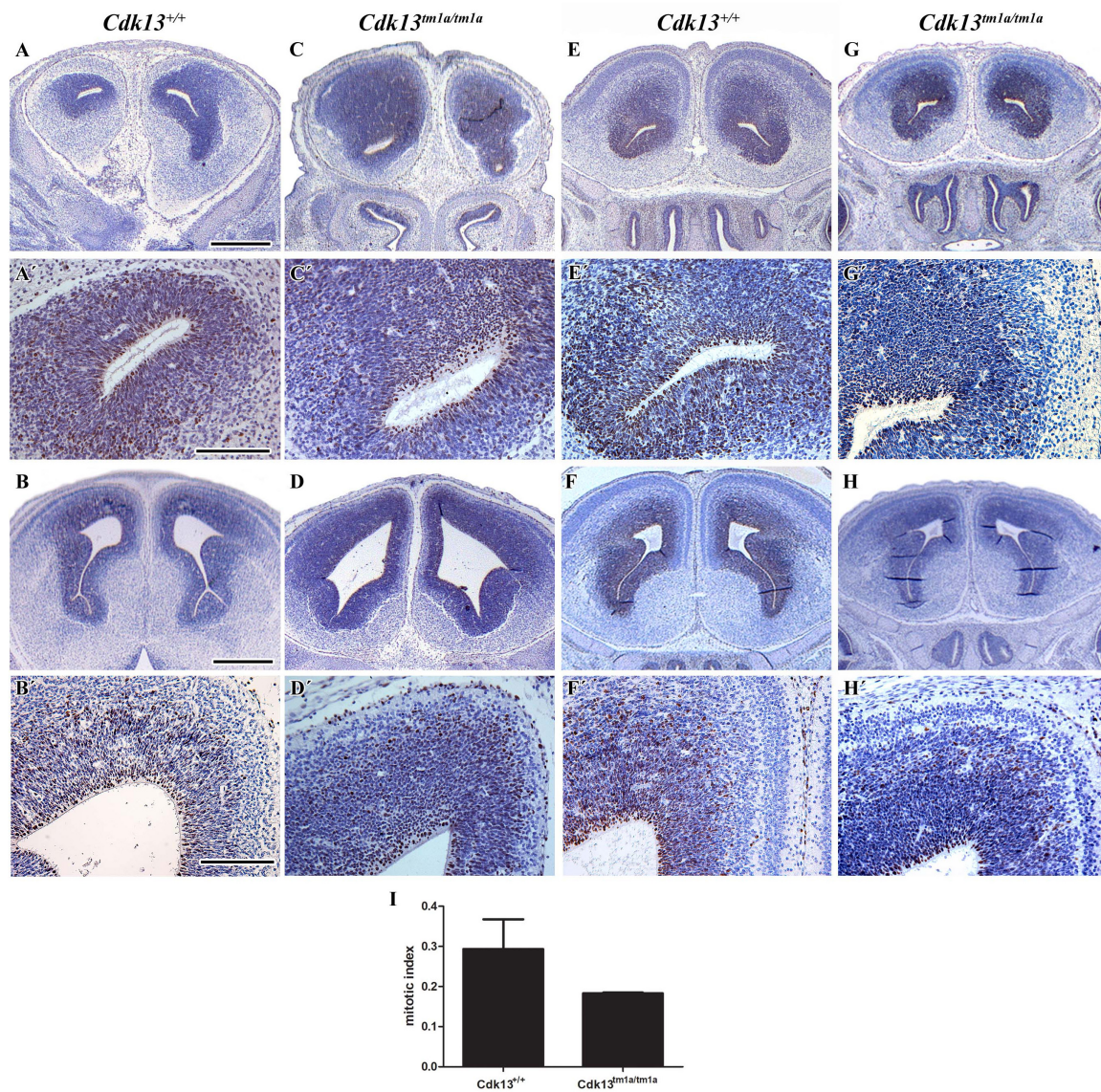


FIGURE 5 | Cell proliferation in brain area in wild-type and *Cdk13*^{tm1a/tm1a} embryos. (A,A',B,B') *Cdk13*^{+/+} and (C,C',D,D') *Cdk13*^{tm1a/tm1a} embryos before palatal shelves fusion. (E,E',F,F') *Cdk13*^{+/+} and (G,G',H,H') *Cdk13*^{tm1a/tm1a} embryos after palatal shelves fusion. Immunohistochemical nuclear labeling of Ki67-positive cells in the frontal head sections in the lower power view (A–H) and in detail (A'–H'). (I) Mitotic index was counted as the ratio between Ki67-positive cells and total amount of prosencephalon cells in three biological triplicates for each group. The graph values denote mean ± s.d, difference is not statistically significant according to unpaired *t*-test (*p*-value: 0.1047). Ki67-positive cells - brown nuclei, Ki67-negative cells - blue nuclei (hematoxylin). Scale bar (A–C) = 1 mm; scale bar (A'–C') = 100 μm.

Cdk13 Is Expressed in Affected Organs in the Prenatal and Also Postnatal Period

Currently, there is limited information about protein expression pattern of CDK13 either in developing or adult organs; therefore, we decided to evaluate expression of CDK13 protein in developing organs. First, the western blot of CDK13 protein was carried out in selected developing organs (Figure 9). As expected, expression of CDK13 was detected in organs with abnormal embryonic development. The highest protein level of CDK13 was detected in the brain, then lung, kidney and heart (Figure 9).

In case of detection of CDK13 in the developing heart, four times concentrated protein lysates had to be used to detect any reproducible signal.

To explore gene expression of *Cdk13* in adult tissues and organs, the particular organs were isolated and the expression of Cdk13 was examined by activity of β-galactosidase (Supplementary Figure S6). *Cdk13* was strongly expressed in the retina of the eye, testes, ovary, uterus, gall bladder (Supplementary Figures S6A,F–I). To a lesser extent, the *Cdk13* was detected in the urinary bladder (Supplementary Figure S6D). Interestingly, rather localized, yet strong expression

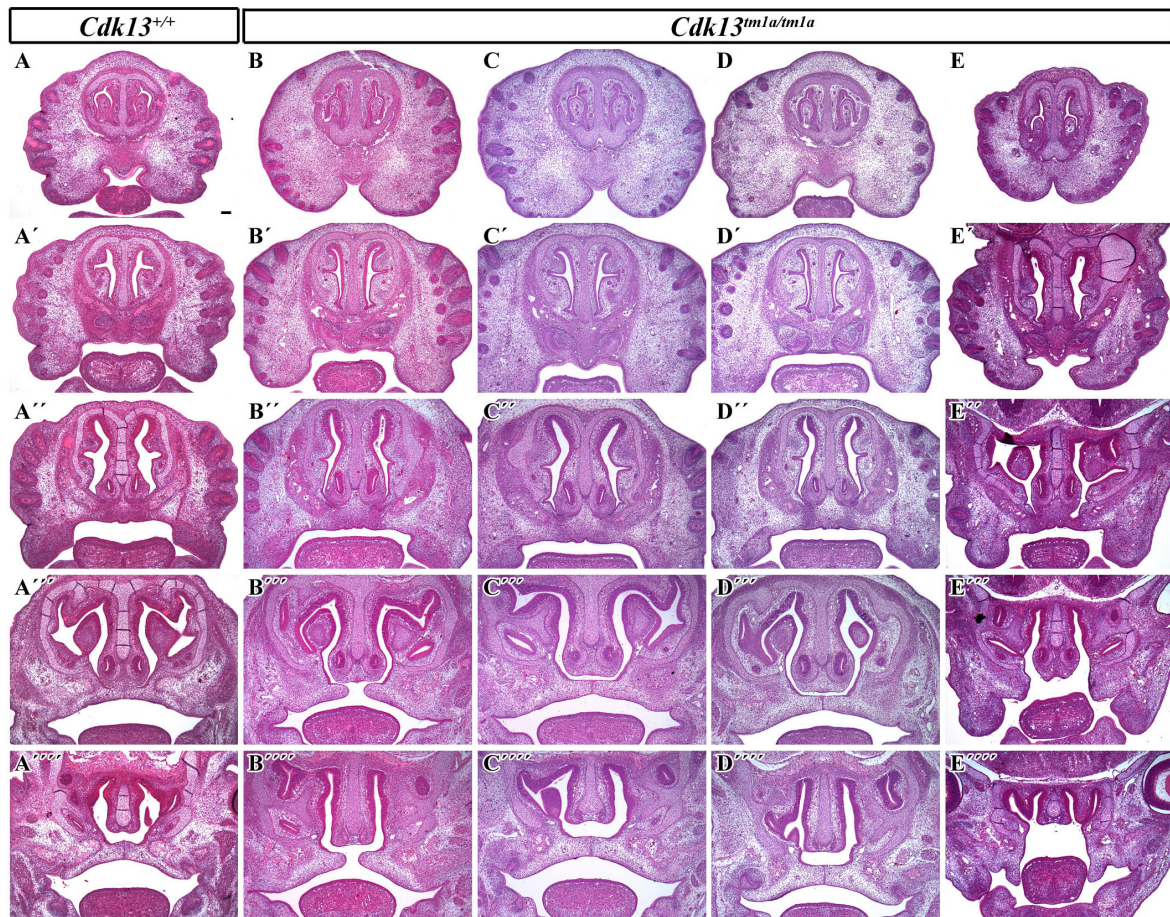


FIGURE 6 | Transversal sections of the head in control *Cdk13*^{+/+} and *Cdk13*^{tm1a/tm1a} embryos at E15.5. Rostro-caudal view in *Cdk13*^{+/+} animal (A) and four *Cdk13*^{tm1a/tm1a} mutant mice to show variability in the secondary palate morphology (B–E). Palatal shelves do not meet each other in the midline (B''', E''') and cleft of secondary palate is visible. Abnormal shape of palatal shelves was observed also caudally with cleft expanding into the soft palate area. (A'–A''', B'–B''', C'–C''', D'–D''', E'–E''') are transversal sections of head in individual embryos in rostrocaudal direction. Scale bar = 100 μm.

within organ structure was observed in renal pelvis in kidney, thyroid gland and heart atrium, with substantial expression in the heart ventricle (Supplementary Figures S6B,C,E).

Cdk13^{tm1d/tm1d} Mice Exhibits More Severe Phenotype and Earlier Lethality

As we observed residual expression of *Cdk13* in analyzed organs of hypomorphic *Cdk13*^{tm1a/tm1a} mice, we decided to cross *Cdk13*^{tm1a} mice with Flp-deleter mice and Cre-deleter (detailed description of the utilized transgenic strains is provided at the Section “Experimental Procedure”) mice to generate *Cdk13*^{tm1d} allele with deleted exons 3 and 4 (Figure 10A). As in case of *Cdk13*^{tm1a} mice, the expression of CDK13 protein was investigated in the *Cdk13*^{tm1d} mice. High expression of CDK13 was detected in the developing brain of WT *Cdk13*^{+/+} embryos (Figure 10B). Greatly downregulated expression of CDK13 was detected in heterozygous *Cdk13*^{tm1d/+} brain with undetectable expression of CDK13 protein in homozygous *Cdk13*^{tm1d/tm1d} brain (Figure 10B). As in the case of *Cdk13*^{tm1a} mice, no

significant reproducible downregulation of Ser2 phosphorylation was observed in *Cdk13*^{tm1d/tm1d} brain extract (Figure 10B). Interestingly, expected Mendelian ratios were reflected in the portion of *Cdk13*^{tm1d/tm1d} mice. High number of empty decidua at E12.5 were detected reflecting increased mortality before this stage (Table 3). Critically, only 19 litters out of 42 contained *Cdk13*^{tm1d/tm1d} embryos suggesting homozygous mice carrying *Cdk13*^{tm1d} alleles exhibited more severe defects in phenotype than *Cdk13*^{tm1a/tm1a} mice, especially in craniofacial area with midline facial cleft (Figure 10C). The prevalence of the midline orofacial deficiency and pericardial effusion was 60.5% in *Cdk13*^{tm1d} homozygous mice at E12.5–E14.5. Out of 94 cases, only two cases of *Cdk13*^{tm1a/tm1a} mice had externally visible orofacial clefting (Supplementary Table S1). The prevalence of the pericardial effusion (PE) in *Cdk13*^{tm1a/tm1a} embryos at E12.5–E14.5 was less than 20% in comparison to high occurrence in *Cdk13*^{tm1d/tm1d} embryos (Supplementary Table S1). No PE or orofacial cleft was recorded in any WT, though 6 embryos from 262 heterozygotes exhibited PE.

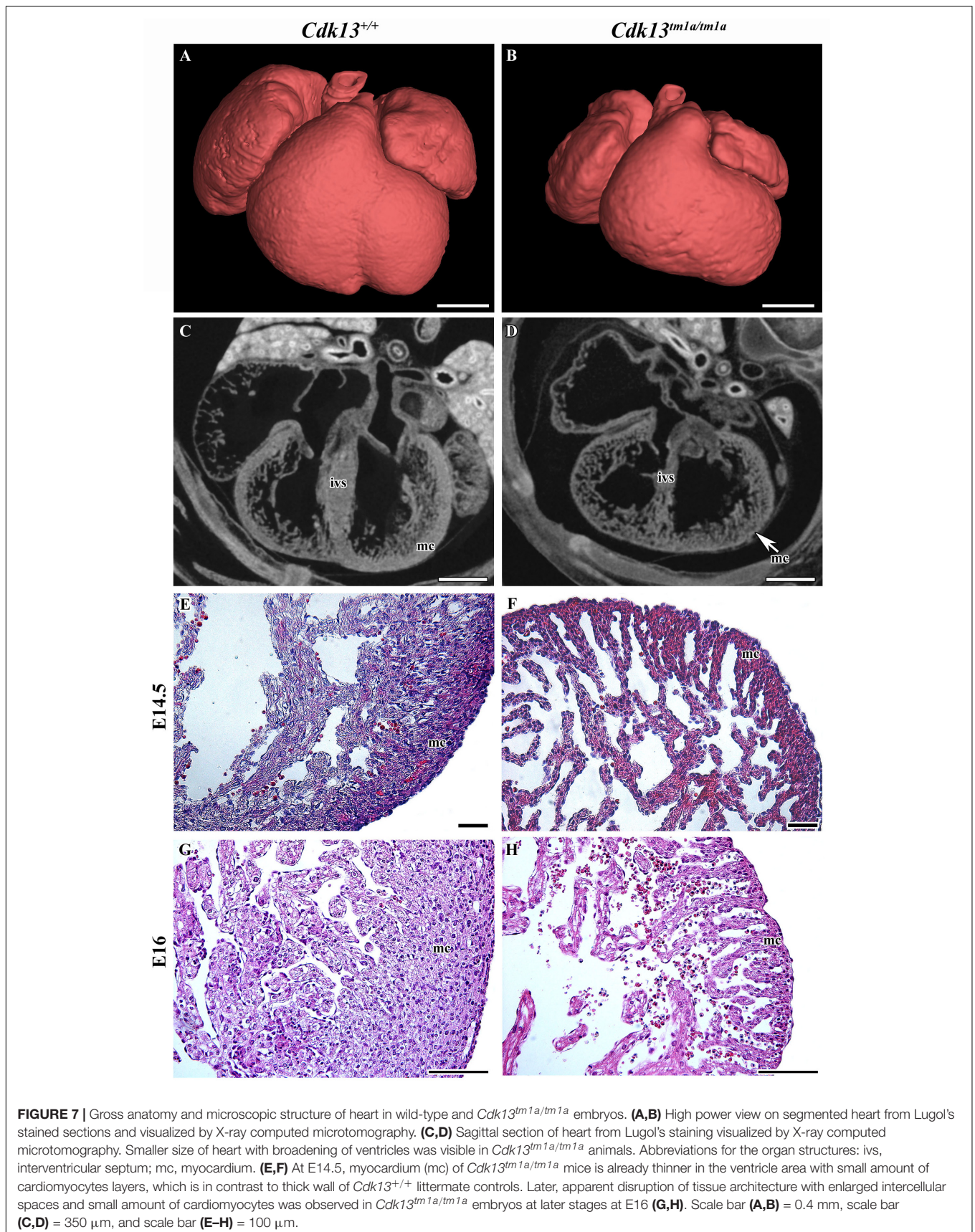


TABLE 2 | Summary of ultrasound scanned embryos at E14.5 and E15.5.

Stage	Number of embryos			Litters	Number of <i>Cdk13^{tm1a/tm1a}</i>	
	<i>Cdk13^{+/+}</i>	<i>Cdk13^{tm1a/+}</i>	<i>Cdk13^{tm1a/tm1a}</i>		Heart beating	Dying/dead
E14.5	11	27	9	6	8	1
E15.5	14	36	17	8	6	11

Comparison of *Cdk13^{tm1a/tm1a}* and *Cdk13^{tm1d/tm1d}* Mice at E13.5

Finally, the phenotype of *Cdk13^{tm1a/tm1a}* mice was compared to *Cdk13^{tm1d/tm1d}* mice (Figure 11 and Supplementary Figures S7, S8). High-contrast differentiation resolution by X-ray computed microtomography was used to assess gross morphology of the *Cdk13^{+/+}*, *Cdk13^{tm1a/tm1a}* and *Cdk13^{tm1d/tm1d}* embryos at E13.5. Both *Cdk13* mutants exhibited smaller body size with severe growth retardation in *Cdk13^{tm1d/tm1d}* animals (Figures 11A–D). Hypoplasia of midfacial structures was observed in *Cdk13^{tm1d/tm1d}* embryos (Figure 11, compare H to G). The hearts were smaller in both *Cdk13^{tm1a/tm1a}* as well as *Cdk13^{tm1d/tm1d}* embryos in comparison to littermate control mice with severe ventricle deficiency detected in *Cdk13^{tm1d/tm1d}* animals (Figure 11, compare J to I and L to K). Generally smaller liver were detected in *Cdk13^{tm1a/tm1a}* and *Cdk13^{tm1d/tm1d}* embryos in comparison to control *Cdk13^{+/+}* mice. Liver in *Cdk13^{tm1d/tm1d}* mice exhibited abrogated liver lobes arrangement (Figure 11, compare P to O and N to M). Kidneys in *Cdk13^{tm1d/tm1d}* mice do not follow right left kidney asymmetry (Figure 11, compare T to S).

DISCUSSION

Our analysis revealed a new function of *Cdk13* in the context of the mouse development and found that this protein is critical for proper development at later stages of embryogenesis. Loss of *Cdk13* affects negatively several organs and tissue structures during mouse development and its inactivation leads to late embryonic lethality.

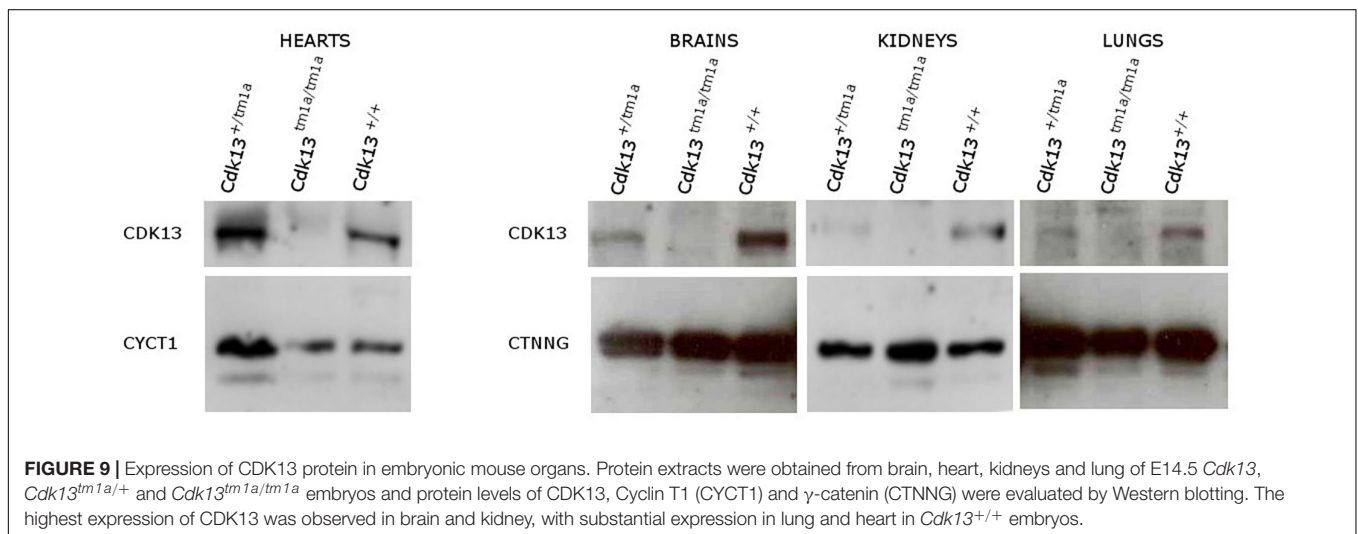
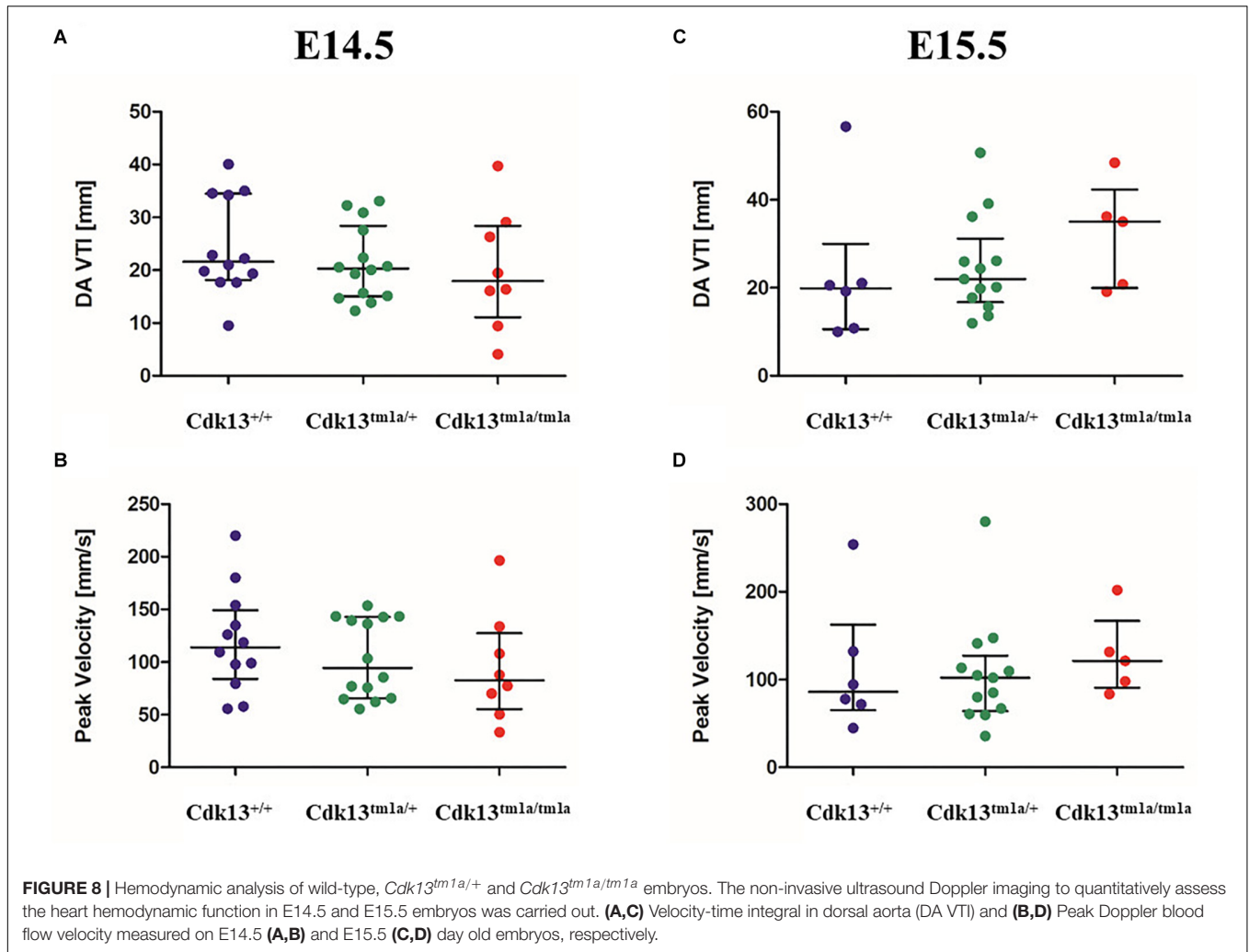
Animals with hypomorphic allele (*Cdk13^{tm1a}*) retained low residual expression of CDK13 and they were lethal by E16.5 most due to heart failure and delayed development of several organs was caused likely due to insufficient supply of oxygen and nutrients. Interestingly, several miRNAs able to target *Cdk13* mRNA for degradation were recently recognized during the acute myocardial infarctions (Wang et al., 2015) supporting the idea of CDK13 as a strategic molecule for optimal heart function. In addition, the expression of CDK13 was detectable not just in the heart, but also in other organs during embryonic development, such as craniofacial area or brain. However, the expression only cannot explain the complexity of phenotype exclusively in tissue autonomous manner or by insufficient nutrients and oxygen distribution. Thus, we assume that the organs with higher expression might be affected either by non-functional CDK13 in cell autonomous manner and/or by underdevelopment of

cardiovascular system and lack of nutrients, mostly by insufficient heart function. Importantly, the affected cardiovascular system is superior to development of other organ systems and can drive systemic developmental phenotype; the example of such phenotype is growth retardation in the whole embryo with no respect to local CDK13 expression levels, which is affecting size of all organs within the embryo body. Therefore, in organs where the expression of CDK13 is under detection limit, we suggest that the phenotype is caused mostly by failure of cardiovascular system development and its systemic influence.

It is also interesting why the *Cdk13^{tm1a}* allele exhibits the hypomorphic mutant phenotype. One possible explanation might be due to the insertion of neomycin selection cassette in non-coding region that has been shown to affect gene expression, both at the DNA and RNA levels (Pham et al., 1996; Meyers et al., 1998; Scacheri et al., 2001). Moreover, *in silico* analyses of post-transcriptional exon shuffling (PTES) events in humans revealed high PTES frequencies in *CDK13* gene enabling the formation of aberrant functional CDK13 transcripts (Al-Balool et al., 2011).

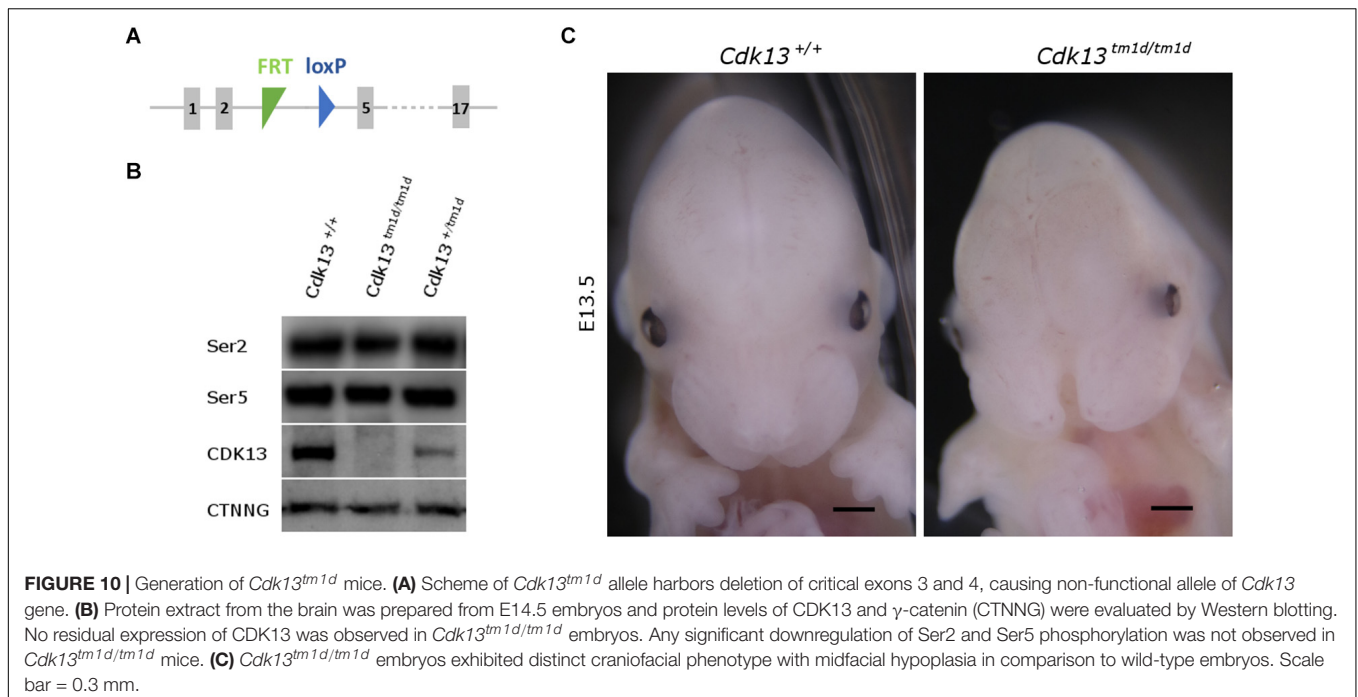
In contrast to our observations, genetic depletion of *Cdk12*, a kinase with high amino acid similarity to *Cdk13*, resulted in early developmental lethality at the blastocyst stage due to deregulated expression of DNA-damage repair genes leading to enhanced genomic instability (Juan et al., 2016). Importantly, KO of *CycK* resembled the same lethal phenotype at the blastocyst stage as *Cdk12* animals (Blazek et al., 2011). Besides clear effect of *CycK* during preimplantation stage, *CycK* is highly expressed in mouse embryonic stem cells and testes in a developmentally regulated manner (Dai et al., 2012). During neonatal spermatogenesis, *CycK* is highly expressed in gonocytes, spermatogonial stem cells and is absent in differentiating spermatogonia, spermatids and spermatozoa (Xiang et al., 2014). Similar expression in testes, ovary and uterus was also documented for CDK13 in our heterozygous mice.

Downregulation of *Cdk13* had also significant impact on brain development. It is known from previous studies that *CycK*, a *Cdk13* binding partner, has been identified in a genome-wide screen as one of the factors involved in the formation of the nervous system in *Drosophila* (Neumuller et al., 2011). In parallel, function of CDK12 in process of embryonic neural development was described in the conditional KO mouse model for this gene (Chen et al., 2014, 2017). When neuronal differentiation model of mouse embryonic carcinoma cell (P19) was employed, CDK12 and CDK13 kinases participated in the axonal elongation through a common signaling pathway that modulates protein expression of CDK5 (Chen et al., 2014). Recently, CDK13 was found remarkably dysregulated in hippocampus and suggested



as one of the hub genes useful to elucidate Alzheimer's disease (Pang et al., 2017). Importantly, studies of patients with *CDK13* mutations suggested their essential role in brain development. As

demonstrated in **Figure 5**, we were able to observe alteration of proliferation in neural tissue in *Cdk13^{tm1a}* mice (as analyzed by Ki67 expression) however overall changes in brain morphology



were not determined. On the other hand, observed proliferation changes can be also associated with developmental delay of *Cdk13^{tm1a}* animals and subventricular zone in brains may significantly expands later in development. However, it is also possible that a prominent role of CDK13 may be apparent in later stages of brain development, for instance, in the axon pathfinding, synapse formation and etc. Confirmation of this statement, however, has to be proven in future by employing the nestin-Cre or CreErt-Flox systems.

Importantly, developmental defects within craniofacial formation was documented for *Cdk13^{tm1a}* mice followed by complete loss of frontonasal part in *Cdk13^{tm1d}* mice. It is probably the most surprising observation in respect to patients with heterozygous mutation of *CDK13* gene (Sifrim et al., 2016; Bostwick et al., 2017; Carneiro et al., 2018; Hamilton et al., 2018). Moreover, gradual deregulation of CDK13 in mice resulted in enhanced craniofacial phenotype. The hypomorphic *Cdk13^{tm1a}* mice exhibited in the rostral area, altered shape of nasal septa and later at E15.5, incomplete formation of the secondary palate was observed in several animals, where palatal shelves

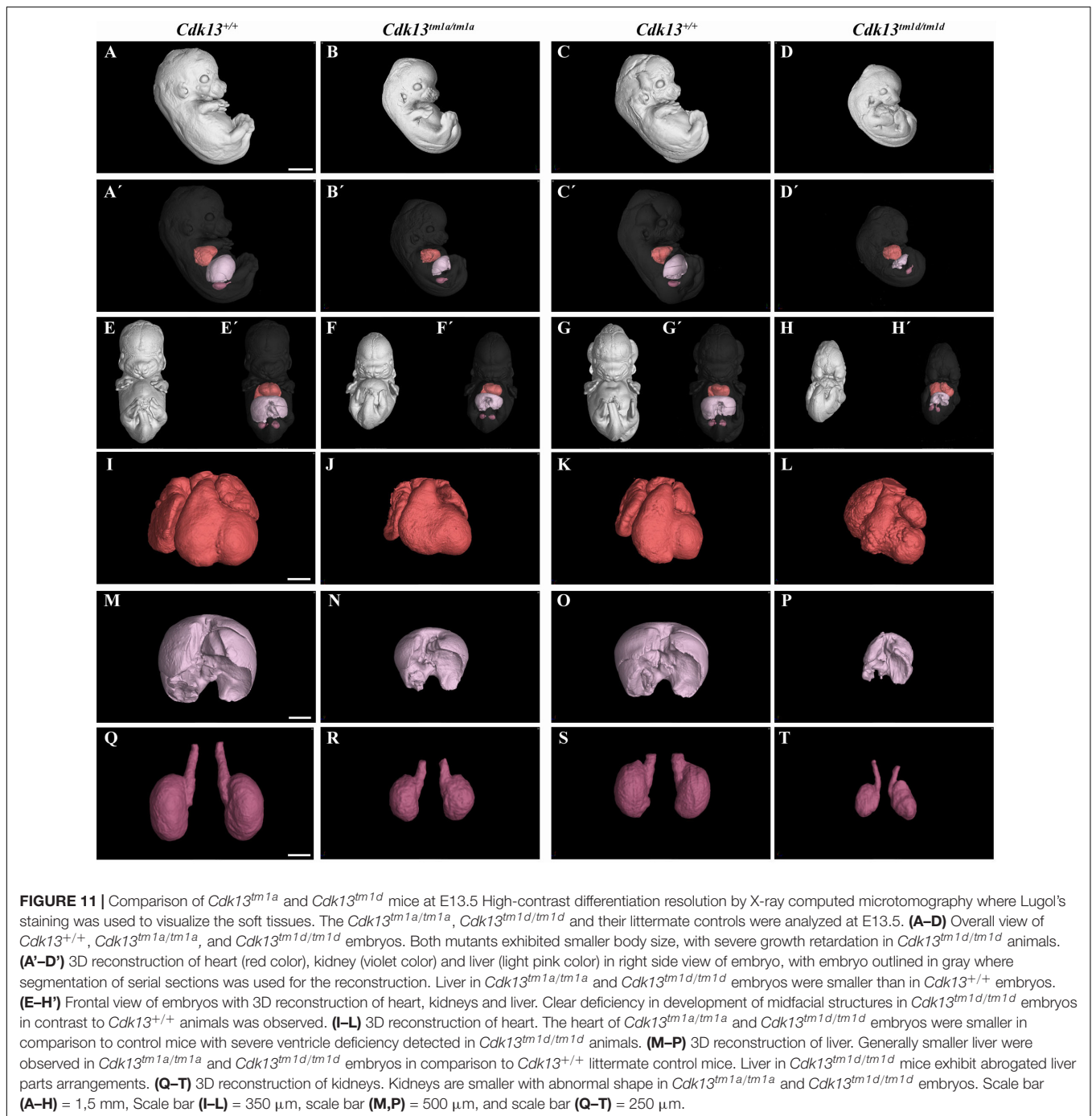
did not reach the midline, while control animals exhibited complete fusion of palatal processes. Nevertheless, complete depletion of CDK13 in the *Cdk13^{tm1d/tm1d}* mice led to ablation of the midline area of the head. There is a limited information regarding the role of CDK13 in this developmental process at the moment, yet. The association between SNP polymorphism rs373711932 located within *CDK13* gene and cranial base width was recently documented (Lee et al., 2017). Importantly, heterozygous copy number loss of *CCNK* gene in humans caused a syndromic neurodevelopmental disorder with distinctive facial dysmorphism (Fan et al., 2018). Therefore, it seems highly probable that CDK13 is indeed associated with craniofacial development, however, with unclear function, which will be necessary to uncover in the future.

From the functional point of view, it is surprising that only heterozygous mutation in one allele of the *CDK13* gene was sufficient to cause the CHDFIDD in human patients. Common feature in all studies depicting deleterious effect of pathogenic CDK13 in patients was presence of missense substitutions in the protein kinase domain around ATP-binding and magnesium binding sites (Sifrim et al., 2016; Bostwick et al., 2017; Hamilton et al., 2018). In addition, two nonsense variants and a frame-shift variant accompanying production of aberrant CDK13 transcripts have been identified (van den Akker et al., 2018). Based on crystal structure of CDK13/CycK complex, it is very possible that all these mutations most likely caused inactivation of catalytic activity of CDK13 or disrupted binding of CycK, its associating partner, leading to abrogated function of CDK13 (Kohoutek and Blazek, 2012; Greifenberg et al., 2016; Hamilton et al., 2018). Nevertheless, some of identified mutations in patients were predicted to retain binding to cyclin K with affected catalytic activity. If this is the case, then CDK13/CycK complex represents

TABLE 3 | Genotypes of offspring from *Cdk13^{tm1d/+}* intercross.

Stage	<i>Cdk13</i> ^{+/+}	<i>Cdk13</i> ^{tm1d/+}	<i>Cdk13</i> ^{tm1d/tm1d}	Litter	Empty decidua
	(25%)	(50%)	(25%)		
E12.5	33 (27.5%)	69 (57.5%)	18 (15%)*,#	18	24
E13.5	29 (31.5%)	52 (56.5%)	11 (12%)*,#	14	5
E14.5	24 (31.2%)	44 (57.1%)	9 (11.7%)*,#	10	4

*Growth retardation. #Dead embryos.



a dominant negative complex in cells (Hamilton et al., 2018). It is of note that two patients carrying stop codons at the end of the kinase domain represented milder phenotypes, although obvious genotype-phenotype correlation has not been recorded (van den Akker et al., 2018). From all these results, we can postulate that even loss of function of one *CDK13* allele is enough to interfere with developmental pathways and cause the CHDFIDD in humans, while complete abrogation of *CDK13* gene would lead to embryonic lethality as documented in our mouse model.

Currently, we can only speculate how CDK13 contributes to the developmental processes: if it participates in phosphorylation of Ser2 within CTD of RNAPII, it is highly probable that inhibition of CDK13 will block or dramatically affect ability of RNAPII to effectively synthesize nascent RNA. CDK13 was demonstrated to bind various splicing factors or proteins involved in splicing (Davidson et al., 2014; Bartkowiak and Greenleaf, 2015; Liang et al., 2015). Moreover, CDK13 was found to associate with ASF/SF2 factor, a member of the

spliceosome complex (Even et al., 2006). CDK13 was also identified in perinucleolar compartments enriched for proteins primarily implicated in pre-mRNA processing; therefore, lack of CDK13 could abrogate also RNA processing of given metazoan genes (Even et al., 2016). Thus, it is possible that a loss of kinase activity or associating potential of CDK13 will cripple proper splicing of transcribed RNA by RNAPII resulting in production of improperly spliced mRNA of proteins engaged in development processes.

It has been postulated that CDK13 phosphorylates Ser2 and Ser5 within CTD of RNAPII, if Ser7 is prephosphorylated at the C terminus of heptapeptide (Greifenberg et al., 2016). However, we were not able to detect any effect on Ser2 or Ser5, either in *Cdk13^{tm1a/tm1a}* or *Cdk13^{tm1d/tm1d}* animals with substantial decreased level of CDK13 in developing brain, where physiologically high level of CDK13 is present. Even though the global effect on Ser2 or Ser5 was not documented in *Cdk13^{tm1a/tm1a}* developing brains, CDK13 could still orchestrate phosphorylation of RNAPII at the specific sets of genes as earlier described for the CDK9/cyclin T2 or CDK12/cyclin K complexes in mouse and human cells (Zhu et al., 2009; Blazek et al., 2011; Johnson et al., 2016). When CDK13 was downregulated in HCT116 cells, gene ontology analysis revealed enrichment of functions connected to various extracellular and growth signaling pathways (Liang et al., 2015; Greifenberg et al., 2016). Similar *modus operandi* was implicated for CDK9 activation by MEK-1 and MSK1 in response to extracellular cues (Fujita et al., 2008; Smerdova et al., 2014). In addition, transcriptional kinase CDK8 was described to affect canonical Notch signaling by targeting activated *Notch* intracellular domain for proteasomal degradation (Fryer et al., 2004). In addition, CDK8 was suggested to stabilize β -catenin interaction with the promoter of WNT targets to achieve regulatory control (Firestein et al., 2008). Therefore, it is possible to envision that CDK13 regulates a specific set of genes at a specific developmental stage of embryonic development or in specialized cell types. Therefore, it will be critical in the near future to identify unique genes under control of CDK13 at given tissue or organ by employment of exome RNA-sequencing analyses in WT and *Cdk13*-deficient mice, which will be our next goal.

We believe that the *Cdk13^{tm1a}* hypomorphic mouse can be a very instrumental animal model to delineate cellular pathways or mechanisms participating in the onset or propagation of severe developmental cues in humans with mutated form of CDK13. Moreover, our *Cdk13^{tm1d}* mouse model with enhanced craniofacial phenotype may be invaluable for further clarification of molecular processes, which are responsible for clinical symptoms of human patients.

EXPERIMENTAL PROCEDURES

Mice, Genotyping, Breeding of *Cdk13^{tm1a}* Mice

Mouse embryos (*Cdk13^{tm1a}(EUCOM)HmgU*) bearing splicing acceptor, β -galactosidase and neomycine resistance gene both with poly A signals (Figure 1A) were obtained from

the Infrafrontier Research Infrastructure–Mouse disease Models¹. The acquired embryos carrying *Cdk13^{tm1a}* allele were transferred into pseudopregnant females of C57BL/6N mouse strain and the heterozygous *Cdk13^{tm1a}* mice were obtained at the Transgenic and Archiving Module, CCP (IMG, Prague, Czechia). Heterozygous mice for *Cdk13^{tm1a}* allele were bred and newborn mice were genotyped by PCR amplification (94°C, 30 s; 62°C/65°C, 20 s; 72°C, 30 s; 35 cycles) of *Cdk13* gene to distinguish WT (*Cdk13^{+/+}*) and *Cdk13^{tm1a/tm1a}* alleles. For PCR analysis, the following sets of primers were used for KO and WT alleles: (KOf, 5'-CCA GCT TTA AAG GCG CAT AAC-3'; KOr, 5'-TGA CCT TGG GCA AGA ACA TAA-3'; WtF, 5'-TAG CTG GCC AAT GAG CTT TC-3'; WtR, 5'-AGT CTA GGA AGC TGG GAA GAT- 3'). Primers KOf and KOr amplify a 257-bp fragment from *Cdk13^{tm1a}* allele while primers WtF and WtR amplify a 179-bp fragment from WT allele. Genomic DNA was isolated from mouse ears by NaOH extraction (Truett et al., 2000). Heterozygous mice carrying *Cdk13^{tm1a}* allele were bred and after mating, females were examined for vaginal plugs, embryonic day 0.5 (E0.5) was determined at noon at the day of vaginal plaque record. Embryos at various stages were obtained from uteri of pregnant heterozygous female mice, genotyped and the Mendelian ratios were defined.

To generate mouse carrying the *Cdk13^{tm1d}* allele, the *Cdk13^{tm1a/tm1a}* mice were crossed with the Flp-deleter mouse strain *Gt(ROSA)26Sor^{tm2(CAG- β po,-EYFP)lcs}* (MGI: 5285396, Philippe Soriano) and Cre-deleter strain *Gt(ROSA)26Sor^{tm1(ACTB-cre,-EGFP)lcs}* (MGI: 5285392, Philippe Soriano) in order to delete critical exons 3 and 4 within *Cdk13* gene. All animal procedures were performed in strict accordance to the Guide for the Care and Use of Laboratory Animals and approved by the Institutional Animal Care and Use Committee (Veterinary Research Institute, Brno, Czechia).

Western Blotting

Particular organ from *Cdk13^{tm1a/tm1a}*, *Cdk13^{tm1a/+}* and *Cdk13^{+/+}* embryos at E14.5 were lysed in lysis buffer (100 mM Tris, pH 7.4; 1% SDS; 10% glycerol) and sonicated. The brain from *Cdk13^{tm1d/tm1d}*, *Cdk13^{tm1d/+}* and *Cdk13^{+/+}* were lysed in lysis buffer (100 mM Tris, pH 7.4; 1% SDS; 10% glycerol) and sonicated. Concentrations of total proteins were determined with bicinchoninic acid (BCA). Lysates were diluted to the same concentration, mixed with the 3xLaemmli sample buffer and boiled for 5 min. Western blotting was performed using anti-mouse CDK13 polyclonal antibody (SAB1302350, Sigma-Aldrich), γ -catenin (CTNNG) antibody (2309, Cell Signaling Technology), cyclin T1 (CYCT1) (sc-10750, Santa Cruz Biotechnology) and anti-serine 2 (Ser2) and serine 5 (Ser5) rat monoclonal antibodies (clones 3E10 and 3E8 respectively, ChromoTek GmbH, Germany).

Histological Analysis

Wild-type and homozygous *Cdk13^{tm1a/tm1a}* embryos at E14.5 to E16.5 were fixed in 4% paraformaldehyde and dehydrated. After that hearts, brains, kidneys and livers were dissected,

¹<https://www.infrafrontier.eu/>

embedded in paraffin, and sectioned at 5 μm . Hematoxylin-eosin (H&E) staining was performed. Images were taken under bright field using a Leica compound microscope (DMLB2) with a Leica camera (DFC480) attached (Leica Microsystems, Wetzlar, Germany).

Immunohistochemistry

Proliferating cells were visualized on E14.5 brain sections by labeling of Ki67 (positive cells are brown). Sections were pretreated in Citrate buffer, pH6, 10 mM, 20 min/97°C in water bath and were labeled with Ki67 primary antibody (RBK027-05, Zytomed Systems). For primary antibody detection, specific secondary antibody and avidin-biotin complex were used (Vectastain kit, PK-6101, Vector laboratories). The signal was developed by DAB chromogen system (K3468, DAKO). Nuclei were counterstained by hematoxylin (blue). Mitotic index was counted as the ratio between Ki67-positive cells and total amount of cells in three biological samples for each group (three *Cdk13*^{+/+} embryos, three *Cdk13*^{tm1a/tm1a} embryos). Statistical significance in cell number differences between control and deficient mice were evaluated by unpaired *t*-test.

E14.5 heart sections were pretreated in DAKO Target Retrieval (32367, DAKO) solution for 15 min/97°C in water bath and labeled using primary antibodies against actin (sc-1615-R, Santa Cruz Biotechnology) and myosin (sc-32732, Santa Cruz Biotechnology). To detect primary antibodies, secondary Alexa Fluor antibodies (A11004, A11008, Invitrogen) were used. Nuclei were counterstained by DRAQ5TM (62251, Thermo Scientific). Images were captured on fluorescence confocal microscope Leica SP8 (Leica).

Micro-Computed Tomography (micro-CT)

The embryos at E13.5 or E15.5 were contrasted with Lugol's solution to visualize gross morphology of individual soft tissues by microCT. For the purpose of motion stabilization during the micro CT scan, mouse embryo was embedded in 1% agarose gel in Falcon conical centrifuge tube. The micro-CT scan was performed using laboratory system GE Phoenix v|tome|x L 240 (GE Sensing & Inspection Technologies GmbH, Germany), equipped with a 180 kV/15W maximum power nanofocus X-ray tube and high contrast flat panel detector DXR250 2048 px \times 2048 px with 200 μm \times 200 μm pixel size. The measurement was carried out in the air-conditioned cabinet (21°C) at acceleration voltage of 60 kV and X-ray tube current of 200 μA . Thousand nine hundred projections were taken over 360° with exposure time 900 ms resulting in 5.5 μm voxel resolution. The tomographic reconstruction was realized by software GE phoenix datos|x 2.0 (GE Sensing & Inspection Technologies GmbH, Germany). Reconstructed slice data were processed using VG Studio MAX 3.1 software (Volume Graphics GmbH, Germany) and segmentation of liver, kidneys and heart was completed manually.

Embryonic Ultrasound Imaging and Doppler Echocardiography

Pregnant females were anesthetized on gestational day 14.5 or 15.5 (before noon) with an isoflurane/oxygen mixture (anesthesia was initiated with 3–4%, and maintained with 1–2% isoflurane), and maintained on a temperature-controlled mouse platform (with sensors for monitoring of maternal electrocardiogram, respiration and core body temperature). Maternal temperature was maintained at 34–37°C, and maternal heart beat at \sim 400 beats/minute by adjusting the level of anesthesia. An incision of about 2–3 cm in the lower abdomen was made, and a uterine horn was externalized through the incision to provide imaging access. The number of fetuses in right and left uterine horns was counted from the mother's bladder and later during echocardiographic imaging, labeled as R1, R2, R3, etc (right side) and L1, L2, L3, etc (left side). Pre-warmed ultrasound gel (37°C) without bubbles was applied between the individual fetuses and the transducer. B-mode imaging scanning of the whole embryo with the focus on the heart and Color Doppler and PW Doppler measurements for heart aorta and dorsal aorta were obtained using a high-frequency ultrasound system (Vevo 2100, FUJIFILM VisualSonics, Inc., Toronto, ON, Canada) equipped with a MS-550S transducer operating at a center frequency of 44 MHz. At the end of imaging of all fetuses, the mother was sacrificed by cervical dislocation and a small piece of yolk sac of each fetus was taken for genotyping.

DATA AVAILABILITY

All datasets generated for this study are included in the manuscript and/or the **Supplementary Files**.

ETHICS STATEMENT

All animal procedures were performed in strict accordance to the Guide for the Care and Use of Laboratory Animals and approved by the Institutional Animal Care and Use Committee (Veterinary Research Institute, Brno, Czechia).

AUTHOR CONTRIBUTIONS

JKo conceptualized and supervised the project, acquired the funding, wrote the original draft, and administrated the project. MN conceptualized the project, contributed to formal analysis, investigation, and visualization, and wrote, review, and edited the manuscript. DV contributed to investigation and visualization. MH contributed to formal analysis, investigation, and visualization. JP contributed to conceptualization, formal analysis, supervision, and investigation and wrote, review, and edited the manuscript. SP and MP contributed to investigation and visualization. RS supervised the project. MK, TZ, and JKa contributed to software development and visualization. H-CJ contributed to investigation, and wrote, review, and edited the manuscript. M-JF and MB contributed to formal analysis, supervision, writing, review, and editing.

FUNDING

This research was supported by grants n. 16-24043J of the Czech Science Foundation to JKo, MN, and DV. The research for this manuscript was financially supported by the Ministry of Agriculture n. MZE-RO0518, by the Ministry of Education, Youth and Sports, n. LM2015040 and LQ1604 by, and by the Ministry of Education, Youth and Sports and European Fund for Regional Development n. OP RDE CZ.02.1.01/0.0/0.0/16_013/0001789 and n. OP RDI CZ.1.05/1.1.00/02.0109 and OP RDI CZ.1.05/2.1.00/19.0395 to JP, MP, SP, and RS. Work by MB and MH was supported by the Ministry of Education, Youth and Sports of the Czech Republic (CZ.02.1.01/0.0/0.0/15_003/0000460). The cooperation between MB and TZ labs is supported by the Czech Science Foundation (17-14886S). MicroCT analyses performed by MK, TZ, and JKa were carried out under the project CEITEC 2020 (LQ1601) with financial support from the Ministry of Education, Youth and Sports of the Czech Republic under the National Sustainability Program II. Work by H-CJ and M-JF was supported by Ministry of Science and Technology, Taiwan (MOST 106-2811-B-010-046 and MOST 105-2923-B-010 -002 -MY3).

ACKNOWLEDGMENTS

We would like to thank Assoc. Prof. S. Sevcikova for a critical comments to the manuscript and other members of the laboratory for helpful inputs.

SUPPLEMENTARY MATERIAL

The Supplementary Material for this article can be found online at: <https://www.frontiersin.org/articles/10.3389/fcell.2019.00155/full#supplementary-material>

FIGURE S1 | Truncated form of CDK13 protein. **(A)** Predicted amino acid sequence of truncated CDK13 protein due to transcriptional block mediated by two Poly A sites introduced into the intron 2 as part of trap vector in mice bearing *Cdk13^{tm1a}* allele. Black and Blue capital letters represent amino acids encoded within Exon 1 and Exon 2 of *Cdk13* gene, respectively. Predicted Molecular weight of truncated *CDK13* protein is 66.22 kDa (https://www.bioinformatics.org/sms/prot_mw.html). **(B)** Brain extracts were prepared from E14.5 embryos of given genotype and protein levels of wild-type and truncated form of CDK13 was evaluated by Western Blotting. The antibody used throughout our study recognizes N-terminal part of CDK13, which is expressed in both forms of Cdk13, wild-type as well as truncated one. The *Cdk13^{+/+}* mice contained only the wild-type CDK13 protein (WT-CDK13). The heterozygous *Cdk13^{tm1a/+}* mice

REFERENCES

- Al-Balool, H. H., Weber, D., Liu, Y., Wade, M., Guleria, K., Nam, P. L., et al. (2011). Post-transcriptional exon shuffling events in humans can be evolutionarily conserved and abundant. *Genome Res.* 21, 1788–1799. doi: 10.1101/gr.116442.110
- Bakre, A., Andersen, L. E., Meliopoulos, V., Coleman, K., Yan, X., Brooks, P., et al. (2013). Identification of host kinase genes required for Influenza virus replication and the regulatory role of MicroRNAs. *PLoS One* 8:e66796. doi: 10.1371/journal.pone.0066796

included wild-type (WT-CDK13) and truncated (TR-CDK13) forms of CDK13 protein. The *Cdk13^{tm1a}* expressed the truncated form of CDK13 and minor wild-type CDK13 as demonstrated by immunoblot.

FIGURE S2 | Comparison of gross morphology of *Cdk13*-deficient mice phenotype. **(A–H)** Wild-type *Cdk13^{+/+}*, **(I–P)** heterozygous *Cdk13^{tm1a/+}*, and **(Q–X)** *Cdk13^{tm1a}* embryos at various stages. Growth retardation of *Cdk13*-deficient mice was apparent from early developmental stages **(Q,R)**. Some embryos exhibited nuchal edema and peripheral hypervascularization **(U)** and abnormal craniofacial shape **(S,T)**. Developmental delay was observed at later stages **(V,W)**. At E16.5, each of the *Cdk13^{tm1a/tm1a}* embryos was undergoing resorption **(X)**. No morphological differences between wild-type and heterozygous embryos were observed. Scale bar = 0.1 mm.

FIGURE S3 | The 3D reconstruction of selected organs in micro-CT of control *Cdk13^{+/+}* and *Cdk13^{tm1a/tm1a}* embryos. Overall view on embryos of *Cdk13^{+/+}* **(A)** and *Cdk13^{tm1a/tm1a}* **(B)** with 3D reconstruction of heart, liver and kidney (left). Gross morphology is well visible on movable model on the right side. To visualize only one organ, click on the lower row and select heart (orange), liver (pink) or kidney (purple) organ only. Scale bar = 1 mm.

FIGURE S4 | Transversal sections of the head of control *Cdk13^{+/+}* and *Cdk13^{tm1a/tm1a}* embryos. Transversal sections through the mouse head with details of the nasal cavity area. At E14.5, no obvious differences were observed and only one epithelial protrusion (marked by arrow) were developed close to each nasal cavity (nc) (compare **A** to **D**). Later at E15.5, the number of nasal glands was reproducibly smaller in *Cdk13^{tm1a/tm1a}* mice in comparison to control animals (compare **B** to **E**). **(C,F)** Coronal section through the head of embryos at the level of the eyes. White arrows depict different complexity of the nasal cavity in wild-type, *Cdk13^{+/+}*, and *Cdk13^{tm1a/tm1a}* animals. Abbreviations nc – nasal cavity, arrowhead – nasal gland. Scale bar **(A,B,D,F)** = 100 μ m and scale bar **(C,F)** = 1 mm.

FIGURE S5 | Immunohistochemical detection of myosin and actin in the heart of *Cdk13^{+/+}* and *Cdk13^{tm1a/tm1a}* embryos. Sagittal sections through the mouse heart were prepared and immunohistochemical detection of myosin and actin was carried out with specific antibodies. Decreased expression of myosin was detected in ventricle myocardium, compare B and B' to E and E'. Scale bar **(A,D)** = 500 μ m; Scale bar **(B–F)**, without D) – 100 μ m.

FIGURE S6 | The expression of *Cdk13* in adult mouse organs visualized by β -galactosidase activity. The expression of *Cdk13* was examined by activity of β -galactosidase in adult mouse organs **(A)** eye, **(B)** heart, **(C)** thyroid gland, **(D)** urinary bladder, **(E)** kidney, **(F)** uterus, **(G)** gall bladder, **(H)** testes, and **(I)** ovary.

FIGURE S7 | Sagittal sections through heads of *Cdk13^{tm1a}* and *Cdk13^{tm1d}* and *Cdk13^{tm1a}* and *Cdk13^{tm1d}* mice. High-contrast differentiation resolution by X-ray computed microtomography where Lugol's staining was used to visualize the soft tissues. The *Cdk13^{tm1a/tm1a}*, *Cdk13^{tm1d/tm1d}* and their littermate controls are displayed at E13.5 to show overall developmental delay.

FIGURE S8 | Horizontal sections through heads of *Cdk13^{tm1a}* and *Cdk13^{tm1d}* mice. High-contrast differentiation resolution by X-ray computed microtomography where Lugol's staining was used to visualize the soft tissues. The *Cdk13^{tm1a/tm1a}*, *Cdk13^{tm1d/tm1d}* and their littermate controls are displayed at E13.5.

TABLE S1 | The prevalence of developmental defects in *Cdk13^{tm1a}* and *Cdk13^{tm1d}* transgenic mice.

- Bartkowiak, B., and Greenleaf, A. L. (2015). Expression, purification, and identification of associated proteins of the full-length hCDK12/CyclinK complex. *J. Biol. Chem.* 290, 1786–1795. doi: 10.1074/jbc.M114.612226
- Bartkowiak, B., Liu, P., Phatnani, H. P., Fuda, N. J., Cooper, J. J., Price, D. H., et al. (2010). CDK12 is a transcription elongation-associated CTD kinase, the metazoan ortholog of yeast Ctk1. *Genes Dev.* 24, 2303–2316. doi: 10.1101/gad.1968210
- Berro, R., Pedati, C., Kehn-Hall, K., Wu, W., Klase, Z., Even, Y., et al. (2008). CDK13, a new potential human immunodeficiency virus type 1 inhibitory

- factor regulating viral mRNA splicing. *J. Virol.* 82, 7155–7166. doi: 10.1128/JVI.02543-07
- Blazek, D., Kohoutek, J., Bartholomeeusen, K., Johansen, E., Hulinkova, P., Luo, Z., et al. (2011). The Cyclin K/Cdk12 complex maintains genomic stability via regulation of expression of DNA damage response genes. *Genes Dev.* 25, 2158–2172. doi: 10.1101/gad.16962311
- Bostwick, B. L., McLean, S., Posey, J. E., Streff, H. E., Gripp, K. W., Blesson, A., et al. (2017). Phenotypic and molecular characterisation of CDK13-related congenital heart defects, dysmorphic facial features and intellectual developmental disorders. *Genome Med.* 9:73. doi: 10.1186/s13073-017-0463-8
- Carneiro, T. N., Krepischi, A. C., Costa, S. S., Tojal da Silva, I., Vianna-Morgante, A. M., Valieris, R., et al. (2018). Utility of trio-based exome sequencing in the elucidation of the genetic basis of isolated syndromic intellectual disability: illustrative cases. *Appl. Clin. Genet.* 11, 93–98. doi: 10.2147/TACG.S165799
- Chen, H. R., Juan, H. C., Wong, Y. H., Tsai, J. W., and Fann, M. J. (2017). Cdk12 Regulates Neurogenesis and Late-Arising Neuronal Migration in the Developing Cerebral Cortex. *Cereb. Cortex* 27, 2289–2302. doi: 10.1093/cercor/bhw081
- Chen, H. R., Lin, G. T., Huang, C. K., and Fann, M. J. (2014). Cdk12 and Cdk13 regulate axonal elongation through a common signaling pathway that modulates Cdk5 expression. *Exp. Neurol.* 261, 10–21. doi: 10.1016/j.expneurol.2014.06.024
- Cheng, S. W., Kuzyk, M. A., Moradian, A., Ichu, T. A., Chang, V. C., Tien, J. F., et al. (2012). Interaction of cyclin-dependent kinase 12/CrkRS with cyclin K1 is required for the phosphorylation of the C-terminal domain of RNA polymerase II. *Mol. Cell. Biol.* 32, 4691–4704. doi: 10.1128/MCB.06267-11
- Dai, Q., Lei, T., Zhao, C., Zhong, J., Tang, Y. Z., Chen, B., et al. (2012). Cyclin K-containing kinase complexes maintain self-renewal in murine embryonic stem cells. *J. Biol. Chem.* 287, 25344–25352. doi: 10.1074/jbc.M111.321760
- Davidson, L., Muniz, L., and West, S. (2014). 3' end formation of pre-mRNA and phosphorylation of Ser2 on the RNA polymerase II CTD are reciprocally coupled in human cells. *Genes Dev.* 28, 342–356. doi: 10.1101/gad.231274.113
- Deciphering Developmental Disorders Study (2017). Prevalence and architecture of de novo mutations in developmental disorders. *Nature* 542, 433–438. doi: 10.1038/nature21062
- Even, Y., Durieux, S., Escande, M. L., Lozano, J. C., Peaucellier, G., Weil, D., et al. (2006). CDC2L5, a Cdk-like kinase with RS domain, interacts with the ASF/SF2-associated protein p32 and affects splicing in vivo. *J. Cell. Biochem.* 99, 890–904. doi: 10.1002/jcb.20986
- Even, Y., Escande, M. L., Fayet, C., and Genevriere, A. M. (2016). CDK13, a Kinase Involved in Pre-mRNA Splicing, Is a Component of the Perinuclear Compartment. *PLoS One* 11:e0149184. doi: 10.1371/journal.pone.0149184
- Fan, Y., Yin, W., Hu, B., Kline, A. D., Zhang, V. W., Liang, D., et al. (2018). De Novo mutations of CCNK cause a syndromic neurodevelopmental disorder with distinctive facial dysmorphism. *Am. J. Hum. Genet.* 103, 448–455. doi: 10.1016/j.ajhg.2018.07.019
- Firestein, R., Bass, A. J., Kim, S. Y., Dunn, I. F., Silver, S. J., Guney, I., et al. (2008). CDK8 is a colorectal cancer oncogene that regulates beta-catenin activity. *Nature* 455, 547–551. doi: 10.1038/nature07179
- Fryer, C. J., White, J. B., and Jones, K. A. (2004). Mastermind recruits CycC:CDK8 to phosphorylate the Notch ICD and coordinate activation with turnover. *Mol. Cell.* 16, 509–520. doi: 10.1016/j.molcel.2004.10.014
- Fujita, T., Ryser, S., Piuz, I., and Schlegel, W. (2008). Up-regulation of P-TEFb by the MEK1-extracellular signal-regulated kinase signaling pathway contributes to stimulated transcription elongation of immediate early genes in neuroendocrine cells. *Mol. Cell. Biol.* 28, 1630–1643. doi: 10.1128/mcb.01767-07
- Greenleaf, A. L. (2018). Human CDK12 and CDK13, multi-tasking CTD kinases for the new millennium. *Transcription* 10, 91–110. doi: 10.1080/21541264.2018.1535211
- Greifenberg, A. K., Honig, D., Pilarova, K., Duster, R., Bartholomeeusen, K., Bosken, C. A., et al. (2016). Structural and functional analysis of the Cdk13/Cyclin K complex. *Cell Rep.* 14, 320–331. doi: 10.1016/j.celrep.2015.12.025
- Hamilton, M. J., Caswell, R. C., Canham, N., Cole, T., Firth, H. V., Foulds, N., et al. (2018). Heterozygous mutations affecting the protein kinase domain of CDK13 cause a syndromic form of developmental delay and intellectual disability. *J. Med. Genet.* 55, 28–38. doi: 10.1136/jmedgenet-2017-104620
- Johnson, S. F., Cruz, C., Greifenberg, A. K., Dust, S., Stover, D. G., Chi, D., et al. (2016). CDK12 inhibition reverses de novo and acquired PARP inhibitor resistance in BRCA wild-type and mutated models of triple-negative breast cancer. *Cell Rep.* 17, 2367–2381. doi: 10.1016/j.celrep.2016.10.077
- Juan, H. C., Lin, Y., Chen, H. R., and Fann, M. J. (2016). Cdk12 is essential for embryonic development and the maintenance of genomic stability. *Cell Death Differ.* 23, 1038–1048. doi: 10.1038/cdd.2015.157
- Kim, H. E., Kim, D. G., Lee, K. J., Son, J. G., Song, M. Y., Park, Y. M., et al. (2012). Frequent amplification of CENPF, GMNN and CDK13 genes in hepatocellular carcinomas. *PLoS One* 7:e43223. doi: 10.1371/journal.pone.0043223
- Ko, T. K., Kelly, E., and Pines, J. (2001). CrkRS: a novel conserved Cdc2-related protein kinase that colocalizes with SC35 speckles. *J. Cell Sci.* 114, 2591–2603.
- Kohoutek, J. (2009). P-TEFb- the final frontier. *Cell Div.* 4:19. doi: 10.1186/1747-1028-4-19
- Kohoutek, J., and Blazek, D. (2012). Cyclin K goes with Cdk12 and Cdk13. *Cell Div.* 7:12. doi: 10.1186/1747-1028-7-12
- Lee, M. K., Shaffer, J. R., Leslie, E. J., Orlova, E., Carlson, J. C., Feingold, E., et al. (2017). Genome-wide association study of facial morphology reveals novel associations with *FREM1* and *PARK2*. *PLoS One* 12:e0176566. doi: 10.1371/journal.pone.0176566
- Liang, K., Gao, X., Gilmore, J. M., Florens, L., Washburn, M. P., Smith, E., et al. (2015). Characterization of human cyclin-dependent kinase 12 (CDK12) and CDK13 complexes in C-terminal domain phosphorylation, gene transcription, and RNA processing. *Mol. Cell. Biol.* 35, 928–938. doi: 10.1128/MCB.01426-14
- Meyers, E. N., Lewandoski, M., and Martin, G. R. (1998). An *Fgf8* mutant allelic series generated by Cre- and FLP-mediated recombination. *Nat. Genet.* 18, 136–141. doi: 10.1038/ng0298-136
- Neumuller, R. A., Richter, C., Fischer, A., Novatchkova, M., Neumuller, K. G., and Knoblich, J. A. (2011). Genome-wide analysis of self-renewal in *Drosophila* neural stem cells by transgenic RNAi. *Cell Stem Cell* 8, 580–593. doi: 10.1016/j.stem.2011.02.022
- Pan, J., Xue, Y., Chen, S., Qiu, H., Wu, C., Jiang, H., et al. (2012). Establishment and characterization of a new human acute myelomonocytic leukemia cell line J1H-3. *Leuk. Res.* 36, 889–894. doi: 10.1016/j.leukres.2012.01.012
- Pang, X., Zhao, Y., Wang, J., Zhou, Q., Xu, L., Kang, et al. (2017). The bioinformatic analysis of the dysregulated genes and microRNAs in entorhinal cortex, hippocampus, and blood for Alzheimer's disease. *Biomed. Res. Int.* 2017:9084507. doi: 10.1155/2017/9084507
- Pham, C. T., MacIvor, D. M., Hug, B. A., Heusel, J. W., and Ley, T. J. (1996). Long-range disruption of gene expression by a selectable marker cassette. *Proc. Natl. Acad. Sci. U.S.A.* 93, 13090–13095. doi: 10.1073/pnas.93.23.13090
- Scacheri, P. C., Crabtree, J. S., Novotny, E. A., Garrett-Beal, L., Chen, A., Edgemon, K. A., et al. (2001). Bidirectional transcriptional activity of PGK-neomycin and unexpected embryonic lethality in heterozygote chimeric knockout mice. *Genesis* 30, 259–263. doi: 10.1002/gene.1072
- Sifrim, A., Hitz, M. P., Wilsdon, A., Breckpot, J., Turki, S. H., Thienpont, B., et al. (2016). Distinct genetic architectures for syndromic and nonsyndromic congenital heart defects identified by exome sequencing. *Nat. Genet.* 48, 1060–1065. doi: 10.1038/ng.3627
- Smerdova, L., Smerdova, J., Kabatkova, M., Kohoutek, J., Blazek, D., Machala, M., et al. (2014). Upregulation of CYP1B1 expression by inflammatory cytokines is mediated by the p38 MAP kinase signal transduction pathway. *Carcinogenesis* 35, 2534–2543. doi: 10.1093/carcin/bgu190
- Truett, G. E., Heeger, P., Mynatt, R. L., Truett, A. A., Walker, J. A., and Warman, M. L. (2000). Preparation of PCR-quality mouse genomic DNA with hot sodium hydroxide and tris (HotSHOT). *Biotechniques* 29, 52, 54. doi: 10.2144/00291bm09
- Uehara, T., Takenouchi, T., Kosaki, R., Kurosawa, K., Mizuno, S., and Kosaki, K. (2018). Redefining the phenotypic spectrum of de novo heterozygous CDK13 variants: three patients without cardiac defects. *Eur. J. Med. Genet.* 61, 243–247. doi: 10.1016/j.ejmg.2017.12.004
- van den Akker, W. M. R., Brummelman, I., Martis, L. M., Timmermans, R. N., Pfundt, R., Kleefstra, T., et al. (2018). De novo variants in CDK13 associated with syndromic ID/DD: molecular and clinical delineation of 15

- individuals and a further review. *Clin. Genet.* 93, 1000–1007. doi: 10.1111/cge.13225
- Wang, Y., Pan, X., Fan, Y., Hu, X., Liu, X., Xiang, M., et al. (2015). Dysregulated expression of microRNAs and mRNAs in myocardial infarction. *Am. J. Transl. Res.* 7, 2291–2304.
- Xiang, X., Deng, L., Zhang, J., Zhang, X., Lei, T., Luan, G., et al. (2014). A distinct expression pattern of cyclin K in mammalian testes suggests a functional role in spermatogenesis. *PLoS One* 9:e101539. doi: 10.1371/journal.pone.0101539
- Zhu, H., Doherty, J. R., Kuliye, E., and Mead, P. E. (2009). CDK9/cyclin complexes modulate endoderm induction by direct interaction with Mix.3/mixer. *Dev. Dyn.* 238, 1346–1357. doi: 10.1002/dvdy.21920
- Conflict of Interest Statement:** The authors declare that the research was conducted in the absence of any commercial or financial relationships that could be construed as a potential conflict of interest.
- Copyright © 2019 Nováková, Hampl, Vrábel, Procházka, Petreselyová, Procházková, Sedláček, Kavková, Zikmund, Kaiser, Juan, Fann, Buchtová and Kohoutek. This is an open-access article distributed under the terms of the Creative Commons Attribution License (CC BY). The use, distribution or reproduction in other forums is permitted, provided the original author(s) and the copyright owner(s) are credited and that the original publication in this journal is cited, in accordance with accepted academic practice. No use, distribution or reproduction is permitted which does not comply with these terms.



Role of ciliopathy protein TMEM107 in eye development: insights from a mouse model and retinal organoid

Marija Dubaic^{1,2}, Lucie Peskova³, Marek Hampel^{1,2}, Kamila Weissova^{1,3} , Canan Celiker³, Natalia A Shylo^{4,5}, Eva Hrubá¹, Michaela Kavkova⁶, Tomas Zikmund⁶, Scott D Weatherbee^{4,7} , Jozef Kaiser⁶, Tomas Barta^{1,3} , Marcela Buchtova^{1,2}

Primary cilia are cellular surface projections enriched in receptors and signaling molecules, acting as signaling hubs that respond to stimuli. Malfunctions in primary cilia have been linked to human diseases, including retinopathies and ocular defects. Here, we focus on TMEM107, a protein localized to the transition zone of primary cilia. TMEM107 mutations were found in patients with Joubert and Meckel–Gruber syndromes. A mouse model lacking *Tmem107* exhibited eye defects such as anophthalmia and microphthalmia, affecting retina differentiation. *Tmem107* expression during prenatal mouse development correlated with phenotype occurrence, with enhanced expression in differentiating retina and optic stalk. TMEM107 deficiency in retinal organoids resulted in the loss of primary cilia, down-regulation of retina-specific genes, and cyst formation. Knocking out TMEM107 in human ARPE-19 cells prevented primary cilia formation and impaired response to *Smoothed* agonist treatment because of ectopic activation of the SHH pathway. Our data suggest TMEM107 plays a crucial role in early vertebrate eye development and ciliogenesis in the differentiating retina.

DOI [10.26508/lsa.202302073](https://doi.org/10.26508/lsa.202302073) | Received 4 April 2023 | Revised 27 September 2023 | Accepted 28 September 2023 | Published online 20 October 2023

Introduction

The primary cilium is a cellular organelle that projects from the surface of most cell types. It performs sensory, mechanical, and signal processing functions, and regulates numerous critical developmental processes, including neurogenesis, skeletogenesis, and kidney formation (Chang et al, 2015; Marra et al, 2016). Primary cilia are also crucial coordinators of the Sonic Hedgehog (Shh) pathway and other signaling processes (Huangfu et al, 2003; Caspary et al, 2007; Wheway et al, 2018). During early eye development, primary cilia are present on the surface of the optic neuroepithelium, surface ectoderm, and periocular mesenchyme (Lupu et al, 2018). They also play an important role in the transport

of proteins involved in visual transduction in photoreceptors, making ciliary signaling critical for both retinal structure formation and retinal physiology in postnatal stages (Wheway et al, 2014).

A broad range of defects known as ciliopathies can result from alterations in ciliary biogenesis or function (Lee & Gleeson, 2011). These defects include ocular deformities, such as retinitis pigmentosa and macular degeneration in humans, and eye defects observed in several mouse strains with ciliopathies (Badano et al, 2006; Gorivodsky et al, 2009; Qin et al, 2011; Cela et al, 2018). The protein composition and function of cilia is precisely controlled through a specialized domain located at the base of the cilium known as the transition zone (TZ) (Gonçalves & Pelletier, 2017). TMEM107 is a protein located at the TZ that has been shown to recruit ciliopathy-associated proteins such as MKS-1, TMEM-231 (JBTS20), and JBTS-14 (TMEM237) to this domain (Lambacher et al, 2016). The *TMEM107* locus has recently been found to be mutated in patients with Meckel–Gruber syndrome, Orofaciodigital syndrome, and Joubert syndrome (Iglesias et al, 2014; Shaheen et al, 2015; Lambacher et al, 2016; Shylo et al, 2016; Chinen et al, 2022). These syndromes are associated with altered primary cilia morphology and function, highlighting the role of TMEM107 in ciliary function.

Human patients with *TMEM107* mutations exhibit numerous developmental defects, such as polydactyly or facial dysmorphic features (Iglesias et al, 2014; Lambacher et al, 2016; Shylo et al, 2016; Chinen et al, 2022). Mouse strains with mutations in *Tmem107* demonstrate similar defects to human patients, including extra digits and a spectrum of craniofacial anomalies such as exencephaly, microphthalmia or skeletal defects in *Tmem107^{schlei}* embryos (Christopher et al, 2012). *Tmem107^{null}* mouse embryos display even stronger phenotypes, including shorter snouts, expanded facial midlines, cleft palates, and extensive exencephaly (Cela et al, 2018). Whereas the association between *Tmem107* deficiency and craniofacial defects has been previously described, the role of this gene in eye development is not yet fully understood.

Here, we used mouse embryos, retinal organoids, and retinal cell culture models to closely investigate the role of TMEM107 in eye

¹Laboratory of Molecular Morphogenesis, Institute of Animal Physiology and Genetics, Czech Academy of Sciences, Brno, Czech Republic ²Department of Experimental Biology, Faculty of Science, Masaryk University, Brno, Czech Republic ³Department of Histology and Embryology, Faculty of Medicine, Masaryk University, Brno, Czech Republic ⁴Department of Genetics, Yale University, School of Medicine, New Haven, CT, USA ⁵Stowers Institute for Medical Research, Kansas City, MO, USA ⁶CEITEC - Central European Institute of Technology, Brno University of Technology, Brno, Czech Republic ⁷Biology Department, Fairfield University, Fairfield, CT, USA

Correspondence: buchtova@iach.cz; tbarta@med.muni.cz

development. We found that *Tmem107* is specifically enriched in the neural retina (NR) during mouse eye development. Its loss leads to the distinctive ocular phenotypes associated with primary cilia defects, including microphthalmia and anophthalmia; and altered expression of crucial transcription factors involved in eye development. *TMEM107*-deficient human retinal organoid model enabled us to determine its role in the human retina, and it also allowed us to study the role of this gene in neural retina formation without any influence of surrounding or closely associated eye structures and tissues including the brain or surface ectoderm. We found that *TMEM107*-deficient retinal organoids largely corroborated the results from the mouse model, failing to form neural retina structures and exhibiting primary cilia defects. Finally, using the retinal cell culture model, we found that *TMEM107* is critical for SHH signaling and its loss aberrantly up-regulates the SHH pathway. Taken together, our findings suggest that *TMEM107* plays a crucial role in eye development and SHH signaling in both mice and humans, providing a better understanding of eye abnormalities that may potentially lead to therapeutic interventions for related conditions.

Results

Loss of *Tmem107* leads to distinctive ocular phenotypes in mouse embryos

We used *Tmem107*^{-/-} mouse model to determine the function of *Tmem107* in eye development (Christopher et al, 2012). Mutant embryos through all analyzed stages (E10.5–E15.5) exhibited a variety of eye abnormalities (Figs 1A and S1A–F and Table S1) (Video 1 and Video 2). Heterozygous embryos did not exhibit an abnormal phenotype. Two most frequently observed phenotypes included complete loss of an eye (*anophthalmia*), observed in 33.3% of examined mutants, and abnormally small eye (*microphthalmia*) with 47% occurrence (Fig 1D). In nine examined cases, both phenotypes were present within the same embryo. In anophthalmic animals, a small area of pigment residue was present, whereas embryos exhibiting microphthalmia often displayed other defects, such as total absence of the lens (*aphakia*) and/or optic nerve (ON) hypoplasia (Fig 1A). The mice retina with microphthalmic phenotype was smaller and elongated, compared with retina in WT animals. Additional morphometric analyses performed using micro-CT approach revealed decreased retina volume and shortened ON in mutant embryos (Fig 1B and C).

Tmem107 is highly expressed in the retina during eye development

To investigate the role of *Tmem107* in the development of specific eye structures, we analyzed in situ expression of *Tmem107* using the RNAscope approach during critical stages of eye development (E10–E15). At early stages of optic vesicle outgrowth (E10 and E11) (Fig 2A and B), *Tmem107* expression was detected in the bilayered optic cup, where the inner layer represents the presumptive neural retina (NR) and the outer layer will give rise to the retinal pigment epithelium (RPE). Although *Tmem107* expression was observed

throughout all these structures, the signal was particularly enriched in the presumptive NR (Fig 2A'''–F'''), whereas the lens placode and RPE layer exhibited lower expression (Fig 2A'–F' and A''–F''). The patterns of *Tmem107* expression remained similar during later stages (E12, E13), with the signal located in the anterior and posterior lens epithelium (Fig 2C and D) and in the newly formed cornea (Fig 2C' and D'). At E13, the formation of a ganglion cell layer (GCL) is associated with lower expression of *Tmem107* compared with the rest of NR (Fig 2D''). Later, at E14 and E15, the neuroblast cell layer (NCL), which contains neuronal progenitors, expresses high levels of *Tmem107* (Fig 2E''' and F'''), whereas differentiated neurons of GCL exhibit low expression of this gene. Interestingly, *Tmem107* mRNA expression in the ciliary marginal zone (CMZ) was very low compared with the rest of the NR (Figs 2F'' and S2A–D). Thus, our findings indicate that *Tmem107* is strongly expressed during early stages of eye development (E10–E15), particularly in the NR.

Key factors in eye development are altered in *Tmem107*^{-/-} animals

To gain more insight into molecular changes caused by *Tmem107* deletion, we analyzed in situ expression of key proteins involved in eye patterning. Because the phenotypic analysis revealed distinct anomalies affecting certain eye areas including retina, lens, and optic stalk, we further focused on the evaluation of the expression patterns of proteins that are critical for morphogenesis of the retina (PAX6, SOX2), the optic stalk (PAX2), and the lens (SOX1). PAX6 and SOX2 are transcription factors associated with anophthalmia and microphthalmia in humans (Matsushima et al, 2011). Furthermore, SOX1 is a key regulator expressed in the developing lens (Nishiguchi et al, 1998), and PAX2 has previously been linked to the development of optic stalk and closure of optic fissure (Bosze et al, 2021). Because it is well established that all of these transcription factors are expressed at the early stages of eye development, we performed the analyses at E10.5 and E11.5 (Fig 3). We observed altered expression of PAX6 (Fig 3A–A'' compared with Fig 3B–B''), PAX2 (Fig 3C–C'' compared with Fig 3D–D'') and SOX1 (Fig 3E–E'' compared with Fig 3F–F'') in *Tmem107*^{-/-} embryos already at E10.5 with more striking differences found at E11.5 (Fig 3G–L). We analyzed the expression of PAX6, PAX2, and SOX1 in microphthalmia mutants because structures expressing these proteins are missing in animals with anophthalmia, which we also see in our mutants. Interestingly, SOX2 expression in microphthalmic *Tmem107*^{-/-} mutants at E10.5 was still maintained in NR (Fig S3C–C'' compared with Fig S3A–A'') and profound differences were found later at E11.5 (Fig S3F–F''' compared with Fig S3D–D''). In anophthalmic *Tmem107*^{-/-} mutants, the expression of SOX2 was reduced in the optic stalk, whereas in the optic cup, it was completely lost at E10.5 and E11.5 (Fig S3B'' and E'').

Moreover, the reduction of SOX1 expression was found in the lens of *microphthalmia* mutants, whereas PAX2 and PAX6 were down-regulated in the distal part of NR (Fig 3). In summary, our data indicate that *TMEM107* is important for early eye patterning in mice and it may establish the proper expression of pivotal players during crucial stages of the optic cup and stalk morphogenesis.

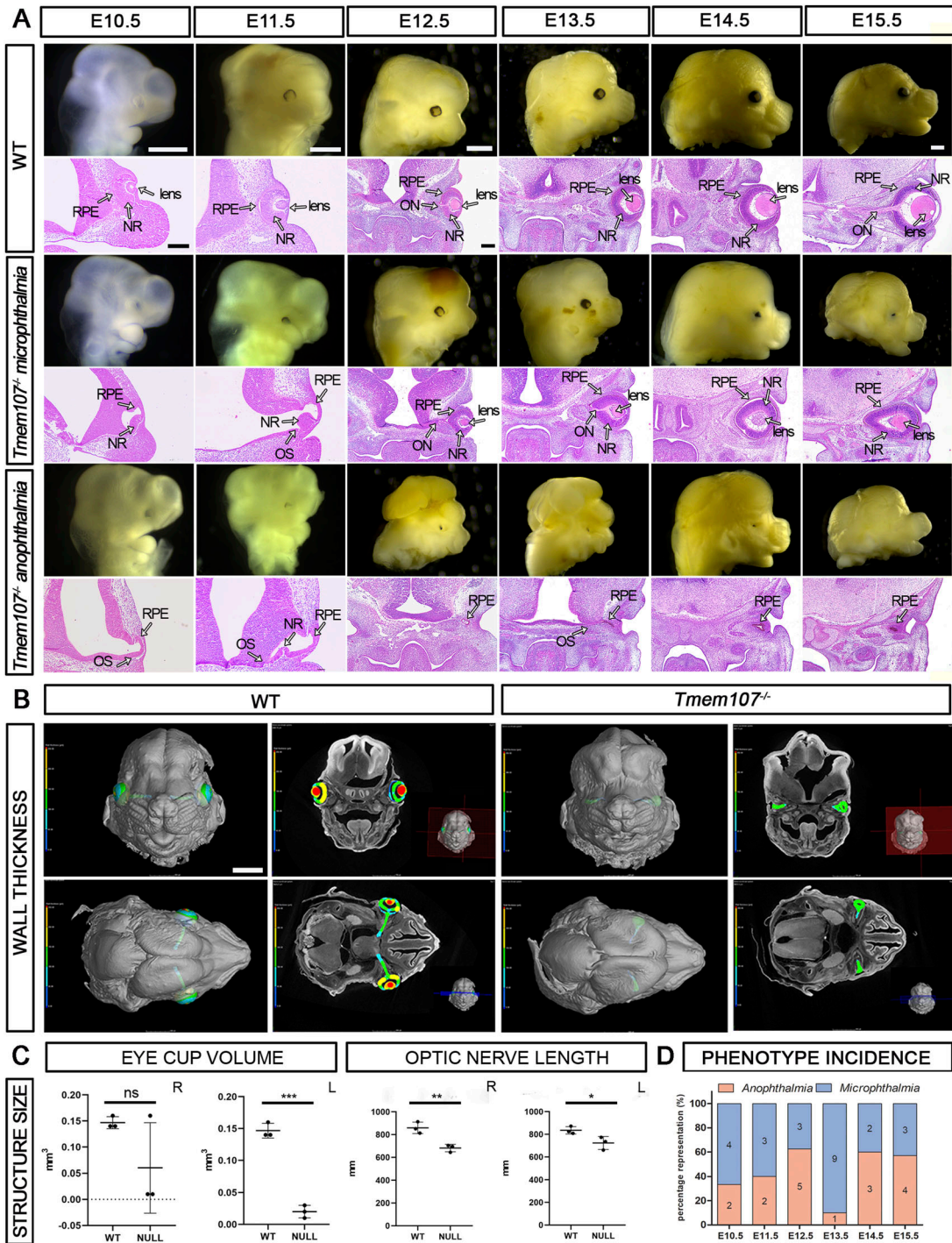


Figure 1. *Tmem107*^{-/-} mutants display severe morphological defects in eye regions.

(A) Macroscopic pictures and HE-stained sections illustrating *microphthalmia* and *anophthalmia* in E10.5–E15.5 mutant embryos compared with WT. (B) Micro-CT reconstruction of stage E15.5 WT and *Tmem107*^{-/-} eyes. Wall thickness is displayed as a color gradient from blue (the thinnest, 0 μ m) to red (the thickest, up to 200 μ m) demonstrated in the color legend. (C) Graphical representation of changes in eye structure size at stage E15.5 measured from micro-CT scans (left—volume of eyes in mm^3 ; right—optic nerve length in mm) in *Tmem107*^{-/-} embryos. Paired, nonparametric, two-tailed t test; ns, nonsignificant; * $P < 0.05$; ** $P < 0.01$; *** $P < 0.001$; $n = 3$. (D) Variability of an eye phenotype present in different stages of examined mutant specimens. RPE, retinal pigment epithelium; NR, neural retina; OS, optic stalk; ON, optic nerve. Scale bars: macroscopic pictures = 700 μ m; hematoxylin–eosin (HE)-stained sections = 200 μ m; micro-CT = 800 μ m.

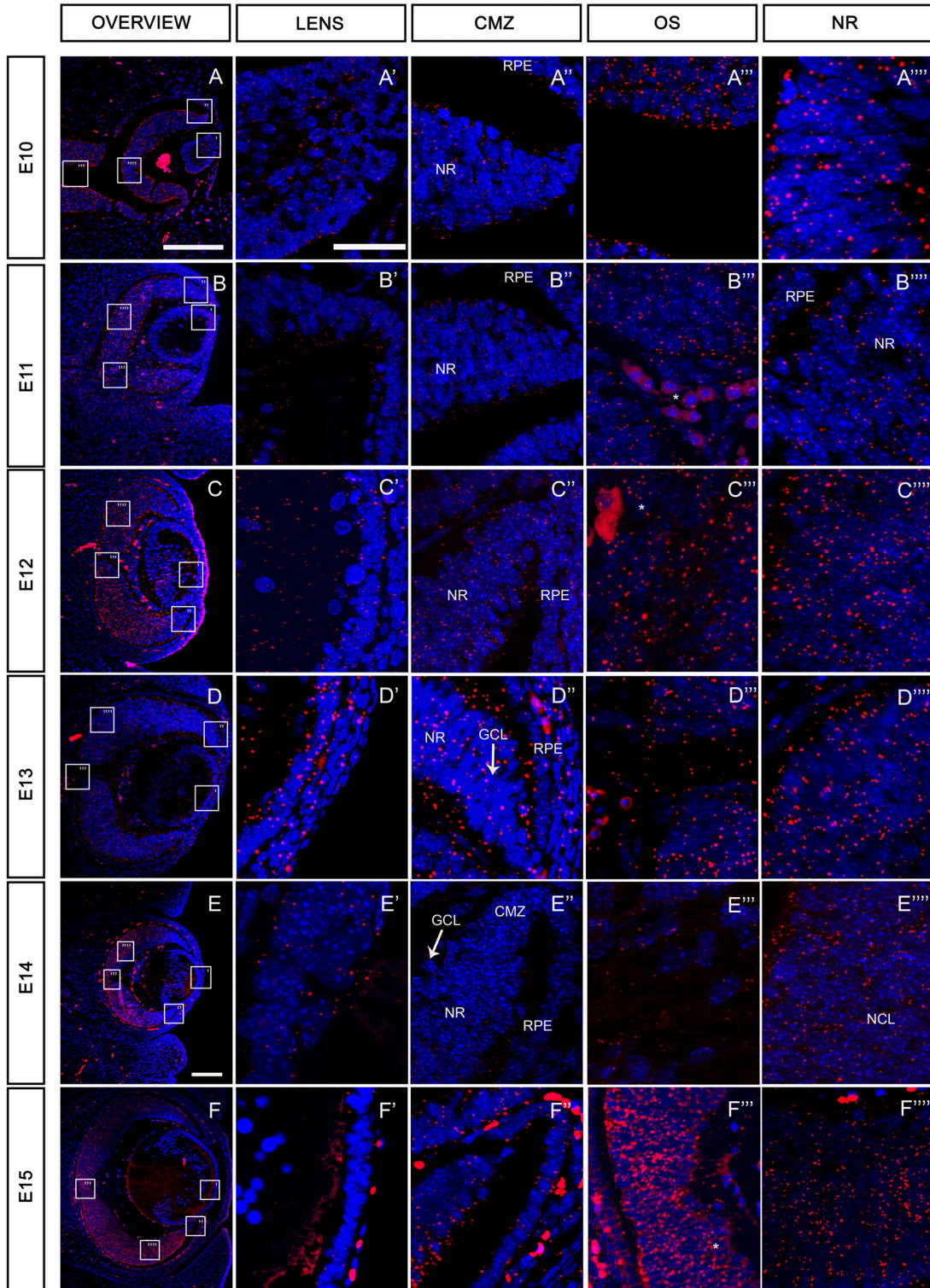


Figure 2. *Tmem107* expression during eye development.

(A, B, C, D, E, F) Representation of RNAScope signal for *Tmem107* (shown in red) at low magnification in the whole eye at stages from E10 to E15. (A', A'', A''', A''', B', B'', B''', B''', C', C'', C''', C''', D', D'', D''', D''', E', E'', E''', E''', F', F'', F''', F''') Details of *Tmem107* expression in lens, (A', B', C', D', E', F') in ciliary marginal zone region, (A'', B'', C'', D'', E'', F'') in optic stalk/optic nerve region (OS), (A''', B''', C''', D''', E''', F''') and in the neural retina region. Nuclei are counterstained with DAPI (blue). NR, neural retina; RPE, retinal pigment epithelium; GCL ganglion cell layer; NCL neuroblast cell layer; CMZ, ciliary marginal zone; * autofluorescent blood cells. Scale bar: lower power = 150 μ m; higher power = 15 μ m.

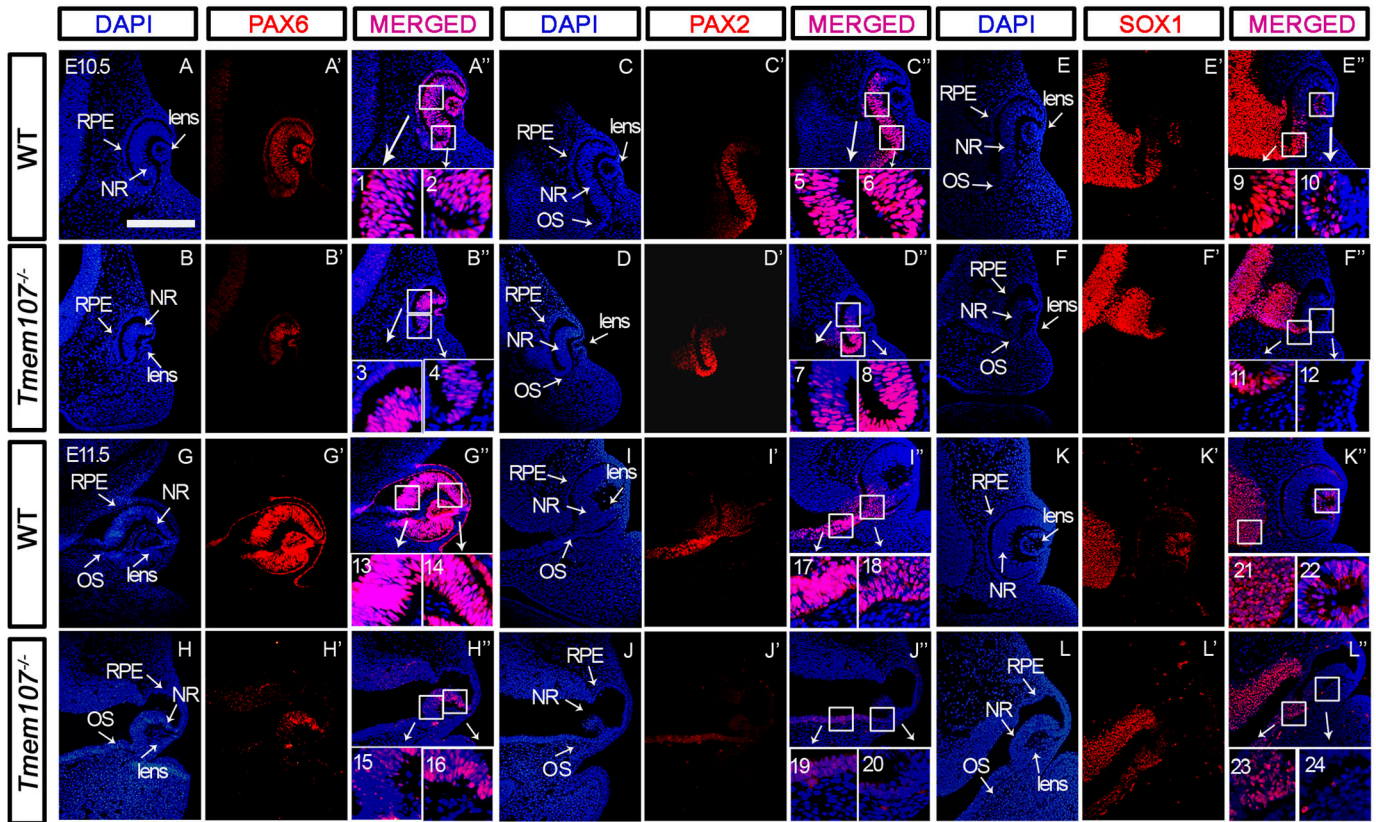


Figure 3. Key players of eye development are altered in *Tmem107*^{-/-} animals at E10.5–E11.5.

(A, A', A'', B, B', B'', C, C', C'', D, D', D'', E, E', E'', F, F', F'', G, G', G'', H, H', H'', I, I', I'', J, J', J'', K, K', K'', L, L', L'') Immunohistochemical detection of PAX6 (A, A', A'', B, B', B'', G, G', G'', H, H', H''), PAX2 (C, C', C'', D, D', D'', I, I', I'', J, J', J''), and SOX1 (E, E', E'', F, F', F'', K, K', K'', L, L', L'') PAX6 (red) expression in the neural retina, lens, pigment epithelium, and optic stalk in WT (A, A', A'', G, G', G'') in comparison with *Tmem107*^{-/-} animals (B, B', B'', H, H', H''). PAX2 (red) expression in optic stalk and distal part of neural retina in WT (C, C', C'', I, I', I'') in comparison with *Tmem107*^{-/-} animals (D, D', D'', J, J', J''). SOX1 (red) expression in lens vesicle of WT (E, E', E'') was higher in contrast with *Tmem107*^{-/-} (F, F', F'') similar as in E11.5 WT (K, K', K'') in comparison with *Tmem107*^{-/-} mutants (L, L', L''). Nuclei are counterstained with DAPI. NR, neural retina; RPE, retinal pigment epithelium; OS, optic stalk. Scale bar = 200 μm.

***TMEM107* deficiency leads to the failure of neural retina formation in human retinal organoids**

Given the striking retinal phenotype observed in *Tmem107*^{-/-} animals, we aimed to further test if the human *TMEM107* gene is essential for the development of the retina. We used retinal organoids differentiated from hESCs as a model to closely investigate the roles for *TMEM107* in human retinal development. Moreover, this approach allowed us to evaluate the direct role of *TMEM107* in retinal differentiation without the effects of surrounding or closely associated eye structures and tissues including the brain or surface ectoderm.

We generated *TMEM107*^{-/-} hESCs using CRISPR/Cas9 approach (Figs S4 and S5) and differentiated them into retinal organoids using an already published protocol (Kuwahara et al, 2015; Peskova et al, 2020; Celiker et al, 2023). Retinal organoids were analyzed at day 30 (D30, early stage) and day 150 (D150, late stage) of the differentiation process. Early differentiation steps during the retinal organoid formation include the generation of NR epithelium

containing progenitors that give rise to photoreceptors (*RAX*+), ganglion cells (*VSX2*+), and other cell types of the human retina, whereas the late stage is characterized by photoreceptor maturation (*CRX*+, *RHODOPSIN*+) and appearance of inner and outer photoreceptor segments (Burmeister et al, 1996; Furukawa et al, 1997b; Irie et al, 2015).

At D30 of the differentiation process, WT organoids contained NR epithelium, whereas *TMEM107*^{-/-} organoids lacked NR epithelium and contained cystic structures (Figs 4A and D and S4A–L). RT-qPCR analysis confirmed that *TMEM107*^{-/-} organoids failed to generate NR, as demonstrated by significant down-regulation of genes that are typically expressed in the developing NR structure including *RAX*, *PAX6*, *SOX2*, and *VSX2* (Fig 4B, top row) (Furukawa et al, 1997a; Kozmik, 2008; Matsushima et al, 2011; Burmeister et al, 1996).

Interestingly, scanning electron microscopy (SEM) analysis revealed that *TMEM107*^{-/-} organoids at D30 lack primary cilia on their surface (Fig 4C). In addition, we confirmed the absence of primary cilia using immunofluorescence staining of primary cilia

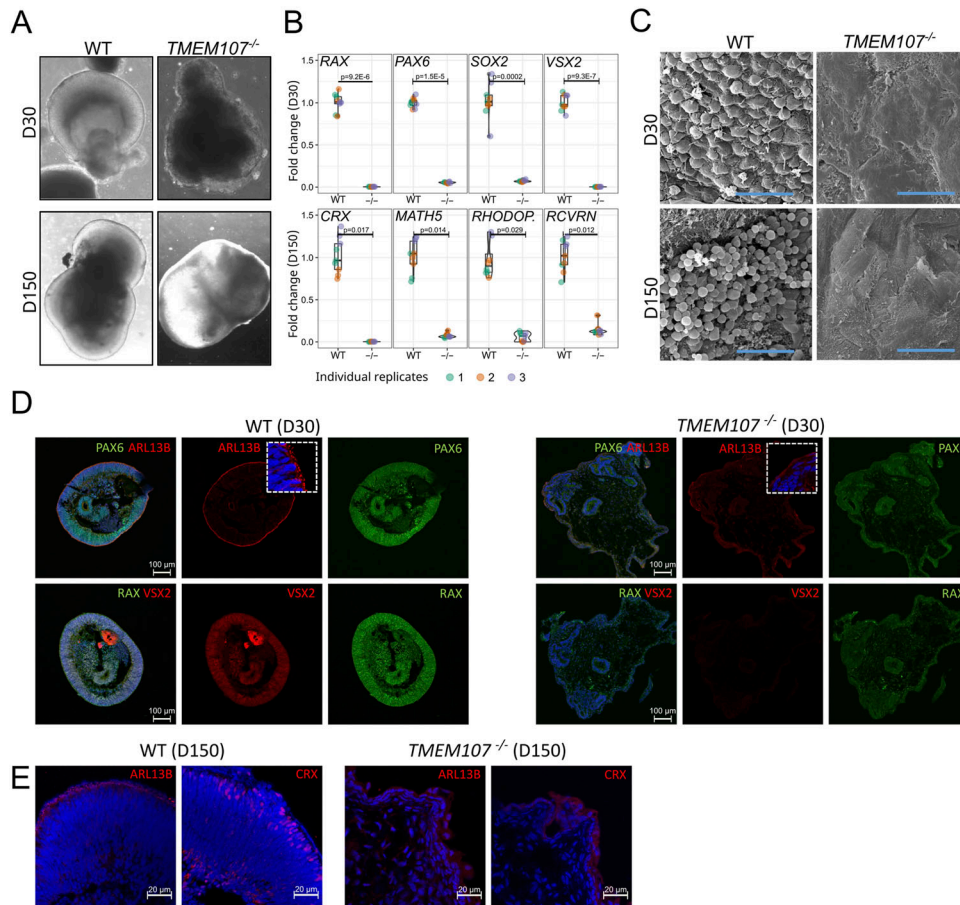


Figure 4. *TMEM107* is essential for human retinal development.

(A) Morphology of retinal organoids at D30 and D150, as demonstrated using brightfield microscopy. (B) Expression of retinal genes at early stage (D30—upper row) and late stage (D150—bottom row) of the differentiation process in WT and *TMEM107*^{-/-} retinal organoids, as demonstrated using RT-qPCR; parametric paired, two-tailed t test; n = 3. (C) Microphotograph of retinal organoid surface (D30—upper row, D150—bottom row), as demonstrated using SEM. Scale bars represent 10 μm. (D) Expression of PAX6 (green), ARL13B (red), RAX (green), and VSX2 (red) in WT and *TMEM107*^{-/-} retinal organoids at D30, as demonstrated using immunofluorescence staining. Nuclei are counterstained with DAPI. (E) Expression of ARL13B and CRX in WT and *TMEM107*^{-/-} retinal organoids, as demonstrated using immunofluorescence staining. Nuclei are counterstained with DAPI.

marker ARL13B (Fig 4D). To reveal whether the absence of *TMEM107* leads to the impaired maturation of the retinal organoids and failure to generate photoreceptors and other retinal cell types, we cultured retinal organoids until D150. *TMEM107*^{-/-} retinal organoids at the late stage completely failed to generate NR demonstrated by: (I) altered organoid morphology (Fig 4A), (II) lack of photoreceptor outer segments demonstrated by SEM and immunofluorescence staining for ARL13B (Fig 4C and E), (III) significant down-regulation of photoreceptor markers (CRX, RHODOPSIN, RCVRN) and retinal ganglion cell marker (MATH5), as demonstrated by RT-qPCR analysis (Fig 4B, bottom row). Interestingly, Hematoxylin/Eosin staining of retinal organoid cross sections revealed the presence of cysts and Oil Red O lipid staining identified increased the presence of lipids in *TMEM107*-deficient organoids (Fig S4).

To corroborate the phenotype of *TMEM107*^{-/-} organoids, we used a different loss-of-function approach—the shRNA-mediated knockdown of *TMEM107* in human induced pluripotent stem cells (hiPSCs). We generated lentiviral particles containing mCherry reporter and doxycycline (DOX)-inducible expression of shRNA for *TMEM107* down-regulation. Upon transduction, puromycin selection, and FACS sorting, hiPSCs and the generated retinal organoids expressed mCherry reporter (Fig S6A and B). DOX was applied from D2 of the differentiation process, and the retinal organoids were

harvested and analyzed at D25. We found ~50% down-regulation of *TMEM107* gene expression as determined by RT-qPCR in the presence of DOX (Fig S6C) that led to alterations in primary cilia formation including extremely elongated or very short cilia with expanded bulges in their tip (Fig S6D), cyst formation inside of the organoids (Fig S6B), and failure to form NR structures in retinal organoids (Fig S6E), thus corroborating the results generated using the knock-out approach.

Taken together, our results indicate that the absence of *TMEM107* leads to the following: (I) absence of primary cilia on early-stage organoids and outer segments on late stage retinal organoids, (II) the down-regulation of retina-specific genes, (III) the failure to generate the NR structures and cell types in the human retinal organoid model, (IV) the generation of organoid with cysts containing lipids.

Tmem107^{-/-} animals have primary cilia defects in pigment epithelium and neural retina

Primary cilia defect in different organs in *Tmem107*^{-/-} embryos have been previously reported (Cela et al, 2018; Shylo et al, 2020). However, the potential ciliary anomalies in the retina of these animals remain elusive. To test whether *Tmem107*^{-/-} eye phenotype in the mouse model is associated with primary cilia

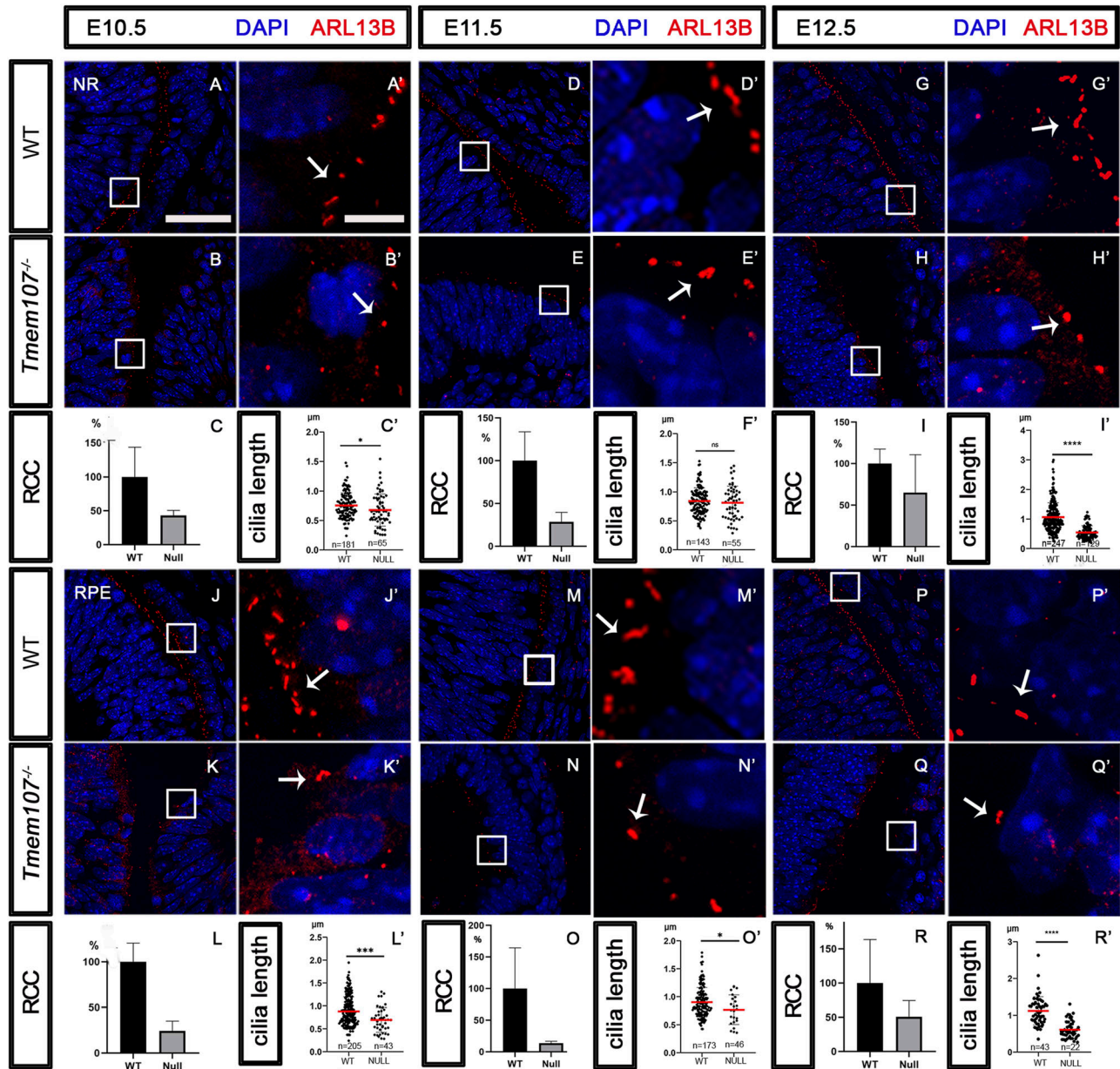


Figure 5. Primary cilia in neural retina (NR) and retinal pigment epithelium (RPE) Labeling of primary cilia using ARL13B (red) ciliary protein. (A, A', B, B', D, D', E, E', G, G', H, H') In comparison with WT animals (A, A', D, D', G, G'), reduced number and length of primary cilia in NR of E10.5 (B, B'), E11.5 (E, E'), and E12.5 (H, H') *Tmem107*^{-/-} compared with WT embryos. (C, C', F, F', I, I') Graphs representing difference in cilia number in WT (RCC, ratio of ciliated cells) and *Tmem107*^{-/-} NR (C, F, I) and difference in cilia length (μm) in WT and *Tmem107*^{-/-} NR (C', F', I'). (J, J', K, K', M, M', N, N', P, P', Q, Q') Comparison of primary cilia in RPE area between WT (J, J'; M, M'; P, P') and *Tmem107*^{-/-} display reduced number and length of primary cilia in RPE of E10.5 (K, K'), E11.5 (N, N'), and E12.5 (Q, Q'). (L, L', O, O', R, R') Graphs representing difference in cilia number in WT and *Tmem107*^{-/-} RPE (L, O, R) and difference in cilia length in WT and *Tmem107*^{-/-} RPE (L', O', R'). Nuclei are counterstained with DAPI. Scale bars: lower magnification = 35 μm; higher magnification = 5 μm. n = number of measured cilia; nonparametric unpaired two-tailed t test; ns, nonsignificant; *P < 0.05; **P < 0.01; ****P < 0.0001.

defects, we labeled cilia using anti-ARL13B antibody, counted the number of ciliated cells, and measured the length of primary cilia. We analyzed primary cilia in distinct eye structures with a special focus on RPE and NR at developmental stages E10.5, E11.5 or E12.5. Analysis of the NR region revealed a reduced number of primary cilia (RCC–ratio of ciliated cells) at stages E10.5 (Fig 5A–C), E11.5 (Fig 5D–F), and E12.5 (Fig 5G–I) associated with

significantly reduced cilia length at E10.5 (Fig 5C') and E12.5 (Fig 5I'). In addition, the length of cilia was also reduced at E11.5, but not with the statistical significance (Fig 5F'). However, more profound changes were observed in the RPE region, where we found a decreased length and cilia number in all analyzed samples of different developmental stages: E10.5 (Fig 5J–L'), E11.5 (Fig 5M–O'), and E12.5 (Fig 5P–R'). These data suggest that

TMEM107 plays a role in cilia biogenesis in vivo and regulation of ciliary length in the developing eye.

Loss of *TMEM107* leads to aberrant SHH signaling in retinal cells

The evident association of primary cilia disruption with eye phenotypes in all our *TMEM107*^{-/-} models prompted us to proceed with the analysis of the effects of TMEM107 loss at the molecular level. Because the function of the Shh pathway fully relies on the formation of primary cilium (Huangfu & Anderson, 2005), we aimed to closely investigate the effects of TMEM107 loss on this signaling pathway. Retinal organoids do not represent a suitable model to specifically address affected molecular pathways in individual cells, because of the heterogeneity of different cell types they contain, therefore it is challenging to study signaling pathways using an organoid model. We, therefore, used the ARPE-19 cell line, derived from retinal pigmented epithelium, to address the effects of TMEM107 loss on the Shh pathway by generating ARPE-19 *TMEM107*^{-/-} and *TMEM107*^{+/-} cell lines, using CRISPR/Cas9 technology.

First, we assessed the expression of the crucial components of the Shh pathway *GLI1* and *PTCH1* using RT-qPCR. Whereas there was no significant difference in *PTCH1* expression between WT and mutant cells, we detected ~15-fold up-regulation of *GLI1* expression in *TMEM107*^{-/-} cells (Fig 6A), indicating an aberrant activation of the Shh pathway in the absence of *TMEM107*. To confirm the activation of the Shh pathway and to reveal whether ARPE-19 cells possess the functional Shh pathway, we treated the cells using Shh activator smoothed agonist (SAG). Upon SAG treatment, WT and *TMEM107*^{+/-} cells up-regulated the expression of *GLI1* and *PTCH1* by ~twofold, but *TMEM107*^{-/-} cells failed to up-regulate *GLI1* and *PTCH1* (Fig 6B and C). Therefore, high *GLI1* expression and no response to SAG treatment of *TMEM107*^{-/-} cells indicate that the Shh pathway is aberrantly activated in *TMEM107*^{-/-} cells and that TMEM107 is critical for Shh signaling.

The aberrant Shh signaling in *TMEM107*^{-/-} cells could be explained by altered primary cilia formation that we, indeed, also observed in *TMEM107*^{-/-} retinal organoids. To test this, we stained ARPE-19 cells for the ciliary marker ARL13B. WT and *TMEM107*^{+/-} formed primary cilia, whereas *TMEM107*^{-/-} completely failed to form these structures (Fig 6D and E). To test SHH activation, we used the SAG treatment approach as described above, and assessed in situ localization of other critical Shh players SMO and GLI2. Immunofluorescence staining revealed that upon SAG treatment SMO localizes into the primary cilia and GLI2 becomes up-regulated and localized into nuclei of WT and *TMEM107*^{+/-} cells. *TMEM107*^{-/-} failed to form primary cilia and GLI2 was up-regulated even in the absence of SAG (Fig 6D and E).

Previous studies showed down-regulated SHH in mice with *Tmem107* mutation (Christopher et al, 2012; Cela et al, 2018; Shylo et al, 2020). However, because of distinct ciliary transmission of SHH in different organs, both up-regulation and down-regulation have been observed in different tissues of the developing embryo (Burnett et al, 2017). In models that lack primary cilia, an up-regulation of SHH has been observed in the embryonic retina (Burnett et al, 2017). To test how the altered

morphology of primary cilia affected Shh signaling in the mouse model, we analyzed the expression of SHH protein and *Ptch1* RNA at stage E12.5 (Fig 7). Whereas in WT eyes, SHH localized to discrete regions in the distal part of the eye (Fig 7A'), *Tmem107*^{-/-} animals exhibited higher expression of this ligand in proximal and distal parts of the NR and in optic stalk (Fig 7B). The differences were most prominent in the lens and the optic stalk regions (Fig 7B' and B"). On the contrary, RNAScope analysis of *Ptch1* revealed no distinct changes in its expression in the eyes of E12.5 mutant animals (Fig 7D–D"), as compared with WT (Fig 7C–C"). These data demonstrate that although the expression of SHH was elevated, decrease in primary cilia keeps the pathway dysfunctional in mice mutants.

Taken together, our results indicate that the absence of TMEM107 leads to the following: (I) failure to form primary cilia in retinal pigmented epithelial cells, (II) aberrant up-regulation of the Shh pathway demonstrated by the up-regulation of *GLI1*, *GLI2*, and *GLI3 FL*, (III) incapability of *TMEM107*^{-/-} cells to respond to SAG treatment, because lack of cilia, and (IV) increased level of SHH ligands in vivo.

Discussion

Ciliopathies are a group of genetic disorders characterized by defects in the structure and function of cilia, which are hair-like organelles present on the surface of many cells. Previous research has shown that ciliopathy proteins are important for a variety of developmental processes, including eye development (Waters & Beales, 2011). The protein TMEM107 has been previously implicated in ciliopathy-associated eye abnormalities (Christopher et al, 2012). However, the specific mechanisms by which TMEM107 functions in eye development and the wide range of ocular abnormalities associated with its deficiency have not been fully elucidated.

Here, we used mouse embryos, retinal organoid, and retinal cell culture models to closely investigate the role of TMEM107 in eye development. We found that (I) TMEM107 is specifically and strongly expressed in NR of the developing eye; (II) loss of TMEM107 leads to distinctive ocular phenotypes including anophthalmia and microphthalmia associated with a truncated ON; (III) the expression of crucial genes in eye development is altered in the absence of TMEM107; (IV) TMEM107 is critical for ciliogenesis and Shh signaling, and its absence leads to the disruption of primary cilia and aberrant Shh signaling; and (V) TMEM107 deficiency is associated with the generation of cysts.

All examined *Tmem107*^{-/-} mouse mutants manifested eye malformations including anophthalmia and microphthalmia. Interestingly, similar phenotypes have been observed in humans. Patients who appear as homozygotes or compound heterozygotes for *TMEM107* mutant allele have been diagnosed with Joubert (JS), Meckel-Gruber (MKS) or orofacioidigital syndrome (OFD) (Iglesias et al, 2014; Shaheen et al, 2015; Lambacher et al, 2016; Shylo et al, 2016; Chinen et al, 2022). All abovementioned syndromes have been recognized as ciliopathies associated with eye defects like *anophthalmia*, *microphthalmia*, retinal defects, coloboma or lid anomalies (Hartill et al, 2017; Hartill et al, 2017). Patients with *TMEM107* pathological

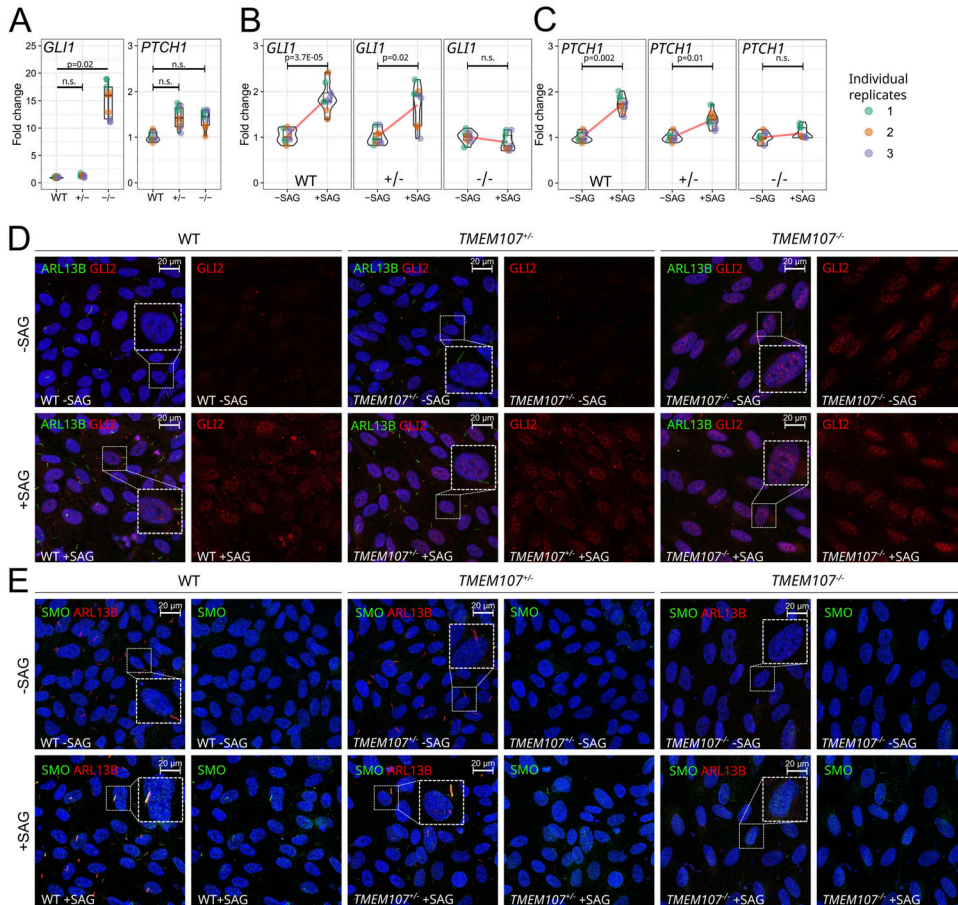


Figure 6. Loss of *TMEM107* leads to aberrant Shh signaling in retinal cells.

(A) Expression of *GLI1* and *PTCH1* in WT, *TMEM107*^{-/-}, and *TMEM107*^{-/-} ARPE-19 cells, as demonstrated using RT-qPCR; Paired, two-tailed t test; n.s. = non-significant; n = 3. (B, C) Expression of *GLI1* and *PTCH1* upon SAG treatment in WT, *TMEM107*^{-/-}, and *TMEM107*^{-/-} ARPE-19 cells, as demonstrated using RT-qPCR; Paired, two-tailed t test; n.s., nonsignificant; n = 3. (D) Expression of ARL13B (green) and GLI2 (red) upon SAG treatment in WT, *TMEM107*^{-/-}, and *TMEM107*^{-/-} ARPE-19 cells, as demonstrated using immunofluorescence staining. (E) Expression of ARL13B (red) and SMO (green) upon SAG treatment in WT, *TMEM107*^{-/-}, and *TMEM107*^{-/-} ARPE-19 cells. Nuclei are counterstained with DAPI (blue).

variants were diagnosed with a stronger phenotype in case of MKS with bilateral *anophthalmia* (Shaheen et al, 2015), and milder phenotypes with OFD and JBT with oculomotor apraxia and retinopathy (Lambacher et al, 2016), and OFD with strabismus (Chinen et al, 2022). Severity of exhibited symptoms seems to be correlated with the type of patients' mutations. In the case of two OFD patients, the sequencing analysis detected a homozygous missense variant, whereas in the Joubert syndrome patient, a compound heterozygous mutation containing a frameshift deletion and an in-frame deletion was discovered (Lambacher et al, 2016). On the other hand, the patient carrying one intronic base pair insertion causing frameshift and premature protein truncation developed more severe defects (Shaheen et al, 2015). Similarly, in ciliopathic mice, different eye defects have been described (Burnett et al, 2017; Fiore et al, 2020). Homozygous hypomorphic *Tmem107*^{schlei} mouse embryos develop milder phenotype—*microphthalmia* (Christopher et al, 2012), whereas mutant mice used in this study exhibit more severe eye defects when compared with those containing hypomorphic alleles. We have shown that all of the examined mutants manifest eye malformations with the most severe form—*anophthalmia* (33% mutants). One of the reasons why all of the examined *Tmem107*-deficient embryos develop severe phenotypes whereas milder defects are observed in humans could be because of differences between species and the fact that our models exhibit total lack of *TMEM107*

protein. Although mutations occurring in humans could lead to expression of a truncated version of the protein, which still partially retains the function, the complete loss of the protein may lead to more severe consequences. Another fact to be considered is that human embryos carrying *TMEM107* mutations die at early pregnancy and are not being diagnosed. Interestingly, *Tmem107*^{-/-} mice display ON hypoplasia, which can also occur in patients with Meckel-Gruber syndrome (MacRae et al, 1972). Furthermore, these mutants were shown to have other defects such as *exencephaly*, polydactyly, and cleft palate, which are observed in human *TMEM107* homozygous patients and are also often present in other ciliopathic cases (Waters & Beales, 2011). Animals carrying only one mutated *Tmem107* allele do not exhibit any obvious phenotype which corresponds to findings on human patients' parents who do not develop any of the symptoms present in children (Cela et al, 2018).

Given the striking eye phenotype in *Tmem107*^{-/-} mouse embryos and the lack of current knowledge about in situ *Tmem107* expression in developing eye structures, we aimed to assess *Tmem107* expression during eye development. We found an elevated *Tmem107* expression in the presumptive NR. High *Tmem107* expression in NR and *micro-/anophthalmia* phenotypes in the absence of this gene indicates a critical role for *Tmem107* in the development of the NR. Because eyes develop as brain evaginations, one could note that the observed eye phenotypes could be a consequence of not properly

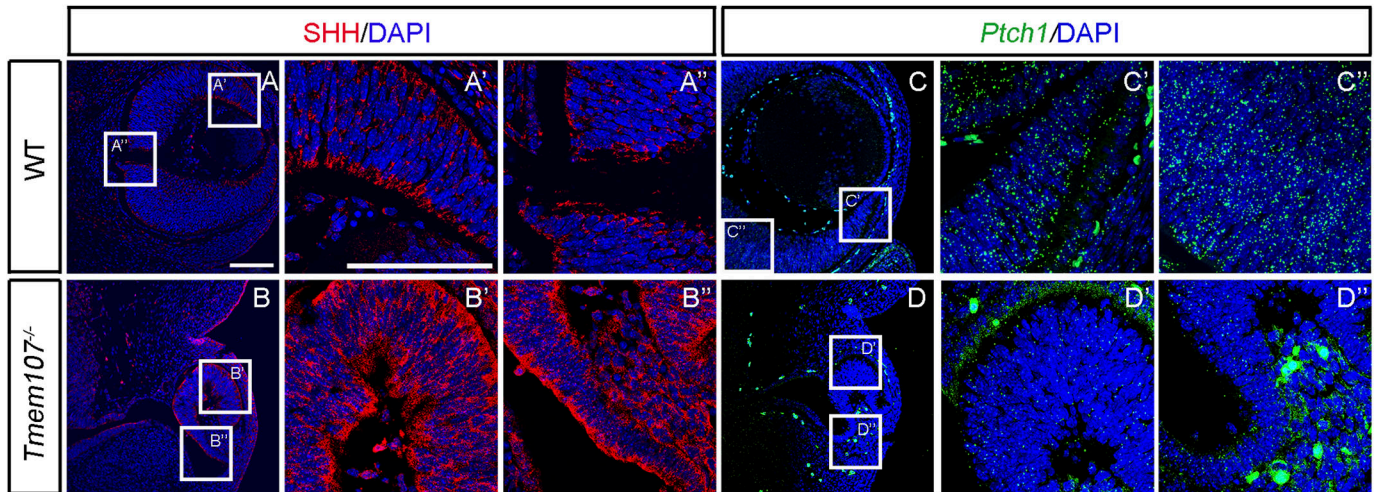


Figure 7. Expression of HH pathway members in E12.5 *Tmem107*^{-/-} animals. (A, A', A'', B, B', B'') Immunostaining of WT embryos (A, A', A'') and *Tmem107*^{-/-} (B, B', B'') revealed higher expression of SHH (red) protein in neural retina of *Tmem107*-deficient animals. (C, C', C'', D, D', D'') WT embryos (C, C', C'') exhibits revealed higher expression of *Ptch1* (green) mRNA in lens and neural retina in *Tmem107*^{-/-} (D, D', D'') as analyzed by RNAScope. Nuclei are counterstained with DAPI. Scale bar = 100 μ m.

developed brain rather than “stand alone” phenomena. To address this question, we performed 3D *in vitro* experiments using a human retinal organoid model. The retinal organoid system provided us not only the opportunity to examine the effects of *TMEM107* loss on retinal development without any possible influence of other tissues and structures, but also to study the role of this gene in humans. Similarly, as in the mouse model, retinal organoids generated from *TMEM107* knock-out hESCs were unable to form the NR.

Early morphogenesis of the eye is characterized by distinctive spatial and structure specific expression of different transcription factors. *SOX2* expression is detected in presumptive eyes from the early developmental stages (Kamachi et al, 1998) and has multiple roles during eye maturation. Importantly, it has been demonstrated that retinal progenitor cells with conditionally ablated *SOX2* lose competence to both proliferate and terminally differentiate (Taranova et al, 2006). Interestingly, we found profound differences of *SOX2* expression between anophthalmic and microphthalmic mutants at E11.5 (Fig S3). This could be explained by the different molecular mechanisms driving the expression of *SOX2* at different stages of eye development and as a consequence of losing *SOX2* expression in the optical cup leading to inability of retinal cells to proliferate and differentiate in the absence of *TMEM107* protein. *SOX1* is a transcription factor that plays an important role in eye development. During early stages, *SOX1* is expressed in the optic stalk, presumptive retina, and lens, whereas at later stages, its expression is restricted to lenses where it plays a critical role in γ -crystallin production (Nishiguchi et al, 1998). In *Tmem107*^{-/-} mutants, we observed a loss of *SOX1* in the lens area, whereas presumptive retina and optic stalk remain positive at E10.5 (Fig 3). *TMEM107*-deficient human retinal organoids largely support this scenario and do not express all these transcription factors or in different extents (Fig S6).

Previous analysis of *Tmem107*^{-/-} animals revealed reduced ciliogenesis in mesenchymal cells associated with altered morphology of primary cilia (Cela et al, 2018; Shylo et al, 2020). These findings corroborated the results previously reported in *Tmem107*^{schlei} mice

and in fibroblasts derived from human patients (Christopher et al, 2012; Shaheen et al, 2015; Shylo et al, 2016). Similar to already published studies, our data revealed profoundly reduced ciliogenesis in NR and RPE cells in mice mutants. However, the length of primary cilia was significantly reduced in all eye regions examined, which is in agreement with our observations in the nodal cilia of *Tmem107* null animals (Shylo et al, 2020), however in contrast with the previous findings showing elongation of some primary cilia in fibroblasts of both *Tmem107*^{Null} and *Tmem107*^{schlei} mutants (Christopher et al, 2012; Cela et al, 2018) and on fibroblasts derived from patients (Shaheen et al, 2015; Shylo et al, 2016). The distinct ciliary phenotype in different tissues indicates tissue-specific requirements of *TMEM107* for ciliogenesis. This might be even more specific for the eye area with the elevated *TMEM107* expression.

Importantly, *TMEM107*^{-/-} organoids form cysts containing lipids and accumulated liquid inside. Cysts are typically formed in numerous organs of ciliopathic patients, including polycystic kidneys (Wilson, 2004). Liquid accumulation during the cyst initiation is usually caused by the altered function of gated channels, commonly present in ciliary membrane and at the ciliary base bordering with the TZ, where *TMEM107* is localized (Gallagher et al, 2006; Slaats et al, 2015). For example, in the *retinoschisis* organoid model, a protein *NPHP5* that typically localizes to the TZ was down-regulated resulting in reduced ciliogenesis and generation of congenital retinal cysts by splitting of inner layers of the peripheral retina (Tantri et al, 2004; Huang et al, 2019). Importantly, the loss of adhesion in the cystic retinal organoid model also represents a common mechanism of renal cyst development (van Adelsberg, 2000; Roitbak et al, 2004; Huang et al, 2019). Interestingly, despite the fact that neural retina is not properly developed in *Tmem107*-deficient animals and retinal organoids, small pigment residues are still formed in both models. This is fully in line with the current understanding of eye development, as RPE differentiation is regulated by Wnt signaling that does not fully rely on a functional

primary cilium (Eiraku et al, 2011), although some crosstalk between Wnt and SHH pathways has been documented (Wiegering et al, 2019).

SHH pathway is known to regulate ocular development in humans and mice (Cavodeassi et al, 2019). Anophthalmic and microphthalmic eye phenotypes and other defects in *Tmem107*^{-/-} mice suggest an altered activation of the SHH pathway. In fact, we found elevated expression of SHH ligand despite a reduced number of primary cilia in *Tmem107*-deficient animals. This implies the possibility of ciliary involvement in the negative regulation of *Shh* gene expression or altered functionality of the remaining primary cilia. Indeed, the role of SHH in the regulation of dorso-ventral patterning of an optic cup has been also described (Zhao et al, 2010). SHH induces *Pax2* expression, PAX2 then binds the α -enhancer to antagonize *Pax6* expression in the ventral optic vesicle (Chiang et al, 1996; Heavner & Pevny, 2012). Here, we have shown down-regulated PAX6 in proximal optic cup regions at early developmental stages (E10.5 and E11.5), which is probably a consequence of elevated SHH levels in the absence of primary cilia. Moreover, it points to the fact that *microphthalmia* in *Tmem107*^{-/-} animals is likely caused by down-regulated *Pax6*, whereas *anophthalmia* is rather caused by altered expression of *Sox2*. Nevertheless, our analyses of differentiation stages revealed a strong down-regulation of *Pax6* in the retina, which might be the consequence of partially restored function of remaining cilia in the retina or as a result of interrupted communication between developing tissues in the eye.

Recent studies have determined the association between primary cilia and early eye development. Mouse models lacking crucial ciliary proteins have aberrant or no primary cilia, exhibit patterning defects, and abnormal eye morphology induced by ectopic activation of SHH signaling (Burnett et al, 2017). Furthermore, loss of ciliary gene *Arl13b* in mice produced a distinct eye phenotype characterized by an inverted optic cup (Fiore et al, 2020). These eye phenotypes were associated with aberrant SHH signaling and were rescued by *Gli2* deletion (Burnett et al, 2017; Fiore et al, 2020). We observed aberrantly activated *Shh* pathway with up-regulated SHH in mice and up-regulated GLI1/2 in human ARPE-19 cells. In addition, because of the aberrantly activated *Shh* pathway, *TMEM107*^{-/-} human cells are not able to further up-regulate *Shh* downstream molecules. These data suggest a mechanism for *Shh* signaling in eye development, whereby eye development is probably driven by the repressive Gli transcription factor signaling, rather than their transcription-activating roles.

Thus far, all described stem cells were found to have primary cilia (Yanardag & Pugacheva, 2021). The primary cilium displays a critical role in regulating stemness and primary cilia-dependent signaling is required for MSCs' proliferation and pluripotency (Yanardag & Pugacheva, 2021). Previous research has shown correlation between high doses of *Sox2* and repression of proliferative genes in slow-cycling stem cells (Hagey & Muhr, 2014) and the expression of stem cell marker *Sox2* is down-regulated after the deciliation (Ma et al, 2020). In contrast, upon differentiation, reduction of *Sox2* levels is needed for cyclin D1-dependent entrance of rapidly dividing states (Hagey & Muhr, 2014). Furthermore, ciliary disassembly is needed to release brakes on G1/S transition for cells to enter into a fast proliferating state (Izawa et al, 2015). Our data reveal overlapping expression patterns of

Tmem107 and *Sox2* genes in NR (Figs S2 and S3). Both of them are abundantly present in pluripotent neuroepithelial cells and down-regulated in differentiating GCL cells (Taranova et al, 2006; Zhang & Cui 2014). Furthermore, we have shown positive correlation between *Tmem107* absence and SOX2 down-regulation, suggesting that SOX2 role in maintaining pluripotency could be directly regulated by TMEM107. Interestingly, CMZ exhibits no expression of SOX2 together with very low expression of *Tmem107* (Fig S2). This area generates new neurons that are incorporated into the retina as it enlarges continually throughout the lifetime of an animal (Harris & Perron, 1998; Reh & Levine, 1998). This peripheral area of the adult eye may also contain retinal stem cell pools (Ahmad et al, 2000; Tropepe et al, 2000; Coles et al, 2006). These findings further confirm a key role of TMEM107 in differentiation of neural retina and also suggest that SOX2 regulation specifically requires TMEM107.

In conclusion, our results enhance the understanding of developmental processes in ciliopathies where ocular phenotypes occur and help us gain deeper knowledge into the mechanisms involved in primary cilia function during morphogenesis of eye structures. Our findings give insight into the relationship between primary cilia-mediated signaling and eye development, revealing reduced ciliogenesis and aberrant *Shh* signaling as the cause of anophthalmic and microphthalmic phenotypes and could expand diagnostic tools for these diseases in humans by classifying *Tmem107* as one of the diagnostic markers. Furthermore, we introduce retinal organoids as a useful tool to study mechanisms of primary cilia disruption and for the testing of potential therapeutic approaches to treat ciliopathy-related diseases.

Materials and Methods

Animals

Embryos of mice containing *Tmem107*^{null} allele were generated as described previously (Tang et al, 2010; Christopher et al, 2012). The details on the generation of the mutant can be found via the MMRRRC strain information page (https://www.mmrrc.org/catalog/sds.php?mmrrc_id=32632). Targeted or gene trap mutations were generated in strain 129/SvEvBrd-derived embryonic stem (ES) cells. The chimeric mice are bred to C57BL/6J albino mice to generate F1 heterozygous animals. All of the mouse husbandry was performed in accordance with Yale's Institutional Animal Care and Use Committee guidelines.

Immunofluorescent staining on paraffin-embedded sections of mice

Embryonic mouse samples were collected (Table S2) and fixed in 4% paraformaldehyde overnight and then processed for paraffin embedding and sectioned in transversal planes. Before immunofluorescent analysis, sections underwent the xylene/ethanol series for deparaffinization and rehydration. For antigen retrieval, 0.1 M sodium-citrate buffer pH6 with 0.04% Tween was used. Retrieval was performed under 98°C for 25 min.

Sections were incubated with primary antibodies (Table S3) for 1 h at room temperature and subsequently with the following secondary antibodies for 1 h at room temperature: anti-mouse Alexa Fluor 488 (1:200, cat. No. A11001), anti-mouse Alexa Fluor 568 (1:200, cat. No. A11004), anti-rabbit Alexa Fluor 488 (1:200, cat. No. A11008), and anti-rabbit Alexa Fluor 594 (1:200, cat. No. A11037; all Thermo Fisher Scientific). Sections were washed in PBS and coverslipped in Fluoroshield with DAPI (cat. No. F6057; Sigma-Aldrich, Merck). The pictures were taken under a fluorescence microscope Leica DM LB2 (Leica) and the Leica SP8 confocal microscope (Leica). Individual images were assembled into Figures in Adobe Photoshop 5.0. Pictures of wild-type and mutant specimens were taken under the same microscope settings.

Immunofluorescent staining of organoids

For frozen sections staining, organoids were fixed in 4% paraformaldehyde for 30 min at room temperature, washed with PBS, cryopreserved in 30% sucrose (16104; Sigma-Aldrich) in PBS overnight at 4°C, embedded in Tissue-Tek O.C.T. Compound medium (Sakura) and sectioned on a cryostat (CM1850; Leica) with thickness of slides ~10 µm. For cells grown on coverslips, cells were fixed in 4% paraformaldehyde for 15 min at room temperature. Samples were washed with PBS and blocked in a blocking buffer (PBS with 0.3% Triton X-100 [T8787; Sigma-Aldrich] and 5% normal goat serum [G9023; Sigma-Aldrich]) for 1 h at room temperature in a humidified chamber. The primary antibodies were diluted in antibody diluent (PBS with 0.3% Triton X-100 and 1% bovine serum albumin [A9647; Sigma-Aldrich]) and applied to the sections overnight at 4°C in a humidified chamber. List of primary antibodies is provided in Table S3. The sections were washed with antibody diluent and a secondary antibody (anti-Mouse AlexaFluor 488; Thermo Fisher Scientific, 1:1,000 and anti-rabbit AlexaFluor 594; Thermo Fisher Scientific, 1:1,000) was applied for 1 h at room temperature in a humidified chamber. The nuclei were stained with 1 µg/ml DAPI in PBS for 4 min at room temperature and the sections were mounted using Fluoromount Aqueous Mounting Medium (F4680; Sigma-Aldrich). Sections were scanned using Zeiss LSM 880 confocal microscope and files were processed using ZEN Blue Edition software (Zeiss).

In situ gene expression analysis using RNAScope technique

The embryos were fixed in 4% PFA for 24–36 h and proceeded for dehydration in an ethanol series. After embedding in paraffin, 5-µm transverse sections were obtained. The sections were deparaffinized in xylene and dehydrated in 100% ethanol. To detect mRNA expression of *Tmem107* (805841; ACD Bio) and *Ptch1* (476231; ACD Bio) in mouse embryos, we used the RNAScope R Multiplex Fluorescent v2 Assay kit (Cat. No. 323 110; ACD Bio) for formalin-fixed paraffin-embedded tissues according to the manufacturer's instructions. All reactions were performed at 40°C in the HybEZTM II Oven (ACD Bio). Visualization of hybridized probes was done using the TSA-Plus Cyanine 3 system (NEL744001KT; Perkin-Elmer), according to the manufacturer's protocol. DAPI (cat. n. 323 108; ACD Bio) was used for nuclear staining. Pictures were taken with a

fluorescence microscope Leica DM LB2 (Leica) and the Leica SP8 confocal microscope (Leica).

CRISPR/Cas9-mediated gene editing

Cells were transfected with a PX458 vector containing gRNA sequences for *TMEM107* knockout. The pSpCas9(BB)-2A-GFP (PX458) was a gift from Feng Zhang (Plasmid #48138; Addgene; <http://n2t.net/addgene:48138>; RRID:Addgene_48138). gRNA was designed using Benchling [Biology Software] (2021), retrieved from <https://benchling.com>, to target the *NcoI* restriction site (Fig S7A) in the first exon of *TMEM107* (FWD: CACCGAAGCCCTGAGACCCGGCCCA, REV: aaacTGGGCCGGTCTCAGGGCTTC). 48 h after transfection, GFP-positive cells were bulk FACS-sorted using BD FACS Aria. Then, the cells were transfected for the second time and individual clones were generated using single-cell FACS sorting. Selected clones were screened by PCR using the following primers flanking the first *TMEM107* exon (FWD: CTAGATTTGTCGGCTTGCGG, REV: GCAGGGTAGGACTAGGACCA). PCR products were digested using the *NcoI* restriction enzyme (Fig S7B and C). Clones that lacked the *NcoI* restriction site were selected for the final next-generation sequencing screen using the Illumina platform (Malcikova et al, 2015) and compared with the wild-type sequence (Figs S8 and S9).

shRNA-mediated gene knockdown

DNA sequences for shRNA-mediated *TMEM107* down-regulation were designed using a web tool (Gu et al, 2014). Generated sequences: shRNA-TMEM107-F: CCGGGACATTAAGACTTATATAAaacctgaccattaTTA-TATAAGTCTTAATGTCTTTTGG, shRNA-TMEM107-R: AATTCAAAAAGACATTAAGACTTATATAAaatgggtcaggttaTTATATAAGTCTTAATGTC were cloned into a lentiviral vector containing DOX-inducible U6 promoter and TetRep-P2A-Puro-P2A-mCherry (Eshtad et al, 2016) (vector kindly provided by Mikael Altun). Lentiviral particles were generated as described previously (Barta et al, 2016; Peskova et al, 2019, 2020) using pMD2.G (#12259; Addgene) and psPAX2 (#12260; Addgene) (gift from Didier Trono, École Polytechnique Fédérale de Lausanne, Lausanne, Switzerland). We generated non-clonal hiPSC lines using fluorescent activated cell sorting of mCherry-positive hiPSCs. After transduction, at least 5,000 mCherry-positive hiPSCs were sorted using BD FACSAria (BD Biosciences). Generated cell lines were then propagated in the presence of puromycin (1 µg/ml). DOX 0.5 µg/ml was applied from day (D)2 to D25 of the differentiation of retinal organoids.

Analysis of primary cilia length

Ciliary axonemes were visualized using ARL13B immunostaining as described above. Imaging was performed with a Leica SP8 laser scanning microscope using the 63× oil objective, and image acquisition was performed using LAS X software (Leica). Image data were acquired as Z-stacks of images and a 0.3-µm distance separated neighboring Z-sections. Cilia length measurements were done using the Imaris Cell module (Imaris v9.5; Oxford Instruments) using the methodology of fitting an ellipsoid into the surface analysis to obtain ellipsoid axis length. Statistical analyses were performed using a two-tailed t test.

Generation of retinal organoids

Retinal organoids were generated from human embryonic stem cells (hESCs) (H9 cell line, WiCell Bank) or hiPSCs (M8 cell line, [Peskova et al, 2020]), according to the protocol described elsewhere (Kuwahara et al, 2015; Peskova et al, 2020) with small modifications. Briefly, cells in E8 medium were seeded into a U-shaped, cell-repellent 96-well plate (5,000 cells/well) (Item No: 650970; Cellstar, Greiner) in the presence of 20 μM ROCK inhibitor (Y-27632; STEMCELL Technologies). After 48 h (Day 0 of the differentiation process) the culture medium was changed to gfCDM (Kuwahara et al, 2015) (45% IMDM [Item No: 21980-032; Gibco], 45% Hams F12 [F12, Item No: 21765-029; Gibco], 10% KnockOut Serum Replacement [Item No: 10828-028; Gibco], 1% chemically defined lipid concentrate [Cat. No. 11905-031; Gibco], 1 \times penicillin–streptomycin solution [Item No: XC-A4122; Biosera], 10 μM β -mercaptoethanol [Item No: M3148; Sigma-Aldrich]). On day 6, recombinant human BMP4 (Peprotech) was added to the culture to the final concentration 2.2 nM and then the medium was changed every third day. On day 18 of the differentiation process, gfCDM was changed to a NR medium (DMEM/F12 [Item No: 21331-020; Gibco], 1% N-2 supplement [Item No: 17502001; Gibco], 1% GlutaMAX supplement [Item No: 35050061; Gibco], 10% FBS [Item No: FB-1101; Biosera], 0.5 μM retinoic acid [Item No: R2625; Sigma-Aldrich], 0.1 mM taurine [Item No: T8691; Sigma-Aldrich], 1 \times penicillin–streptomycin solution [Item No: XC-A4122; Biosera]).

Cell cultures and their treatments

ARPE-19 (ATCC - American Type Culture Collection) cells were cultured in media Knockout DMEM (Invitrogen, Life Technologies Ltd.), containing 10% FBS, 1 \times GlutaMAX (Invitrogen, Life Technologies Ltd.), 1 \times MEM nonessential amino acid solution (Invitrogen, Life Technologies Ltd.), 1 \times penicillin/streptomycin (PAA), and 10 μM β -mercaptoethanol (Sigma-Aldrich). The cells were incubated at 37°C/5% CO₂ and regularly passaged using trypsin (Sigma-Aldrich). For the small-molecule agonist of the Shh-Smo pathway (SAG) treatment, confluent ARPE-19 cells were cultured 24 h in the presence of 1 μM SAG (Tocris) without FBS and harvested or fixed for downstream processing. H9 hESCs and M8 hiPSCs were cultured in Essential 8 Medium (Invitrogen, Life Technologies Ltd.) on cell culture dishes coated with vitronectin and regularly passaged using 0.5 mM EDTA in PBS.

Gene expression analyses by RT–qPCR

ARPE-19 cells were washed with PBS and harvested into 1 ml of RNA Blue Reagent (an analog of Trizol) (Top-Bio). For retinal organoid analysis, at least eight organoids were washed with PBS and homogenized using a 1 ml insulin syringe in 1 ml RNA Blue Reagent. RNA was isolated using chloroform extraction, and then reverse-transcribed using a High-Capacity cDNA Reverse Transcription Kit (Applied Biosystems). The RT product was amplified by real-time PCR (Roche LightCycler 480 PCR instrument) using PowerUp SYBR Green Master Mix (Applied Biosystems TM). Primer sequences are

shown in Table S4. All experiments were performed using at least three independent replicates.

Micro-CT analyses

Before micro-CT scan the samples of E15.5 mouse embryos were dehydrated in the alcohol grades (30%, 50%, 70%, 80%, and 90%). The samples were then stained in the solution of 1% iodine in 90% MeOH to enhance the contrast of soft tissue. For the purpose of motion stabilization during the scan, the embryos were embedded in 1% agarose gel in a 2-ml Eppendorf tube.

The micro-CT scanning was performed using laboratory system GE phoenix v|tome|x L 240 (Waygate Technologies), equipped with a 180 kV/15W maximum power nanofocus X-ray tube and high-contrast flat panel detector dynamic 41|100 (dimension - 4,048 \times 4,048 pixels, with pixel size of 100 μm). The measurements were carried out in an air-conditioned cabinet (21°C). The tomographic reconstruction was performed using the software GE phoenix datos|x 2.0 (Waygate Technologies, Germany). The measurements were acquired with the following settings: acceleration voltage 60 kV, X-ray tube current 200 μA , exposition time was 900 ms, 2,200 images were taken over the 360° rotation, and voxel resolution of 3.6 μm .

The manual segmentation of the eyes was carried out using Avizo 9.5 software (Thermo Fisher Scientific). All 3D visualizations, measurements, and specialized analyses were performed in VG Studio MAX 2022 software (Volume Graphics GmbH).

The wall thickness analysis was performed in the VG Studio software. The analysis is based on fitting the spheres in the 3D space into the defined object of the eye. The larger the space in between the walls of the object in 3D can fit a larger sphere. The quantification of this analysis is showing the count of the voxels (voxel = 3D pixel) with the appointed wall thickness.

The optic stalk length was measured with the polyline tool. This tool enables the length measurement of the not-straight objects by placing the individual points defining the line alongside the shape of the measured object. The volumes of the segmented eyes were measured in the VG Studio software.

SEM

SEM was performed as described previously (Peskova et al, 2020). Briefly, the organoids were fixed with 3% glutaraldehyde in a 0.1 M cacodylate buffer, then washed three times with 0.1 M cacodylate buffer, dehydrated using ascending ethanol grade (30, 50, 70, 80, 90, 96, and 100%), and dried in a critical point dryer (CPD 030; BAL-TEC Inc.) using liquid carbon dioxide. The dried organoids were sputtered with gold in a sputter coater (SCD 040; Balzers Union Limited) and observed in a scanning electron microscope (VEGA TS 5136 XM; Tescan Orsay Holding) using a secondary emission detector and a 20-kV acceleration voltage.

Statistical analysis

All results are expressed as means \pm SD of three replicates for each condition. For the testing of normal distribution, Shapiro–Wilk test was used and data were further compared by either paired in case

of RT-qPCR and micro-CT analysis or nonparametric unpaired two-tailed *t* test in case of primary cilia length measurements and Western blot analyses. Differences were considered to be significant at $P < 0.05$.

Data Availability

Materials described in the article, including all relevant raw data, will be freely available to any researcher wishing to use them for noncommercial purposes, without breaching participant confidentiality.

Supplementary Information

Supplementary Information is available at <https://doi.org/10.26508/lsa.202302073>.

Acknowledgements

This work was supported by the Czech Science Foundation (21-05146S) and by the Ministry of Education, Youth and Sports of the Czech Republic (CZ.02.1.01/0.0/0.0/15_003/0000460) to M Buchtova. We acknowledge the core facility CELLIM supported by the Czech-Bioluminescence large RI project (LM2023050 funded by MEYS CR) for their support with obtaining the scientific data presented in this article. T Barta is supported also by the Ministry of Health (NU22-07-00380).

Author Contributions

M Dubaïc: formal analysis, investigation, visualization, methodology, and writing—original draft.

L Peskova: formal analysis, investigation, visualization, methodology, and writing—original draft.

M Hampl: formal analysis, investigation, methodology, and writing—original draft.

K Weissova: formal analysis, investigation, visualization, and methodology.

C Celiker: formal analysis, investigation, and methodology.

NA Shylo: resources, formal analysis, methodology, and writing—original draft, review, and editing.

E Hrubá: formal analysis, investigation, and methodology.

M Kavkova: formal analysis, investigation, methodology, and writing—original draft.

T Zikmund: resources, software, funding acquisition, methodology, and writing—original draft.

SD Weatherbee: resources, methodology, and writing—review and editing.

J Kaiser: resources, software, methodology, and writing—review and editing.

T Barta: conceptualization, data curation, formal analysis, supervision, funding acquisition, investigation, visualization, methodology, and writing—original draft, review, and editing.

M Buchtova: conceptualization, resources, supervision, funding acquisition, methodology, and writing—review and editing.

Conflict of Interest Statement

The authors declare that they have no conflict of interest.

References

- Ahmad I, Tang L, Pham H (2000) Identification of neural progenitors in the adult mammalian eye. *Biochem Biophys Res Commun* 270: 517–521. doi:10.1006/bbrc.2000.2473
- Badano JL, Mitsuma N, Beales PL, Katsanis N (2006) The ciliopathies: An emerging class of human genetic disorders. *Annu Rev Genomics Hum Genet* 7: 125–148. doi:10.1146/annurev.genom.7.080505.115610
- Barta T, Peskova L, Hampl A (2016) miRNAsong: A web-based tool for generation and testing of miRNA sponge constructs in silico. *Sci Rep* 6: 36625. doi:10.1038/srep36625
- Bosze B, Suarez-Navarro J, Soofi A, Lauderdale JD, Dressler GR, Brown NL (2021) Multiple roles for Pax2 in the embryonic mouse eye. *Dev Biol* 472: 18–29. doi:10.1016/j.ydbio.2020.12.020
- Burmeister M, Novak J, Liang MY, Basu S, Ploder L, Hawes NL, Vidgen D, Hoover F, Goldman D, Kalnins VI, et al (1996) Ocular retardation mouse caused by Chx10 homeobox null allele: Impaired retinal progenitor proliferation and bipolar cell differentiation. *Nat Genet* 12: 376–384. doi:10.1038/ng0496-376
- Burnett JB, Lupu FI, Eggenschwiler JT (2017) Proper ciliary assembly is critical for restricting hedgehog signaling during early eye development in mice. *Dev Biol* 430: 32–40. doi:10.1016/j.ydbio.2017.07.012
- Caspary T, Larkins CE, Anderson KV (2007) The graded response to Sonic Hedgehog depends on cilia architecture. *Dev Cell* 12: 767–778. doi:10.1016/j.devcel.2007.03.004
- Cavodeassi F, Creuzet S, Etchevers HC (2019) The hedgehog pathway and ocular developmental anomalies. *Hum Genet* 138: 917–936. doi:10.1007/s00439-018-1918-8
- Cela P, Hampl M, Shylo NA, Christopher KJ, Kavkova M, Landova M, Zikmund T, Weatherbee SD, Kaiser J, Buchtova M (2018) Ciliopathy protein tmem107 plays multiple roles in craniofacial development. *J Dent Res* 97: 108–117. doi:10.1177/0022034517732538
- Celiker C, Weissova K, Cerna KA, Oppelt J, Dorgau B, Gambin FM, Sebestikova J, Lako M, Sernagor E, Liskova P, et al (2023) Light-responsive microRNA molecules in human retinal organoids are differentially regulated by distinct wavelengths of light. *iScience* 26: 107237. doi:10.1016/j.isci.2023.107237
- Chang C-F, Schock EN, Attia AC, Stottmann RW, Brugmann SA (2015) The ciliary baton: Orchestrating neural crest cell development. *Curr Top Dev Biol* 111: 97–134. doi:10.1016/bs.ctdb.2014.11.004
- Chiang C, Litingtung Y, Lee E, Young KE, Corden JL, Westphal H, Beachy PA (1996) Cyclopia and defective axial patterning in mice lacking Sonic hedgehog gene function. *Nature* 383: 407–413. doi:10.1038/383407a0
- Chinen Y, Nakamura S, Yanagi K, Kaneshi T, Goya H, Yoshida T, Satou K, Kaname T, Naritomi K, Nakanishi K (2022) Additional findings of tibial dysplasia in a male with orofaciocaudal syndrome type XVI. *Hum Genome Var* 9: 9. doi:10.1038/s41439-022-00187-9
- Christopher KJ, Wang B, Kong Y, Weatherbee SD (2012) Forward genetics uncovers Transmembrane protein 107 as a novel factor required for ciliogenesis and Sonic hedgehog signaling. *Dev Biol* 368: 382–392. doi:10.1016/j.ydbio.2012.06.008
- Coles BL, Horsford DJ, McInnes RR, van der Kooy D (2006) Loss of retinal progenitor cells leads to an increase in the retinal stem cell population in vivo. *Eur J Neurosci* 23: 75–82. doi:10.1111/j.1460-9568.2005.04537.x

- Eiraku M, Takata N, Ishibashi H, Kawada M, Sakakura E, Okuda S, Sekiguchi K, Adachi T, Sasai Y (2011) Self-organizing optic-cup morphogenesis in three-dimensional culture. *Nature* 472: 51–56. doi:[10.1038/nature09941](https://doi.org/10.1038/nature09941)
- Eshtad S, Mavajian Z, Rudd SG, Visnes T, Boström J, Altun M, Helleday T (2016) hMYH and hMTH1 cooperate for survival in mismatch repair defective T-cell acute lymphoblastic leukemia. *Oncogenesis* 5: e275. doi:[10.1038/oncsis.2016.72](https://doi.org/10.1038/oncsis.2016.72)
- Fiore L, Takata N, Acosta S, Ma W, Pandit T, Oxendine M, Oliver G (2020) Optic vesicle morphogenesis requires primary cilia. *Dev Biol* 462: 119–128. doi:[10.1016/j.ydbio.2020.02.016](https://doi.org/10.1016/j.ydbio.2020.02.016)
- Furukawa T, Zokac CA, Cepko CL (1997a) Rax, a novel paired-type homeobox gene, shows expression in the anterior neural fold and developing retina. *Proc Natl Acad Sci U S A* 94: 3088–3093. doi:[10.1073/pnas.94.7.3088](https://doi.org/10.1073/pnas.94.7.3088)
- Furukawa T, Morrow EM, Cepko CL (1997b) Crx, a novel otx-like homeobox gene, shows photoreceptor-specific expression and regulates photoreceptor differentiation. *Cell* 91: 531–541. doi:[10.1016/s0092-8674\(00\)80439-0](https://doi.org/10.1016/s0092-8674(00)80439-0)
- Gallagher AR, Hoffmann S, Brown N, Cedzich A, Meruvu S, Podlich D, Feng Y, Könecke V, de Vries U, Hammes H-P, et al (2006) A truncated polycystin-2 protein causes polycystic kidney disease and retinal degeneration in transgenic rats. *J Am Soc Nephrol* 17: 2719–2730. doi:[10.1681/ASN.2005090979](https://doi.org/10.1681/ASN.2005090979)
- Gonçalves J, Pelletier L (2017) The ciliary transition zone: Finding the pieces and assembling the gate. *Mol Cell* 40: 243–253. doi:[10.14348/molcells.2017.0054](https://doi.org/10.14348/molcells.2017.0054)
- Gorivodsky M, Mukhopadhyay M, Wilsch-Braeuning M, Phillips M, Teufel A, Kim C, Malik N, Huttner W, Westphal H (2009) Intraflagellar transport protein 172 is essential for primary cilia formation and plays a vital role in patterning the mammalian brain. *Dev Biol* 325: 24–32. doi:[10.1016/j.ydbio.2008.09.019](https://doi.org/10.1016/j.ydbio.2008.09.019)
- Gu S, Zhang Y, Jin L, Huang Y, Zhang F, Bassik MC, Kampmann M, Kay MA (2014) Weak base pairing in both seed and 3' regions reduces RNAi off-targets and enhances si/shRNA designs. *Nucleic Acids Res* 42: 12169–12176. doi:[10.1093/nar/gku854](https://doi.org/10.1093/nar/gku854)
- Hagey DW, Muhr J (2014) Sox2 acts in a dose-dependent fashion to regulate proliferation of cortical progenitors. *Cell Rep* 9: 1908–1920. doi:[10.1016/j.celrep.2014.11.013](https://doi.org/10.1016/j.celrep.2014.11.013)
- Harris WA, Perron M (1998) Molecular recapitulation: The growth of the vertebrate retina. *Int J Dev Biol* 42: 299–304.
- Hartill V, Szymanska K, Sharif SM, Wheway G, Johnson CA (2017) Meckel-gruber syndrome: An update on diagnosis, clinical management, and research advances. *Front Pediatr* 5: 244. doi:[10.3389/fped.2017.00244](https://doi.org/10.3389/fped.2017.00244)
- Heavner W, Pevny L (2012) Eye development and retinogenesis. *Cold Spring Harb Perspect Biol* 4: a008391. doi:[10.1101/cshperspect.a008391](https://doi.org/10.1101/cshperspect.a008391)
- Huang K-C, Wang M-L, Chen S-J, Kuo J-C, Wang W-J, Nhi Nguyen PN, Wahlin KJ, Lu J-F, Tran AA, Shi M, et al (2019) Morphological and molecular defects in human three-dimensional retinal organoid model of X-linked juvenile retinoschisis. *Stem Cell Rep* 13: 906–923. doi:[10.1016/j.stemcr.2019.09.010](https://doi.org/10.1016/j.stemcr.2019.09.010)
- Huangfu D, Anderson KV (2005) Cilia and Hedgehog responsiveness in the mouse. *Proc Natl Acad Sci U S A* 102: 11325–11330. doi:[10.1073/pnas.0505328102](https://doi.org/10.1073/pnas.0505328102)
- Huangfu D, Liu A, Rakeman AS, Murcia NS, Niswander L, Anderson KV (2003) Hedgehog signalling in the mouse requires intraflagellar transport proteins. *Nature* 426: 83–87. doi:[10.1038/nature02061](https://doi.org/10.1038/nature02061)
- Iglesias A, Anyane-Yeboah K, Wynn J, Wilson A, Truitt Cho M, Guzman E, Sisson R, Egan C, Chung WK (2014) The usefulness of whole-exome sequencing in routine clinical practice. *Genet Med* 16: 922–931. doi:[10.1038/gim.2014.58](https://doi.org/10.1038/gim.2014.58)
- Irie S, Sanuki R, Muranishi Y, Kato K, Chaya T, Furukawa T (2015) Rax homeoprotein regulates photoreceptor cell maturation and survival in association with crx in the postnatal mouse retina. *Mol Cell Biol* 35: 2583–2596. doi:[10.1128/MCB.00048-15](https://doi.org/10.1128/MCB.00048-15)
- Izawa I, Goto H, Kasahara K, Inagaki M (2015) Current topics of functional links between primary cilia and cell cycle. *Cilia* 4: 12. doi:[10.1186/s13630-015-0021-1](https://doi.org/10.1186/s13630-015-0021-1)
- Kamachi Y, Uchikawa M, Collignon J, Lovell-Badge R, Kondoh H (1998) Involvement of Sox1, 2 and 3 in the early and subsequent molecular events of lens induction. *Development* 125: 2521–2532. doi:[10.1242/dev.125.13.2521](https://doi.org/10.1242/dev.125.13.2521)
- Kozmik Z (2008) The role of Pax genes in eye evolution. *Brain Res Bull* 75: 335–339. doi:[10.1016/j.brainresbull.2007.10.046](https://doi.org/10.1016/j.brainresbull.2007.10.046)
- Kuwahara A, Ozone C, Nakano T, Saito K, Eiraku M, Sasai Y (2015) Generation of a ciliary margin-like stem cell niche from self-organizing human retinal tissue. *Nat Commun* 6: 6286. doi:[10.1038/ncomms7286](https://doi.org/10.1038/ncomms7286)
- Lambacher NJ, Bruel A-L, van Dam TJP, Szymańska K, Slaats GG, Kuhns S, McManus GJ, Kennedy JE, Gaff K, Wu KM, et al (2016) TMEM107 recruits ciliopathy proteins to subdomains of the ciliary transition zone and causes Joubert syndrome. *Nat Cell Biol* 18: 122–131. doi:[10.1038/ncb3273](https://doi.org/10.1038/ncb3273)
- Lee JE, Gleeson JG (2011) Cilia in the nervous system: Linking cilia function and neurodevelopmental disorders. *Curr Opin Neurol* 24: 98–105. doi:[10.1097/WCO.0b013e3283444d05](https://doi.org/10.1097/WCO.0b013e3283444d05)
- Lupu FI, Burnett JB, Eggenschwiler JT (2018) Cell cycle-related kinase regulates mammalian eye development through positive and negative regulation of the Hedgehog pathway. *Dev Biol* 434: 24–35. doi:[10.1016/j.ydbio.2017.10.022](https://doi.org/10.1016/j.ydbio.2017.10.022)
- Ma Z, Qin M, Liang H, Chen R, Cai S, Huang Z, Tai G (2020) Primary cilia-dependent signaling is involved in regulating mesenchymal stem cell proliferation and pluripotency maintenance. *J Mol Histol* 51: 241–250. doi:[10.1007/s10735-020-09876-7](https://doi.org/10.1007/s10735-020-09876-7)
- MacRae DW, Howard RO, Albert DM, Hsia YE (1972) Ocular manifestations of the Meckel syndrome. *Arch Ophthalmol* 88: 106–113. doi:[10.1001/archophth.1972.0100030108028](https://doi.org/10.1001/archophth.1972.0100030108028)
- Malcikova J, Stano-Kozubik K, Tichy B, Kantorova B, Pavlova S, Tom N, Radova L, Smardova J, Pardy F, Doubek M, et al (2015) Detailed analysis of therapy-driven clonal evolution of TP53 mutations in chronic lymphocytic leukemia. *Leukemia* 29: 877–885. doi:[10.1038/leu.2014.297](https://doi.org/10.1038/leu.2014.297)
- Marra AN, Li Y, Wingert RA (2016) Antennas of organ morphogenesis: The roles of cilia in vertebrate kidney development. *Genesis* 54: 457–469. doi:[10.1002/dvg.22957](https://doi.org/10.1002/dvg.22957)
- Matsushima D, Heavner W, Pevny LH (2011) Combinatorial regulation of optic cup progenitor cell fate by SOX2 and PAX6. *Development* 138: 443–454. doi:[10.1242/dev.055178](https://doi.org/10.1242/dev.055178)
- Nishiguchi S, Wood H, Kondoh H, Lovell-Badge R, Episkopou V (1998) Sox1 directly regulates the gamma-crystallin genes and is essential for lens development in mice. *Genes Dev* 12: 776–781. doi:[10.1101/gad.12.6.776](https://doi.org/10.1101/gad.12.6.776)
- Peskova L, Cerna K, Oppelt J, Mraz M, Barta T (2019) Oct4-mediated reprogramming induces embryonic-like microRNA expression signatures in human fibroblasts. *Sci Rep* 9: 15759. doi:[10.1038/s41598-019-52294-3](https://doi.org/10.1038/s41598-019-52294-3)
- Peskova L, Jurcikova D, Vanova T, Krivanek J, Capandova M, Sramkova Z, Sebestikova J, Kolouskova M, Kotasova H, Streit L, et al (2020) miR-183/96/182 cluster is an important morphogenetic factor targeting PAX6 expression in differentiating human retinal organoids. *Stem Cells* 38: 1557–1567. doi:[10.1002/stem.3272](https://doi.org/10.1002/stem.3272)
- Qin J, Lin Y, Norman RX, Ko HW, Eggenschwiler JT (2011) Intraflagellar transport protein 122 antagonizes sonic hedgehog signaling and controls ciliary localization of pathway components. *Proc Natl Acad Sci U S A* 108: 1456–1461. doi:[10.1073/pnas.1011410108](https://doi.org/10.1073/pnas.1011410108)

- Reh TA, Levine EM (1998) Multipotential stem cells and progenitors in the vertebrate retina. *J Neurobiol* 36: 206–220.
- Roitbak T, Ward CJ, Harris PC, Bacallao R, Ness SA, Wandering-Ness A (2004) A polycystin-1 multiprotein complex is disrupted in polycystic kidney disease cells. *Mol Biol Cell* 15: 1334–1346. doi:[10.1091/mbc.e03-05-0296](https://doi.org/10.1091/mbc.e03-05-0296)
- Shaheen R, Almoisheer A, Faqieh E, Babay Z, Monies D, Tassan N, Abouelhoda M, Kurdi W, Al Mardawi E, Khalil MMI, et al (2015) Identification of a novel MKS locus defined by TMEM107 mutation. *Hum Mol Genet* 24: 5211–5218. doi:[10.1093/hmg/ddv242](https://doi.org/10.1093/hmg/ddv242)
- Shylo NA, Christopher KJ, Iglesias A, Daluiski A, Weatherbee SD (2016) TMEM107 is a critical regulator of ciliary protein composition and is mutated in orofacioidigital syndrome. *Hum Mutat* 37: 155–159. doi:[10.1002/humu.22925](https://doi.org/10.1002/humu.22925)
- Shylo NA, Emmanouil E, Ramrattan D, Weatherbee SD (2020) Loss of ciliary transition zone protein TMEM107 leads to heterotaxy in mice. *Dev Biol* 460: 187–199. doi:[10.1016/j.ydbio.2019.12.014](https://doi.org/10.1016/j.ydbio.2019.12.014)
- Slaats GG, Wheway G, Foletto V, Szymanska K, van Balkom BWM, Logister I, Den Ouden K, Keijzer-Veen MG, Lilien MR, Knoers NV, et al (2015) Screen-based identification and validation of four new ion channels as regulators of renal ciliogenesis. *J Cell Sci* 128: 4550–4559. doi:[10.1242/jcs.176065](https://doi.org/10.1242/jcs.176065)
- Tang T, Li L, Tang J, Li Y, Lin WY, Martin F, Grant D, Solloway M, Parker L, Ye W, et al (2010) A mouse knockout library for secreted and transmembrane proteins. *Nat Biotechnol* 28: 749–755. doi:[10.1038/nbt.1644](https://doi.org/10.1038/nbt.1644)
- Tantri A, Vrabcic TR, Cu-Unjieng A, Frost A, Annesley WH, Donoso LA (2004) X-Linked retinoschisis: A clinical and molecular genetic review. *Surv Ophthalmol* 49: 214–230. doi:[10.1016/j.survophthal.2003.12.007](https://doi.org/10.1016/j.survophthal.2003.12.007)
- Taranova OV, Magness ST, Fagan BM, Wu Y, Surzenko N, Hutton SR, Pevny LH (2006) SOX2 is a dose-dependent regulator of retinal neural progenitor competence. *Genes Dev* 20: 1187–1202. doi:[10.1101/gad.1407906](https://doi.org/10.1101/gad.1407906)
- Tropepe V, Coles BL, Chiasson BJ, Horsford DJ, Elia AJ, McInnes RR, van der Kooy D (2000) Retinal stem cells in the adult mammalian eye. *Science* 287: 2032–2036. doi:[10.1126/science.287.5460.2032](https://doi.org/10.1126/science.287.5460.2032)
- van Adelsberg J (2000) Polycystin-1 interacts with E-cadherin and the catenins—clues to the pathogenesis of cyst formation in ADPKD? *Nephrol Dial Transplant* 15: 1–2. doi:[10.1093/ndt/15.1.1](https://doi.org/10.1093/ndt/15.1.1)
- Waters AM, Beales PL (2011) Ciliopathies: An expanding disease spectrum. *Pediatr Nephrol* 26: 1039–1056. doi:[10.1007/s00467-010-1731-7](https://doi.org/10.1007/s00467-010-1731-7)
- Wheway G, Parry DA, Johnson CA (2014) The role of primary cilia in the development and disease of the retina. *Organogenesis* 10: 69–85. doi:[10.4161/org.26710](https://doi.org/10.4161/org.26710)
- Wheway G, Nazlamova L, Hancock JT (2018) Signaling through the primary cilium. *Front Cell Dev Biol* 6: 8. doi:[10.3389/fcell.2018.00008](https://doi.org/10.3389/fcell.2018.00008)
- Wiegeling A, Petzsch P, Köhrer K, Rütger U, Gerhardt C (2019) GLI3 repressor but not GLI3 activator is essential for mouse eye patterning and morphogenesis. *Dev Biol* 450: 141–154. doi:[10.1016/j.ydbio.2019.02.018](https://doi.org/10.1016/j.ydbio.2019.02.018)
- Wilson PD (2004) Polycystic kidney disease. *N Engl J Med* 350: 151–164. doi:[10.1056/NEJMra022161](https://doi.org/10.1056/NEJMra022161)
- Yanardag S, Pugacheva EN (2021) Primary cilium is involved in stem cell differentiation and renewal through the regulation of multiple signaling pathways. *Cells* 10: 1428. doi:[10.3390/cells10061428](https://doi.org/10.3390/cells10061428)
- Zhang S, Cui W (2014) Sox2, a key factor in the regulation of pluripotency and neural differentiation. *World J Stem Cell* 6: 305–311. doi:[10.4252/wjsc.v6.i3.305](https://doi.org/10.4252/wjsc.v6.i3.305)
- Zhao L, Saitou H, Sun X, Shiota K, Ishibashi M (2010) Sonic hedgehog is involved in formation of the ventral optic cup by limiting Bmp4 expression to the dorsal domain. *Mech Dev* 127: 62–72. doi:[10.1016/j.mod.2009.10.006](https://doi.org/10.1016/j.mod.2009.10.006)



License: This article is available under a Creative Commons License (Attribution 4.0 International, as described at <https://creativecommons.org/licenses/by/4.0/>).

Ciliopathy Protein Tmem107 Plays Multiple Roles in Craniofacial Development

Journal of Dental Research
2018, Vol. 97(1) 108–117
© International & American Associations
for Dental Research 2017
Reprints and permissions:
sagepub.com/journalsPermissions.nav
DOI: 10.1177/0022034517732538
journals.sagepub.com/home/jdr

P. Cela^{1,2}, M. Hampl^{1,3}, N.A. Shylo⁴, K.J. Christopher⁴, M. Kavkova⁵,
M. Landova^{1,3}, T. Zikmund⁵, S.D. Weatherbee⁴, J. Kaiser⁵,
and M. Buchtova^{1,3}

Abstract

A broad spectrum of human diseases called ciliopathies is caused by defective primary cilia morphology or signal transduction. The primary cilium is a solitary organelle that responds to mechanical and chemical stimuli from extracellular and intracellular environments. Transmembrane protein 107 (TMEM107) is localized in the primary cilium and is enriched at the transition zone where it acts to regulate protein content of the cilium. Mutations in *TMEM107* were previously connected with oral-facial-digital syndrome, Meckel-Gruber syndrome, and Joubert syndrome exhibiting a range of ciliopathic defects. Here, we analyze a role of *Tmem107* in craniofacial development with special focus on palate formation, using mouse embryos with a complete knockout of *Tmem107*. *Tmem107*^{-/-} mice were affected by a broad spectrum of craniofacial defects, including shorter snout, expansion of the facial midline, cleft lip, extensive exencephaly, and microphthalmia or anophthalmia. External abnormalities were accompanied by defects in skeletal structures, including ossification delay in several membranous bones and enlargement of the nasal septum or defects in vomeronasal cartilage. Alteration in palatal shelves growth resulted in clefting of the secondary palate. Palatal defects were caused by increased mesenchymal proliferation leading to early overgrowth of palatal shelves followed by defects in their horizontalization. Moreover, the expression of epithelial stemness marker SOX2 was altered in the palatal shelves of *Tmem107*^{-/-} animals, and differences in mesenchymal SOX9 expression demonstrated the enhancement of neural crest migration. Detailed analysis of primary cilia revealed region-specific changes in ciliary morphology accompanied by alteration of acetylated tubulin and IFT88 expression. Moreover, *Shh* and *Gli1* expression was increased in *Tmem107*^{-/-} animals as shown by in situ hybridization. Thus, TMEM107 is essential for proper head development, and defective TMEM107 function leads to ciliary morphology disruptions in a region-specific manner, which may explain the complex mutant phenotype.

Keywords: craniofacial anomalies, growth/development, mineralized tissue/development, orofacial clefts, cell signaling, oral pathology

Introduction

A defect in primary cilium morphology or function was revealed as one cause of cleft lip/palate formation (Tian et al. 2017). Primary cilia are small, microtubule-based projections from the cellular surface, covered by membrane with unique receptor and other signaling protein composition. Primary cilia were shown to be key organelles for the coordination of SHH, WNT, and PDGF signaling pathways (Haycraft et al. 2005; Schneider et al. 2005; Veland et al. 2009; Lee and Gleeson 2011). They play important roles in many developmental processes, such as neurulation, skeleton formation, and neural crest cell (NCC) migration (Chang et al. 2015), suggesting a key role for cilia during craniofacial development (Hu and Nelson 2011).

Mutations in genes encoding proteins important for cilia formation, structure, and function cause diseases called ciliopathies (Badano et al. 2006; Lee and Gleeson 2011). The number of syndromes classified as ciliopathies is still increasing, and it is estimated that one in a thousand children is born with a ciliary defect (Brugmann, Cordero, et al. 2010). Therefore, the identification of new ciliopathy genes is at the forefront of craniofacial research.

A primary cilium is composed of 9 pairs of microtubules, covered by a membrane and separated from the cytoplasm by transition fibers (Sorokin 1962). The transition zone in the proximal part of the cilium, distal to transition fibers, functions as a selective barrier, which regulates the movements of specific proteins between cilium and the cell body and therefore controls the signaling intensity (Hu and Nelson 2011).

¹Institute of Animal Physiology and Genetics, CAS, Brno, Czech Republic

²Department of Physiology, University of Veterinary and Pharmaceutical Sciences, Brno, Czech Republic

³Department of Experimental Biology, Faculty of Sciences, Masaryk University, Brno, Czech Republic

⁴Department of Genetics, Yale University, School of Medicine, New Haven, CT, USA

⁵CEITEC—Central European Institute of Technology, Brno University of Technology, Brno, Czech Republic

A supplemental appendix to this article is available online.

Corresponding Author:

M. Buchtova, Institute of Animal Physiology and Genetics, v.v.i., Academy of Sciences of the Czech, Veveri 97, 602 00 Brno, Czech Republic.
Email: buchtova@iach.cz

RECEIVED: December 5, 2017

REVISED: January 31, 2018

ACCEPTED: January 31, 2018

PUBLISHED: February 22, 2018

INTERNATIONAL WORKSHOP ON IMAGING II
4–8 SEPTEMBER 2017
VARENNA, ITALY

High-contrast differentiation resolution 3D imaging of rodent brain by X-ray computed microtomography

T. Zikmund,^a M. Novotná,^a M. Kavková,^a M. Tesařová,^a M. Kaucká,^{b,c} B. Szarowská,^c
I. Adameyko,^{b,c} E. Hrubá,^d M. Buchtová,^d E. Dražanová,^e Z. Starčuk^e and J. Kaiser^{a,1}

^aCentral European Institute of Technology, Brno University of Technology, CEITEC - BUT,
Purkyňova 123, 612 00 Brno, Czech Republic

^bDepartment of Physiology and Pharmacology, Karolinska Institutet,
Nanna Svartz väg 2, Stockholm 17177, Sweden

^cDepartment of Molecular Neurosciences, Center for Brain Research, Medical University of Vienna,
Spitalgasse 4, Vienna, Austria 1090

^dLaboratory of Molecular Morphogenesis, Institute of Animal Physiology and Genetics AS CR,
v. v. i., Brno, Czech Republic

^eInstitute of Scientific Instruments of the CAS, v. v. i., Brno, Czech Republic

E-mail: jozef.kaiser@ceitec.vutbr.cz

ABSTRACT: The biomedically focused brain research is largely performed on laboratory mice considering a high homology between the human and mouse genomes. A brain has an intricate and highly complex geometrical structure that is hard to display and analyse using only 2D methods. Applying some fast and efficient methods of brain visualization in 3D will be crucial for the neurobiology in the future. A post-mortem analysis of experimental animals' brains usually involves techniques such as magnetic resonance and computed tomography. These techniques are employed to visualize abnormalities in the brains' morphology or reparation processes. The X-ray computed microtomography (micro CT) plays an important role in the 3D imaging of internal structures of a large variety of soft and hard tissues. This non-destructive technique is applied in biological studies because the lab-based CT devices enable to obtain a several-micrometer resolution. However, this technique is always used along with some visualization methods, which are based on the tissue staining and thus differentiate soft tissues in biological samples. Here, a modified chemical contrasting protocol of tissues for a micro CT usage is introduced as the best tool for *ex vivo* 3D imaging of a post-mortem mouse brain. This way, the micro CT provides a high spatial resolution

¹Corresponding author.





Ablation of CNTN2+ Pyramidal Neurons During Development Results in Defects in Neocortical Size and Axonal Tract Formation

Maria Eleni Kastri^{1,2,3,4}, Aikaterini Stratigi^{1,2,5†}, Dimitris Mariatos^{1,2†}, Marina Theodosiou^{1,2,6†}, Maria Savvaki^{1,2}, Michaela Kavkova⁷, Kostas Theodorakis^{1,2}, Marina Vidaki^{1,2,8,9}, Tomas Zikmund⁷, Jozef Kaiser⁷, Igor Adameyko^{3,4} and Domna Karago^{1,2*}

¹ Department of Basic Science, Faculty of Medicine, University of Crete, Heraklion, Greece, ² Foundation for Research and Technology, Institute of Molecular Biology and Biotechnology, Heraklion, Greece, ³ Department of Physiology and Pharmacology, Karolinska Institutet, Stockholm, Sweden, ⁴ Center for Brain Research, Medical University Vienna, Vienna, Austria, ⁵ Laboratory of Neurophysiology, Université Libre de Bruxelles, UNL, Brussels, Belgium, ⁶ Department of Molecular Medicine, Max Planck Institute of Biochemistry, Martinsried, Germany, ⁷ CEITEC-Central European Institute of Technology, Brno University of Technology, Brno, Czechia, ⁸ The Koch Institute for Integrative Cancer Research, Massachusetts Institute of Technology, Cambridge, MA, United States, ⁹ Department of Biology, Massachusetts Institute of Technology, Cambridge, MA, United States

OPEN ACCESS

Edited by:

Josef Bischofberger,
University of Basel, Switzerland

Reviewed by:

Gianfranco Gennarini,
University of Bari Aldo Moro, Italy
Zoltan Molnar,
University of Oxford, United Kingdom

*Correspondence:

Domna Karago^{1,2*}
karago@imbb.forth.gr

†These authors have contributed
equally to this work

Specialty section:

This article was submitted to
Cellular Neurophysiology,
a section of the journal
Frontiers in Cellular Neuroscience

Received: 22 May 2019

Accepted: 23 September 2019

Published: 01 November 2019

Citation:

Kastri ME, Stratigi A, Mariatos D, Theodosiou M, Savvaki M, Kavkova M, Theodorakis K, Vidaki M, Zikmund T, Kaiser J, Adameyko I and Karago D (2019) Ablation of CNTN2+ Pyramidal Neurons During Development Results in Defects in Neocortical Size and Axonal Tract Formation. *Front. Cell. Neurosci.* 13:454. doi: 10.3389/fncel.2019.00454








Corticothalamic axons express *Contactin-2* (CNTN2/TAG-1), a neuronal recognition molecule of the immunoglobulin superfamily involved in neurogenesis, neurite outgrowth, and fasciculation. TAG-1, which is expressed transiently by cortical pyramidal neurons during embryonic development, has been shown to be fundamental for axonal recognition, cellular migration, and neuronal proliferation in the developing cortex. Although *Tag-1*^{-/-} mice do not exhibit any obvious defects in the corticofugal system, the role of TAG-1+ neurons during the development of the cortex remains elusive. We have generated a mouse model expressing EGFP under the *Tag-1* promoter and encompassing the coding sequence of Diphtheria Toxin subunit A (DTA) under quiescence with no effect on the expression of endogenous *Tag-1*. We show that while the line recapitulates the expression pattern of the molecule, it highlights an extended expression in the forebrain, including multiple axonal tracts and neuronal populations, both spatially and temporally. Crossing these mice to the *Emx1-Cre* strain, we ablated the vast majority of TAG-1+ cortical neurons. Among the observed defects were a significantly smaller cortex, a reduction of corticothalamic axons as well as callosal and commissural defects. Such defects are common in neurodevelopmental disorders, thus this mouse could serve as a useful model to study physiological and pathophysiological cortical development.

Keywords: CNTN2/TAG-1, corticofugal system, corticothalamic axons, anterior commissure, corpus callosum, central nervous system

INTRODUCTION

The multilayered neocortex evolved in mammals and is responsible for a variety of higher functions, seen for the first time in this phylum. Among these higher cognitive functions is the integration of stimuli from different sensory modalities such as vision and olfaction, the control of motor commands, consciousness, decision-making, and particularly in humans, speech.

Developmental mechanisms driving complex tooth shape in reptiles

Marie Landova Sulcova^{1,2} | Oldrich Zahradnicek³ | Jana Dumkova⁴ |
 Hana Dosedelova¹ | Jan Krivanek⁴ | Marek Hampel^{1,2} | Michaela Kavkova⁵  |
 Tomas Zikmund⁵  | Martina Gregorovicova^{6,7}  | David Sedmera^{6,7}  |
 Jozef Kaiser⁵  | Abigail S. Tucker^{3,8}  | Marcela Buchtova^{1,2} 

¹Laboratory of Molecular Morphogenesis, Institute of Animal Physiology and Genetics, Czech Academy of Science, Brno, Czech Republic

²Department of Experimental Biology, Faculty of Science, Masaryk University, Brno, Czech Republic

³Institute of Experimental Medicine, Czech Academy of Science, Prague, Czech Republic

⁴Department of Histology and Embryology, Faculty of Medicine, Masaryk University, Brno, Czech Republic

⁵CEITEC-Central European Institute of Technology, University of Technology, Brno, Czech Republic

⁶Institute of Anatomy, Medical Faculty, Charles University, Prague, Czech Republic

⁷Institute of Physiology, Czech Academy of Sciences, Prague, Czech Republic

⁸Centre for Craniofacial and Regenerative Biology, Faculty of Dentistry, Oral and Craniofacial Sciences, King's College London, London, UK

Correspondence

Marcela Buchtova, Laboratory of Molecular Morphogenesis, Institute of Animal Physiology and Genetics, v.v.i., Czech Academy of Sciences, Veveří 97, Brno 602 00, Czech Republic.
 Email: buchtova@iach.cz

Funding information

Czech Science Foundation, Grant/Award Number: 17-14886S; Ministry of Education, Youth and Sports of the Czech Republic, Grant/Award Numbers: CZ.02.1.01/0.0/0.0/15_003/0000460, LM2015062, LQ1601

Abstract

Background: In mammals, odontogenesis is regulated by transient signaling centers known as enamel knots (EKs), which drive the dental epithelium shaping. However, the developmental mechanisms contributing to formation of complex tooth shape in reptiles are not fully understood. Here, we aim to elucidate whether signaling organizers similar to EKs appear during reptilian odontogenesis and how enamel ridges are formed.

Results: Morphological structures resembling the mammalian EK were found during reptile odontogenesis. Similar to mammalian primary EKs, they exhibit the presence of apoptotic cells and no proliferating cells. Moreover, expression of mammalian EK-specific molecules (SHH, FGF4, and ST14) and GLI2-negative cells were found in reptilian EK-like areas. 3D analysis of the nucleus shape revealed distinct rearrangement of the cells associated with enamel groove formation. This process was associated with ultrastructural changes and lipid droplet accumulation in the cells directly above the forming ridge, accompanied by alteration of membranous molecule expression (Na/K-ATPase) and cytoskeletal rearrangement (F-actin).

Conclusions: The final complex shape of reptilian teeth is orchestrated by a combination of changes in cell signaling, cell shape, and cell rearrangement. All these factors contribute to asymmetry in the inner enamel epithelium development, enamel deposition, ultimately leading to the formation of characteristic enamel ridges.



Polarized Sonic Hedgehog Protein Localization and a Shift in the Expression of Region-Specific Molecules Is Associated With the Secondary Palate Development in the Veiled Chameleon

Marek Hampl^{1,2}, Jana Dumkova³, Michaela Kavkova⁴, Hana Dosedelova¹, Anna Bryjova⁵, Oldrich Zahradnicek^{6,7}, Martin Pyszko⁸, Milos Macholan⁹, Tomas Zikmund⁴, Jozef Kaiser⁴ and Marcela Buchtova^{1,2*}

OPEN ACCESS

Edited by:

Pedro Martinez,
University of Barcelona, Spain

Reviewed by:

Kristin Artinger,
University of Colorado Anschutz
Medical Campus, United States
Raul Diaz,
Southeastern Louisiana University,
United States

*Correspondence:

Marcela Buchtova
buchtova@iach.cz

Specialty section:

This article was submitted to
Evolutionary Developmental Biology,
a section of the journal
Frontiers in Cell and Developmental
Biology

Received: 20 February 2020

Accepted: 15 June 2020

Published: 28 July 2020

Citation:

Hamp M, Dumkova J, Kavkova M, Dosedelova H, Bryjova A, Zahradnicek O, Pyszko M, Macholan M, Zikmund T, Kaiser J and Buchtova M (2020) Polarized Sonic Hedgehog Protein Localization and a Shift in the Expression of Region-Specific Molecules Is Associated With the Secondary Palate Development in the Veiled Chameleon. *Front. Cell Dev. Biol.* 8:572. doi: 10.3389/fcell.2020.00572

¹ Laboratory of Molecular Morphogenesis, Institute of Animal Physiology and Genetics, Czech Academy of Sciences, Brno, Czechia, ² Department of Experimental Biology, Faculty of Science, Masaryk University, Brno, Czechia, ³ Department of Histology and Embryology, Faculty of Medicine, Masaryk University, Brno, Czechia, ⁴ Laboratory of Computed Tomography, Central European Institute of Technology, Brno University of Technology, Brno, Czechia, ⁵ Institute of Vertebrate Biology, Czech Academy of Sciences, Brno, Czechia, ⁶ Department of Developmental Biology, Institute of Experimental Medicine, Czech Academy of Sciences, Prague, Czechia, ⁷ Department of Radiation Dosimetry, Nuclear Physics Institute, Czech Academy of Sciences, Prague, Czechia, ⁸ Department of Anatomy, Histology, and Embryology, Faculty of Veterinary Medicine, University of Veterinary and Pharmaceutical Sciences, Brno, Czechia, ⁹ Laboratory of Mammalian Evolutionary Genetics, Institute of Animal Physiology and Genetics, Czech Academy of Sciences, Brno, Czechia

Secondary palate development is characterized by the formation of two palatal shelves on the maxillary prominences, which fuse in the midline in mammalian embryos. However, in reptilian species, such as turtles, crocodylians, and lizards, the palatal shelves of the secondary palate develop to a variable extent and morphology. While in most Squamates, the palate is widely open, crocodylians develop a fully closed secondary palate. Here, we analyzed developmental processes that underlie secondary palate formation in chameleons, where large palatal shelves extend horizontally toward the midline. The growth of the palatal shelves continued during post-hatching stages and closure of the secondary palate can be observed in several adult animals. The massive proliferation of a multilayered oral epithelium and mesenchymal cells in the dorsal part of the palatal shelves underlined the initiation of their horizontal outgrowth, and was decreased later in development. The polarized cellular localization of primary cilia and Sonic hedgehog protein was associated with horizontal growth of the palatal shelves. Moreover, the development of large palatal shelves, supported by the pterygoid and palatine bones, was coupled with the shift in *Meox2*, *Msx1*, and *Pax9* gene expression along the rostral-caudal axis. In conclusion, our results revealed distinctive developmental processes that contribute to the expansion and closure of the secondary palate in chameleons and highlighted divergences in palate formation across amniote species.

Keywords: secondary palate, SHH, primary cilia, skeletogenesis, chameleon, reptile

Microcomputed tomographic, biomechanical and histological analyses of lumbar interbody fusion with iliac crest bone graft in a pig model

Milan Krtička¹, Vladimír Nekuda¹, Daniel Ira¹, Radek Sedláček², Tomáš Suchý³,
Michaela Kavková⁴, Adam Břínek⁴, Eduard Göpfert⁵, Andrej Bilik¹, Jozef Kaiser⁴,
Leoš Křen⁶, Ladislav Plánka⁷

¹Masaryk University and The University Hospital Brno, Faculty of Medicine, Trauma Surgery Department, Brno, Czech Republic

²Czech Technical University in Prague, Faculty of Mechanical Engineering, Department of Mechanics, Biomechanics and Mechatronics, Prague, Czech Republic

³The Czech Academy of Sciences, Institute of Rock Structure and Mechanics, Department of Composites and Carbon Materials, Prague, Czech Republic

⁴Brno University of Technology, Central European Institute of Technology, Brno, Czech Republic

⁵Veterinary Research Institute, Brno, Czech Republic

⁶Masaryk University and The University Hospital Brno, Faculty of Medicine, Department of Pathology, Brno, Czech Republic

⁷Masaryk University and The University Hospital Brno, Faculty of Medicine, Department of Pediatric Surgery, Orthopaedics and Traumatology, Brno, Czech Republic

Received November 30, 2020

Accepted February 24, 2021

Abstract

The main goal of this study was to assess the progress of vertebral stability after lumbar interbody fusion related to microcomputed tomography (micro CT), biomechanical analysis, and histological assessment towards spine fusion. Twelve male pigs were used; each underwent L2-3 discectomy and implantation of an iliac crest bone graft in two groups; six spines were harvested eight weeks (A1) and six spines 16 weeks (A2) after surgery (7 native spines for biomechanical analysis). The CT was performed by GE phoenix datos|x 2.0 with a sample drift correction. The samples were divided according to fusion quality. Biomechanical evaluation was carried out on the MTS Mini Bionix testing system. In the nondestructive mode, three cycles of pure bending moments were applied (5 Nm load limit) at a rate of 20 °/min in flexion (+40 °) and extension (-40 °). Two representative histological sections from four samples were obtained (A1, n = 2; A2, n = 2); areas of mature bone were quantified. In micro CT, better results were achieved in group A2 (not significant). Eight weeks after the operation, flexural stiffness decreased to 48% of its initial value for native cadavers ($P < 0.05$); after 16 weeks it was comparable to native cadavers, demonstrating the suitability of the implanted graft ($P < 0.05$). The newly formed bone tissue occupied an average area of 94.205 mm² (A1) and 26.240 mm² (A2). It was confirmed that micro CT, biomechanical analysis, and histological assessment are technically feasible and suitable for the evaluation of results of other methods of large bone defect treatment.

Bone replacement, spine, injury

The use of lumbar fusion procedures has rapidly increased in the USA and Europe over the last decade (Deyo et al. 2004; Resnick 2007). A large number of these procedures involve the use of bone grafts (Boden 2002). The most frequent indications for lumbar fusion involve degenerative spinal diseases leading to chronic pain, comminuted fractures of the vertebral body, congenital spine malformations, and bone defects after tumour resection. Despite the technical progress of spinal surgery and operative materials, the risk of vertebral fusion failure occurs in 5–35% of cases (Boden 1998). Successful fusion depends on a number of surgical and host factors including the selection of a bone graft or bone substitute with adequate osteoconductive, osteoinductive and osteogenic properties (Aebi 2007). Autografting has been considered the gold standard for bone graft

Address for correspondence:

prof. MUDr. Ladislav Plánka, Ph.D.
Department of Pediatric Surgery, Orthopaedics and Traumatology
University Hospital Brno
Jihlavská 20, 625 00 Brno, Czech Republic

Phone: +420 532 234 360
E-mail: planka.ladislav@fnbrno.cz, lplanka@seznam.cz
<http://actavet.vfu.cz/>

DUCT reveals architectural mechanisms contributing to bile duct recovery in a mouse model for Alagille syndrome

Simona Hankeova^{1,2†}, Jakub Salplachta^{3†}, Tomas Zikmund^{3†}, Michaela Kavkova^{3†}, Noémi Van Hul^{1‡}, Adam Brinek³, Veronika Smekalova³, Jakub Laznovsky³, Feven Dawit⁴, Josef Jaros⁵, Vítězslav Bryja², Urban Lendahl⁶, Ewa Ellis⁴, Antal Nemeth⁷, Björn Fischler⁴, Edouard Hannezo⁸, Jozef Kaiser^{3*}, Emma Rachel Andersson^{1,6*}

¹Department of Biosciences and Nutrition, Karolinska Institutet, Solna, Sweden; ²Department of Experimental Biology, Masaryk University, Brno, Czech Republic; ³CEITEC – Central European Institute of Technology, Brno University of Technology, Brno, Czech Republic; ⁴Department of Pediatrics, Clinical Science, Intervention and Technology (CLINTEC), Karolinska Institutet and Karolinska University Hospital, Solna, Sweden; ⁵Department of Histology and Embryology, Masaryk University, Brno, Czech Republic; ⁶Department of Cell and Molecular Biology, Karolinska Institutet, Solna, Sweden; ⁷Department of Laboratory Medicine, Karolinska Institutet, Solna, Sweden; ⁸Institute of Science and Technology, Klosterneuburg, Austria

*For correspondence:

Jozef.Kaiser@ceitec.vutbr.cz (JK); emma.andersson@ki.se (ERA)

[†]These authors contributed equally to this work

[‡]These authors also contributed equally to this work

Competing interests: The authors declare that no competing interests exist.

Funding: See page 26

Received: 09 July 2020

Accepted: 14 January 2021

Published: 26 February 2021

Reviewing editor: Anna Mae Diehl, Duke University School of Medicine, United States

© Copyright Hankeova et al. This article is distributed under the terms of the [Creative Commons Attribution License](https://creativecommons.org/licenses/by/4.0/), which permits unrestricted use and redistribution provided that the original author and source are credited.

Abstract Organ function depends on tissues adopting the correct architecture. However, insights into organ architecture are currently hampered by an absence of standardized quantitative 3D analysis. We aimed to develop a robust technology to visualize, digitalize, and segment the architecture of two tubular systems in 3D: double resin casting micro computed tomography (DUCT). As proof of principle, we applied DUCT to a mouse model for Alagille syndrome (*Jag1^{Ndr/Ndr}* mice), characterized by intrahepatic bile duct paucity, that can spontaneously generate a biliary system in adulthood. DUCT identified increased central biliary branching and peripheral bile duct tortuosity as two compensatory processes occurring in distinct regions of *Jag1^{Ndr/Ndr}* liver, leading to full reconstitution of wild-type biliary volume and phenotypic recovery. DUCT is thus a powerful new technology for 3D analysis, which can reveal novel phenotypes and provide a standardized method of defining liver architecture in mouse models.

Introduction

The correct three-dimensional (3D) architecture of lumenized structures in our bodies is essential for function and health. The cardiovascular system, lungs, kidneys, liver, and other organs depend on precisely patterned tubular networks. Several diseases are caused by, or result in, alterations in the 3D architecture of lumenized structures. Vascular architecture defects contribute to Alzheimer's disease (Klohs et al., 2014), opportunistic infections cause narrowing of bile ducts in liver (De Angelis et al., 2009), and branching morphogenesis defects in the renal urinary system cause hypertension (Short and Smyth, 2016). In some pathologies, several lumenized structures are affected at once. Visualizing multiple tubular systems in tandem in 3D, in animal disease models, is necessary to allow investigation of how these systems interact in vivo in development, homeostasis, and disease.

BONE

An RNA aptamer restores defective bone growth in FGFR3-related skeletal dysplasia in mice

Takeshi Kimura^{1†}, Michaela Bosakova^{2,3,4†}, Yosuke Nonaka^{5†}, Eva Hrubá⁴, Kie Yasuda¹, Satoshi Futakawa⁵, Takuo Kubota¹, Bohumil Fafílek^{2,3,4}, Tomas Gregor^{2,3}, Sara P. Abraham², Regina Gomolkova^{2,4}, Silvie Belaskova³, Martin Pesl^{2,3,6}, Fabiana Csukasi^{7,8}, Ivan Duran^{7,8}, Masatoshi Fujiwara⁵, Michaela Kavkova⁹, Tomas Zikmund⁹, Josef Kaiser⁹, Marcela Buchtova^{4,10}, Deborah Krakow⁷, Yoshikazu Nakamura^{5,11*}, Keiichi Ozono^{1*}, Pavel Krejci^{2,3,4*}

Copyright © 2021
The Authors, some
rights reserved;
exclusive licensee
American Association
for the Advancement
of Science. No claim
to original U.S.
Government Works

Achondroplasia is the most prevalent genetic form of dwarfism in humans and is caused by activating mutations in FGFR3 tyrosine kinase. The clinical need for a safe and effective inhibitor of FGFR3 is unmet, leaving achondroplasia currently incurable. Here, we evaluated RBM-007, an RNA aptamer previously developed to neutralize the FGFR3 ligand FGF2, for its activity against FGFR3. In cultured rat chondrocytes or mouse embryonal tibia organ culture, RBM-007 rescued the proliferation arrest, degradation of cartilaginous extracellular matrix, premature senescence, and impaired hypertrophic differentiation induced by FGFR3 signaling. In cartilage xenografts derived from induced pluripotent stem cells from individuals with achondroplasia, RBM-007 rescued impaired chondrocyte differentiation and maturation. When delivered by subcutaneous injection, RBM-007 restored defective skeletal growth in a mouse model of achondroplasia. We thus demonstrate a ligand-trap concept of targeting the cartilage FGFR3 and delineate a potential therapeutic approach for achondroplasia and other FGFR3-related skeletal dysplasias.

INTRODUCTION

Achondroplasia (ACH) is the most common dwarfism in humans, occurring in between 1:15,000 and 1:40,000 live births (1). ACH is caused by mutations in the *FGFR3* gene, which encodes a transmembrane receptor tyrosine kinase. Fibroblast growth factor receptor 3 (FGFR3) transduces the communication signals delivered by fibroblast growth factors (FGFs) (2). In addition to ACH, activating mutations in *FGFR3* cause hypochondroplasia, SADDAN (severe achondroplasia with developmental delay and acanthosis nigricans), and lethal thanatophoric dysplasia. These conditions are collectively termed FGFR3-related skeletal dysplasias. In addition, many cases of idiopathic short stature may also be associated with mutations in *FGFR3*, identifying *FGFR3* as a major cause of genetic dwarfism in humans (3).

In ACH, most patients carry the p.G380R substitution in the transmembrane domain of FGFR3 that activates FGFR3 signaling by increasing dimerization and phosphorylation of mutant FGFR3 dimers (4). Aberrant activation of FGFR3 alters several signaling systems necessary for proper chondrocyte proliferation and differentiation such as wingless-related integration site (WNT) pathway,

cytokine/signal transducer and activator of transcription (STAT) signaling, and bone morphogenetic protein (BMP) and Hedgehog signaling (5–7). The complex molecular phenotypes induced by FGFR3 affect chondrocyte behavior, inducing proliferation arrest, degradation of cartilaginous extracellular matrix, and premature senescence. Collectively, these changes lead to disruption of the growth plate cartilage and defective endochondral ossification (8).

No therapy exists for ACH except for growth hormone, which is approved for ACH in Japan and shows limited effect (9). Several experimental approaches for targeting FGFR3 are being tested, including small chemical inhibitors of FGFR3 catalytic activity or biomolecules targeting downstream pathways of FGFR3 signaling (10). The clinical implementation of these inhibitors in ACH is complicated because the disease affects skeletal growth rather than development and, therefore, defects accumulate gradually during a growth period lasting 12 to 14 years. Because of this gradual effect, the prospective FGFR3 inhibitor must remain active during the entire period of the treatment. Toxicity of the FGFR3 therapy is unlikely to be tolerated in ACH, complicating application of chemical FGFR inhibitors (11). Alternative approaches must therefore be developed to target FGFR3 and its signaling, either alone or in combination with drugs currently in clinical evaluation for ACH.

When overexpressed in vitro, the FGFR3-G380R has a higher propensity for ligand-independent activation compared to wild-type FGFR3 (4). However, the FGFR3 is produced in low quantities in chondrocytes in vivo and thus the FGF ligand is necessary to activate both wild-type and FGFR3-G380R or their heterodimers existing in chondrocytes (12). Neutralization of FGF may therefore be a viable option to treat ACH. An RNA aptamer RBM-007, designed to neutralize the cognate FGFR3 ligand, FGF2, was recently developed. RBM-007 is composed of 36 nucleotides and binds stably and specifically to FGF2 but not to the other FGFs (13, 14). The K_d (dissociation constant) values of RBM-007 for FGF2s from human, rat, and mouse ranged between 2 and 7 pM, indicating high-affinity binding. RBM-007 blocked FGF2 interaction with FGFR1 to FGFR4,

¹Department of Pediatrics, Osaka University Graduate School of Medicine, 565-0871 Osaka, Japan. ²Department of Biology, Faculty of Medicine, Masaryk University, 62500 Brno, Czech Republic. ³International Clinical Research Center, St. Anne's University Hospital, 65691 Brno, Czech Republic. ⁴Institute of Animal Physiology and Genetics, Czech Academy of Sciences, 60200 Brno, Czech Republic. ⁵RIBOMIC Inc., Tokyo 108-0071, Japan. ⁶First Department of Internal Medicine-Cardioangiopathy, St. Anne's University Hospital, Masaryk University, 65691 Brno, Czech Republic. ⁷Department of Orthopaedic Surgery, University of California Los Angeles, Los Angeles, CA 90095, USA. ⁸Networking Research Center on Bioengineering, Biomaterials, and Nanomedicine (CIBER-BBN)-LABRET, University of Málaga, IBIMA-BIONAND, 29071 Málaga, Spain. ⁹Central European Institute of Technology, Brno University of Technology, 61200 Brno, Czech Republic. ¹⁰Department of Experimental Biology, Faculty of Science, Masaryk University, 62500 Brno, Czech Republic. ¹¹Institute of Medical Science, University of Tokyo, Tokyo 108-8639, Japan.

*Corresponding author. Email: nak@ims.u-tokyo.ac.jp (Y.N.); keioz@ped.med.osaka-u.ac.jp (K.O.); krejci@med.muni.cz (P.K.)

†These authors contributed equally to this work.



Article

Lumbar Interbody Fusion Conducted on a Porcine Model with a Bioresorbable Ceramic/Biopolymer Hybrid Implant Enriched with Hyperstable Fibroblast Growth Factor 2

Milan Krticka ¹, Ladislav Planka ², Lucy Vojtova ^{3,*}, Vladimír Nekuda ¹, Premysl Stastny ³, Radek Sedlacek ⁴, Adam Brinek ³, Michaela Kavkova ³, Eduard Gopfert ⁵, Vera Hedvicakova ^{6,7}, Michala Rampichova ^{6,7}, Leos Kren ⁸, Kvetoslava Liskova ⁸, Daniel Ira ¹, Jana Dorazilová ³, Tomas Suchy ⁹, Tomas Zikmund ³, Jozef Kaiser ³, David Stary ², Martin Faldyna ⁵ and Martin Trunec ³

- ¹ Trauma Surgery Department, Faculty of Medicine, Masaryk University and The University Hospital Brno, 625 00 Brno, Czech Republic; krticka.milan@fnbrno.cz (M.K.); nekuda.vladimir@fnbrno.cz (V.N.); ira.daniel@fnbrno.cz (D.I.)
- ² Department of Paediatric Surgery, Orthopedics and Traumatology, Faculty of Medicine, Masaryk University and The University Hospital Brno, 662 63 Brno, Czech Republic; plank.ladislav@fnbrno.cz (L.P.); stary.david@fnbrno.cz (D.S.)
- ³ CEITEC-Central European Institute of Technology, Brno University of Technology, 612 00 Brno, Czech Republic; premyl.stastny@ceitec.vutbr.cz (P.S.); adam.brinek@ceitec.vutbr.cz (A.B.); michaela.kavkova@ceitec.vutbr.cz (M.K.); jana.dorazilova@ceitec.vutbr.cz (J.D.); tomas.zikmund@ceitec.vutbr.cz (T.Z.); jozef.kaiser@ceitec.vutbr.cz (J.K.); martin.trunec@ceitec.vutbr.cz (M.T.)
- ⁴ Department of Mechanics, Biomechanics and Mechatronics, Faculty of Mechanical Engineering, Czech Technical University in Prague, 160 00 Prague, Czech Republic; radek.sedlacek@fs.cvut.cz
- ⁵ Veterinary Research Institute, 621 00 Brno, Czech Republic; gopfert@vri.cz (E.G.); faldyna@vri.cz (M.F.)
- ⁶ University Center for Energy Efficient Buildings, Czech Technical University in Prague, 273 43 Buzehrad, Czech Republic; vera.hedvicakova@iem.cas.cz (V.H.); michala.rampichova@iem.cas.cz (M.R.)
- ⁷ Department of Tissue Engineering, Institute of Experimental Medicine of the Czech Academy of Sciences, Videnska 1083, 142 20 Prague, Czech Republic
- ⁸ Department of Pathology, Faculty of Medicine of Masaryk University and The University Hospital Brno, 625 00 Brno, Czech Republic; kren.leos@fnbrno.cz (L.K.); liskova.kvetoslava@fnbrno.cz (K.L.)
- ⁹ Department of Composites and Carbon Materials, Institute of Rock Structure and Mechanics, The Czech Academy of Sciences, 182 09 Prague, Czech Republic; suchyt@irsm.cas.cz
- * Correspondence: lucy.vojtova@ceitec.vutbr.cz; Tel.: +420-54114-9832



Citation: Krticka, M.; Planka, L.; Vojtova, L.; Nekuda, V.; Stastny, P.; Sedlacek, R.; Brinek, A.; Kavkova, M.; Gopfert, E.; Hedvicakova, V.; et al. Lumbar Interbody Fusion Conducted on a Porcine Model with a Bioresorbable Ceramic/Biopolymer Hybrid Implant Enriched with Hyperstable Fibroblast Growth Factor 2. *Biomedicines* **2021**, *9*, 733. <https://doi.org/10.3390/biomedicines9070733>

Academic Editor: Jessika Bertacchini

Received: 6 June 2021

Accepted: 22 June 2021

Published: 25 June 2021

Publisher's Note: MDPI stays neutral with regard to jurisdictional claims in published maps and institutional affiliations.



Copyright: © 2021 by the authors. Licensee MDPI, Basel, Switzerland. This article is an open access article distributed under the terms and conditions of the Creative Commons Attribution (CC BY) license (<https://creativecommons.org/licenses/by/4.0/>).

Abstract: Many growth factors have been studied as additives accelerating lumbar fusion rates in different animal models. However, their low hydrolytic and thermal stability both in vitro and in vivo limits their workability and use. In the proposed work, a stabilized vasculogenic and prohealing fibroblast growth factor-2 (FGF2-STAB[®]) exhibiting a functional half-life in vitro at 37 °C more than 20 days was applied for lumbar fusion in combination with a bioresorbable scaffold on porcine models. An experimental animal study was designed to investigate the intervertebral fusion efficiency and safety of a bioresorbable ceramic/biopolymer hybrid implant enriched with FGF2-STAB[®] in comparison with a tricortical bone autograft used as a gold standard. Twenty-four experimental pigs underwent L2/3 discectomy with implantation of either the tricortical iliac crest bone autograft or the bioresorbable hybrid implant (BHI) followed by lateral intervertebral fixation. The quality of spinal fusion was assessed by micro-computed tomography (micro-CT), biomechanical testing, and histological examination at both 8 and 16 weeks after the surgery. While 8 weeks after implantation, micro-CT analysis demonstrated similar fusion quality in both groups, in contrast, spines with BHI involving inorganic hydroxyapatite and tricalcium phosphate along with organic collagen, oxidized cellulose, and FGF2-STAB[®] showed a significant increase in a fusion quality in comparison to the autograft group 16 weeks post-surgery ($p = 0.023$). Biomechanical testing revealed significantly higher stiffness of spines treated with the bioresorbable hybrid implant group compared to the autograft group ($p < 0.05$). Whilst histomorphological evaluation showed significant progression of new bone formation in the BHI group besides non-union and fibrocartilage tissue formed in the autograft



Nerve-associated Schwann cell precursors contribute extracutaneous melanocytes to the heart, inner ear, supraorbital locations and brain meninges

Marketa Kaucka¹ · Bara Szarowska² · Michaela Kavkova³ · Maria Eleni Kastriti^{2,4} · Polina Kameneva⁴ · Inga Schmidt¹ · Lucie Peskova⁵ · Alberto Joven Araus⁶ · Andras Simon⁶ · Jozef Kaiser³ · Igor Adameyko^{2,4}

Received: 28 May 2020 / Revised: 7 June 2021 / Accepted: 18 June 2021 / Published online: 18 July 2021
© The Author(s) 2021

Abstract

Melanocytes are pigmented cells residing mostly in the skin and hair follicles of vertebrates, where they contribute to colouration and protection against UV-B radiation. However, the spectrum of their functions reaches far beyond that. For instance, these pigment-producing cells are found inside the inner ear, where they contribute to the hearing function, and in the heart, where they are involved in the electrical conductivity and support the stiffness of cardiac valves. The embryonic origin of such extracutaneous melanocytes is not clear. We took advantage of lineage-tracing experiments combined with 3D visualizations and gene knockout strategies to address this long-standing question. We revealed that Schwann cell precursors are recruited from the local innervation during embryonic development and give rise to extracutaneous melanocytes in the heart, brain meninges, inner ear, and other locations. In embryos with a knockout of the *EdnrB* receptor, a condition imitating Waardenburg syndrome, we observed only nerve-associated melanoblasts, which failed to detach from the nerves and to enter the inner ear. Finally, we looked into the evolutionary aspects of extracutaneous melanocytes and found that pigment cells are associated mainly with nerves and blood vessels in amphibians and fish. This new knowledge of the nerve-dependent origin of extracutaneous pigment cells might be directly relevant to the formation of extracutaneous melanoma in humans.

Keywords Extracutaneous pigment cell · Targeted recruitment · Endothelin 3 and endothelin receptor B · Glial precursor · Peripheral nerves · Hypopigmentation-associated deafness

Abbreviations

SC	Schwann cell
SCP	Schwann cell precursor
NCC	Neural crest cell
EdnrB	Endothelin receptor B
EDN3	Endothelin 3
DRG	Dorsal root ganglion

✉ Marketa Kaucka
kaucka@evolbio.mpg.de

✉ Igor Adameyko
igor.adameyko@ki.se

¹ Max Planck Institute for Evolutionary Biology, Plön, Germany

² Department of Neuroimmunology, Center for Brain Research, Medical University Vienna, Vienna, Austria

³ Central European Institute of Technology BUT, Brno, Czech Republic

⁴ Department of Physiology and Pharmacology, Karolinska Institutet, Stockholm, Sweden

⁵ Department of Histology and Embryology, Masaryk University, Brno, Czech Republic

⁶ Department of Cell and Molecular Biology, Karolinska Institutet, Stockholm, Sweden

Introduction

Melanocytes inhabit the skin, hair follicles, and the iris of the eye [1–4]. These cells are responsible for the protection from UV radiation damage and provide colour to the skin or fur, which is crucial for various aspects of the animal's life, including display and camouflage [4–7]. However, melanocytes are also present in locations deep inside the body that are not directly exposed to UV radiation. These extracutaneous pigment cells are found in the *stria vascularis* of the inner ear, in the leptomeninges,

Loss of Sprouty Produces a Ciliopathic Skeletal Phenotype in Mice Through Upregulation of Hedgehog Signaling

Eva Hruba,^{1,2} Michaela Kavkova,³ Linda Dalecka,^{4,5} Miloš Macholan,¹ Tomas Zikmund,³ Miroslav Varecha,⁶ Michaela Bosakova,^{1,6} Jozef Kaiser,³ Pavel Krejci,^{1,6} Maria Hovorakova,⁴ and Marcela Buchtova^{1,2}

¹Institute of Animal Physiology and Genetics, Czech Academy of Sciences, Brno, Czech Republic

²Department of Experimental Biology, Faculty of Science, Masaryk University, Brno, Czech Republic

³Central European Institute of Technology, Brno University of Technology, Brno, Czech Republic

⁴Institute of Histology and Embryology, First Faculty of Medicine, Charles University, Prague, Czech Republic

⁵Department of Cell Biology, Faculty of Science, Charles University, Prague, Czech Republic

⁶Department of Biology, Faculty of Medicine, Masaryk University, Brno, Czech Republic

ABSTRACT

The Sprouty family is a highly conserved group of intracellular modulators of receptor tyrosine kinase (RTK)-signaling pathways, which have been recently linked to primary cilia. Disruptions in the structure and function of primary cilia cause inherited disorders called ciliopathies. We aimed to evaluate *Sprouty2* and *Sprouty4* gene-dependent alterations of ciliary structure and to focus on the determination of its association with Hedgehog signaling defects in chondrocytes. Analysis of the transgenic mice phenotype with *Sprouty2* and *Sprouty4* deficiency revealed several defects, including improper endochondral bone formation and digit patterning, or craniofacial and dental abnormalities. Moreover, reduced bone thickness and trabecular bone mass, skull deformities, or chondroma-like lesions were revealed. All these pathologies might be attributed to ciliopathies. Elongation of the ciliary axonemes in embryonic and postnatal growth plate chondrocytes was observed in *Sprouty2*^{-/-} and *Sprouty2*^{+/-}/*Sprouty4*^{-/-} mutants compared with corresponding littermate controls. Also, cilia-dependent Hedgehog signaling was upregulated in *Sprouty2/4* mutant animals. *Ptch1* and *Ihh* expression were upregulated in the autopodium and the proximal tibia of *Sprouty2*^{-/-}/*Sprouty4*^{-/-} mutants. Increased levels of the GLI3 repressor (GLI3R) form were detected in *Sprouty2/4* mutant primary fibroblast embryonic cell cultures and tissues. These findings demonstrate that mouse lines deficient in Sprouty proteins manifest phenotypic features resembling ciliopathic phenotypes in multiple aspects and may serve as valuable models to study the association between overactivation of RTK and dysfunction of primary cilia during skeletogenesis. © 2021 American Society for Bone and Mineral Research (ASBMR).

KEY WORDS: BONE QCT/ μ CT; ANALYSIS/QUANTITATION OF BONE; GENETIC ANIMAL MODELS; MOLECULAR PATHWAYS – DEVELOPMENT; LIMB PATTERNING; BONE MODELING AND REMODELING; HEDGEHOG; CELL/TISSUE SIGNALING

Introduction

Sprouty protein was first identified in *Drosophila* as an inhibitor of *breathless*, the fly equivalent of the human fibroblast growth factor receptor that functions throughout the development in tracheal branching.⁽¹⁾ Based on sequence similarity, subsequent research identified four orthologues (*Sprouty1*–*Sprouty4*) of *Drosophila Sprouty* (*dSprouty*) in mammals. Among these, *Sprouty2* exhibits the highest degree of homology with *dSprouty*.⁽²⁾ Expression patterns for mammalian Sprouty isoforms were found to exhibit a strictly local expression pattern in vertebrate embryos. In some cases, expression placement appeared

to be remarkably coincident with known sites of receptor tyrosine kinase (RTK) signaling, which includes fibroblast growth factor (FGF) signaling.^(3–5) However, some Sprouty isoforms such as Sprouty2 are expressed more ubiquitously.^(3,6) Sprouty genes are expressed in several organs throughout development such as craniofacial structures including the brain, nasal epithelium, cochlea, vibrissal follicles, teeth, salivary glands, lungs, digestive tract, kidneys, and limb buds.⁽⁵⁾ At later developmental stages, mouse *Sprouty2* and *Sprouty4* mRNA transcripts were detected in cartilage and bone tissues.⁽⁷⁾ Notably, the distributions of different Sprouty isoforms vary in particular compartments of organs, including the epithelium and mesenchyme. Such

Received in original form December 11, 2020; revised form August 13, 2021; accepted August 18, 2021.

Address correspondence to: Marcela Buchtova, PhD, Laboratory of Molecular Morphogenesis, Institute of Animal Physiology and Genetics, v.v.i., Czech Academy of Sciences, Veveří 97, 602 00 Brno, Czech Republic. E-mail: buchtova@iach.cz

Additional Supporting Information may be found in the online version of this article.

Journal of Bone and Mineral Research, Vol. 36, No. 11, November 2021, pp 2258–2274.

DOI: 10.1002/jbmr.4427

© 2021 American Society for Bone and Mineral Research (ASBMR).

DUCT: Double Resin Casting followed by Micro-Computed Tomography for 3D Liver Analysis

Simona Hankeova^{*1}, Jakub Salplachta^{*2}, Noemi Van Hul¹, Michaela Kavkova², Afshan Iqbal¹, Tomas Zikmund², Jozef Kaiser², Emma R. Andersson¹

¹ Karolinska Institutet ² Central European Institute of Technology

*These authors contributed equally

Corresponding Authors

Jozef Kaiser

jozef.kaiser@ceitec.vutbr.cz

Emma R. Andersson

emma.andersson@ki.se

Citation

Hankeova, S., Salplachta, J., Van Hul, N., Kavkova, M., Iqbal, A., Zikmund, T., Kaiser, J., Andersson, E.R. DUCT: Double Resin Casting followed by Micro-Computed Tomography for 3D Liver Analysis. *J. Vis. Exp.* (175), e62941, doi:10.3791/62941 (2021).

Date Published

September 28, 2021

DOI

10.3791/62941

URL

jove.com/video/62941

Abstract

The liver is the biggest internal organ in humans and mice, and high auto-fluorescence presents a significant challenge for assessing the three-dimensional (3D) architecture of the organ at the whole-organ level. Liver architecture is characterized by multiple branching lumenized structures, which can be filled with resin, including vascular and biliary trees, establishing a highly stereotyped pattern in the otherwise hepatocyte-rich parenchyma. This protocol describes the pipeline for performing double resin casting micro-computed tomography, or "DUCT". DUCT entails injecting the portal vein and common bile duct with two different radiopaque synthetic resins, followed by tissue fixation. Quality control by clearing one lobe, or the entire liver, with an optical clearing agent, allows for pre-screening of suitably injected samples. In the second part of the DUCT pipeline, a lobe or the whole liver can be used for micro-computed tomography (microCT) scanning, (semi-)automated segmentation, and 3D rendering of the portal venous and biliary networks. MicroCT results in 3D coordinate data for the two resins allowing for qualitative as well as quantitative analysis of the two systems and their spatial relationship. DUCT can be applied to postnatal and adult mouse liver and can be further extended to other tubular networks, for example, vascular networks and airways in the lungs.

Introduction

Organ resin casting is a technique that dates back to the 17th century¹. One of the first examples of modern resin casting was performed on the human liver from an autopsy. Intrahepatic bile ducts were filled with a contrast agent mixed with gelatin, followed by imaging with an x-ray CT scan².

The aim of the DUCT technique is to visualize, digitalize and analyze two tubular resin-casted networks, in tandem, in 3D.

DUCT is based on the extensive existing knowledge of single-system liver resin casting^{3,4,5,6,7,8} and extends to simultaneous 3D visualization and analysis of two systems⁹.



Sex differences and risk factors for bleeding in Alagille syndrome

Simona Hankeova^{1,2} , Noemi Van Hul¹ , Jakub Laznovsky³ , Elisabeth Verboven¹, Katrin Mangold¹, Naomi Hensens^{1,4} , Csaba Adori⁵ , Elvira Verhoef^{1,4} , Tomas Zikmund³, Feven Dawit⁶, Michaela Kavkova³, Jakub Salplachta³, Marika Sjöqvist¹, Bengt R Johansson⁷ , Mohamed G Hassan^{8,9} , Linda Fredriksson¹⁰, Karsten Baumgärtel¹¹, Vitezslav Bryja² , Urban Lendahl¹ , Andrew Jheon⁸, Florian Alten¹², Kristina Teär Fahnehjelm^{13,14}, Björn Fischler⁶, Jozef Kaiser³ & Emma R Andersson^{1,*}

Abstract

Spontaneous bleeds are a leading cause of death in the pediatric *JAG1*-related liver disease Alagille syndrome (ALGS). We asked whether there are sex differences in bleeding events in patients, whether *Jag1*^{Ndr/Ndr} mice display bleeds or vascular defects, and whether discovered vascular pathology can be confirmed in patients non-invasively. We performed a systematic review of patients with ALGS and vascular events following PRISMA guidelines, in the context of patient sex, and found significantly more girls than boys reported with spontaneous intracranial hemorrhage. We investigated vascular development, homeostasis, and bleeding in *Jag1*^{Ndr/Ndr} mice, using retina as a model. *Jag1*^{Ndr/Ndr} mice displayed sporadic brain bleeds, a thin skull, tortuous blood vessels, sparse arterial smooth muscle cell coverage in multiple organs, which could be aggravated by hypertension, and sex-specific venous defects. Importantly, we demonstrated that retinographs from patients display similar characteristics with significantly increased vascular tortuosity. In conclusion, there are clinically important sex differences in vascular disease in ALGS, and retinography allows non-invasive vascular analysis in patients. Finally, *Jag1*^{Ndr/Ndr} mice represent a new model for vascular compromise in ALGS.

Keywords Alagille syndrome; Bleeding; Jagged1; Notch; Vasculature

Subject Categories Cardiovascular System; Vascular Biology & Angiogenesis

DOI 10.15252/emmm.202215809 | Received 1 February 2022 | Revised 27

September 2022 | Accepted 5 October 2022 | Published online 8 November 2022

EMBO Mol Med (2022) 14: e15809

Introduction

Alagille syndrome (ALGS) is a pediatric disorder characterized by liver and heart defects, vertebral abnormalities, distinctive facial features, and posterior embryotoxon (Alagille *et al*, 1975; Emerick *et al*, 1999). However, up to 25% of deaths in these patients are attributed to intracranial hemorrhage (Emerick *et al*, 1999; Quiros-Tejeira *et al*, 1999; Kamath *et al*, 2004). Vascular defects in ALGS represent a significant burden of the disease (Hoffenberg *et al*, 1995; Emerick *et al*, 1999; Lykavieris *et al*, 2003; Kamath *et al*, 2004) and lead to transplant-associated complications (Kamath *et al*, 2004). It is currently not well understood why some patients experience spontaneous bleeds. No animal model has been reported for ALGS bleeding, and risk factors for bleeding have not been systematically addressed. Furthermore, vascular disease is currently assessed in patients using computed tomography (CT) or magnetic resonance imaging which necessitates exposure to radiation and can require sedation, making analysis in pediatric patients medically and ethically challenging.

Alagille syndrome is caused by mutations in the Notch ligand *JAGGED1* or the receptor *NOTCH2* (Li *et al*, 1997; Oda *et al*, 1997;

1 Department of Cell and Molecular Biology, Karolinska Institutet, Stockholm, Sweden

2 Department of Experimental Biology, Masaryk University, Brno, Czech Republic

3 CEITEC – Central European Institute of Technology, Brno University of Technology, Brno, Czech Republic

4 University of Applied Sciences Utrecht, Utrecht, The Netherlands

5 Department of Neuroscience, Karolinska Institutet, Stockholm, Sweden

6 Department of Pediatrics, Clinical Science, Intervention and Technology (CLINTEC), Karolinska Institutet and Karolinska University Hospital, Huddinge, Sweden

7 EM Unit, Institute of Biomedicine, University of Gothenburg, Gothenburg, Sweden

8 University of San Francisco, San Francisco, CA, USA

9 Department of Orthodontics, Faculty of Dentistry, Assiut University, Assiut, Egypt

10 Department of Medical Biochemistry and Biophysics, Karolinska Institutet, Stockholm, Sweden

11 Traver Therapeutics, San Diego, CA, USA

12 Department of Ophthalmology, University of Muenster Medical Center, Münster, Germany

13 Department of Pediatric Ophthalmology, Strabismus, Electrophysiology and Ocular Oncology, St. Erik Eye Hospital, Karolinska Institutet, Stockholm, Sweden

14 Department of Clinical Neuroscience, Karolinska Institutet, Stockholm, Sweden

*Corresponding author. Tel: +46852487360; E-mail: emma.andersson@ki.se

Altered developmental programs and oriented cell divisions lead to bulky bones during salamander limb regeneration

Received: 18 March 2021

Accepted: 14 October 2022

Published online: 14 November 2022

 Check for updates

Marketa Kauccka ^{1,17}, Alberto Joven Arous ^{2,17}, Marketa Tesarova ³, Joshua D. Currie⁴, Johan Boström⁵, Michaela Kavkova ³, Julian Petersen^{5,6}, Zeyu Yao², Anass Bouchnita^{7,8}, Andreas Hellander⁷, Tomas Zikmund ³, Ahmed Elewa^{2,9}, Phillip T. Newton ^{10,11}, Ji-Feng Fei ^{12,13}, Andrei S. Chagin ^{14,15}, Kaj Fried¹⁶, Elly M. Tanaka ¹², Jozef Kaiser ³, András Simon ²  & Igor Adameyko ^{5,14} 

There are major differences in duration and scale at which limb development and regeneration proceed, raising the question to what extent regeneration is a recapitulation of development. We address this by analyzing skeletal elements using a combination of micro-CT imaging, molecular profiling and clonal cell tracing. We find that, in contrast to development, regenerative skeletal growth is accomplished based entirely on cartilage expansion prior to ossification, not limiting the transversal cartilage expansion and resulting in bulkier skeletal parts. The oriented extension of salamander cartilage and bone appear similar to the development of basicranial synchondroses in mammals, as we found no evidence for cartilage stem cell niches or growth plate-like structures during neither development nor regeneration. Both regenerative and developmental ossification in salamanders start from the cortical bone and proceeds inwards, showing the diversity of schemes for the synchrony of cortical and endochondral ossification among vertebrates.

Salamanders (such as newts and the axolotl) are the only tetrapods that regenerate entire limbs during their lifespan¹. Limb regeneration starts with scarless wound healing and proceeds with the subsequent formation of a blastema that gives rise to lost limb elements distal to the plane of amputation^{2,3}. Single-cell sequencing data in axolotl

showed that a majority of blastema cells are funneled through a transient embryonic limb bud-like state before re-differentiation to various tissues^{1,4}. Although this transient cell state indicates that limb regeneration is a recapitulation of embryonic development, regeneration has distinctive features. One such process is reversing the terminally

¹Max Planck Institute for Evolutionary Biology, Plön 24306, Germany. ²Department of Cell and Molecular Biology, Biomedicum, Karolinska Institute, Stockholm 17165, Sweden. ³Central European Institute of Technology, Brno University of Technology, Brno 61200, Czech Republic. ⁴Department of Biology, Wake Forest University, Winston-Salem, NC, USA. ⁵Department of Neuroimmunology, Center for Brain Research, Medical University Vienna, Vienna 1090, Austria. ⁶Department of Orthodontics, University of Leipzig Medical Center, Leipzig 04103, Germany. ⁷Department of Information Technology, Uppsala University, Uppsala, Sweden. ⁸Department of Mathematical Sciences, The University of Texas at El Paso, El Paso, TX 79902, USA. ⁹Department of Genetics, Microbiology and Statistics, Faculty of Biology, University of Barcelona, Barcelona, Spain. ¹⁰Department of Women's and Children's Health, Karolinska Institute, Solna, Sweden. ¹¹Astrid Lindgren Children's Hospital, Karolinska University Hospital, Solna, Sweden. ¹²The Research Institute of Molecular Pathology (IMP), Vienna 1030, Austria. ¹³Department of Pathology, Guangdong Provincial People's Hospital, Guangdong Academy of Medical Sciences, Guangzhou 510080, China. ¹⁴Department of Physiology and Pharmacology, Karolinska Institutet, Stockholm 17165, Sweden. ¹⁵Department of Internal Medicine and Clinical Nutrition, University of Gothenburg, Göteborg 41346, Sweden. ¹⁶Department of Neuroscience, Biomedicum, Karolinska Institute, Stockholm 17165, Sweden. ¹⁷These authors contributed equally: Marketa Kauccka, Alberto Joven Arous. ✉ e-mail: andras.simon@ki.se; igor.adameyko@ki.se

A previously uncharacterized Factor Associated with Metabolism and Energy (FAME/C14orf105/CCDC198/1700011H14Rik) is related to evolutionary adaptation, energy balance, and kidney physiology

Received: 24 September 2021

Accepted: 11 May 2023

Published online: 29 May 2023

 Check for updates

A list of authors and their affiliations appears at the end of the paper

In this study we use comparative genomics to uncover a gene with uncharacterized function (*1700011H14Rik/C14orf105/CCDC198*), which we hereby name *FAME* (Factor Associated with Metabolism and Energy). We observe that *FAME* shows an unusually high evolutionary divergence in birds and mammals. Through the comparison of single nucleotide polymorphisms, we identify gene flow of *FAME* from Neandertals into modern humans. We conduct knockout experiments on animals and observe altered body weight and decreased energy expenditure in *Fame* knockout animals, corresponding to genome-wide association studies linking *FAME* with higher body mass index in humans. Gene expression and subcellular localization analyses reveal that *FAME* is a membrane-bound protein enriched in the kidneys. Although the gene knockout results in structurally normal kidneys, we detect higher albumin in urine and lowered ferritin in the blood. Through experimental validation, we confirm interactions between *FAME* and ferritin and show co-localization in vesicular and plasma membranes.

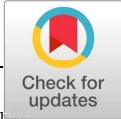
Through natural selection, major animal groups have developed unique mechanisms for adaptations to the environment. The genetic landscape corresponds to developmental, morphological, and physiological adaptations¹. Gene regulatory regions undergo rapid evolutionary change to tune the production of mRNAs encoding the actual effectors of adaptation, the proteins. The gene products also undergo natural selection, which shapes them according to various benefits derived from their functions². Importantly, not all such products, including mainly proteins, are essential for basic embryonic development and the mere survival of animals. Numerous gene knockout experiments in mice have highlighted a cohort of proteins that are functionally important to some extent, and yet the animals can live perfectly without them under beneficial circumstances³. These non-essential proteins convey an adaptive advantage to their hosts when

the animals are exposed to the diversity of challenging natural environments⁴.

Furthermore, these seemingly non-essential genes might become a basis for diverse pathologies or loss of fitness^{5,6}. Finally, similar to essential genes, non-essential genes might be a perfect substrate for evolution, especially for tuning metabolic, stress- and energy-related features. Being non-essential, such genes can evolve much faster to provide the necessary evolvability under intense selective pressure. In extreme cases, the evolution of proteins (especially when it comes to a non-essential group) might result in a complete change of function^{7,8} or a pseudogenization, which occurs in genes involved in dental genesis in birds, turtles, and toothless mammals⁹.

The comparative genomics approach¹⁰ is perfectly designed to elucidate genomic protein-coding and non-coding regions responsible

✉ e-mail: julian.petersen@medizin.uni-leipzig.de; igor.adameyko@meduniwien.ac.at



DEVELOPMENTAL BIOLOGY

Spatiotemporal monitoring of hard tissue development reveals unknown features of tooth and bone development

Marcos Gonzalez Lopez¹, Barbora Huteckova^{2,3†}, Josef Lavicky^{1†}, Nikodem Zezula², Vladislav Rakultsev¹, Vendula Fridrichova¹, Haneen Tuaima¹, Cita Nottmeier⁴, Julian Petersen⁴, Michaela Kavkova^{1,5}, Tomas Zikmund⁵, Jozef Kaiser⁵, Rupali Lav⁶, Haza Star⁶, Vítězslav Bryja², Petr Henyš⁷, Miroslav Vořechovský⁸, Abigail S. Tucker^{6,9}, Jakub Harnos², Marcela Buchtova^{2,3}, Jan Krivanek^{1,*}

Mineralized tissues, such as bones or teeth, are essential structures of all vertebrates. They enable rapid movement, protection, and food processing, in addition to providing physiological functions. Although the development, regeneration, and pathogenesis of teeth and bones have been intensely studied, there is currently no tool to accurately follow the dynamics of growth and healing of these vital tissues in space and time. Here, we present the BEE-ST (Bones and tEEth Spatio-Temporal growth monitoring) approach, which allows precise quantification of development, regeneration, remodeling, and healing in any type of calcified tissue across different species. Using mouse teeth as model the turnover rate of continuously growing incisors was quantified, and role of hard/soft diet on molar root growth was shown. Furthermore, the dynamics of bones and teeth growth in lizards, frogs, birds, and zebrafish was uncovered. This approach represents an effective, highly reproducible, and versatile tool that opens up diverse possibilities in developmental biology, bone and tooth healing, tissue engineering, and disease modeling.

INTRODUCTION

Most of hard tissues in vertebrate bodies are centered on the generation of calcium-based crystalline compounds. This calcium-based biomineralization provides hard tissues, such as bones and teeth, with essential mechanical properties. Therefore, these tissues are responsible for providing a strong supporting body structure, which allows for efficient movement, protects the body surface and internal organs, or, in the case of teeth, ensures hard food processing or predation (1, 2).

Having precise information about growth, regeneration, and biomineralization dynamics in teeth and bones, is one of the basic requirements for research in many fields including developmental biology, tissue healing, bone remodeling, tissue engineering, and disease modeling. One of the major obstacles in current studies is the absence of methodological approaches that enable observation of these dynamic processes, which require high-resolution three-dimensional imaging and temporal information. Current techniques such as micro-computed tomography (microCT), magnetic

resonance, or ground sectioning provide only limited end-point information, missing the spatiotemporal dynamics occurring during the growth, regeneration, and remodeling of calcified structures (3–6). Thus, these approaches do not provide the information uncovering the hard tissue dynamics.

Here, we have developed an approach that enables monitoring of the dynamics of development, growth, healing, and remodeling of any calcified hard tissues in a three-dimensional context and over long periods of time (Fig. 1) This technique was adapted for selected model species across the vertebrates (*Mus musculus* representing mammals, *Chamaeleo calypttratus* representing reptiles, *Gallus gallus* representing birds, *Danio rerio* representing fish, and *Xenopus laevis* representing amphibians) (Fig. 2A).

Our approach is based on the sequential controlled administration of dyes with the natural ability to incorporate into any currently calcifying tissues at designated time points, followed by the clearing of the nondecalcified hard tissue and high-resolution three-dimensional imaging. The ability of substances to incorporate into forming calcified tissues has been known for more than 50 years, first observed in tetracycline antibiotics (7, 8). These substances not only incorporate into newly forming bone tissues but also incorporate into dentin, enamel, and cementum, if administered during their formation (9, 10). Their fluorescence enables the tracking of the exact site of matrix deposition during the period of their presence after in vivo administration. Dozens of these compounds with different binding efficiencies and fluorescence parameters have been described (10). The most commonly used include calcein (green), alizarin (red), xylenol orange, calcein blue, or oxytetracycline (11). In contrast to tetracycline antibiotics, these substances have been reported to be harmless in different animal species, such as mice, guinea pigs, amphibians, rabbits, or dogs at effective

¹Department of Histology and Embryology, Faculty of Medicine, Masaryk University, Brno, Czech Republic. ²Department of Experimental Biology, Faculty of Science, Masaryk University, Brno, Czech Republic. ³Institute of Animal Physiology and Genetics, Czech Academy of Sciences, Brno, Czech Republic. ⁴Department of Orthodontics, University of Leipzig Medical Center, Leipzig, Germany. ⁵Central European Institute of Technology, Brno University of Technology, Brno, Czech Republic. ⁶Centre for Craniofacial and Regenerative Biology, King's College London, London, UK. ⁷Institute of New Technologies and Applied Informatics, Faculty of Mechatronics, Informatics and Interdisciplinary Studies, Technical University of Liberec, Liberec, Czech Republic. ⁸Institute of Structural Mechanics, Faculty of Civil Engineering, Brno University of Technology, Czech Republic. ⁹Institute of Histology and Embryology, First Faculty of Medicine, Charles University, Prague, Czech Republic.

*Corresponding author. Email: jan.krivanek@med.muni.cz

†These authors contributed equally to this work.

Article

SorCS2 binds progranulin to regulate motor neuron development

Pernille Bogetofte Thomasen,^{1,2,8} Alena Salasova,^{1,2,8,*} Kasper Kjaer-Sorensen,³ Lucie Woloszczuková,^{1,2} Josef Lavický,⁴ Hande Login,^{1,2} Jeppe Tranberg-Jensen,^{1,2} Sergio Almeida,^{1,2} Sander Beel,⁵ Michaela Kavková,⁴ Per Qvist,² Mads Kjolby,^{1,2} Peter Lund Ovesen,^{1,2} Stella Nolte,^{1,2} Benedicte Vestergaard,^{1,2} Andreea-Cornelia Udrea,^{1,2} Lene Niemann Nejsum,⁶ Moses V. Chao,⁷ Philip Van Damme,⁵ Jan Krivanek,⁴ Jeremy Dasen,⁷ Claus Oxvig,³ and Anders Nykjaer^{1,2,9,*}

¹Danish Research Institute of Translational Neuroscience DANDRITE-Nordic EMBL Partnership for Molecular Medicine, and Center of Excellence PROMEMO, 8000 Aarhus C, Denmark

²Department of Biomedicine, Aarhus University, 8000 Aarhus C, Denmark

³Department of Molecular Biology and Genetics, Aarhus University, 8000 Aarhus C, Denmark

⁴Department of Histology and Embryology, Faculty of Medicine, Masaryk University, 62500 Brno, Czech Republic

⁵Department of Neurology and Department of Neurosciences, KU Leuven and Center for Brain & Disease Research VIB, 3000 Leuven, Belgium

⁶Department of Clinical Medicine, Aarhus University, 8200 Aarhus N, Denmark

⁷Department of Neuroscience and Physiology, NYU Langone Health, New York, NY 10016, USA

⁸These authors contributed equally

⁹Lead contact

*Correspondence: alena.salasova@biomed.au.dk (A.S.), an@biomed.au.dk (A.N.)

<https://doi.org/10.1016/j.celrep.2023.113333>

SUMMARY

Motor neuron (MN) development and nerve regeneration requires orchestrated action of a vast number of molecules. Here, we identify SorCS2 as a progranulin (PGRN) receptor that is required for MN diversification and axon outgrowth in zebrafish and mice. In zebrafish, SorCS2 knockdown also affects neuromuscular junction morphology and fish motility. In mice, SorCS2 and PGRN are co-expressed by newborn MNs from embryonic day 9.5 until adulthood. Using cell-fate tracing and nerve segmentation, we find that SorCS2 deficiency perturbs cell-fate decisions of brachial MNs accompanied by innervation deficits of posterior nerves. Additionally, adult SorCS2 knockout mice display slower motor nerve regeneration. Interestingly, primitive macrophages express high levels of PGRN, and their interaction with SorCS2-positive motor axon is required during axon pathfinding. We further show that SorCS2 binds PGRN to control its secretion, signaling, and conversion into granulins. We propose that PGRN-SorCS2 signaling controls MN development and regeneration in vertebrates.

INTRODUCTION

Motor neurons (MNs) are the final relay transmitting signals from the central nervous system (CNS) to skeletal muscles, thereby enabling muscle contraction and movement. Their complex development requires a concerted action of trophic factors and guidance cues that determine cell-fate decisions, survival, axonal outgrowth, muscle targeting, and formation of functional neuromuscular junctions (NMJs).^{1,2} These processes rely on fine-tuned, spatiotemporal distribution of ligands, receptors, and transcription factors expressed by MNs themselves and by cells in close proximity, including macrophages or microglia. The same processes are often reactivated during axonal regeneration after nerve injury, supporting neuronal survival and axonal regrowth.^{3–5} Although MN diversification and motor axon outgrowth have been extensively studied, the cell communication and molecular mechanisms involved are not fully understood.

Murine spinal cord MNs develop from proliferating Olig2⁺ progenitors already found in the ventricular zone of ventral neural tube at embryonic day 9.5 (E9.5). They differentiate into postmitotic neurons by E10.5 and migrate laterally to initiate the anterior-posterior patterning. MNs mature in a stepwise manner.^{1,2} From E11, MNs start establishing six distinct anatomical structures called motor columns. While the lateral motor column (LMC) in brachial spinal cord innervates the forelimb, the neighboring medial motor column (MMC) innervates the epaxial muscle of the trunk.^{1,2,6} Nascent motor axons start innervating their target muscles between E11 and E13.5.^{1,2,7} Once they establish major axonal trajectories, MNs within each motor column initiate more refined differentiating and branching programs. They form diverse, muscle-specific clusters called motor pools, which is accompanied by terminal arborization.^{1,2} MN subclasses are distinguished by specific expression of transcription factors including *Islet1/2*, *Foxp1*, *Pea3*, and *Homeobox* proteins. Motor circuits fully mature between postnatal day 4 (P4) and P21.^{1,2,8}



1 **Region-specific gene expression profiling of early mouse mandible uncovered SATB2**
2 **as a key molecule for teeth patterning**

3
4 Petra Nevoránková^{1,2,3}, Marie Šulcová^{1,4}, Michaela Kavková⁵, Simona Moravcová Balková¹,
5 Kristýna Peléšková¹, Daniela Kristeková^{1,4}, Veronika Jakešová¹, Tomáš Zikmund⁵, Jozef Kaiser⁵,
6 Lydie Izakovičová Holá^{2,3}, Michal Kolář⁶, Marcela Buchtová^{1,4}

7
8 1 Laboratory of Molecular Morphogenesis, Institute of Animal Physiology and Genetics, v.v.i.,
9 Czech Academy of Sciences, Brno, Czech Republic

10 2 Department of Stomatology, Faculty of Medicine, Masaryk University, Brno, Czech Republic

11 3 Department of Stomatology, St. Anne's University Hospital Brno, Czech Republic

12 4 Department of Experimental Biology, Faculty of Science, Masaryk University Brno, Czech
13 Republic

14 5 Laboratory of Computed Tomography, CEITEC BUT, Brno, CR

15 6 Laboratory of Genomics and Bioinformatics, Institute of Molecular Genetics of the Czech
16 Academy of Sciences, Prague, Czech Republic

17
18 **Running title:** Gene expression profiling of mandible

19
20 **Corresponding address:**

21 Dr. Marcela Buchtova

22 Laboratory of Molecular Morphogenesis

23 Czech Academy of Sciences, v.v.i.

24 Veveri 97, Brno, 602 00

25 Czech Republic

26 Tel. +420 532 290 157

27 E-mail: buchtova@iach.cz